Atom trapping in non-trivial geometries for micro-fabrication applications

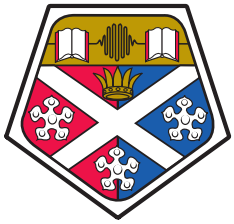

Matthieu Vangeleyn

Department of Physics and SUPA

University of Strathclyde

A thesis presented in the fulfilment of the requirements for the degree of

Doctor of Philosophy

2011

'This thesis is the result of the author's original research. It has been composed by the author and has not been previously submitted for examination which has led to the award of a degree.'

Signed: Date:

A mes parents

Abstract

In this thesis, we investigate several aspects of atom trapping techniques for micro-fabrication applications. In order to create a compact cold atom system, that could be used for e.g. precision sensing, several elements are required. In the case of ^{87}Rb, two lasers are required with a frequency difference in the GHz range. They are used to cool and trap atoms, along with a quadrupole magnetic field, in a magneto-optical trap. Such a system is usually not readily usable for compact and portable applications as it comprises many optical elements.

Direct current modulation of semiconductor lasers is investigated. This technique allows one to use only a single laser, by creating sidebands in the diode optical spectrum. A modulated laser is also required for applications that need two phase locked frequencies. One of these techniques, Coherent Population Trapping, is briefly investigated, using a modulated diode laser, as a way of performing magnetic sensing with compact systems.

A novel geometry for magneto-optical trapping (MOT) in a four beam configuration is presented. A single beam incident is split and steered by a reflector or diffractor element, generating all required beams. A complete theory of the four beam MOT is first developed, followed by the experimental demonstration. A single beam single laser MOT is demonstrated using a mirror pyramid and a modulated laser diode. Sub-Doppler cooling is realised in a four beam MOT with a grating triplet.

Finally, a novel toroidal ring trap is discussed theoretically. Using an ac-coupled conductive loop, atoms can be trapped in an annular time averaged potential that can be used to perform atom interferometry. A small-size version of the trap is presented, making use of radio-frequency dressed potentials to create a micro-fabricated ring trap to be used for portable sensing applications or the study of rotational quantum gases.

Acknowledgements

First, of course, I'd like to thank my two supervisors Aidan and Erling, who have been always present and helpful when I needed (and it happened quite a few times). I really enjoyed working with you guys during that time. Aidan, thanks for all these useful discussions we had when I came in your office and kept you busy for a long time while you had other thing to do. Erling, I really appreciated your way of explaining physics in such clear and simple terms that you make anyone understand any complicated physical process. However, there is one thing I will always disagree with you on, and I'm doing that for all engineers who encounter difficulties communicating with physicists. The truth is

$$\underline{\underline{j}}^2 = -1$$

Even if you're not "officially" one of my supervisors, I am very grateful to Dr. Paul Francis Griffin, PhD in Awesomeness, you're a bit like our big brother. You have been keeping your eye on everything that happened in the labs and in the office, all the time, and you'll been always happy to help. One drawback with you though, you know too many things on every single topic, and sometimes it is a little bit frustrating! Make an effort and stop reading!

Thanks as well to all my fellow PhD buddies: Aline, for all the cool things and s***. — Steeve-Brandon-Bernard-Champion-Seurge, your name sounds a little bit like a detergent — Neal the Rad, I think everything is in the name — Chris, without you, there would have been so many things I would have dropped without noticing them — Aleeeeeeeeeeeeessio (ma!), I hope you finally found a good quality mattress in Antibes. Thanks as well to all those who left for the dark side: Stef, Chuck, Mateusz and Kenneth.

Thanks as well to our two mechanicians, Ewan and Bob, who can turn any piece of bulk metal into a perfectly stabilised and accurate laser mount masterpiece.

Thanks to our electronics technicians: Mark, Ged, John and Ken for their priceless help and advices.

I am also particularly grateful to all the COMETA group members at the Laboratoire de Physique des Lasers, and especially to Hélène Perrin, for the very nice two months I spent with them. Probably, none of the work on the dressed state ring would have been possible without the very good lectures and discussions I had there.

Thanks to Barry Garraway from the University of Sussex who came specially in rainy Scotland to clarify our ideas on the dressed state theory.

I'd like to thank Iain Thayne and Ian McGregor form the University of Glasgow for their valuable help on impedance matching and the possibility to use their facilities to measure the diodes impedance and fabricate the PCBs.

Thanks to Rudy Romain for his precious help on the CPT stuff during last summer. I hope you'll enjoy your PhD in Lille.

Et la petite partie en français maintenant, pour ceux qui n'attendent que ça et qui s'arrêteront de lire ici!. Mes premiers remerciements vont bien sûr à ma môman and mon pôpa, ainsi qu'à mes sœurs Laure et Cécile qui ont toujours été là, même quand ça a pas été évident. J'ai de la chance d'avoir une super famille comme vous. Coucou à Andie aussi et bon début dans la vie, piny!

Merci à mon "beautiful brother" Glenn (et oui, maintenant t'es dans la French part) pour le super temps passé à l'obs et à Nice en général.

Merci aux copains d'Ecosse : Jeff, Laurent, Chau, Emilie, Noah et Stéfie, pour avoir amené un peu de culture local avec vous et l'avoir partagé.

Merci beaucoup à Tof' pour m'avoir orienté dans la bonne direction à la bonne époque, et même si tu fais de la fausse interférométrie! Alors, on le fait où et quand ce grand voyage??

Merci à FIP pour les voix douces de ses animatrices et ses très bonnes musiques qui m'ont accompagné pendant toute la rédaction de cette thèse.

Salut à tous ceux qui sont de l'autre côté de la Manche : Joss, Meuh, Mac, Manu (aussi appelés la fine équipe à ten taouzende kip), Caro, Gidz, Plamen et aussi tous ceux qui ne sont pas cités ici, volontairement ou non, mais qui sauront se reconnaître.

Contents

List of Figures

Chapter 1

Introduction

Experimental atomic physics has seen a huge development in the last three decades, since the first demonstrations of cooling [1] and trapping [2] of neutral atoms. The relatively simple but remarkably ingenious trapping system developed by Steven Chu and co-workers, known as magneto-optical trapping, has opened new horizons with experiments with cold and trapped gases. One of the main achievement of atomic cooling is, of course, the first realisation of Bose-Einstein quantum gases [3, 4] in dilute gases, predicted long ago [5, 6], where all bosonic atoms occupy the same quantum state. An equivalent phase transition has also been observed with fermionic gases [7]. New regimes have been since observed, using quantum gases, such as the Mott insulator [8] or Anderson localisation [9, 10]. The development of magneto-optical trapping, the discovery and understanding of more subtle cooling mechanisms [11, 12, 13, 14] and the realisation of the first BEC [3, 4] were rewarded by Nobel Prizes in 1997 [15, 16, 17] and 2002 [18, 19].

Along with these fundamental investigations, cold atoms are very good candidates for precise sensing applications, such as magnetometry [20, 21], gravimetry [22] or gyrometry [23]. Also, today's atom-based clocks are the most precise available time references [23]. There has been a lot of work to achieve compact and portable sensors [24, 25] and clocks [26].

This thesis investigates different aspects of micro-fabricated atom traps. In Chap. 2, we will investigate current modulation in a semiconductor laser and the

possibilities to maximise the optical component amplitude for compact applications. Indeed, most cold atom applications with alkalis require a magneto-optical trap as the first cooling state, which implies to use two lasers with frequencies roughly separated by the ground states splitting. In the alkalis, this frequency difference is in the GHz range. One way to get a more compact experiment is to make the same laser generate both wavelengths by modulating the current of the diode laser [27]. This results in an optical spectrum containing several frequency components separated by the modulation frequency. These components are in addition phase locked, which is overkill for repumping but required for, e.g. Coherent Population Trapping (CPT), which is one way to achieve compact size magnetometers [24] and clocks [28]. The frequency modulated laser studied in this first chapter will then be used in Chaps. 3 and 4.

As outlined, CPT spectroscopy can be used to create a compact atom based magnetometer. One can probe the energy shift, induced by a local magnetic field, between two hyperfine levels of alkali atoms such as rubidium and consequently deduce the magnetic field amplitude. In Chap. 3, we will briefly develop the theory behind CPT spectroscopy and present preliminarily experimental investigations on CPT spectroscopy as a way to probe dc magnetic fields.

In Chaps. 4 and 5, we introduce a new geometry for small-size Magneto-Optical Trapping. Indeed, most standard MOTs need three pairs of orthogonal counter-propagating laser beams. One can reduce the experiment size by retro-reflecting the MOT beams, but still, this application is far from ideal for compact traps. People have used hollow mirror pyramids [29] to achieve magneto-optical trapping with a single incident beam, thus greatly reducing the experimental apparatus. This scheme has some drawbacks however, that we will discuss in Chap. 5, such as a limited optical access to the atom cloud. On surface atom chips, where optical access is intrinsically limited, one can make a mirror MOT [30] but this requires three independent beams. Based on the original idea from Shimizu *et al.* [31], we present a four beam MOT and a triplet of reflective or diffractive elements to generate all beams from a single incident one. In Chap. 4, we first present the basics of magneto-optical trapping and optical molasses, that is Doppler and sub-Doppler cooling and Zeeman trapping. We then present our theoretical model of the four beam MOT and how trapping is achieved along

the axial and radial directions of the quadrupole magnetic field. In the latter, we discuss how the intensity imbalance between beams, the relative angle between the beams and the change in the beams polarisation impact the trapping and cooling forces. The four beam MOT is then experimentally demonstrated in Chap. 5. Two different configurations are presented, using either mirrors or gratings to split and steer the single incident beam. With the mirrors MOT, we use the frequency modulated laser of Chap. 2 to achieve a compact single beam single laser MOT. The grating configuration constitutes a totally flat apparatus, and is therefore ideal for micro-fabricated applications. Using this scheme, we present the realisation of in-MOT sub-Doppler cooling.

Atom interferometry with quantum gases [32] is based on the wave-like nature of atoms in a degenerate quantum regime. With toroidal traps, one could perform very precise measurements of gravitational and inertial effects by splitting and interfering the waves that propagate along opposite directions along the ring potential. Macroscopic ring traps have been proposed and designed for atom interferometry [33, 34, 35, 36, 37] and nowadays, there is a big run towards microscopic ring traps [38, 39, 40, 41, 42, 43, 44, 45] that could be used, in addition to sensitive interferometry, to study e.g. quantised rotation in superfluids [46, 47]. In Chap. 6, we discuss two different ways to achieve a smooth annular trapping potential based on an ac-magnetically induced toroidal conductor. The first configuration [48] uses a magnetic time average potential and is currently being experimentally implemented at the University of Strathclyde. The second idea relies on dressed state potentials [49] and allows for much smaller ring dimensions, suitable for a micro-fabricated annular trap.

Chapter 2

Optical spectrum modulation in a laser diode

Signal modulation is an aspect of signal processing [50] in which a normally constant signal, the carrier, is modified in time by another signal, the modulating signal, evolving at a slower rate than the carrier. In this sense, modulation has first been used by Samuel Morse as a basic way of communicating: the carrier is an audible signal of constant frequency, and the amplitude is switched off and on in order to transmit bits of information over long distances. Since then different kinds of modulation have been invented by engineers and all of them were first designed to be used as a means of communication. This chapter is mainly intended to give a brief review of the different basic modulation techniques as these constitute an important part of the work presented here, whether for obtaining repumping light from the trapping laser or for Coherent Population Trapping (CPT) spectroscopy that requires two phase locked optical frequencies. As the time evolution of a signal is perturbed, then its frequency spectrum is also modified and one can easily use this feature to engineer, for example, the frequency spectrum of a laser to create the frequency components which would otherwise require more complicated ways. A two-frequency laser for magneto-optical trapping of alkali species (as investigated in Secs. 2.2 and 5.3) obtained by direct modulation of a laser diode is, for instance, an inexpensive alternative of the usual two laser setup. In atomic physics, and more generally in laser sciences,

modulation of a laser is commonly used and the two main applications are the creation of extra frequency components near resonant with atomic transitions (for instance for dual wavelength generation in magneto-optical trapping [27, 51] or to couple different magnetic sub-levels [52, 53]) and frequency locking techniques that require modulation in order to obtain a reference error signal [54]. Diodes used in atomic physics experiments are often put into an external cavity to reduce the laser linewidth. This completely changes the laser's dynamics, and the cavity length has an impact on the modulation amplitude, with a larger sideband amplitude when the cavity round trip time matches the modulation period. Also, we will investigate ways to electronically increase the coupling of the modulation signal into the diode by matching the diode impedance to the one of the transmission line. Finally, one can take advantage of the relaxation oscillations that happen in the GHz range in semiconductor lasers to make the laser resonate with the modulation signal and thus maximise the sidebands amplitude.

There are two main kinds of signal modulation : digital and analog. They relate to the nature of the modulating signal and the way it affects the carrier. Morse code is an example of a digital modulation, as the coded message can have only a discrete number of values (two in this case). Other (and more modern) commonly found digital modulation techniques include amplitude-shift keying (ASK), frequency-shift keying (FSK) and phase-shift keying (PSK). Morse code is a special case of ASK called on-off keying (OOK) In these methods, a message is coded in one of the parameters (amplitude, frequency or phase) of an analog carrier signal, usually a pure sinusoidal wave. This parameters can then take only a certain number of values. Other and more complex modulations can be derived from these simple concepts : quadruple phase-shift keying (QPSK), minimum-shift keying (MSK) or pulse-position modulation (PPM). Digital modulation has proven to be one of the most robust ways of communicating thanks to its inherently reduced sensitivity to any analog noise encountered during transmission. They are therefore mostly used nowadays in a wide range of applications that includes mobile telephony, digital television and radio. For a more complete review of digital modulation techniques, see for example [55].

2.1 Analog modulations of electromagnetic signals

We will now focus on analog modulation only, as these are the techniques used for the work presented here. These modulations, as shown in the name, use an analog signal to modify the waveform of a sinusoidal wave used as the carrier signal. The three main and most simple analog modulations affect either the amplitude (AM), the frequency (FM) or the phase (ΦM) of the carrier signal and as a result, its temporal shape is modified. However, the temporal behaviour is not of great interest compared to what happens in the frequency domain. Indeed, for use in atomic physics, the attractive feature is the creation of extra frequency components in the spectrum of laser light. In the most general case, the electric field of a modulated electromagnetic wave is

$$E(t) = E_0(t)e^{i(\int \omega(t)\mathrm{d}t + \Delta\phi(t))} + \text{c.c.}\ , \tag{2.1}$$

where $E_0(t)$, $\omega(t)$ and $\Delta\phi(t)$ are the (time varying) amplitude, angular frequency and phase of the wave and c.c. is short for complex conjugate. The notation $\Delta\phi$ is used for the phase difference to distinguish from the instantaneous phase ϕ which will be used later. In the following, either terms "angular frequency" or "frequency" will be used when referring to the quantity $\omega = 2\pi\nu$, although the proper naming should be "angular frequency". The spatial dependence has been dropped as only the time behaviour is of interest for the study of the frequency spectrum.

For a non-modulated, monochromatic laser light, E_0 and ω are kept constant, and ϕ may be eliminated as the absolute phase of an electromagnetic signal can always be set to 0 with an appropriate choice of the reference frame. In this case, the frequency spectrum can simply be obtained by Fourier transforming the time signal $E(t)$ and reads

$$\mathscr{F}_E(\omega) = \int_{-\infty}^{+\infty} E(t)e^{-i\omega t}\mathrm{d}t = E_0\ \left(\delta(\omega_0) + \delta(-\omega_0)\right)\ , \tag{2.2}$$

which contains only one (physical) frequency component at $\omega = \omega_0$. Here ω is

the Fourier variable in the frequency space. As a consequence of the linearity of the Fourier transform, any linear superposition of monochromatic waves of the form

$$E_{\mathrm{sup}}(t) = \sum_{\mathrm{n}} E_{\mathrm{n}} e^{i\omega_{\mathrm{n}} t} + \mathrm{c.c.} \tag{2.3}$$

contains only discrete frequency components at $\omega = \omega_{\mathrm{n}}$ with amplitude E_{n}. It will be shown later in this chapter that all three types of modulation with an oscillating modulation signal of frequency ω_{m} result in the creation of sidebands at frequencies $\omega = \omega_0 + k\,\omega_{\mathrm{m}}$ ($k \in \mathbb{Z}$), the amplitudes of which depend on the type of modulation applied. For the following sections, we will discuss the effects of a pure cosine modulating signal on the frequency spectrum of a monochromatic electromagnetic wave and emphasize the differences between all of them.

2.1.1 Amplitude modulation (AM)

In the case of an amplitude modulation, the carrier amplitude is simply multiplied by a modulating signal. The temporal evolution of the waveform is usually

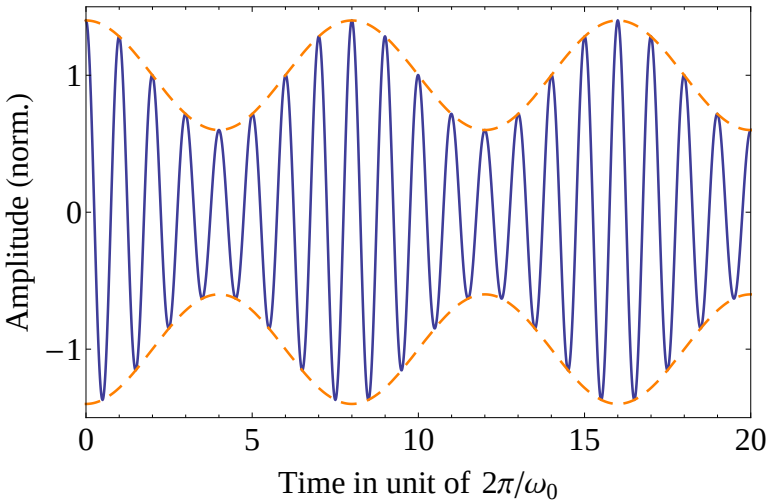

Figure 2.1: Time evolution of an amplitude modulated signal with $\omega_0/\omega_{\mathrm{m}} = 8$ and $m = 0.4$. The orange dashed lines show the variation of the envelope at the frequency ω_{m}.

expressed in the form

$$E_{\mathrm{AM}}(t) = E_0 e^{i\omega_0 t}(1 + m\cos\omega_m t) + \text{c.c.}\ . \tag{2.4}$$

Here, ω_0 and ω_{m} are, respectively, the carrier and modulation frequencies, and the number $0 \leq m \leq 1$ is the AM depth. An example waveform is shown in Fig. 2.1. The frequency spectrum is easily obtained by expressing cos in terms of exponential functions in Eqn. 2.4:

$$E_{\mathrm{AM}}(t) = E_0(e^{i\omega_0 t} + \frac{m}{2}e^{i(\omega_0+\omega_{\mathrm{m}})t} + \frac{m}{2}e^{i(\omega_0-\omega_{\mathrm{m}})t}) + \text{c.c.}\ . \tag{2.5}$$

The spectrum contains, in addition to the carrier, two sidebands of amplitude $m/2$ separated by ω_{m} on each side of the carrier. The case when $m > 1$ is called overmodulation, as the two envelopes (orange dashed lines in Fig. 2.1) cross each other. In signal transmission, this results in distorsion of the modulated signal. Fig. 2.2 shows the representation of an amplitude modulated frequency spectrum on a phase diagram [56]. The angles made by each sideband in the Phase-Quadrature (P-Q) plane with respect to the P axis represents the phase difference of this sideband compared to the carrier at $t = 0$. As time evolves, each

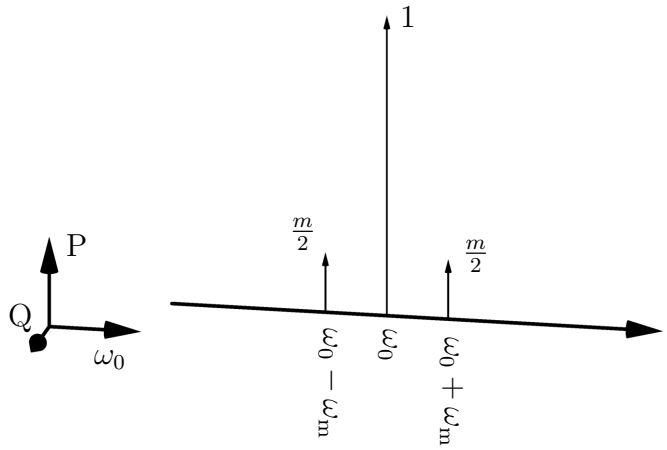

Figure 2.2: Phasor diagram of an amplitude modulated signal with $m = 0.4$.

sideband of order k spins around the frequency axis at the rate $k\,\omega_\mathrm{m}$. AM can be simply seen as a shift of the spectrum of the modulating signal $m\cos\omega_\mathrm{m}t$ (which has two symmetrical positive and negative frequency components of amplitude $m/2$) relative to the carrier frequency ω_0.

2.1.2 Frequency modulation (FM)

For frequency modulation, the instantaneous frequency of the electric field is time modulated:

$$\omega(t) = \omega_0 + \delta\omega\cos(\omega_\mathrm{m}t), \tag{2.6}$$

which gives an instantaneous phase

$$\phi(t) = \int \omega(t)\mathrm{d}t = \omega_0 t + \delta_\mathrm{m}\sin\omega_\mathrm{m}t, \tag{2.7}$$

where $\delta_\mathrm{m} = \frac{\delta\omega}{\omega_\mathrm{m}}$ is the FM depth. The electric field therefore reads

$$E_\mathrm{FM}(t) = E_0 e^{i\omega_0 t}e^{i\delta_\mathrm{m}\sin\omega_\mathrm{m}t} + \text{c.c.}\ . \tag{2.8}$$

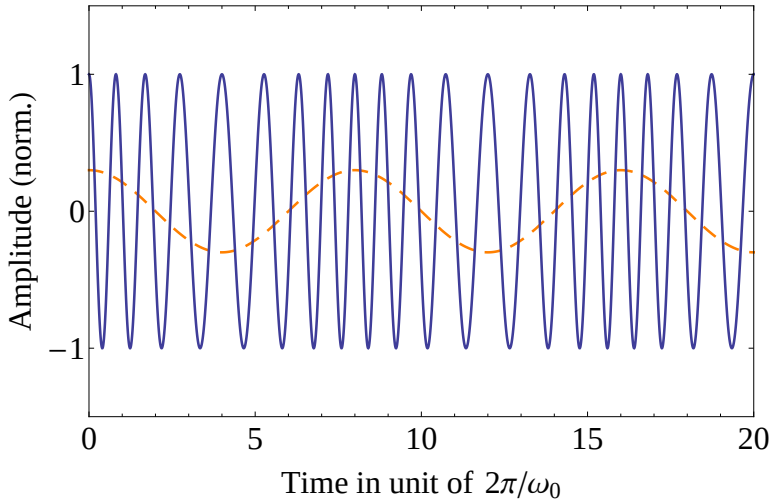

Figure 2.3: Time evolution of a frequency modulated signal with $\omega_0/\omega_\mathrm{m} = 8$ and $\delta_\mathrm{m} = \delta\omega/\omega_\mathrm{m} = 2$. The orange dashed line shows the modulation signal.

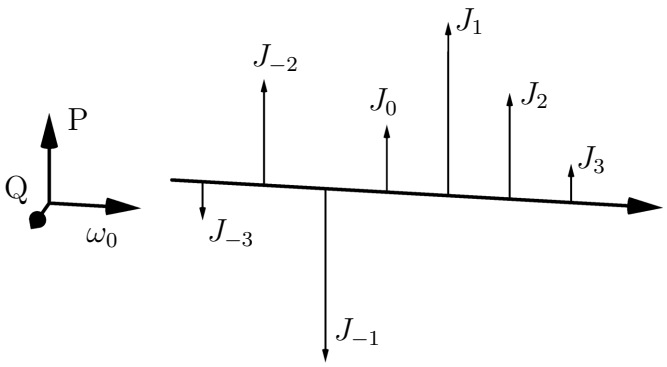

Figure 2.4: Phasor diagram of a frequency modulated signal with $\delta_\mathrm{m} = \delta\omega/\omega_\mathrm{m} = 2$ showing up to the third order sidebands. The frequency information have been left over to clarify the view, and J_k is used to denote $J_k(\delta_\mathrm{m})$.

A typical FM waveform is shown in Fig. 2.3, where the slow varying frequency envelope is clearly visible. Using the Jacobi-Anger expansion [57], the field in Eqn. 2.8 can be expressed as a sum of Bessel function of the first kind $J_k(\delta_\mathrm{m})$ where k is the order of the function:

$$E_\mathrm{FM}(t) = E_0 \sum_{k=-\infty}^{+\infty} J_k(\delta_\mathrm{m}) e^{i(\omega_0 + k\ \omega_\mathrm{m})t} + \text{c.c.}\ . \tag{2.9}$$

This form is more convenient as it shows the creation of sidebands at frequency $k\omega_\mathrm{m}$ compared to the carrier frequency and with amplitudes given by $J_k(\delta_\mathrm{m})$. The spectrum of the modulated signal in Fig. 2.3 is shown in Fig. 2.4 for frequency components $k \in \{-3, 3\}$.

The main difference with amplitude modulation is that, in the present case, the modulated spectrum extends theoretically to infinity. In practice, however, $J_k(\delta_\mathrm{m})$ vanishes very quickly for $k > \delta_\mathrm{m}$, as depicted in Fig. 2.5, and the spectrum containing most of the power can be effectively restricted to $\pm\delta\omega$. It is worth noticing that in the limit of small modulation indices ($\delta_\mathrm{m} \ll 1$), Eqn. 2.8 can be

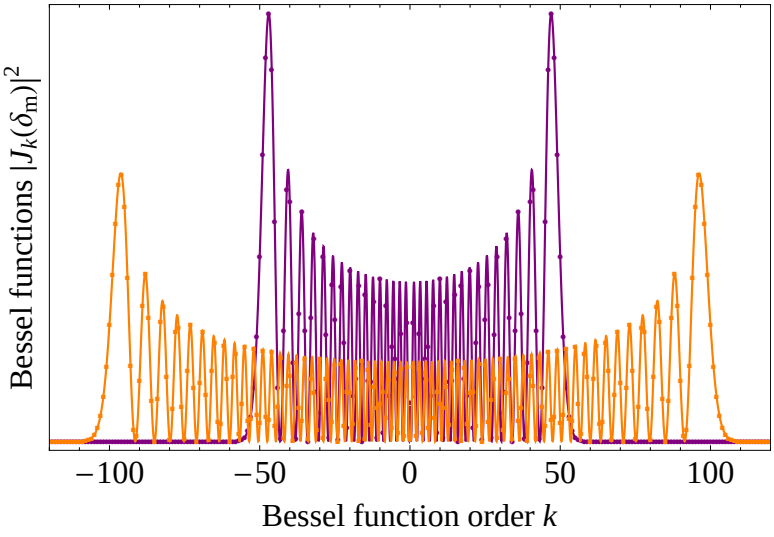

Figure 2.5: Amplitude of the square of the Bessel functions $|J_k(\delta_\mathrm{m})|^2$ as a function of k for $\delta_\mathrm{m} = 50$ (violet circles) and $\delta_\mathrm{m} = 100$ (orange squares) showing the fast decay for $k > \delta_\mathrm{m}$. Points denote the amplitudes for integer values of k and lines show $|J_{|k|}(\delta_\mathrm{m})|^2$ for clarity (taken only for positive k as J_k diverges quickly for non-integer negative values of k).

Taylor-expanded:

$$E_\mathrm{FM}(t) = E_0 e^{i\omega_0 t}(1 + i\delta_\mathrm{m}\sin(\omega_\mathrm{m} t) + o(\delta_\mathrm{m})) + \text{c.c.}\ , \tag{2.10}$$

$$\approx E_0(e^{i\omega_0 t} + \frac{\delta_\mathrm{m}}{2}e^{i(\omega_0+\omega_\mathrm{m})t} - \frac{\delta_\mathrm{m}}{2}e^{i(\omega_0-\omega_\mathrm{m})t}) + \text{c.c.}\ . \tag{2.11}$$

The carrier's amplitude is unchanged and each sideband gets a $\pm\delta_\mathrm{m}/2$ weight. The expression is therefore similar to the one for an AM signal given by Eqn. 2.5 except the lower sideband gets a negative sign.

2.1.3 Phase modulation (ΦM)

In phase modulation, the instantaneous phase is directly modulated:

$$\phi(t) = \int \omega_0 \, \mathrm{d}t + \Delta\phi(t) = \omega_0 t + \delta_\mathrm{m}\cos\omega_\mathrm{m} t, \tag{2.12}$$

where δ_m now represents the ΦM depth. The field reads

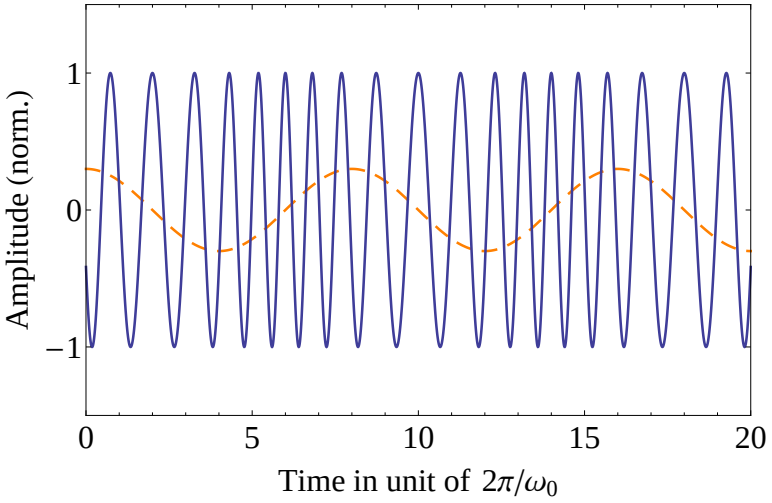

Figure 2.6: Time evolution of a phase modulated signal with $\omega_0/\omega_\mathrm{m} = 8$ and $\delta_\mathrm{m} = 2$ rad. The dashed line shows the modulation signal.

$$E_{\Phi\mathrm{M}}(t) = E_0 e^{i\omega_0 t} e^{i\delta_\mathrm{m}\cos\omega_\mathrm{m} t} + \text{c.c.}\ . \tag{2.13}$$

Comparison between Eqns. 2.8 and 2.13 shows that frequency and phase modulations are closely related. The main difference, other than the definition of the depth (but this does not affect the working principle) is a phase delay of $\pi/2$ that happens for the FM compared to the ΦM, due to the integration in the derivation of the instantaneous phase. This clearly is visible in Fig. 2.6 when compared to Fig. 2.8. The expansion of Eqn. 2.13 using Bessel functions gives a slightly different expression than in the FM case:

$$E_{\Phi\mathrm{M}}(t) = E_0 \sum_{k=-\infty}^{+\infty} i^k J_k(\delta_\mathrm{m}) e^{i(\omega_0 + k\omega_\mathrm{m})t} + \text{c.c.}\ . \tag{2.14}$$

Each component has the same amplitude as in the FM case but gets an extra i^k phase term. Therefore, in the phasor diagram representation 2.7 of ΦM, the k^{th} sideband is rotated by $k\ \pi/2$ clockwise when viewed in the ω_0 axis direction.

As for the frequency modulation, for small modulation depths $\delta_\mathrm{m} \ll 1$, the spectrum reduces to only three components, one carrier of unity amplitude and

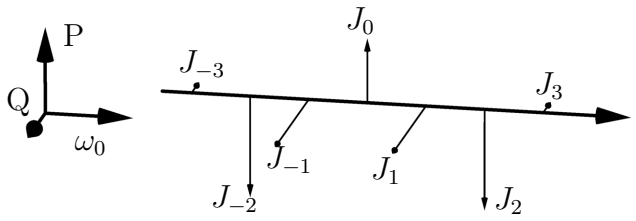

Figure 2.7: Phasor diagram of a phase modulated signal with and $\delta_\mathrm{m} = 2$ rad.

two sidebands of amplitude $i\delta_\mathrm{m}/2$:

$$E_{\Phi\mathrm{M}}(t) = E_0 e^{i\omega_0 t}(1 + i\delta_\mathrm{m}\cos(\omega_\mathrm{m} t) + o(\delta_\mathrm{m})) + \text{c.c.}\ , \tag{2.15}$$

$$\approx E_0(e^{i\omega_0 t} + i\frac{\delta_\mathrm{m}}{2}e^{i(\omega_0+\omega_\mathrm{m})t} + i\frac{\delta_\mathrm{m}}{2}e^{i(\omega_0-\omega_\mathrm{m})t}) + \text{c.c.}\ . \tag{2.16}$$

Although FM and ΦM have the same mathematical expression, they are considered as two different modulations as they are implemented in different ways. For instance, with an electro-optic modulator, the phase is directly modulated, whereas a modulated voltage controlled oscillator gives an FM. Moreover, the modulation depth of a FM is frequency dependent, since $\delta_\mathrm{m} = \delta_\omega/\omega_\mathrm{m}$. Therefore, if the modulation signal has a broad spectrum, then its different frequency components will be transferred with different modulation depths, resulting in a modulated spectrum that can not be obtained with a ΦM, where all frequencies undergo the same modulation depth.

2.1.4 Mixture of modulations and detection

In order to visualise the amount of modulation in a laser, two options are available: monitoring the intensity on a photodetector or directly viewing the amplitude of each sideband on a Fabry-Pérot Interferometer (FPI). The first method could only give information for the AM part. For pure FM and ΦM however, the modulation is eliminated in the calculation of the intensity and only the use of an FPI allows one to measure the square of the amplitude of each spectral component. For an

AM laser, the photodiode signal reads

$$I_{\mathrm{AM}}(t) \propto |E_{\mathrm{AM}}(t)|^2 = |E_0|^2 \left(1 + 2m\cos\omega_{\mathrm{m}}t + \frac{m^2}{2}(1+\cos 2\omega_{\mathrm{m}}t)\right) , \qquad (2.17)$$

and therefore the value of m can be worked out by measuring the amplitude of the component at ω_{m}, either with a narrow band-pass filter or more realistically with a lock-in amplifier technique if access to the modulation frequency is possible. It is also possible to quantify both field and intensity AM by comparing the amplitudes of the ω_{m} and 2 ω_{m} component. However, this requires a good characterisation of the harmonic distortion of the detection chain, as inherent non-linearities of any active electronic equipment tend to bias the measure of the $2\omega_{\mathrm{m}}$ amplitude component. The intensity of each of the spectral components is given for the AM case by

$$I_0 = E_0^2 , \qquad (2.18)$$

$$I_{\pm 1} = \frac{m^2}{4}E_0^2 , \qquad (2.19)$$

and for the FM and ΦM cases by

$$I_k = (J_k\ E_0)^2. \qquad (2.20)$$

It is very hard to distinguish between FM and ΦM experimentally, as both give similar amplitude readings on the measurement system. Although this can be achieved by using a lock-in detection technique and monitoring the two quadratures of the demodulation signal, it requires an accurate knowledge of all delays in the system. A mixture of FM and ΦM has an instantaneous phase of the form

$$\phi_{\mathrm{FM},\Phi\mathrm{M}}(t) = \delta_{\mathrm{FM}}\sin\omega_{\mathrm{m}}t + \delta_{\Phi\mathrm{M}}\cos\omega_{\mathrm{m}}t, \qquad (2.21)$$

$$= \Delta\cos(\omega_{\mathrm{m}}t + \psi), \qquad (2.22)$$

where $\Delta^2 = \delta_{\mathrm{FM}}^2 + \delta_{\Phi\mathrm{M}}^2$ and $\tan\psi = -\delta_{\mathrm{FM}}/\delta_{\Phi\mathrm{M}}$. Thus, the electric field of the mixture reads

$$E_{\mathrm{FM},\Phi\mathrm{M}}(t) = E_0 e^{i\omega_0 t} e^{i\Delta\cos(\omega_\mathrm{m} t+\psi)}, \tag{2.23}$$

$$= E_0 \sum_{k=-\infty}^{+\infty} J_k(\Delta) e^{ik\ \psi} e^{i(\omega_0 + k\ \omega_\mathrm{m})t}. \tag{2.24}$$

Therefore, each spectral component gets a phase delay $k\psi$, but a direct measure of the intensity makes it impossible to determine whether the modulation is pure FM, pure ΦM or if there is a mixture of both. In the case of a mixture of AM and FM (or AM and ΦM) however, it is possible to determine the amount of each modulation. We consider here the general case of a mixture of AM, FM and ΦM. The total electric field can be written

$$E_{\mathrm{A,F},\Phi}(t) = E_0 e^{i\omega_0 t} e^{i\Delta\cos(\omega_\mathrm{m} t+\psi)}(1 + m\cos\omega_\mathrm{m} t), \tag{2.25}$$

$$= E_0 e^{i\omega_0 t} \sum_{k=-\infty}^{+\infty} J_k(\Delta) e^{ik\psi} e^{ik\omega_\mathrm{m} t} \left(1 + \frac{m}{2} e^{i\omega_\mathrm{m} t} + \frac{m}{2} e^{-i\omega_\mathrm{m} t}\right). \tag{2.26}$$

The terms oscillating at ω_0, $\omega_0 + \omega_\mathrm{m}$ and $\omega_0 - \omega_\mathrm{m}$ now show amplitudes modified by the mixture:

$$E_{\omega_0} = \left(J_0 + imJ_1\sin\psi\right) e^{i\omega_0 t}, \tag{2.27}$$

$$E_{\omega_0 \pm \omega_\mathrm{m}} = \left(J_0 \frac{m}{2} \pm J_1 e^{\pm i\psi} + J_2 \frac{m}{2} e^{\pm i2\psi}\right) e^{i(\omega_0 \pm \omega_\mathrm{m})t}, \tag{2.28}$$

where $J_k = J_k(\Delta)$ for clarity, and the relation $J_{-k} = (-1)^k J_k$ has been used. All other frequency components oscillating at $\omega_0 + k\ \omega_\mathrm{m}$ with $|k| > 2$ behave as in a normal FM/ΦM case, hence with amplitude $J_k e^{i\psi}$. As a result, the intensities of

the spectral components are

$$\frac{I_0}{E_0^2} = J_0^2 + (mJ_1 \sin\psi)^2, \tag{2.29}$$

$$\frac{I_{\pm 1}}{E_0^2} = J_1^2 + \frac{m^2}{4}(J_0^2 + J_2^2) \pm mJ_1(J_0 + J_2)\cos\psi + \frac{m^2}{2}J_0 J_2 \cos 2\psi, \tag{2.30}$$

$$\frac{I_k}{E_0^2} = J_k^2, \ \forall k \notin \{-1, 0, 1\}. \tag{2.31}$$

In the case of large enough modulation depths Δ with non-negligible components at $|k| > 2$, one can have an *a priori* knowledge of J_0 and $J_{\pm 1}$ by measuring the ratio of the higher order modes and then work out the values of m and Δ by comparing intensities of I_0 and $I_{\pm 1}$. In the limit of $\Delta \ll 1$, a mixture of AM and pure ΦM cannot be distinguished from an amplitude modulated field as in both cases, the spectra are symmetrical. However, the imbalance between I_1 and I_{-1} happening from a mixture of AM and FM allows one to measure the two modulation depths by looking only at the three central spectral components. The choice of a cosine modulation used here was purely arbitrary. Indeed, if the modulating signal was chosen to be $\cos(\omega_{\mathrm{m}} t + \phi_{\mathrm{m}})$, all frequency components would have had an extra $e^{ik\phi_{\mathrm{m}}}$, regardless of the type of modulation. Only the phase relation between different frequency components would have changed whereas the intensities of each one, measured on an FPI, would have kept the same value.

2.2 Sideband generation in a laser diode

For atomic physics experiments involving laser cooling or manipulation of external or internal states of atoms, monomode laser diodes are particularly appealing as they are compact, have low-power consumption, offer a good inherent stability and are available over a wide range of wavelengths. The industrial development of GaAs diodes at 780 nm, corresponding to the D_2 transition line in both isotopes of rubidium, has been boosted due to the choice of this wavelength for Compact Disk applications and thus prices have dramatically dropped down to £1 for the cheapest models. Noticeably, the same trend is happening with GaN laser diodes at 405 nm for Blu-ray Disk, suitable for instance for potassium, and the wave-

length of DVD diodes at 660 nm is relatively close to transitions in lithium. For these reasons, most of today's Rb experiments use diode in their laser systems. As already outlined, two wavelengths are required in order to get a magneto-optical trap in alkali species (see Sec. 5.2), one to trap the atoms and the other to repump the atoms decaying into the undesired state. So one needs identical set-ups for each laser: current and temperature controllers, locking electronics and two frequency stabilisation modules. As the difference in frequency between the two lasers, corresponding approximately to the atomic species ground state splitting, lies in the gigahertz region, one can think of generating both wavelengths from a single laser [27]. In addition, there are many more applications in which two or more wavelengths are needed: Raman spectroscopy [58], electromagnetically induced transparency (EIT) [59], coherent population trapping (CPT) [60] or stimulated Raman adiabatic passage (STIRAP) [61], which require in addition phase stability between the lasers for the three last of them. A large range of techniques are available to achieve two frequencies laser systems. One can make a constant frequency difference between two lasers with electronics offset [62] or phase [63] locking. Sidebands can be generated externally, by the mean of acousto-optic (AOM) [64] or electro-optics (EOM) [65] modulators. One can combine injection locking [66, 67] and frequency shifting using AOMs or EOMs to maximise the power in the two frequency components. In the work presented here, direct amplitude modulation of the laser diode current has been chosen [27], as it results in the most compact and inexpensive option, and so is perfectly suitable for an all-integrated portable cold atom experiment. Indeed, all previously cited methods include complicated electronics for phase locking or highly expensive AOM/EOMs that work in the GHz frequency range. It is worth noting that current modulation can be used along injection locking to achieved high intensities in the two frequency components [68], but at the cost of a more complicated apparatus.

2.2.1 Modulation frequency for ^{85}Rb and ^{87}Rb magneto-optical trapping

We will focus on a frequency modulated laser that can be used for magneto-optical trapping (MOT) of ^{87}Rb or ^{85}Rb atoms. The working mechanism of the MOT will be further described in Sec. 4.1 and we will only give here the information that is relevant for the present investigation. The reader is invited to refer to Sec. 4.1 for details on the MOT.

In the following, we derive the required modulation frequency using the example of ^{87}Rb MOT, but a similar reasoning can be easily made in the case of ^{85}Rb. In our application, two laser frequencies are required to make a MOT. The first cools the atom using the $F = 2 \rightarrow F' = 3$ transition of the D_2 line (that is between the $5S_{1/2}$ and $5P_{3/2}$ manifolds). Moreover, this laser needs to be red-detuned, compared with the transition frequency, by typically 12 MHz for

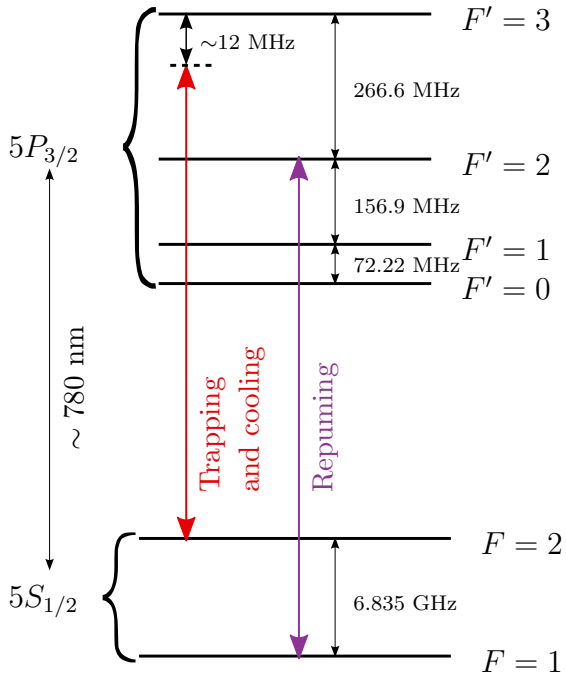

Figure 2.8: Energy level diagram of the $5S_{1/2}$ and $5P_{3/2}$ manifolds in ^{87}Rb. Cooling and trapping is achieved using the $F = 2 \rightarrow F' = 3$ transition with a laser red-detuned by ~12 MHz with respect to the transition. Repumping is done on the $F = 1 \rightarrow F' = 2$ transition.

optimum trapping and cooling in standard MOTs. A second laser is required to repump atoms that decay into the $F = 1$ ground state and regenerate the cooling and trapping cycle. The repumping transition can be chosen to be either between the $F = 1$ and $F' = 1$ or $F = 1$ and $F' = 2$ hyperfine states and we will opt for the second possibility since it requires less repumping intensity [27]. The atomic structure of the $5S_{1/2}$ and $5P_{3/2}$ manifolds is shown in Fig. 2.8, along with the two laser frequencies required. The lasers need to be locked on a frequency reference to avoid drift over time. We use saturation absorption spectroscopy in ^{87}Rb to provide these references. Due to the detuning of the trapping laser, there is no readily usable locking peak at the desired frequency. The trapping laser is locked on the $F = 2 \rightarrow F' = 2, 3$ crossover peak, down-shifted by 133.3 MHz from the trapping transition. An AOM is used to shift the frequency up, such that the trapping laser is finally red-detuned by about 12 MHz. The frequency splitting

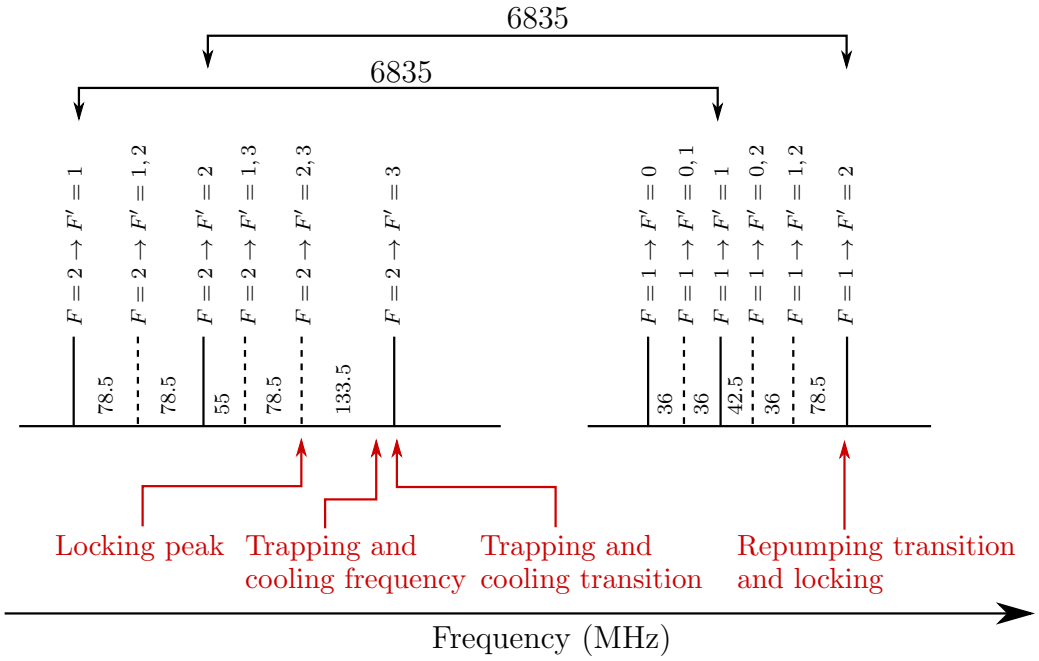

Figure 2.9: Schematics of the saturated absorption peaks frequencies, showing the locking peaks, cooling and repumping transition and the relative position of the cooling laser frequency compared to the cooling transition. The numbers indicate frequency differences expressed in MHz.

between the two ground states is 6835 MHz. On the absorption spectrum, this means there is a shift of the same amount between the $F = 2 \rightarrow F' = 2$ and the $F = 1 \rightarrow F' = 2$ peaks, as shown in Fig. 2.9. Moreover, the spacing between the $F = 2 \rightarrow F' = 2$ and the $F = 2 \rightarrow F' = 3$ peaks is 267 MHz. The frequency difference between the trapping and repumping laser is thus

$$\Delta f_{87} = 6835 - 267 + 12 = 6580 \text{ MHz}, \tag{2.32}$$

which is therefore the required modulation frequency for our two frequency laser. For a ^{85}Rb MOT, a similar derivation yields the frequency difference $\Delta f_{85} = 3036 - 121 + 12 = 2927$ MHz. One of the drawbacks of current modulation is that it usually yields small amplitude sidebands, as seen in Sec. 2.1. For applications such as CPT for instance, this is an issue, since similar intensities are required in the two components. For a ^{87}Rb MOT, trapping is done on the $F = 2 \rightarrow F' = 3$ transition. Atoms on this excited state can only decay back on the $F = 2$ ground state. The trapping laser frequency is close to $F = 2 \rightarrow F' = 3$ transition and the probability of exciting an atom on the $F' = 2$ (or $F' = 1$) state is non zero (hence the necessity of the repumping laser since these states can decay back on the $F = 1$ ground state) but is much lower than the one to excite an

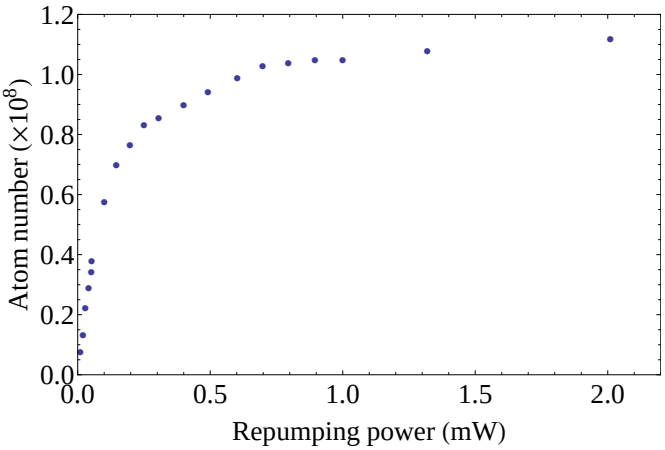

Figure 2.10: Atom number in a ^{87}Rb MOT as a function of the repumping laser power. The atom number saturates above ∼1 mW of repumping power. By comparison, the total power in the trapping beam is about 20 mW.

atom on the desired $F' = 3$ state. Typically, about 1 in 300 excitations will result in an atomic loss. The amount of power required in the repumping laser is thus much lower than the one in the trapping laser. No sensible increase in the atom number are observed above a certain amount of repumping power. As shown in Fig. 2.10, about 1 mW in the repumping beam saturates the atom number in the MOT, with an overall trapping power in the trapping beams of $\sim$ 20 mW. By modulating a laser diode, one can use the carrier as the trapping light and one of the first order sideband as the repumping light. Since a sideband-to-carrier ratio of 5 % is on the order of magnitude one can get with direct current modulation, this technique is totally appropriate for MOT operations with rubidium isotopes.

2.2.2 Origin of modulation

Direct current modulation is a unique feature of semiconductor lasers, where the total current

$$I(t) = I_0 + I_{\mathrm{HF}} \cos \omega_{\mathrm{m}} t \tag{2.33}$$

is a superposition of the bias (DC) current, I_0, and a (usually) high frequency (HF) current, I_{HF}, oscillating at the required modulation frequency, ω_{m}. The transfer of modulation from the current to the optical field occurs from the fact that both frequency and amplitude of a laser are related to the current $I(t)$ via the propagation constant [69, 70]:

$$k(\omega) = \frac{\omega\ n}{c}\left(1 + \frac{(\omega_{\mathrm{gain}} - \omega)c}{\Delta\omega_{\mathrm{gain}}\ \omega\ n}\gamma(I(t))\right) + i\frac{\gamma(I(t)) - \alpha}{2}, \tag{2.34}$$

where ω_{gain} and $\Delta\omega_{\mathrm{gain}}$ are respectively the center and width of the gain medium, ω is the frequency of the electric field, α accounts for the losses in the Fabry-Pérot laser cavity and $\gamma(I(t))$ is the gain parameter, a function of the pumping current. The normalized spectral transmission density of the cavity is [70]

$$I_{\mathrm{N}} = \frac{Te^{-ik(\omega)L}}{1 - Re^{-i2k(\omega)L}}, \tag{2.35}$$

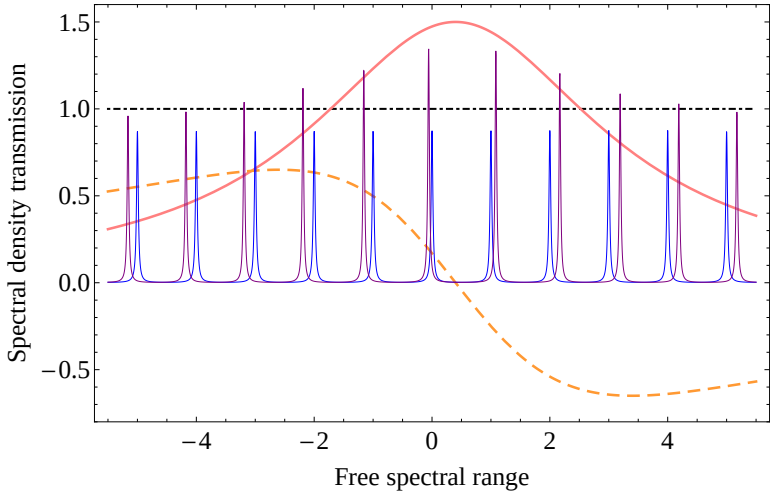

Figure 2.11: Spectral transmission density of the raw cavity and of the set cavity and gain medium. The blue curve is the Airy function of the unperturbed cavity. The normalized gain and dispersion are shown in red and dashed orange. The purple curve of the set cavity and gain shows amplification and peak shifting. Oscillation can happen if the peaks become higher than the threshold shown by the dot-dashed line.

with $R = 1 - T$ the reflectivity of the mirrors and L the length of the cavity. The cavity becomes unstable (i.e. oscillates) when the denominator vanishes, hence

$$R \exp(-i2k(\omega)L) = 1. \tag{2.36}$$

This condition can only be achieved when the gain is large enough to counterbalance the losses α arising from from the mirror reflections. Fig. 2.11 shows the transmission of a cavity with (purple curve) and without (blue curve) the presence of a gain medium inside the mirrors. Here a gain medium with a simple Lorentzian amplification (red)/dispersion (dashed orange) shape is assumed for simple understanding of the phenomenon, although for a quantitative treatment, the real gain curve of a semiconductor laser [69] would have to be considered. The dotted line represents the threshold required for lasing. Initially, the inherent losses of the totally passive cavity results only in attenuation. However, the presence of a gain medium actively provides amplification such that the transmission density peaks get above the critical value of unity, allowing oscillations

to build up from noise. The effect of the dispersion is to shift peaks of the cavity compared to the unperturbed case. Therefore, a modulation of the current results in both modulation in the gain curve and in the position of the lasing peak, respectively translating into amplitude and frequency modulation of the output electric field.

2.2.3 Experimental setup

Our laser diodes have a natural linewidth of a few tens of MHz over a 1 s integration time. A common method to reduce this below the natural width of an atomic transition (and thus making it usable for magneto-optical trapping) is to put the diode in an external cavity (ECDL) with optical feedback provided from a diffraction grating in a Littrow configuration. The first negative order of the grating is sent back into the diode to provide wavelength selective feedback, and light from the zeroth (reflected) order is the output of the laser. In addition, fine tuning of the wavelength is achieve by rotating the grating around its pivot point. In this type of configuration, one has to be careful however as, for the same bias current as in free running-mode, the intra-cavity power is larger when the diode is self-injected. Given that our gratings have a typical 20% efficiency, it is important to limit the maximum current to about 80% of the stated maximal current.

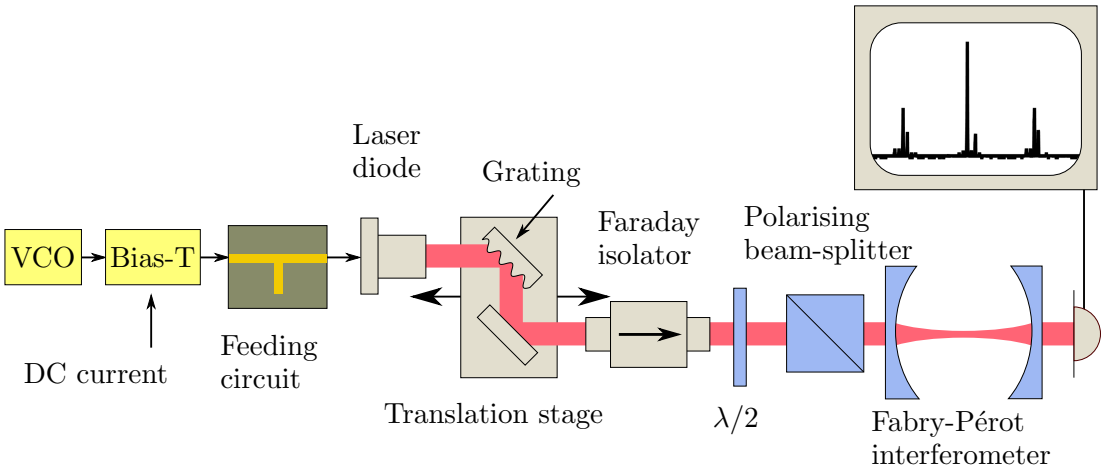

Figure 2.12: Schematics of the diode current modulation test setup.

The experimental setup is depicted in Fig. 2.12. The grating is positioned on a translation stage to allow fine cavity length tuning, along with a steering mirror. The beam passes through an optical Faraday isolator to prevent any unwanted feedback to the laser. The DC current is adjusted with a Thorlabs LD1255 current driver and the temperature is stabilized with a thermoelectric cooler, thermistor and a servo control from Wavelength Electronics. The microwave signal is generated by two different Voltage Control Oscillators (VCO) from Avantek/PhaseMatrix. The VTO-8240 and VTO-8650 models are both ∼13 dBm output power devices and work, respectively, in the frequency ranges 2.4-3.7 GHz (for ^{85}Rb) and 6.5-8.6 GHz (for ^{87}Rb). The RF is mixed with the DC current with a ZX85-12G-S+ Bias-Tee from Mini-Circuits and fed to the laser diode, either directly, or using a matching circuit that will we will discuss in Sec. 2.2.5. In order to achieve minimum losses, high frequency boards RO4350B from Rogers Corporation are used for the VCO and matching Printed Circuit Boards (PCB).

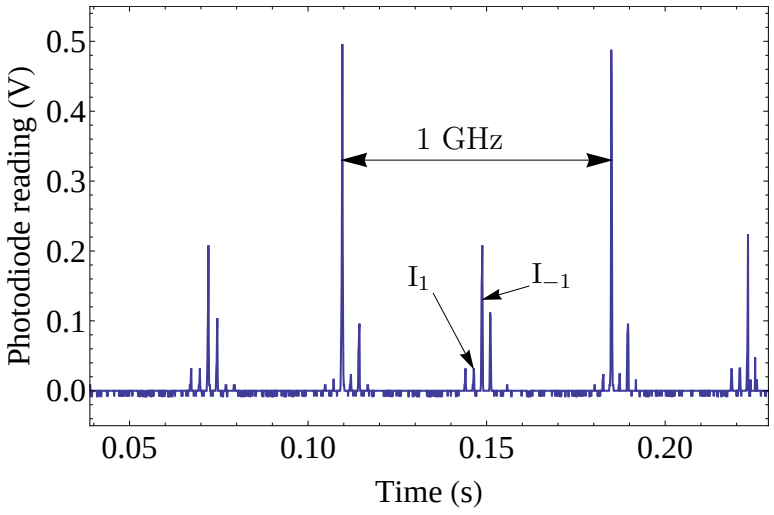

Figure 2.13: Typical Fabry-Pérot spectrum of a modulated laser. The frequency decreases with increasing time. The modulation frequency is 1.518 GHz. Aliasing is visible due to the 1 GHz Free Spectral Range (FSR) of the cavity. Imbalance between the first order sidebands I_1 and I_{-1} implies a mixture of AM and FM. Imbalance between higher order sidebands implies a distortion of the modulation signal.

A high finesse (F >1000) Toptica FPI is used for the measurements of the carrier and sidebands intensities. The amount of light sent to the FPI is set with a half-wave plate and a polarizing beam splitter to avoid saturation of the photodetector. A typical spectrum from the FPI is shown in Fig. 2.13. The amplitude of the sidebands and carrier is directly measured on the oscilloscope and converted into optical power. One has to be careful to operate the photodiode in its linear range, which is ensured by an operational amplifier circuit at the detector's output.

Two diodes are tested, both producing ∼784 nm radiation at room temperature. The Sanyo DL-7140-201 and Sharp GH0781JA2C both output, respectively, about 80 mW and 120 mW of optical power for nominal current of ∼100 mA and ∼140 mA in Continuous Wave (CW) operation. They both come in a ⌀5.6 mm package and the same laser mount can thus be used for the two models.

2.2.4 Laser in a cavity

In an edge-emitter diode laser, the laser cavity is made by the semiconductor medium itself. The reflectivity at the interface between the semiconductor (with refractive index $n \sim 3.6$ for GaAs) and the air results in a very lossy cavity but this is compensated by the very high gain in semiconductors. Thus, for an about $L \approx 1$ mm long diode crystal, the longitudinal modes are separated by the FSR= $c/2nL$, that is about 40 GHz. The presence of the external cavity significantly perturbs the operational mode of the laser diodes. First, by re-injecting part of the output light into the gain medium, it changes the laser dynamics. Also, the external cavity acts as a second FPI that selects only the longitudinal modes that are integer multiples of its own FSR. Therefore, the lasing mode has to verify both FSR conditions. The semiconductor cavity resonances are usually quite broad, due to the very low finesse of the cavity. In the case of a modulated signal that spreads over a few GHz, it is likely that all frequency components can be significantly coupled to the output mode. The external cavity is usually much longer, resulting in a FSR that is of the order of magnitude of the modulation frequency. For example, a 2 cm long cavity has a 7.5 GHz mode spacing. The external cavity is, once again, of relatively poor quality, since the

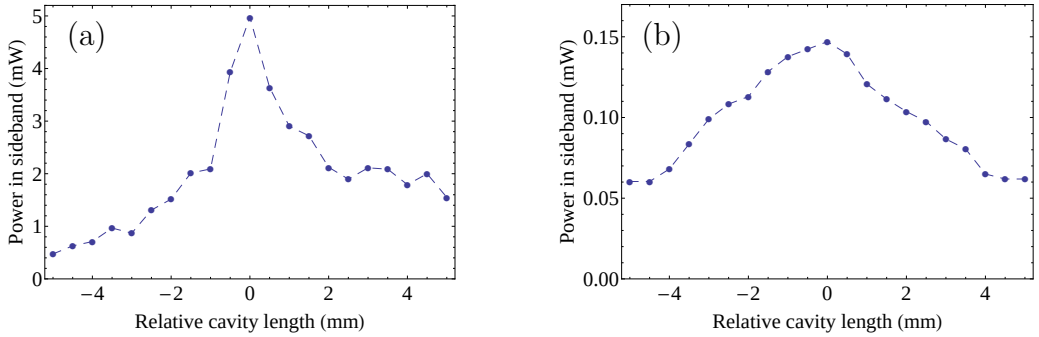

Figure 2.14: Optical power in one first order sideband as a function of the relative cavity length for the Sanyo DL-7140-201 diode. The external cavity length is referenced to (a) $L_{\mathrm{ECDL}} \approx 5$ cm and (b) $L_{\mathrm{ECDL}} \approx 2.3$ cm and the VCO frequency is (a) $f_{\mathrm{VCO}} = 2.927$ GHz and (b) $f_{\mathrm{VCO}} = 6.58$ GHz. The injection current is 52 mA in both configurations.

grating diffraction efficiency is maximum 20 %, but is more critical as carrier and sidebands can sense significantly different attenuation, and this effect was observed in the first current modulated application for atom cooling [27]. One can investigate the dependence of the cavity length by either changing the modulation frequency for a fixed cavity size or by sweeping the cavity length for a constant frequency. Our VCOs have an output power which varies slightly with frequency (on the order of 2 dBm over their operating frequency range). Sweeping the cavity length allows a much more precise measurement. The translation stage on which the grating is set allows us to change the size of the cavity with a resolution of 10 μm. Because the grating always has the same angle with respect to the laser diode, there is no need to realign for optical feedback after each step. Here we present only the results for the Sanyo DL-7140-201, visible in Fig. 2.14. First of all, we didn't observed any increase in the amount of power in the sidebands compared to the case without an external cavity (higher sidebands are achieved at lower frequencies, as expected since usually the efficiency of the modulation decreases at higher frequencies). The power at the optimal cavity length is roughly similar with or without an ECDL configuration, contrary to the results of Ref. [27], where a great increase of the sideband amplitude was seen at resonance. This can results from different grating qualities that changes the finesse cavity. Also, the sideband generation efficiency is extremely sensitive

to the injection current, as we will see in Sec. 2.2.6, due to resonances with the relaxation oscillations. Even if no increase was observed, we see that, especially for the 6.58 GHz, the FWHM of cavity length range is relatively large, about 8 mm (and about 2 mm at 2.927 GHz), and thus the presence of the cavity shouldn't be too restrictive as at it is easy to fine tune the cavity length with a mm resolution. Moreover, according to Fig. 2.10, the maximum atom number in a ^{87}Rb MOT is obtained with no more than 1 mW of repumping power, but only ~ 0.15 mW (as obtained on resonance in Fig. 2.14(b)) still yields about 50 % of this maximum! We finally note that a better way to get high sideband generation efficiency with an external cavity is to use anti-reflection coated diodes [71]. One gets very narrow resonances and total extinction of the carrier is even possible, making this last configuration perhaps more suitable for applications where similar intensity components are required, such as CPT.

2.2.5 Impedance matching

When dealing with radio frequencies of several GHz, the size of the circuit becomes comparable to the wavelength, and one needs to consider the finite velocity of the signal and the effect of the distributed parameters of the line [72]. Any transmission line of infinitesimal length ∂x can be modeled with parasitic series inductance $L\partial x$, series resistance $R\partial x$, parallel capacitance $C\partial x$ and parallel conductance $G\partial x$, as depicted in Fig. 2.15. These happens from natural and unavoidable physical lines, indeed, any conductor has a non-zero transverse cross section and this results in a inductance effect, since for high frequencies, the current flows closer and closer to the conductor surface. The capacitance is due to the finite distance between the two lines, separated by an insulator with a given dielectric constant. Resistance and conductance originate from the series losses in the conductor and parallel losses through the insulator, but for most applications, the typical overall size of the line is usually small enough to neglect these parameters. One finds the differential coupled equations for the current I and voltage V across the inductance and capacitance and, which lead, after differentiation of each equation and substitution in the other, to the telegraphist's equations:

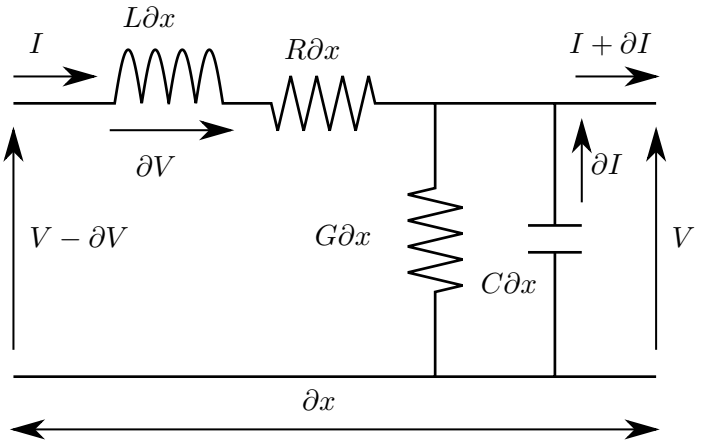

Figure 2.15: Segment of line with the distributed parameters. $C\partial x$, $L\partial x$,$R\partial x$ and $G\partial x$ are respectively the capacitance, inductance, resistance and conductance of a segment of infinitesimal length ∂x. Lossless transmission lines assume $R = G = 0$.

$$\begin{aligned} \frac{\partial^2 V}{\partial x^2} &= LC\frac{\partial^2 V}{\partial t^2}, \\ \frac{\partial^2 I}{\partial x^2} &= LC\frac{\partial^2 I}{\partial t^2}. \end{aligned} \tag{2.37}$$

One can show that the solutions to these partial differential equations consist of a superposition of two counter-propagating waves with phase velocity $v_\pm = \pm 1/\sqrt{LC}$ [72]. Here only the harmonic regime is considered, thus these waves are chosen to be sinusoidal:

$$V(x,t) = V_1 e^{i\left(\omega(t-\sqrt{LC}x)+\phi_1\right)} + V_2 e^{i(\omega\left(t+\sqrt{LC}x\right)+\phi_2)} + \text{c.c.}\ , \tag{2.38}$$

$$I(x,t) = I_1 e^{i\left(\omega(t-\sqrt{LC}x)+\phi_1\right)} + I_2 e^{i(\omega\left(t+\sqrt{LC}x\right)+\phi_2)} + \text{c.c.}\ , \tag{2.39}$$

where ω is the wave frequency, and V_1, I_1, V_2 and I_2 are respectively the amplitudes of the co- and counter-propagating parts, with relative phases ϕ_1 and ϕ_2, for the voltage and current waves. If we differentiate Eqn. 2.38 with respect to x and Eqn. 2.39 with respect to t, and by re-injecting the results into, for instance, the equation that relates voltage and current through the inductance $\partial v/\partial x = -L\partial i/\partial t$, we find that the ratio voltage-current ratio is constant, such

that $V_1 = Z_0 I_1$ and $V_2 = -Z_0 I_2$ where

$$Z_0 = \sqrt{\frac{L}{C}} \tag{2.40}$$

is called the transmission line characteristic impedance. This ratio is, in theory, independent of the frequency. Assume that at some length l, there is a load of (complex) impedance Z_T. The relation $V(l,t) = Z_\mathrm{T} I(l,t)$ holds at this position for all t and we can write, using Eqns. 2.38, 2.39 and 2.40:

$$\frac{Z_\mathrm{T}}{Z_0}\left(1 - \frac{V_2}{V_1} e^{i(\phi_2' - \phi_1')}\right) = 1 + \frac{V_2}{V_1} e^{i(\phi_2' - \phi_1')}, \tag{2.41}$$

where $\phi_1' = -\omega\sqrt{LC}l + \phi_1$ and $\phi_2' = \omega\sqrt{LC}l + \phi_2$. The complex term $V_2/V_1 e^{i\left(\phi_2' - \phi_1'\right)}$ represents the ratio between the reflected (counter-propagating) voltage and the incident one at $x = l$. It is called the voltage reflection coefficient and reads

$$\rho_v = \frac{Z_\mathrm{T} - Z_0}{Z_\mathrm{T} + Z_0}. \tag{2.42}$$

The current reflection coefficient $\rho_i = -\rho_v$ can be defined in a similar manner, and the power reflection coefficient is given by $\rho_p = |\rho_v|^2$. When there is no wave reflected back, all the power couples into the load, thus $\rho_v = 0$ when $Z_\mathrm{T} = Z_0$ and the line is said to be matched. On the other end, complete reflection happens when the circuit is either not terminated ($Z_\mathrm{T} = \infty$, $\rho_v = 1$) or shorted ($Z_\mathrm{T} = 0$, $\rho_v = -1$). An other very often met quantity is the Voltage Standing Wave Ratio (VSWR). Indeed, two waves propagating in opposite directions result in a standing wave and, using the reflection coefficient, one can express the ratio of the maximum of the standing wave over its minimum as

$$\mathrm{VSWR} = \frac{1 + |\rho_v|}{1 - |\rho_v|}. \tag{2.43}$$

As ρ_v stands before -1 and 1, the VSWR is always strictly larger than unity, where the minimum is reached only for perfectly matched lines, whereas the totally reflected wave result in a infinitely high ratio. One might notice that the expression for the reflection coefficient ρ_v between two different impedances Z_T

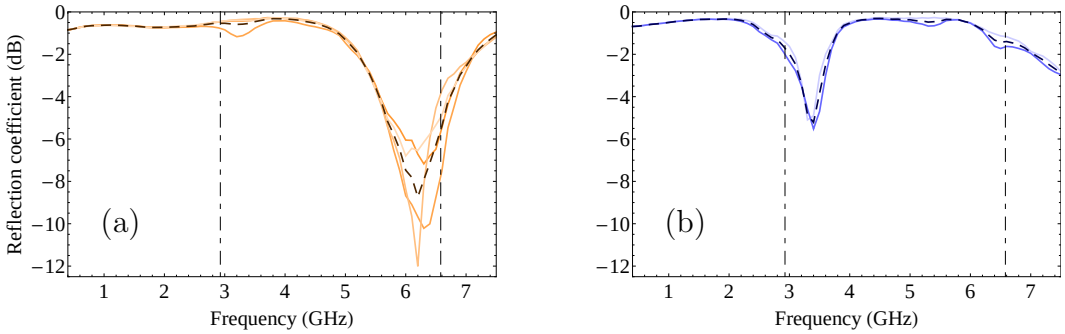

Figure 2.16: Coefficient reflection of the raw (a) DL-7140-201 and (b) GH0781JA2C diodes. Each solid line denotes a single measurement performed on a different diode sample whilst the dashed curves are the averaged values.

and Z_0 is very similar to the one for reflection of electromagnetic waves at the interface between two media with different refraction indices.

Usually, in RF applications, the electronics are designed with an input and output impedance that matches the one of the transmission line, very often chosen to be $Z_0 = 50\ \Omega$, such that the power coupling is maximal. However, the laser diodes we're using are primarily intended to be used in CD drives, where they are used in pulsed mode at a rate that never exceeds a few tens of MHz. It is thus very unlikely that these diodes' impedances match 50 Ω, resulting in a reduced power coupling that can be far from optimal. A device impedance (or equivalently, reflection coefficient) is measured using a network analyser, which sends a signal and records the reflection at the same time, in amplitude and phase. With a precise calibration of the distance between the device under test and the network analyser, one can then work out the complex impedance. The knowledge of the phase is extremely important, as we will see in the following, for matching the impedance. We don't have such equipment in the Photonics group, and all impedance measurements were performed using the facilities of the Ultrafast Systems Group at the University of Glasgow. The power reflection coefficients of the raw diodes in the 0.5-7.5 GHz range are shown in Fig. 2.16. As we can see, the Sanyo DL-7140-201 diode has a naturally relatively low coefficient around 6.58 GHz ($\rho_p \approx 0.32$), but very high around 2.927 GHz ($\rho_p \approx 0.71$). The Sharp GH0781JA2C has similar coefficients at both frequencies $\rho_p \approx 0.89$). It is clear that any RF modulation at 2.927 GHz (for the Sanyo DL-7140-201) or

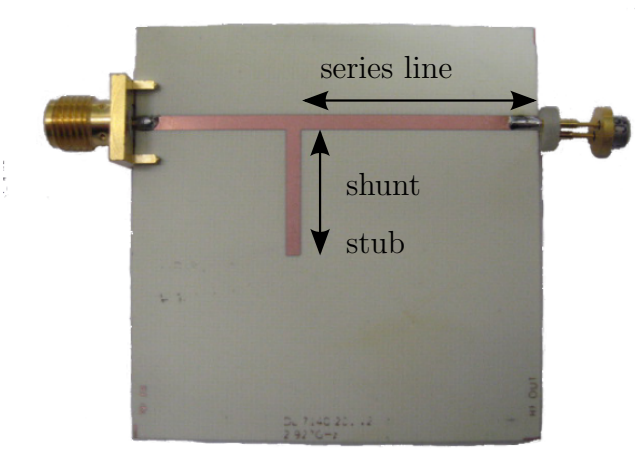

Figure 2.17: Photograph of a matching stub circuit with the laser diode on the right side and the SMA connector (connected to the bias-tee) on the left.

using the Sharp GH0781JA2C is difficult to couple, and one might need amplifiers. This complicates the system and is not desirable in the case of low cost applications. Furthermore, back reflections can damage the output stage of an electronic device, and one has to be careful before using high gain amplifiers. We see from Fig. 2.16 that the reflection coefficient (strictly speaking, both amplitude and phase, although they are not shown here) doesn't change much between samples. Indeed, variation in the manufacturing process might have resulted in totally different RF behaviour between diodes. This implies that the design of a matching circuit is not dependent on one specific sample.

Fortunately, there are relatively easy ways of matching a device impedance, such as quarter-wave line transformers [72]. Here, we investigate impedance matching using a "stub". This circuit is a piece of transmission line connected in parallel to the main line, as shown in Fig. 2.17. The open circuit at the end of the "stub" has the highest possible reflection coefficient, and the reflects all the incident wave. The stub acts exactly as a microwave Michelson interferometer: given the impedance of the load, one can calculate the stub length and where to connect the stub to the main line, such that the signal reflected by the stub interferes constructively in the direction of the load, hence yielding impedance matching. This technique is used as well with diode lasers for telecommunication

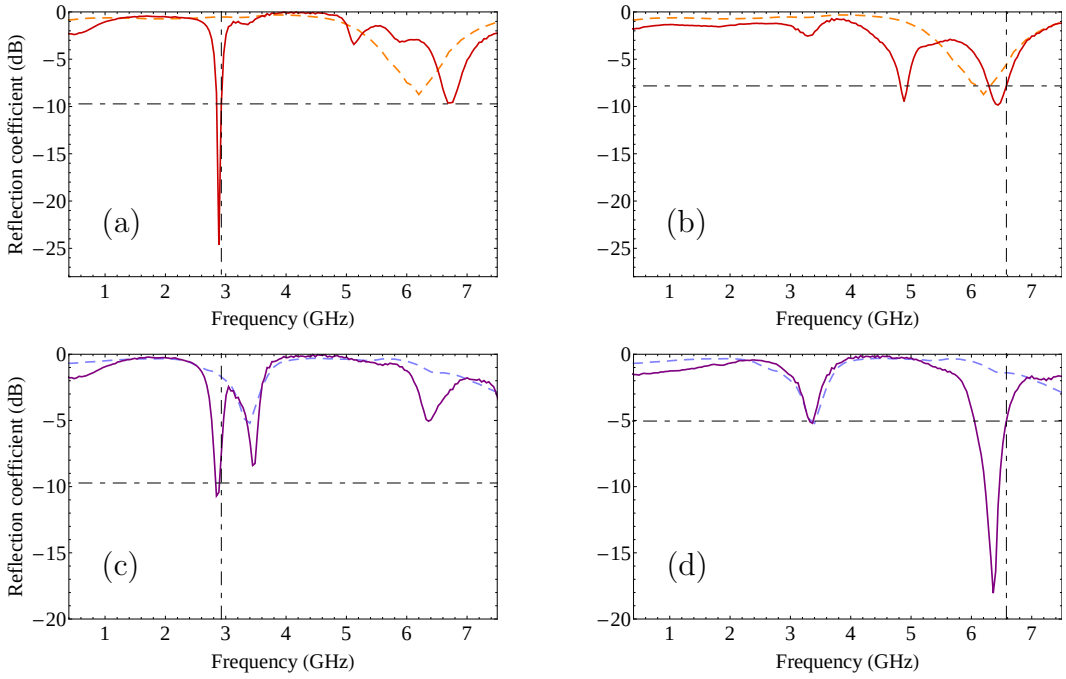

Figure 2.18: Coefficient reflection of the matched DL-7140-201 around (a) 2.927 GHz and (b) 6.58 GHz, and GH0781JA2C around (c) 2.927 GHz and (d) 6.58 GHz. The dashed lines indicated the non-matched reflection for comparison.

applications [73, 74]. The characteristic of the matching stub can be manually calculated using the Smith chart [75, 76]. Nowadays, softwares dedicated to high frequency transmission lines, such as Advanced Design System (ADS) from Agilent, are much more precise, since they account for the real physical parameters of the transmission line, and can directly produce the mask of the PCB. The matching circuits were designed with ADS and fabricated at the University of Glasgow.

The measured reflection cofficient of the matched diodes are shown on Fig. 2.18, with matching circuits designed to operate around both 2.927 GHz and 6.58 GHz. Near the desired operating frequencies, we clearly see a drop of the reflection coefficient. The bottom of the peak is always shifted towards the low frequencies, compared to the exact desired match. This can be due to a difference between the transmission line parameters used for the simulations and the actual one. More likely, the masks were printed using our office 1200 dpi printer, and the constant trend in the shift suggests there is slight difference between the calcu-

lated dimensions and those on the printed mask. However, reflection coefficients of $\rho_p \approx 0.1$ at 2.927 GHz, and $\rho_p \approx 0.18$ (Sanyo DL-7140-201) or $\rho_p \approx 0.32$ (Sharp GH0781JA2C) at 6.58 GHz are obtained, which constitutes a sensible improvement compared to the unmatched diodes.

Unfortunately, we didn't see any clear sideband increase with the matching circuits, which was a real disappointment. With the matching stub in, the Sanyo DL-7140-201 at 2.927 GHz (where the reflection coefficient improves from $\rho_p \approx 0.89$ to $\rho_p \approx 0.1$ between the unmatched and matched scenarios), one expects to see a visible increase in the sideband amplitudes, since the coupled electric power is nine times higher with the matching circuit. Moreover, the matched region is relatively narrow, as can be seen in Fig. 2.18(a), such that the increase should be clearly visible with a rapid sweep of the VCO frequency. It is not clear what the reason is for this inability to get higher sidebands by increasing the coupling of the RF power into the diode. This can be due to extra non-linear loss mechanisms in the semiconductor gain medium, as the presence of multiple frequencies in the laser gain medium is intrinsically linked to the laser dynamics.

2.2.6 Relaxation oscillations

The dynamics of a laser with a two level gain medium can be described with a set of three coupled differential equations known as the Maxwell-Bloch equations [77]. They describe the time evolution of the electric field, the atomic polarisation and the population inversion. Under certain conditions, they reduce to only two equations that are equivalent to the rate equations [78]:

$$\begin{aligned} \frac{\mathrm{d}n(t)}{\mathrm{d}t} &= K\ \Delta N(t)\ n(t) - \gamma_c\ n(t)\ , \\ \frac{\mathrm{d}\Delta N(t)}{\mathrm{d}t} &= G - K\ \Delta N(t)\ n(t) - \gamma_2\ \Delta N(t)\ , \end{aligned} \tag{2.44}$$

where $n(t)$ is the number of photon in the cavity, $\Delta N(t)$ is the population inversion, γ_c is the cavity decay rate, γ_2 is the excited state linewidth, G is the gain parameter and K is a coupling constant. The term $K\ \Delta N(t)\ n(t)$ corresponds to the stimulated emission processes that increase the photon number and decrease the population inversion in the same fashion. Of course, a semiconductor device

is not a two level system, and more complete models have been developed [79], but the rate equations still describe relatively well the experimental observations. These equations are non-linear, since the stimulated emission terms mixes the two quantities and they don't have a general analytical solution. However, such two dimensional phase space systems can show, under certain conditions, an oscillatory behaviour [80]. These oscillations can happen if the excited state linewidth is much larger than the cavity decay rate, that is $\gamma_2 \gg \gamma_c$ [78]. Lasers that verify this condition (such as solid-state and semiconductor lasers) can show laser spiking during a transient that results from a fast exchange between the photon number and the population inversion. The amplitude of the spikes then decreases as the system reaches its steady-state regime for the atom number and population inversion. This phenomenon is known as relaxation oscillations. In this case, one can show that the relaxation oscillation frequency is given, for a semiconductor laser, by [81]

$$\omega_{\mathrm{ro}} = \sqrt{\left(\frac{I}{I_{\mathrm{th}}} - 1\right)\ \gamma_c\ \gamma_2}\ , \tag{2.45}$$

where I_{th} and I are, respectively, the diode threshold and operating currents. These oscillations can be used to enhance the modulation signal, since the amplitude of the sideband is significantly increased when the driving frequency becomes resonant [82]. It as a known phenomena, often used in atom physics experiments with modulated diodes [27, 83].

It is worth noting that no external cavity is used for these measurements, as this would unnecessarily complicate the procedure and perturb the laser dynamics. For each value of the modulation frequency, the injection current is swept and the power in the sideband is recorded. Fig. 2.19 shows the experimental data points for a VCO frequency of 3.8 GHz with the Sanyo DL-7140-201 diode. The increase in the laser response is clearly visible when the relaxation oscillations become resonant with the driving frequency. Ideally, one would first set the value of the current and then sweep the VCO frequency over its full range. However, this is difficult to achieve in our case since the VCOs output power is not linear with frequency. Therefore, we would not be able to distinguish wether a change in the sideband amplitude is due to the microwave frequency being closer or further away from resonance with the relaxation oscillations, or wether this change

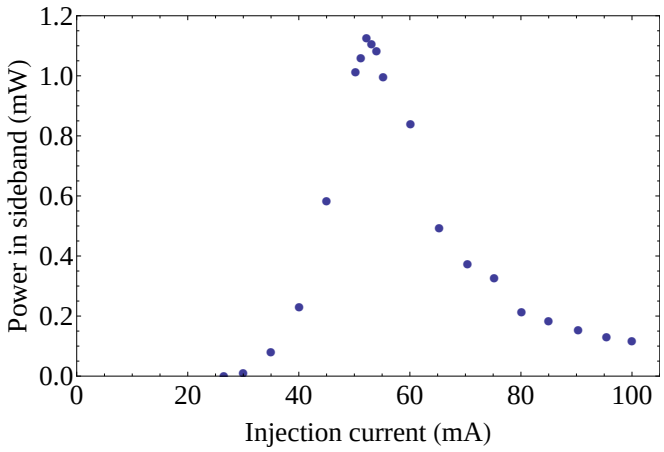

Figure 2.19: Power in a first order sideband as a function of the injection current for the Sanyo DL-7140-201. The VCO frequency is 3.8 GHz and the resonance with the relaxation oscillations is clearly apparent for an injection current of about 53 mA.

is due to a different microwave power level. The current sweeps are performed for different VCO frequencies and for both diode laser. By extracting the maximum (as in Fig. 2.19), we can thus deduct the current that corresponds to each value of the relaxation oscillations. The relaxation oscillations frequency as a function of the injection current are shown in Fig. 2.20. From a fit of the experimental points to Eqn. 2.45, we can extract the parameter $\sqrt{\gamma_c\ \gamma_2}/2\pi$ to be approximately equal to 3.8 GHz for the Sanyo DL-7140-201 and 4.1 GHz for the Sharp GH0781JA2C, that is in the typical range (between 3 GHz and 5.3 GHz) for semiconductor lasers [82]. We see from Fig. 2.20 that, due to the maximal current the diodes can be operated at, the resonance with the relaxation oscillations cannot be used for generating high amplitude sidebands at 6.58 GHz. Indeed, the "resonant" current is 108 mA for the DL-7140-201 and 130 mA for the GH0781JA2C, that is much above the maximal current in an ECDL configuration. However, the "resonant" current is much lower in the case of a modulation frequency at 2.927 GHz, that is about 42 mA for the DL-7140-201 and 56 mA for the GH0781JA2C. Nevertheless, for such low currents, the trapping light intensity is very low. For example, for the DL-7140-201 that is not in an ECDL configuration, a 42 mA injection current gives 18 mW of optical power whilst 100 mA gives about 80 mW. This implies that there is a trade-off between the amount of power one can achieve in

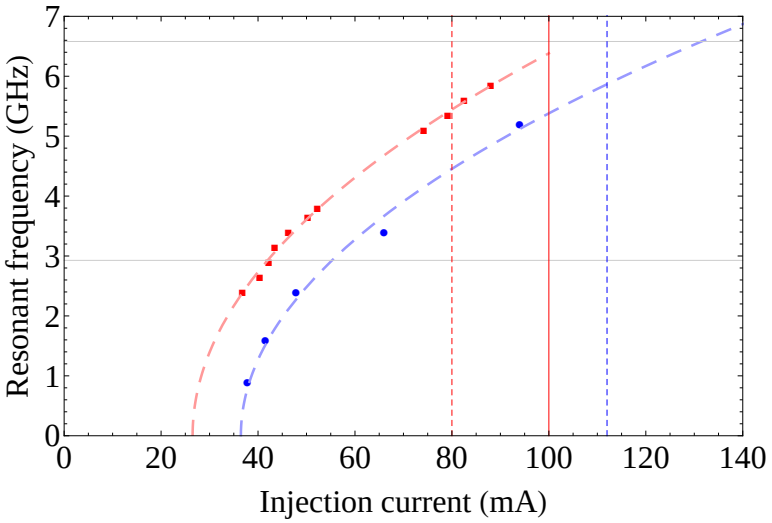

Figure 2.20: Relaxation oscillations frequency as a function of injection current for the Sanyo DL-7140-201 (red squares) and Sharp GH0781JA2C (blue disks) diodes. Points are experimental measurements and dashed lines are fits to Eqn. 2.45. The vertical red line is shows the maximum injection current for the DL-7140-201 (the maximum current for the GH0781JA2C being 140 mA). The two vertical dashed lines show the maximum current in a ECDL configuration for the DL-7140-201 (red) and GH0781JA2C (blue) diodes. The gray horizontal lines indicate the frequencies of interest, that is 2.927 GHz and 6.58 GHz.

the carrier and sideband, since the relaxation oscillations for a driving frequency of 2.927 GHz happen at small currents.

2.3 Conclusion

We have presented the basic modulation techniques and showed how they impact the optical spectrum. Experimentally, we have investigated three different aspects of the modulation into a semiconductor laser: the effect of an external cavity, the optimisation of the RF coupling using a impedance matching circuit and the effect of the oscillation relaxations. We have seen that, even if no increase in the sideband power was obtained with an ECDL, no detrimental decrease was observed as well, and thus our diodes are likely to be usable in a rubidium MOT experiment. Unfortunately, and although this was deeply investigated, no sensible

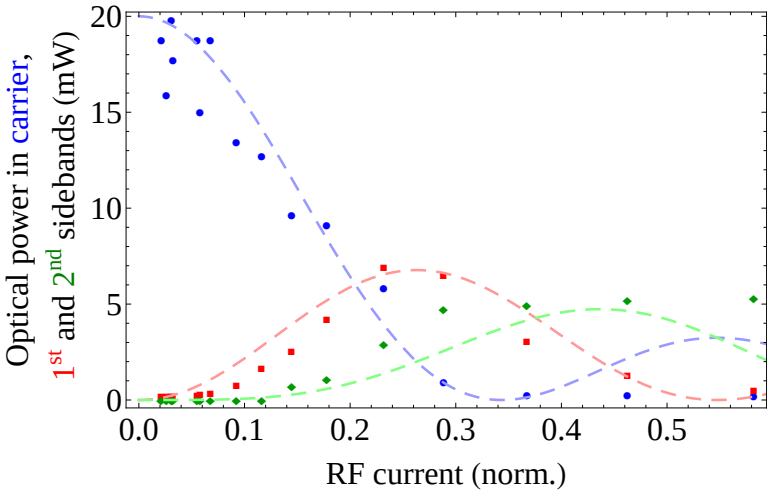

Figure 2.21: Powers in carrier (blue circles), upper 1st (red squares) and upper 2st (green diamonds) sidebands as a function of the RF current in a prototype laser from Compound Semiconductor Technologies LTD. The dashed lines represent the Bessel functions dependence J_0^2, J_1^2 and J_2^2 that best correlate with the experimental data points. The modulation frequency is 3.4 GHz.

enhancement was obtained using the stub matching circuit. The modulation efficiency diode have shown to be particularly sensitive to the injection current, due to a resonance effect with the relaxation oscillations. However, there is a trade-off if one wants to take advantage of this, since small relaxation oscillations happen for low current, that is small trapping light intensity, while large relaxation oscillations are reached for currents that lie above the limit in an ECDL configuration. We note that, we could obtain, with the Sanyo DL-7140-201, about 10 mW in the trapping light and 4 mW in the repumpimg sideband when operating at low current for operations at 2.927 GHz, and about 70 mW in the trapping light and 0.3 mW in the repumpimg sideband when operating at high currents for operations at 6.58 GHz. For the Sharp GH0781JA2C at 2.927 GHz, similar sidebands were obtained ($\sim$4 mW) but with a higher intensity in the carrier (15 mW). The Sharp GH0781JA2C seems to be more suitable for operations around 6.58 GHz, since we could get about 1.5 mW in the sideband and 100 mW in the carrier. In the Chaps. 3 and 5, this is indeed the modulated diode we will use for Coherent Population Trapping or Magneto-Optical Trapping operations. Finally, we note that we recently investigated new prototype diode from Compound Semiconduc-

tor Technologies LTD. These lasers have a very good input power coupling and very high modulation efficiencies can be achieved, as seen in Fig. 2.21. They still have thermal issues that dramatically reduce the overall power but they seem to be a very good candidate for application such as CPT.

Chapter 3

Coherent population trapping as a magnetic field sensing technique

Atomic transitions are well known for being very sensitive to magnetic fields. One very attractive application in atomic physics is thus magnetometry [20], as it allows for very inexpensive and compact devices [24]. By coherently driving two optical transitions, one can trap atoms in a state that is not coupled to the light anymore [60] and thus perform precise spectroscopy between the magnetically sensitive ground states. This phenomenon is known as Coherent Population Trapping (CPT). It has been used in applications that require a very high sensitivity, such as human biomagnetism [84].

In this chapter, we first give a brief theoretical description of the CPT mechanism with a three state system in a Λ configuration. We then show preliminary experimental results on dc magnetic fields CPT magnetometry. Such magnetometers could be used, for example, along with the small-size magneto-optical traps described in Chap. 5 to create portable devices that allow for measurement with precise spatial resolution.

3.1 Two-level atom and Rabi flopping

We first recall the case of two atomic states $|1\rangle$ and $|2\rangle$ coupled by radiation $E(t) = E_0 \cos \omega t$. These states are eigenstates of the Hamiltonian

$$\hat{H}_0 = \sum_i \hbar\omega_i |i\rangle\langle i|. \tag{3.1}$$

When there is a coupling from an electromagnetic field, the total atomic wavefunction $|\phi\rangle$ starts to evolve with time and obey the time-dependent Schrödinger equation

$$i\hbar \frac{\mathrm{d}|\phi\rangle}{\mathrm{d}t} = \hat{H}(t)|\phi\rangle, \tag{3.2}$$

where the complete Hamiltonian $\hat{H}(t) = \hat{H}_0 + \hat{H}_{\mathrm{AL}}(t)$ accounts for the interaction part

$$\hat{H}_{\mathrm{AL}}(t) = -\hat{d}E = -e\hat{r}E_0 \cos \omega t. \tag{3.3}$$

The off-diagonal elements in $\hat{H}_{\mathrm{AL}}(t)$ describe the coupling between the states due to the the field $E(t)$. The wavefunction $|\phi\rangle$ is a superposition of the two states and reads

$$|\phi\rangle = c_1(t)e^{-i\omega_1 t}|1\rangle + c_2(t)e^{-i\omega_2 t}|2\rangle. \tag{3.4}$$

The relative phase evolution of the two eigenstates is due to their energy difference $\omega_0 = \omega_2 - \omega_1$. Squaring the two amplitude factors, c_1 and c_2, gives, respectively, the population of the states $|1\rangle$ and $|2\rangle$. By injecting Eqn. 3.4 into Eqn. 3.2 and using $\hat{H}_0|i\rangle = \hbar\omega_i|i\rangle$, one finds two coupled equation for $c_1(t)$ and $c_2(t)$:

$$i\dot{c_1} = \frac{\Omega}{2} e^{i\delta t} c_2, \tag{3.5}$$

$$i\dot{c_2} = \frac{\Omega}{2} e^{-i\delta t} c_1, \tag{3.6}$$

where the quantity

$$\Omega = -\frac{d_{12}E_0}{\hbar} = -\frac{\langle 1|e\hat{r}|2\rangle E_0}{\hbar} \tag{3.7}$$

is defined as the Rabi frequency and assumed to be real for simplicity. It is assumed that the difference between the field frequency and the atomic transition frequency $\delta = \omega - \omega_0$ is small compared to ω_0. In these conditions, the far-resonant

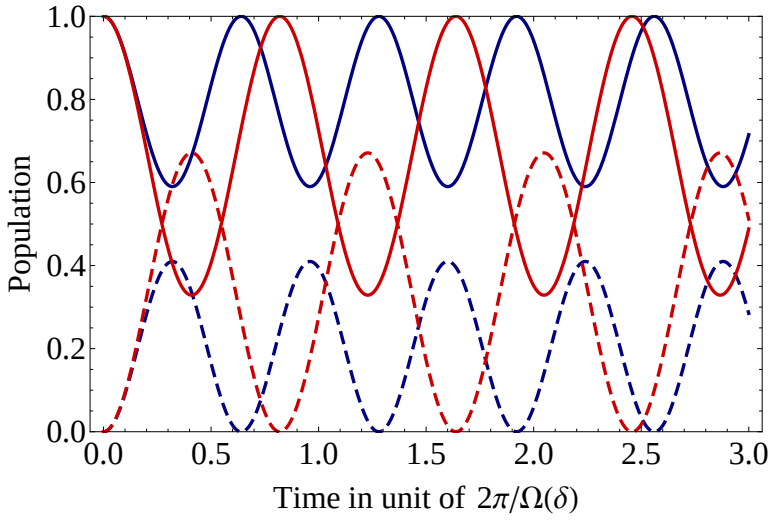

Figure 3.1: Time evolution of a two state system undergoing Rabi oscillations of the population in $|1\rangle$ (solid curve) and $|2\rangle$ (dashed curve) for $\delta/\Omega(\delta) = 1.2$ (blue) and $\delta/\Omega(\delta) = 0.7$ (red).

terms oscillating at the frequency $\omega + \omega_0$ can be neglected as there amplitudes nearly vanish compared to the ones of the near-resonant terms. This is known as the rotating wave approximation [85]. Solving this system with the initial conditions $c_1(0) = 1$ and $c_2(0) = 0$ leads to the solutions

$$c_1(t) = \frac{e^{i\frac{\delta}{2}t}}{\Omega(\delta)} \left(\Omega(\delta) \cos \frac{\Omega(\delta)t}{2} - i\delta \sin \frac{\Omega(\delta)t}{2} \right), \tag{3.8}$$

$$c_2(t) = ie^{-i\frac{\delta}{2}t} \frac{\Omega}{\Omega(\delta)} \sin \frac{\Omega(\delta)t}{2}, \tag{3.9}$$

where $\Omega(\delta) = \sqrt{\delta^2 + |\Omega|^2}$ is called the generalized Rabi frequency. The coupling therefore induces coherent transfer of the populations between the states at a rate $\Omega(\delta)$ known as Rabi flopping, as depicted in Fig. 3.1. When the electric field is resonant with the transition, hence $\delta = 0$, the population undergoes a complete transfer between the states.

3.2 Three level system

The three levels of the system considered here are organised in a Λ configuration, as depicted in Fig. 3.2. Two ground states $|1\rangle$ and $|2\rangle$ can each be coupled to a common excited state $|3\rangle$ via the electric fields $E_\mathrm{a}\cos\omega_\mathrm{a}t$ and $E_\mathrm{b}\cos\omega_\mathrm{b}t$. However, the ground states have the same parity and electric dipole transitions cannot happen between them. Moreover, each electric field is assumed to couple only between two states. Experimentally, this is achieved by choosing the ground states among the hyperfine levels of the $S_{1/2}$ manifold in Rb. The laser line width is usually very small compared to the hyperfine splitting and the coupling to the other state can be neglected. Alternatively, one can choose two magnetic sublevels of the same hyperfine level and play with polarisation of the two fields and optical pumping to create the Λ system. These two fields are used to create a coherent superposition of the two ground states, whose coupling to the electric fields vanishes when the frequency difference corresponds to the ground state splitting. Due to spontaneous emission processes, atoms are pumped into this dark state where they are coherently trapped against the light, hence the name coherent population trapping used to describe this phenomenon.

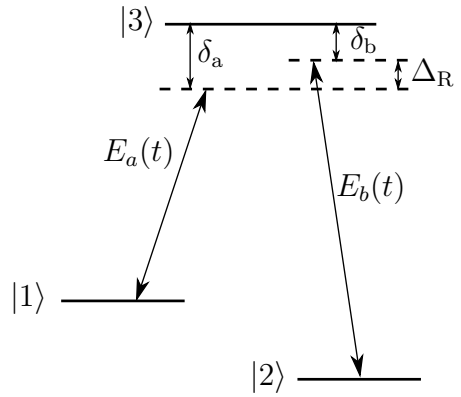

Figure 3.2: Energy structure in a Λ system. Fields $E_\mathrm{a}(t)$ and $E_\mathrm{b}(t)$ couple the excited state $|3\rangle$ respectively to ground states $|1\rangle$ and $|2\rangle$ with strength Ω_a and Ω_b. $\delta_\mathrm{a} = \omega_3 - \omega_1 - \omega_\mathrm{a}$ and $\delta_\mathrm{b} = \omega_3 - \omega_2 - \omega_\mathrm{b}$ are the one-photon detuning of each field compared to their repective atomic transitions. $\Delta_\mathrm{R} = \delta_\mathrm{a} - \delta_\mathrm{b}$ is the two-photon detuning of the two lasers compared to the ground state splitting.

3.2.1 Non-coupling state

A simple approach to understand qualitatively the basics of coherent population trapping can be made by following the same approach as for the two-level system in the previous section. As already outlined, the electric dipole element $\langle 1|\hat{d}|2\rangle$ vanishes as there are no electric transitions allowed between these two states and the interaction hamiltonian reads

$$\hat{H}_{\mathrm{AL}} = \frac{\hbar}{2}\Omega_{\mathrm{a}} e^{i\omega_{\mathrm{a}} t}|1\rangle\langle 3| + \frac{\hbar}{2}\Omega_{\mathrm{b}} e^{i\omega_{\mathrm{b}} t}|2\rangle\langle 3| + \mathrm{h.c.}\ , \tag{3.10}$$

where Ω_{a} and Ω_{b} are the Rabi frequencies associated with the fields $E_{\mathrm{a}}(t)$ and $E_{\mathrm{b}}(t)$ following the definition of Eqn. 3.7. The rotating wave approximation has been applied to eliminate far off-resonant terms. The total atomic wavefunction has a form similar to Eqn. 3.4:

$$|\phi\rangle = c_1(t)e^{-i\omega_1 t}|1\rangle + c_2(t)e^{-i\omega_2 t}|2\rangle + c_3(t)e^{-i\omega_3 t}|3\rangle. \tag{3.11}$$

Substituting this wavefunction into the Schrödinger equation of Eqn. 3.2 with the Hamiltonian $\hat{H} = \hat{H}_0 + \hat{H}_{\mathrm{AL}}$ leads to a system of coupled equations for the amplitudes:

$$i\dot{c}_1 = \frac{\Omega_{\mathrm{a}}}{2} e^{-i\delta_{\mathrm{a}} t} c_3, \tag{3.12}$$

$$i\dot{c}_2 = \frac{\Omega_{\mathrm{b}}}{2} e^{-i\delta_{\mathrm{b}} t} c_3, \tag{3.13}$$

$$i\dot{c}_3 = \frac{\Omega_{\mathrm{a}}}{2} e^{i\delta_{\mathrm{a}} t} c_1 + \frac{\Omega_{\mathrm{b}}}{2} e^{i\delta_{\mathrm{b}} t} c_2, \tag{3.14}$$

where $\delta_{\mathrm{a}} = \omega_3 - \omega_1 - \omega_{\mathrm{a}}$ and $\delta_{\mathrm{b}} = \omega_3 - \omega_2 - \omega_{\mathrm{b}}$ are the one-photon detunings. If there exists one state for which the excited state $|3\rangle$ never gets populated, therefore its amplitude coefficients are found by imposing the condition $c_3(t) = 0$ once the steady-state values are reached. This leads to the relation

$$\Omega_{\mathrm{a}} c_1 = -\Omega_{\mathrm{b}} c_2 e^{i(\delta_{\mathrm{a}} - \delta_{\mathrm{b}})t}, \tag{3.15}$$

which is verified at every time only if the Raman (or two-photon) detuning $\Delta_{\mathrm{R}} = \delta_{\mathrm{a}} - \delta_{\mathrm{b}} = 0$. This is achieved whenever the two lasers have a frequency difference that corresponds to the ground state splitting. It is also worth noticing that the phase difference between the lasers is of critical importance as time dephasing would invalidate the Raman condition, and therefore careful attention has to be paid to maintain the lasers phase-locked. The state that verifies this condition is

$$|\mathrm{NC}\rangle = -\frac{\Omega_{\mathrm{b}}}{\Omega_{\mathrm{ab}}} \mathrm{e}^{-\mathrm{i}\omega_1 \mathrm{t}} |1\rangle + \frac{\Omega_{\mathrm{a}}}{\Omega_{\mathrm{ab}}} \mathrm{e}^{-\mathrm{i}\omega_2 \mathrm{t}} |2\rangle, \tag{3.16}$$

where $\Omega_{\mathrm{ab}} = \sqrt{\Omega_{\mathrm{a}}^2 + \Omega_{\mathrm{b}}^2}$. $|\mathrm{NC}\rangle$ is a *non coupling* state as it does not couple to light, as can be seen when looking at the dipole element between $|\mathrm{NC}\rangle$ and $|3\rangle$:

$$\langle 3|\hat{H}_{\mathrm{AL}}|\mathrm{NC}\rangle = 0. \tag{3.17}$$

$|\mathrm{NC}\rangle$ is therefore called a dark state. Atoms can decay into that state by natural spontaneous emission processes and thereafter they stay trapped without interacting with the external field. By fixing one laser frequency and scanning the other, one expects to see an increase of the transmitted light and can therefore do spectroscopy between the ground states. In this simple view however, spontaneous emission is not considered, as well as collisions and decoherence processes that limit the lifetime of the non coupling state. In order to give a more quantitative description of coherent population trapping, the formalism of the density matrix, introduced in the next section, has to be used.

3.2.2 Optical Bloch equations

The matrix density operator of a pure state $|\phi\rangle$ is a hermitian operator defined as

$$\hat{\rho} = |\phi\rangle\langle\phi|. \tag{3.18}$$

The density matrix allows one to study statistical mixtures of pure states, because the density matrix is independent of the basis chosen to express $|\phi\rangle$ and therefore does not rely on any specific quantisation direction [86]. With the definition of $|\phi\rangle$ given by Eqn. 3.11 and keeping the formulation as in Fig. 3.2, the density

matrix reads

$$\hat{\rho} = \begin{pmatrix} |c_1|^2 & c_1 c_2^* e^{i(\omega_2-\omega_1)t} & c_1 c_3^* e^{i(\omega_3-\omega_1)t} \\ c_2 c_1^* e^{-i(\omega_2-\omega_1)t} & |c_2|^2 & c_2 c_3^* e^{i(\omega_3-\omega_2)t} \\ c_3 c_1^* e^{-i(\omega_3-\omega_1)t} & c_3 c_2^* e^{-i(\omega_3-\omega_2)t} & |c_3|^3 \end{pmatrix}, \tag{3.19}$$

where in the following the notation $\rho_{ij} = c_i c_j^* e^{i(\omega_j-\omega_i)t}$ will be used. The diagonal terms represent the populations of the three states whereas the off-diagonal elements are called *coherences*, which reflect the phase between two states and are the source of interference effects between these states. A very nice feature of the density matrix is its ability to simply calculate the expectation value of any operator $\hat{A}$:

$$\langle \hat{A} \rangle = \mathrm{Tr}(\hat{\rho}\hat{A}). \tag{3.20}$$

The time evolution of $\hat{\rho}$ can be easily derived by injecting Eqn. 3.18 into the Schrödinger equation of Eqn. 3.2:

$$\frac{\mathrm{d}\hat{\rho}}{\mathrm{d}t} = \frac{1}{i\hbar}\left[\hat{H}, \hat{\rho}\right] \ , \tag{3.21}$$

called the von Neumann equation. The population variation and dephasing rate of the coherences due to spontaneous emission and collisions are added thereafter with the help of the relaxation operator $\hat{\mathscr{R}}$. The Lindblad equation then governs the time evolution of the system:

$$\frac{\mathrm{d}\hat{\rho}}{\mathrm{d}t} = \frac{1}{i\hbar}\left[\hat{H}, \hat{\rho}\right] - \hat{\mathscr{R}}\hat{\rho}. \tag{3.22}$$

For the purpose of the present work, the relaxation operator applied to the density matrix reads

$$\hat{\mathscr{R}}\hat{\rho} = \begin{pmatrix} -\frac{\Gamma_0}{2}\rho_{33} & \Gamma_{\mathrm{col}}\ \rho_{12} & \frac{\Gamma_0}{2}\rho_{13} \\ \Gamma_{\mathrm{col}}\ \rho_{21} & -\frac{\Gamma_0}{2}\rho_{33} & \frac{\Gamma_0}{2}\rho_{23} \\ \frac{\Gamma_0}{2}\rho_{31} & \frac{\Gamma_0}{2}\rho_{32} & \Gamma_0\ \rho_{33} \end{pmatrix}, \tag{3.23}$$

where $\Gamma_0 = \tau^{-1}$ is the natural width of the excited state $|3\rangle$. It is assumed that, on average over many atoms, half of the them decay into state $|1\rangle$ and the other half into state $|2\rangle$. As a consequence, coherences between ground and excited

states gets dephased by an amount proportional to Γ_0 [87]. Γ_{col} accounts for the dephasing due to collisions of atoms in states $|1\rangle$ or $|2\rangle$. In order to model accurately a system subject to collisions, population transfer rate between state $|1\rangle$ and $|2\rangle$ and population losses of these two states should also be included [60]. However, the choice of considering only Γ_0 and Γ_{col} is enough to give a simple but qualitative description of the main processes happening in coherent population trapping. Before continuing, a transformation into a rotating frame has to be applied to get rid of the time-dependence of the elements of the density matrix:

$$\begin{aligned}
\rho_{ii} &\rightarrow \tilde{\rho}_{ii}, \\
\rho_{13} &\rightarrow \tilde{\rho}_{13} e^{i\omega_{\text{a}} t}, \\
\rho_{23} &\rightarrow \tilde{\rho}_{23} e^{i\omega_{\text{b}} t}, \\
\rho_{12} &\rightarrow \tilde{\rho}_{12} e^{i(\omega_{\text{a}} - \omega_{\text{b}}) t},
\end{aligned} \tag{3.24}$$

keeping in mind that the matrix elements ρ_{ij} and ρ_{ji} are complex conjugate with interchange of the indices i and j. The following set of equations can be derived and are called *optical Bloch equations*. They describe the dynamics of an atomic system:

$$\begin{aligned}
\dot{\tilde{\rho}}_{11} &= \frac{\Gamma_0}{2}\tilde{\rho}_{33} + i\frac{\Omega_{\text{a}}}{2}(\tilde{\rho}_{13} - \tilde{\rho}_{31}), \\
\dot{\tilde{\rho}}_{22} &= \frac{\Gamma_0}{2}\tilde{\rho}_{33} + i\frac{\Omega_{\text{b}}}{2}(\tilde{\rho}_{23} - \tilde{\rho}_{32}), \\
\dot{\tilde{\rho}}_{33} &= -\Gamma_0\tilde{\rho}_{33} + i\frac{\Omega_{\text{a}}}{2}(\tilde{\rho}_{31} - \tilde{\rho}_{13}) + i\frac{\Omega_{\text{b}}}{2}(\tilde{\rho}_{32} - \tilde{\rho}_{23}), \\
\dot{\tilde{\rho}}_{13} &= (-\frac{\Gamma_0}{2} + i\delta_{\text{a}})\tilde{\rho}_{13} + i\frac{\Omega_{\text{b}}}{2}\tilde{\rho}_{12} + i\frac{\Omega_{\text{a}}}{2}(\tilde{\rho}_{11} - \tilde{\rho}_{33}), \\
\dot{\tilde{\rho}}_{23} &= (-\frac{\Gamma_0}{2} + i\delta_{\text{b}})\tilde{\rho}_{23} + i\frac{\Omega_{\text{a}}}{2}\tilde{\rho}_{21} + i\frac{\Omega_{\text{b}}}{2}(\tilde{\rho}_{22} - \tilde{\rho}_{33}), \\
\dot{\tilde{\rho}}_{21} &= (-\Gamma_{\text{col}} + i\Delta_{\text{R}})\tilde{\rho}_{21} + i\frac{\Omega_{\text{a}}}{2}\tilde{\rho}_{23} - i\frac{\Omega_{\text{b}}}{2}\tilde{\rho}_{31}, \\
\tilde{\rho}_{11} + \tilde{\rho}_{22} + \tilde{\rho}_{33} &= 1.
\end{aligned} \tag{3.25}$$

It is reasonably assumed that the evolution of the populations and coherences are much faster (same order of magnitude as Γ_0) than the variation of the amplitude or frequency of the external field. The steady-state solutions for the $\tilde{\rho}_{ij}$ elements

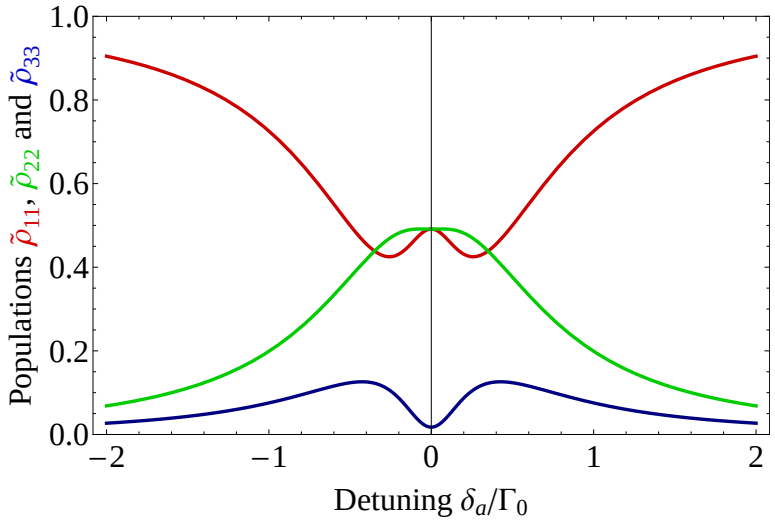

Figure 3.3: Populations of state $|1\rangle$ (red line), $|2\rangle$ (green) and $|3\rangle$ (blue) as a function of the one-photon detuning δ_a. Field E_b is resonant with the $|2\rangle \rightarrow |3\rangle$ transition ($\delta_\mathrm{a} = 0$). Typical experimental values of the couplings $\Omega_\mathrm{a} = \Omega_\mathrm{b} = 0.5\Gamma_0$ are used. Collision rate $\Gamma_\mathrm{col} = \Gamma_0/50$ is exaggerated to enhance the depopulation process.

can then be extracted by imposing $\dot{\tilde{\rho}}_{ij} = 0$. Fig. 3.3 shows the populations of all three states when the detuning δ_a is scanned across the Raman resonance while the field $E_\mathrm{b}(t)$ is kept resonant with its atomic transition, and the same amplitude is set for the two fields ($\Omega_\mathrm{a} = \Omega_\mathrm{b} = \Omega$). For large detunings, atoms are continuously pumped out from $|2\rangle$ and most of them end up in the weakly coupled state $|1\rangle$. As δ_a comes closer to resonance, atoms in $|1\rangle$ start to get pumped into state $|3\rangle$ and one might expect a maximum of population in the excited state at Raman resonance. However, coherences between ground states create the dark state discussed in 3.2.1 where atoms decay by spontaneous emissions processes, hence effectively reducing the population in state $|3\rangle$. In an ideal collisionless system, this population would entirely vanish at resonance, resulting in an equal split of the atoms between the two ground states, as previously suggested by the expression Eqn. 3.16 of the dark state $|\mathrm{NC}\rangle$. In the present situation, collisions induce dephasing between the ground states that reduce the amount of atoms in the dark state. This is seen as a non-zero excited state population in Fig. 3.3 at resonance. In the limit of high collision rate ($\Gamma_\mathrm{col} \approx \Gamma_0$), coherences completely

vanish and population in $|3\rangle$ reaches its maximum at Raman resonance.

3.2.3 Absorption and dispersion

As atoms are trapped in a non-coupling state, transmitted light is expected to exhibit a reduction of aborption when the Raman resonance condition is met. Absorption and dispersion coefficients α and β are related to the real and imaginary parts of the electric susceptibility $\chi = \chi' + i\chi''$ of the medium by [69]

$$\begin{aligned} \alpha &= \chi'' k, \\ \beta &= \frac{\chi'}{2} k, \end{aligned} \tag{3.26}$$

where k is the wave number. These two quantities can be calculated from the coherences in the density operator by first considering the equation of the electric displacement field D:

$$D = \varepsilon_0 E + P = \varepsilon E, \tag{3.27}$$

where ε_0, ε are the electric permittivities in vacuum and in the medium respectively, and P is the polarization of the medium due to the electric field E. Rearranging this equation, replacing E by the superposition of the two coupling fields $E_\mathrm{a}(t)$ and $E_\mathrm{b}(t)$ and writing $\chi = \varepsilon/\varepsilon_0 - 1$ gives for P:

$$P = \frac{\epsilon_0}{2}\left(\chi(\omega_\mathrm{a}) E_\mathrm{a} e^{i\omega_\mathrm{a} t} + \chi(\omega_\mathrm{b}) E_\mathrm{b} e^{i\omega_\mathrm{b} t}\right) + \text{c.c.}\ . \tag{3.28}$$

On the other hand, P is the macroscopic polarisation, and it is related to the expectation value of the electric dipole operator for a single atom by the number density:

$$P = N\langle \hat{d} \rangle = N\left(d_{31}\tilde{\rho}_{13} e^{i\omega_\mathrm{a} t} + d_{32}\tilde{\rho}_{23} e^{i\omega_\mathrm{b} t}\right) + \text{c.c.}\ , \tag{3.29}$$

where the relation of Eqn. 3.20 has been used and N is the number density. P depends explicitly on the coherences $\tilde{\rho}_{13}$ and $\tilde{\rho}_{23}$ and therefore the electric susceptibilty around ω_a can be expressed with the density matrix element by

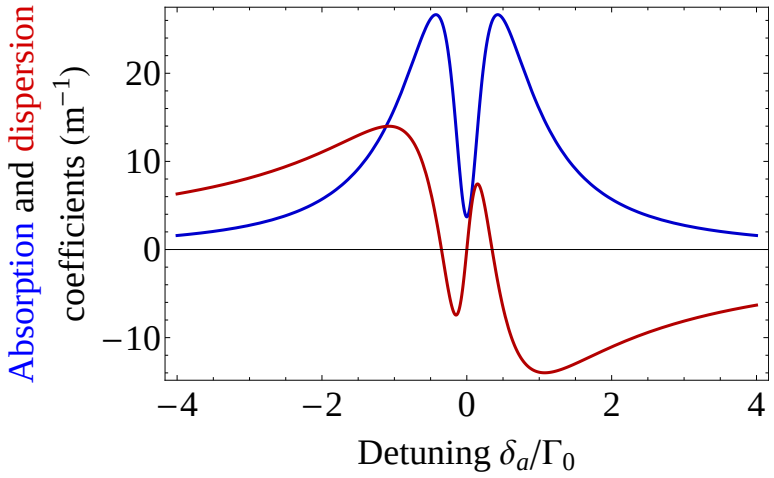

Figure 3.4: Absorption (solid line) and dispersion (dashed line) coefficients as a function of the one-photon detuning δ_{a}. $N = 3\,10^{15}$ m^{-3}, $d_{13} = ea_0$, e is the elementary electric charge, a_0 is the Bohr radius and all other parameters are similar to those used in Fig. 3.3.

comparing Eqns. 3.28 and 3.29:

$$\chi(\omega_{\mathrm{a}}) = \frac{2N|d_{31}|^2\tilde{\rho}_{13}}{\hbar\Omega_{\mathrm{a}}\varepsilon_0}, \tag{3.30}$$

and $\chi(\omega_{\mathrm{b}})$ for $\omega \approx \omega_{\mathrm{b}}$ has a similar expression. Fig. 3.4 shows reduction of absorption at resonance due to the coherently trapped population and the accordingly modified dispersion spectrum. This effect is exploited in electromagnetically induced transparency (EIT) [59], where one strong coupling beam couples two levels in one arm of the Λ system and a weak probe beam is scanned with a frequency close to the transition in the other arm. In the absence of strong coupling beam, the absorption and dispersion spectra show the typical Lorentzian lineshape due to the lifetime of the expected state. They exhibit narrow features at resonance similar to those in Fig. 3.4 when the coupling beam is switched on. Other applications involving similar physical phenomenon include slow light generation [88, 89] and STImulated Raman Adiabatic Passage (STIRAP) [61, 90].

3.2.4 Magnetic field

The actual energy structure of alkalis, such as ^{85}Rb, is more complicated than the simple vision of Fig. 3.2 used to understand the phenomenon of CPT. Each hyperfine level, F, is split into $2F+1$ Zeeman sublevels $|F, m_F\rangle$. The interaction Hamiltonian of the atom with an external static B field is

$$\hat{H} = g_F \mu_{\mathrm{B}} B F_z, \tag{3.31}$$

where F_z is the component of the total angular momentum operator $\hat{\mathrm{F}}$ along the direction of the magnetic field, g_F is the Landé g-factor for the F state considered and μ_{B} is the Bohr magneton [91]. Hence the Zeeman energy shift of each $|F, m_F\rangle$ sublevel is

$$E = g_F \mu_{\mathrm{B}} B m_F. \tag{3.32}$$

The spectroscopy of the ground state Zeeman levels gives a measure of the static magnetic field applied. In alkalis, the ground state is an $S_{1/2}$ shell and the excited states are either $P_{1/2}$ or $P_{3/2}$ shells. The isotope chosen for the experimental investigation is ^{85}Rb and has a 5/2 nuclear spin, therefore there are

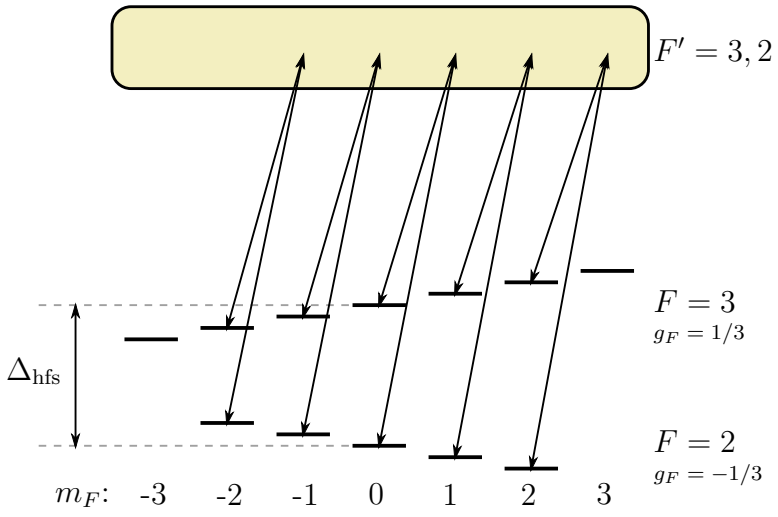

Figure 3.5: Close-up view of the ground state Zeeman splitting in ^{8}5Rb. Five independent Λ CPT systems are created by using only σ^+ and σ^- transitions.

two ground hyperfine levels $F = 2, 3$, and either two $F' = 2, 3$ ($P_{1/2}$) or four $F' = 1, 2, 3, 4$ ($P_{3/2}$) levels for the excited states. The excited state should couple with both ground states, so only excited hyperfine states with $F' = 2$ and $F' = 3$ can be used. Using optical polarisation selective pumping, as in the scheme shown in Fig. 3.5, involving only σ^+ (σ^-) transitions between states $|F = 3, m_F\rangle$ and $|F' = 2, 3, m_F + 1\rangle$ ($|F' = 2, 3, m_F - 1\rangle$) and σ^- (σ^+) transitions between $|F' = 2, 3, m_F + 1\rangle$ ($|F' = 2, 3, m_F - 1\rangle$) and $|F = 2, m_F\rangle$, independent Λ systems are created between each pair of ground states $|F = 2, m_F\rangle$ and $|F = 3, m_F\rangle$ for $|m_F| \leq 2$. As a result, spectroscopy of the ground states shows five CPT resonances which frequency splitting scales with B with the factor

$$\frac{\Delta f}{B} = \frac{(g_{F=3} - g_{F=2})\mu_B}{h} \approx 940\,\text{kHz/G}. \tag{3.33}$$

The central peak corresponds to the two $m_F = 0$ ground states and is not affected by magnetic field (in the limit of small amplitude fields) and it can be used as the frequency reference for CPT atomic clocks [92].

3.3 Experimental investigation

The goal intended here is to experimentally characterise the capabilities of sensing relatively large DC magnetic fields (~ 1 G) with CPT. This work is far from the state-of-the-art techniques that can reaching sensitivity down to the pT level with CPT [93] and down to the fT level using Spin-Exchange Relaxation Free (SERF) [94].

3.3.1 Experimental setup

The experimental setup is depicted in Fig. 3.6. The isotope used is ^{85}Rb as its ground frequency splitting, $\Delta_{\text{hfs}} \approx 3.035\,732\,439\,0(60)$ GHz [95] is half that of ^{87}Rb and electronics in this range are more readily available. In order to eventually design a compact system involing CPT in a magneto-optical trap, the D_2 line (780 nm) between the $5^2\ S_{1/2}$ and $5^2\ P_{3/2}$ manifolds is used, although the D_1 line (795 nm) should be used for enhanced amplitudes and signal widths [96].

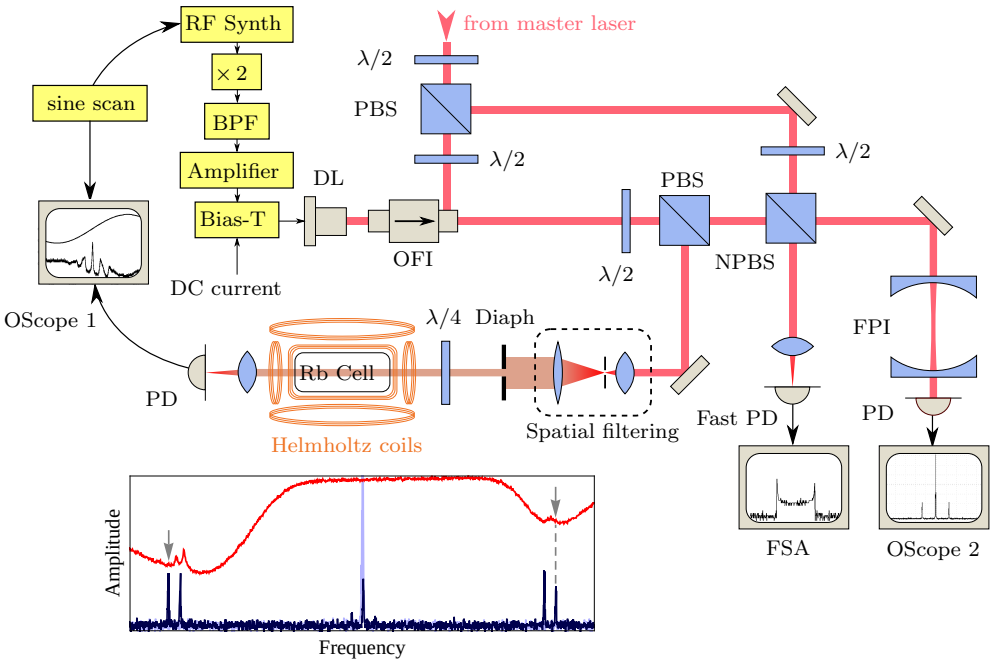

Figure 3.6: Schematics of the experimental CPT setup. DL: Diode laser. PBS: Polarising beam-splitter. NPBS: Non polarising beam-splitter. PD: Photodiode. FPI: Fabry-Pérot inteferometer. OFI: Optical Faraday isolator. $\lambda/2$: Half waveplate. $\lambda/4$: Quarter waveplate. Diaph: Diaphragm. OScope: Oscilloscope. FSA: Frequency spectrum analyser. $\times 2$: Frequency doubler. BPF: Band-pass filter. The inset in the bottom shows the saturated absorption spectrum obtained with the master laser (red), as well as the Fabry-Pérot spectra of the injected modulated (blue) and master (light blue) lasers. The two gray arrows indicate the positions of the $F = 3 \rightarrow F' = 3$ and $F = 2 \rightarrow F' = 3$ transitions.

The two phase-locked frequency components of similar intensities are created in a single laser diode Sharp GH0781JA2C by means of sideband generation as described in Sec. 2.2. The microwave signal at 758.933 MHz generated from a Marconi 2019A frequency synthesiser is doubled to 1.51787 GHz, filtered to remove any other frequency components that could compete in the laser diode with the main desired sidebands, and amplified to match the RF power that gives the highest sideband/carrier intensity ratio. The frequency synthesiser is itself modulated by a low frequency (usually a few tens of Hz) signal that allows scanning across the CPT resonances. Light sent into the CPT Rb cell is first expanded and filtered to reduce the light intensity and remove spatial intensity fluctuations. The 2.5 cm long unshielded room temperature Rb cell contains about 10^{-7} Torr of rubidium without buffer gas. Three orthogonal pairs of coils in Helmholtz configuration are used to cancel external magnetic fields at the cell centre. The coil pair whose axis is parallel to beam propagation is thereafter used to generate the field to be measured and a quarter waveplate sets the circular polarisation of the input beam. A diaphragm limits the magnetic field gradient in the direction tranverse to the beam propagation. The CPT signal is recorded on the transmitted light through the Rb cell and displayed on a two-channel oscilloscope along with the scanning signal. The DC component is removed by low-pass filtering the CPT signal directly on the oscilloscope.

3.3.2 Injection locking of the modulated laser

The CPT signal is maximum when each beam is resonant with its optical transition and decreases whenever the one-photon detuning is increased [60]. For this reason, one wants to have the beam frequency as close as possible to resonance to maintain a relatively high signal amplitude. It is possible to tune the modulated laser to the right wavelength by controlling current and temperature. However, for diodes usually producing ~ 784 nm light at room temperature, cooling down to about 10° C is required, and special care is needed to avoid condensation problems. The diode can be set in an ECDL configuration, but the presence of two cavities does not enhance the sideband generation efficiency, as mentioned in 2.2.4. A very neat way to achieve fine wavelength control is injection locking,

where the frequency of a slave laser is imposed by the master laser [66]. In this case, the unmodulated laser is first injected with an ECDL laser, which can be finely tuned to the right frequency. Once the carrier is locked, RF is switched on to create sidebands in the optical spectrum. Absolute frequency positioning is controlled via a standard saturated absorption technique on the master laser. Inset in Fig. 3.6 shows the Doppler-free spectrum (red) and the approximative corresponding frequency component positions of the modulated (blue) and master (light blue) laser, monitored via the same FPI. The diode ouputs about 10 mW of optical power, when injected, and about on third of the power is found in each first order sideband (the extra inner peaks next to each sideband are due to frequency aliasing on the FPI). Bias current is optimally chosen (45 mA) to give highest efficency, using relaxation oscillation resonances investigated in 2.2.6. High modulation efficiency is obtained via the use of a broadband high gain amplifier, such that about 22 dBm of RF power is sent to the laser diode.

In order to provide efficient CPT spectroscopy, the upper (lower) sideband has to be near resonant with the $F = 2 \rightarrow F' = 3$ ($F = 3 \rightarrow F' = 3$) or $F = 2 \rightarrow F' = 2$ ($F = 3 \rightarrow F' = 2$) transitions; in the room temperature CPT cell, the Doppler broadening is much larger (FWHM$\approx$ 600 MHz) than the frequency difference between the $F' = 2$ and $F' = 3$ states ($\sim$ 63 MHz). It is therefore reasonable to assume that, as long as the sideband frequencies stay in the Doppler-broadened regions, there will always be one velocity class resonant with the two beams. The master laser can then be left free-running, and slight adjustments can be made when the frequency varies due to thermal drifts. Since the sidebands lie in the Doppler broadened parts, the DC component of the detected signal is slowly affected by frequency instabilities of the master laser and one would benefit by locking it to a reference. However, the master frequency lies in a region where there are no readily available saturated absorption peaks, so one needs either to shift it with an AOM [64] or EOM [65], electronic offset locking [62, 63] or Doppler-broadened locking techniques [97]. An other way would be to injection lock one of the sidebands instead of the carrier of the modulated laser [68]. Alternatively, one can combine both efficient sideband generation and fine wavelength control by using anti-reflection coated laser diode in an external cavity configuration [71], where the external cavity round trip time matches the

modulation frequency and does not compete with cavity from the bare diode. The beat frequency of the two lasers is monitored on a frequency spectrum analyser using a fast photodiode. This allows one to check the phase locking as well as the effective modulation depth.

3.3.3 Result processing

To ensure that the scan is not distored through all the electronics and optical components, the signal is chosen to be sinusoidal. As a result, the raw spectroscopy measurements, an example of which are shown in Fig. 3.7(a), have to be scaled in order to restore the correct linear dependence with the frequency axis. The frequency amplitude of the scan is extracted from the beat note with

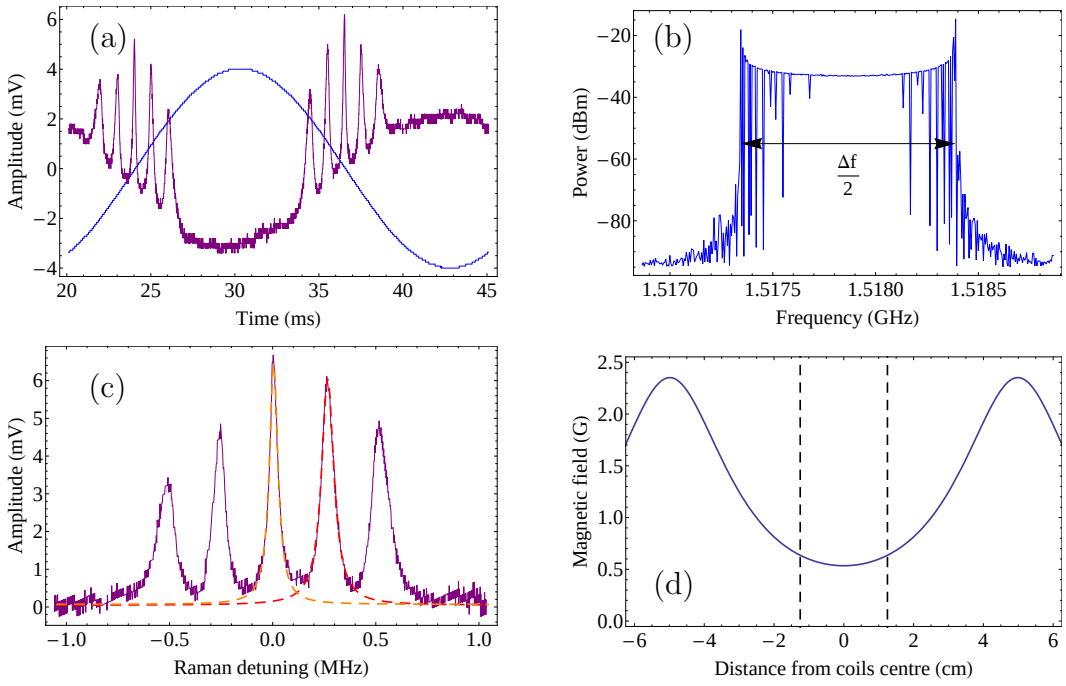

Figure 3.7: Data processing from CPT scans. (a) Raw data from oscilloscope trace. The blue sine curve amplitude of the scan signal is divided by a factor 1000 to fit in the graph. (b) Frequency spectrum of the two laser beat note. (c) Scaled and corrected CPT spectrum. The two dashed lines are Lorentzian fits to the clock and first positive transitions. (d) Shape of the longitudinal static magnetic field generated by the Helmholtz coil pair.

the master laser. The two carriers being locked, the spectrum shows a frequency component at the modulation frequency. When a scan is applied, both sidebands start to swing back and forth on each side of the carrier (Fig. 3.7(b)). Carson bandwidth rule state that for a frequency modulated signal with modulation depth $\delta\omega$ (according to the definition in 2.1.2), 98 % of the power lies into a $2\delta\omega$ large bandwidth centered around the modulation frequency [98]. Therefore, this bandwidth gives a relatively good value for the frequency excursion of one sideband. The total excursion, given that the sidebands move in a symmetrical way on each side of the carrier, can be taken as $\Delta f \approx 4\ \delta\omega$.

The CPT signal shows, overlayed with the resonance peaks, a sinusoidal behaviour similar to the one of the scan, due to each sideband sitting in a Doppler part of the spectrum and therefore undergoing different absorption as the scan is applied. This trend is removed after the frequency axis is correctly restored and then individual peaks are fitted with a Lorentzian function, from which the position of the peak and its full width at half maximum (FWHM) are extracted. Fig. 3.7(c) shows such a corrected spectrum from raw measurements of Fig. 3.7(a). The longitudinal magnetic field, generated by the Helmholtz coils pair and sensed by the atoms along the beam propagation through the cell, is not uniform, as illustrated in Fig. 3.7(d). The central peak corresponds to the clock transition between $m_F = 0$ ground states and therefore is not affected by the magnetic field. However, other resonances get broadened due to this unhomogeneous magnetic field. This, along with residual transverse field, causes the different widths between the central and side peaks in Fig. 3.7(c).

3.3.4 Dependence with B field

As CPT spectroscopy is meant to be used for magnetometry applications, checking the response of the system to an externally applied magnetic is a primary interest. CPT spectra are recorded for different currents flowing in the Helmholtz coils, and therefore for different longitudinal magnetic fields. The frequency information is obtained by applying Eqn. 3.33 on the frequency difference between the centres of the clock transition and the first upper peaks, and uncertainties are taken to be the largest of the FWHM of the Lorentzian fitting curves. Fig. 3.8

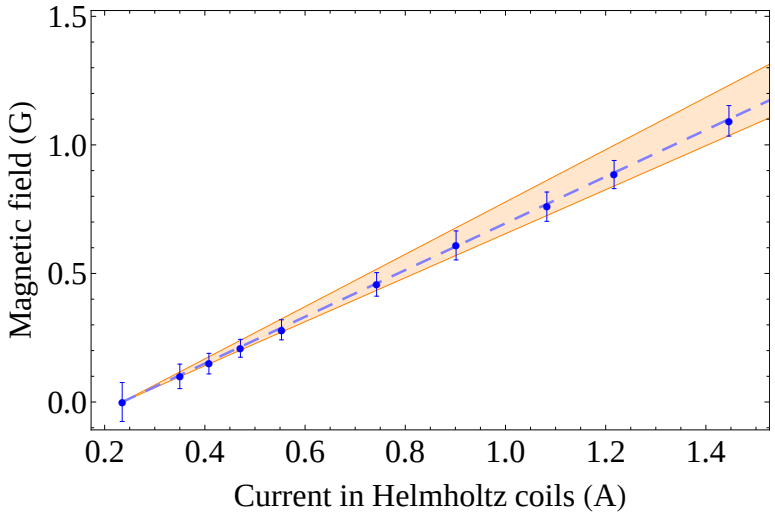

Figure 3.8: Magnetic field from CPT as a function of current in coils. The two solid orange lines indicate the calculated minimum and maximum values of the magnetic field at the centre and on the edges of the cell. The dashed line indicates the averaged calculated value of the magnetic field along the cell.

shows the experimental data points as a function of the coil current. The lower (upper) orange line depicts the minimum (maximum) values of the longitudinal magnetic field felt by the atom at the centre (edges) of the cell, calculated from the geometrical knowledge of the Helmholtz coils. The dashed curves shows the averaged magnetic field along propagation through the cell, and is in good agreement with the expected linear dependence of the experimental points. One will note that, due to the absence of magnetic shielding, the Helmholtz coils are used as well to minimise unwanted ambient DC fields, hence the non-zero value of the current for zero magnetic field.

3.3.5 Amplitude and linewidth of the resonances

In order to detect low values of the magnetic field, one wants to have resonances as fine as possible as well as enough signal amplitude for detection. Using the steady state expressions of the density matrix elements and the complex susceptibility of Eqn. 3.30, the Lorentzian lineshapes of the CPT resonances can be calculated [60].

The linewidth is given by

$$\Delta f_{\mathrm{CPT}} = \frac{1}{\pi}\left(\Gamma_{\mathrm{col}} + \frac{\Omega^2}{\Gamma_0}\right), \tag{3.34}$$

which is linear with light intensity, since $I \propto \Omega^2$, and the amplitude varies as follows

$$A_{\mathrm{CPT}} \propto \frac{\Omega^3}{\Delta f_{\mathrm{CPT}}}. \tag{3.35}$$

It is assumed that both beams have similar intensities ($\Omega_{\mathrm{a}} = \Omega_{\mathrm{b}} = \Omega$), field $E_{\mathrm{a}}(t)$ is resonant with its respective transition ($\delta_{\mathrm{a}} = 0$) while the Raman detuning Δ_{R} is scanned across the two photon resonance. The approximation $\Delta_{\mathrm{R}}, \Gamma_{\mathrm{col}}, \Omega \ll \Gamma_0$ has also been done, justified in most experimental cases. Experimental results for contrast (a), expressed as a ratio of the CPT signal amplitude compared to the DC voltage on the photodetector, and linewidth (b) are displayed in Fig. 3.9. Scan frequency is 40 Hz and the light intensity I_{L} is expressed in normalised Rabi frequencies using the relation [91]

$$\frac{2\Omega^2}{\Gamma_0^2} = \frac{I_{\mathrm{L}}}{I_{\mathrm{sat}}}, \tag{3.36}$$

where the saturation intensity for transition is defined as

$$I_{\mathrm{sat}} = \frac{\pi}{3}\frac{hc}{\lambda^3 \tau}, \tag{3.37}$$

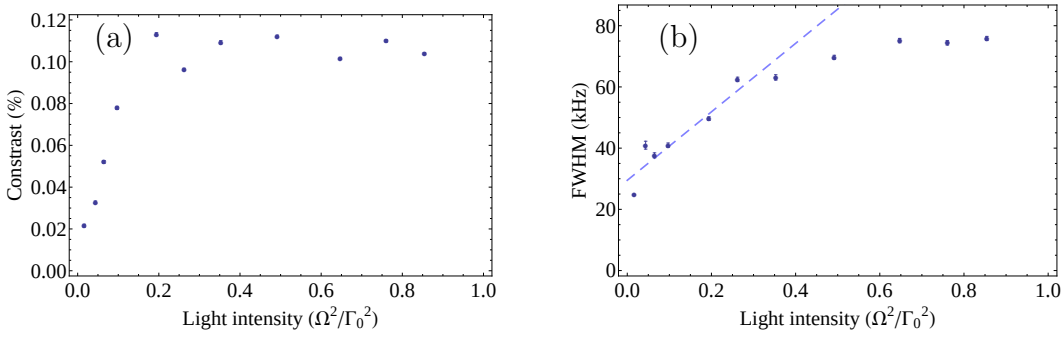

Figure 3.9: Contrast (a) and width (b) of the CPT clock resonance as a function of light intensity. The dashed line in (b) shows the linear dependence for small intensities.

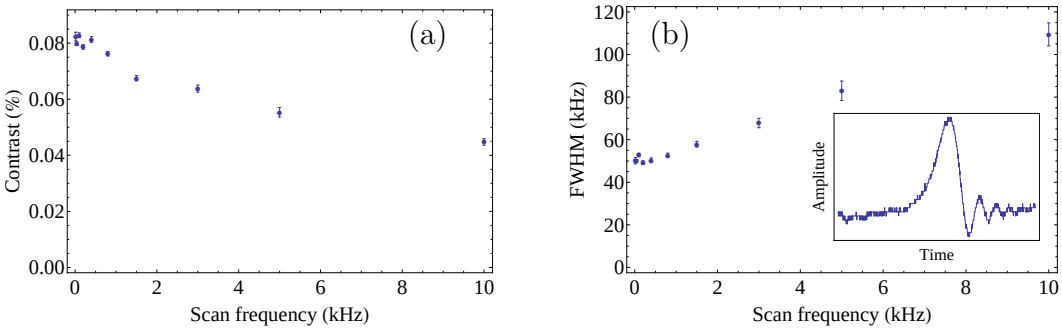

Figure 3.10: Contrast (a) and width (b) of the CPT clock resonance as a function of scan frequency. Inset in (b) shows the ripples for high scan frequencies (f_{scan} = 10)kHz.

with $\tau = \Gamma_0^{-1}$, h is the Planck constant, c is the speed of light and λ is the wavellength that correspond to the optical transition considered. Uncertainties are taken to be the confidence bounds of the fitting parameters. Due to inhomogeneous magnetic fields along the beam propagation through the cell, side peaks are broadened as already outlined in the previous section. Consequently, the following investigations have been conducted on the clock transition only, and with a small applied magnetic field to clearly separate the peaks. The dashed line in Fig. 3.9(b) shows the linear variation of the linewidth for low light intensities, expected from Eqn. 3.34, from which the collisional decoherence rate can be calculated as $\Gamma_{col}/2\pi \approx 15$ kHz. This lower limit to the resonance width is sensibly higher than in other experiments where a quenching gas (such as neon) is present to reduce spin exchange collisions between Rb atoms and to increase the transit time of the atoms across the laser beam, hence effectively dropping the decoherence rate down to a few tens of Hz [99]. The signal amplitude in Fig. 3.9 varies in the same fashion as light intensity, as expected since for low intensities, there are fewer atoms trapped in the dark state. In the limit of low decoherence rate, such that $\Omega_0^2/\Gamma_0 \gg \Gamma_{col}$, one expects a square root dependence of the amplitude with light intensity, since in this case $A_{CPT} \propto \Omega$. Although this behaviour is not particularly evident on the present results, it becomes clearly apparent for experiments including quenching gas [96, 100].

Amplitude and linewidth have also been investigated as the frequency of the scanning signal is varied. Further experimental results are presented in Fig. 3.10,

the light intensity is set such that $\Omega^2/\Gamma_0^2 \approx 0.13$. The signal decreases and broadens as the scanning frequency is increased. Such behaviour was expected since the interaction time between the atoms and the fields is decreased. We noticed that, for high scanning rates (~ 10 kHz), the resonance signal shows an oscillating tail. This results from a fast change in the Raman detuning across the resonance [100, 101].

3.4 Conclusion

In this chapter, we have briefly described the working principle of coherent population trapping and its application to magnetometry. A quick and coarse CPT magnetometer experiment was realised to demonstrate its ease of implementation, even with not optimal equipment. We measured dc magnetic field down to ~ 10 μT, primarily limited by the absence of quenching gas in our rubidium cell that results in resonances not narrower than 40 kHz. We investigated the impact of the scanning frequency and probe beam intensity of the CPT signal amplitude and width with the conclusion than higher quality signals are achieved with low intensity and slow scans.

Chapter 4

Magneto-optical trapping and optical molasses in a tetrahedral configuration

This chapter presents theoretical investigations on the magneto-optical trapping with four laser beams and a quadrupole magnetic field. It first presents the basics of magneto-optical trapping, as well as sub-Doppler cooling. It then gives a model of the trapping and cooling forces in a four beam configuration and investigates the effects of beams angle, intensity imbalance between beams and beam depolarisation on these forces.

4.1 Magneto-optical trapping in alkali atoms

In thermodynamics, temperature is an intensive property (i.e. it does not depend on the size of the system nor the number of particles within) which is a statistical measure of the internal kinetic energy of a many-body system. For gases, it corresponds to the spread of the velocity distribution of the particles (atoms or molecules) in the system. In this approach, high temperatures means that velocities can take a wider range of values than for lower temperatures, as depicted in Fig. 4.1. The two samples on the left and right have, respectively, temperatures T_1 and T_2 with $T_2 > T_1$, and the deviation in the velocity distribution is larger

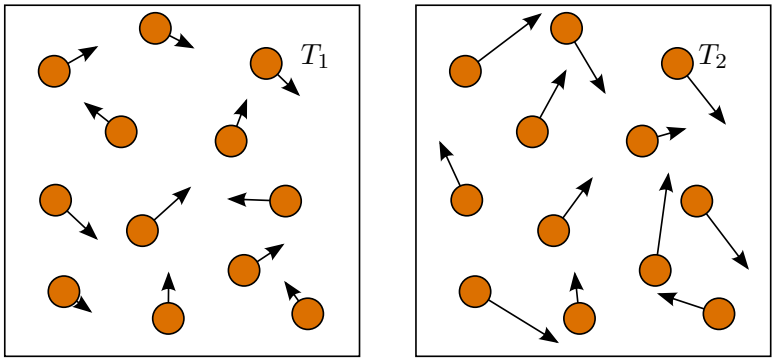

Figure 4.1: Schematics of the thermal energy in two systems with temperature T_1 and T_2. Given that $T_2 > T_1$, the velocity spread of particles on the right is larger than of those on the left.

for particles in the right sample. Atoms well above the degeneracy regime follow Maxwell-Boltzmann statistics [102] and their velocity distribution is given, in the one dimensional case, by the probability density

$$f(v) = \sqrt{\frac{m}{2\pi k_{\mathrm{B}} T}}\ \exp\left(-\frac{m(v-\langle v\rangle)^2}{2k_{\mathrm{B}}T}\right), \tag{4.1}$$

where m is the atomic mass, T is the temperature, k_{B} is the Boltzmann constant and $\langle v^{\mathrm{n}}\rangle$ denotes the n^{th} moment of the stochastic variable v, hence $\langle v\rangle$ is the average velocity. The temperature is related to the standard velocity deviation Δv by

$$\Delta v = \sqrt{\langle v^2\rangle - \langle v\rangle^2} = \sqrt{\frac{k_{\mathrm{B}}T}{m}}. \tag{4.2}$$

It is worth noting that the temperature is only related to the spread of the velocity distribution and not its average, hence a moving ensemble of particles will have the same temperature as the same ensemble at rest. Reducing the temperature thus is equivalent to narrowing this spread in velocities, as depicted in Fig. 4.2.

In atomic physics, cooling finds its interest, first, as a way to ease manipulation of the atomic cloud. One wants to trap atoms and hold them for long enough to carry out the required experiments on them. It turns out that, for neutral atoms, the depth of magnetic or dipolar traps is on the order of a few mK maximum, that is, well below the ambient temperature. This means that, if the temperature

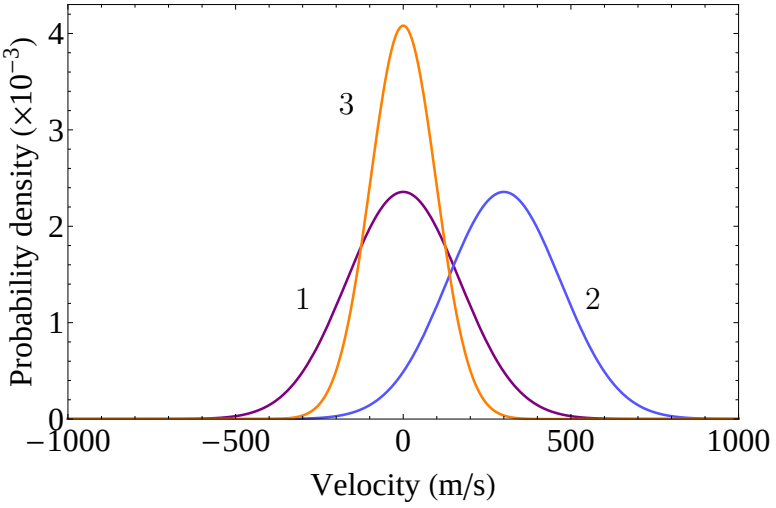

Figure 4.2: Velocity distribution of ^{87}Rb atoms at $T = 300$ K (1 and 2) and $T = 100$ K (3). Distributions 1 and 3 are centered ($\langle v \rangle = 0$ m/s), while distribution 3 have a non zero average velocity ($\langle v \rangle = 300$ m/s).

of the atomic ensemble is too high, atoms with kinetic energies higher than the trap depth can escape the trap. Cooling is therefore a first stage necessary to any further atomic manipulation. To give numerical values that help us see the need of cooling, the velocity deviation for a ^{87}Rb gas at room temperature ($T = 300$ K) is approximately $\Delta v \approx 170$ m/s, as seen in Fig. 4.2, whereas the spread drops to ~ 11 cm/s in a magneto-optical trap (MOT) at typically 140 μK, resulting in a much lower expansion rate of the cloud size, making the atoms easier to trap.

Moreover, the study of quantum gases requires first that the atomic gas is cooled down below a certain critical temperature at which it undergoes a phase transition. Ideally, the statistics of bosons or fermions are described by the Bose-Einstein (BE) or Fermi-Dirac (FD) distributions. At room temperatures however, these two distributions reduce to a classical Maxwell-Boltzmann limit. One has to go at very low temperatures to retrieve a quantum statistical description of bosons or fermions, producing the so-called Bose-Einstein Condensate (BEC) [3, 4] or Degenerate Fermi Gas (DFG) [7].

4.1.1 Doppler cooling

The principle of Doppler cooling uses the radiation force exerted by photons being absorbed to reduce the velocity distribution, hence the temperature, of an atomic cloud. The basic idea relies on momentum transfer between atom and photon from a laser field to carry away kinetic energy from the atom. The laser transfers momentum to the atoms, re-emission transfers energy away. An atom with velocity $\vec{v}$ and mass m absorbs a photon of momentum $\hbar\vec{k}$ and sees its velocity modified such that is becomes $\vec{v} + \hbar\vec{k}/m$. The velocity $\vec{v}$ is depicted in Fig. 4.3 for a two-level atom cooled along one dimension with $\omega_0 = \omega_e - \omega_g$ being the frequency difference between the excited and ground states $|e\rangle$ and $|g\rangle$ respectively. Two laser beams are shone from counter-propagating directions with the same frequency, ω_L, set such that the detuning between the laser and atomic transition frequencies is negative, i.e. $\Delta = \omega_\mathrm{L} - \omega_0 < 0$. The laser is said

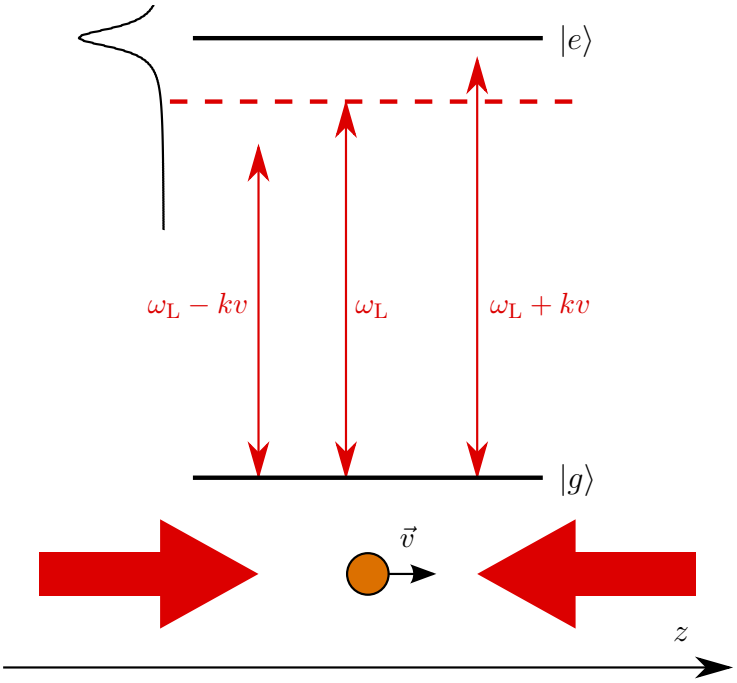

Figure 4.3: Working principle of 1D Doppler cooling in a two level atom. The laser is red-detuned compared to the atomic transition. An imbalance in the absorption rate is created for a moving atom towards one laser due to the Doppler effect bringing this laser frequency closer to resonance.

to be red-detuned compared to the transition. If we first consider only one laser, say the one shining from the left, an atom will continuously absorb and re-emit photons. The momentum change due to isotropic spontaneous emission time-averages to zero, resulting in a net push in the laser propagation direction due to absorption processes only, causing the atom to move towards the right. Now we consider the two laser case as in Fig. 4.3. An atom at rest absorbs statistically the same number of photons from each laser, and therefore stays approximately at rest. However, an atom moving towards the right sees, due to the Doppler effect, the frequency of the right laser closer to resonance than the one from the left laser. As the absorption rate is higher for the right laser, the difference in radiation pressure tends to make the speed to the right decrease. The same phenomenon happens symmetrically for an atom moving towards the left, such that the atomic velocity reduces, kinetic energy being carried away by scattered photons, and thus for a statistical ensemble, the temperature is reduced.

The force exerted from one of the beams on the atom is called the scattering force and can be calculated using Newton's first law

$$\vec{F}_{\mathrm{sc}} = \frac{\mathrm{d}\vec{p}}{\mathrm{d}t} = \hbar\vec{k}\ R_{\mathrm{abs}}, \tag{4.3}$$

where $\hbar\vec{k}$ is the momentum of a single photon and R_{abs} is the photon absorption rate. Following a similar approach as in Sec. 3.2.2 with the two level atom of Fig. 4.3 with ground and excited states $|g\rangle$ and $|e\rangle$ respectively, one can derive the optical Bloch equations, with density, Hamiltonian and relaxation operators defined as [91]

$$\hat{\rho} = \begin{pmatrix} \rho_{gg} & \rho_{ge} \\ \rho_{eg} & \rho_{ee} \end{pmatrix}, \tag{4.4}$$

$$\hat{H} = \hbar \begin{pmatrix} \omega_g & \frac{\Omega}{2}e^{i\omega_{\mathrm{L}}t} \\ \frac{\Omega}{2}e^{-i\omega_{\mathrm{L}}t} & \omega_e \end{pmatrix}, \tag{4.5}$$

$$\hat{\mathscr{R}}\hat{\rho} = \begin{pmatrix} -\Gamma\rho_{ee} & \frac{\Gamma}{2}\rho_{ge} \\ \frac{\Gamma}{2}\rho_{eg} & \Gamma\rho_{ee} \end{pmatrix}, \tag{4.6}$$

where ω_{L} is the laser frequency, $\hbar\omega_e$ and $\hbar\omega_g$ are the energies of states $|g\rangle$ and

$|e\rangle$ and Γ is the natural decay rate from state $|e\rangle$ to state $|g\rangle$. The electric dipole coupling between states is represented by the Rabi frequency Ω proportional to the laser electric field. The steady state value of the excited state population is

$$\tilde{\rho}_{ee} = \frac{\Omega^2}{\Gamma^2 + 2\Omega^2 + 4\Delta^2}, \tag{4.7}$$

where Δ is the detuning as previously defined. An atom absorbs as many photons as it spontaneously emits, therefore the rightmost term in Eqn. 4.3 can be replaced by the spontaneous emission rate $R_{\rm sp}$, which is proportional to the fraction of the atomic population in the excited state [91]:

$$R_{\rm abs} = R_{\rm sp} = \Gamma \tilde{\rho}_{ee}. \tag{4.8}$$

In the one-dimensional case, an atom moving with velocity v sees the light of a laser beam propagating towards the positive z direction (the laser coming from the left in Fig. 4.3) with a shifted frequency $\omega'_{\rm L} = \omega_{\rm L} - \vec{k} \cdot \vec{v} = \omega_{\rm L} - k\ v_z$ (with v_z the component of $\vec{v}$ along the z axis) and the substitution $\Delta \to \Delta - k\ v_z$ can be made in Eqn. 4.7 to account for this Doppler effect. The scattering force is therefore given by

$$F_{\rm sc}^{\rm left} = \hbar k\ \frac{\Gamma}{2}\ \frac{I/I_{\rm sat}}{1 + I/I_{\rm sat} + 4(\Delta - k\ v_z)^2/\Gamma^2}\ , \tag{4.9}$$

where Eqn. 3.36 has been used to introduced light I and saturation $I_{\rm sat}$ intensities. The force $F_{\rm sc}^{\rm right}$ from the counter-propagating laser beam is obtained by changing k to $-k$ in Eqn. 4.9, since the Doppler effect shifts the laser frequency in the opposite direction. The forces from two lasers propagating towards the positive (orange) and negative (purple) z directions is depicted in Fig. 4.4. For a negative detuning (red-detuned light), the push from each laser is larger for an atom moving towards its source, and the action of both lasers results in a viscous force, shown by the dashed brown line in Fig. 4.4. This cooling mechanism is called optical molasses [1] due to its analogy with a particle moving in a viscous fluid. The force can be approximated for low velocities ($k\ v_z \ll \{\Gamma, \Delta\}$) with a linear

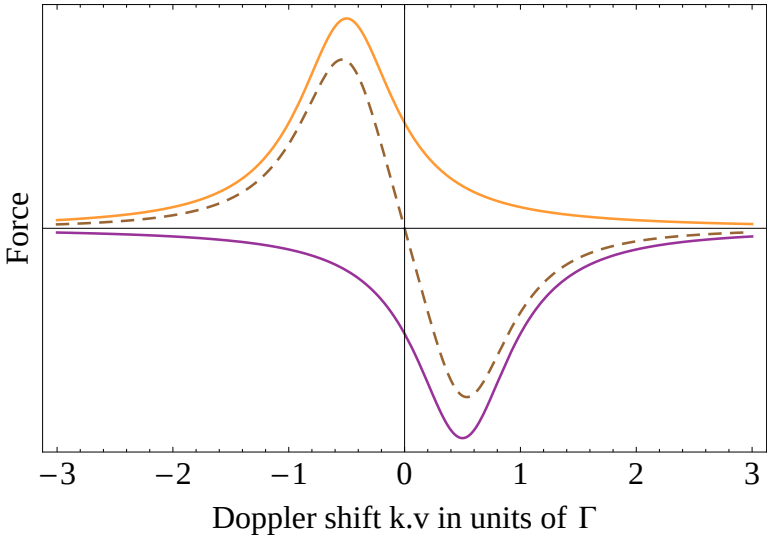

Figure 4.4: Scattering force exerted from two red-detuned counter-propagating lasers on an atom with velocity v and natural linewidth Γ. Laser detuning is $\Delta = -\Gamma/2$. The orange and purple solid lines respectively show the force from left-coming ($k > 0$) and right-coming ($k < 0$) lasers whereas the dashed line is the contribution from both.

dependence to velocity:

$$F_{\text{mol}} \approx -\alpha v, \tag{4.10}$$

for which the viscous constant α has the following expression:

$$\alpha = -8\ \hbar k^2\ \frac{\Delta}{\Gamma}\ \frac{I/I_{\text{sat}}}{(1 + I_{\text{tot}}/I_{\text{sat}} + 4\Delta^2/\Gamma^2)^2}\ . \tag{4.11}$$

The substitution $I \to I_{\text{tot}}$ has been done in Eqn. 4.11 to account for the total beam intensity. According to the above ideal description of optical molasses, the equilibrium temperature seems to be exactly zero. In reality, this approach neglects heating generated from the random processes of absorption and scattering of photons by the atoms. The number of photons an atom absorbs during the same time duration varies due to fluctuations in the field intensity and spontaneous emission is an inherently stochastic phenomenon. The equilibrium temperature point, for which the cooling force exactly balances heating, can be derived and

the molasses temperature is given by [85]

$$T_{\mathrm{mol}} = -\frac{\hbar\Gamma}{8k_{\mathrm{B}}}\frac{1 + I_{\mathrm{tot}}/I_{\mathrm{sat}} + 4\Delta^2/\Gamma^2}{\Delta/\Gamma}, \tag{4.12}$$

which finds its minimum value, in the low intensity limit (i.e. $I_{\mathrm{tot}} \ll I_{\mathrm{sat}}$), for $\Delta = -\Gamma/2$:

$$T_{\mathrm{mol}}^{\mathrm{min}} = \frac{\hbar\Gamma}{2k_{\mathrm{B}}}, \tag{4.13}$$

typically 140 μK for ^{87}Rb.

As shall be seen later on, the actual temperature observed with optical molasses can be more than one order of magnitude lower than the one given by Eqn. 4.13. This enhanced cooling mechanism that allows sub-Doppler temperatures comes from the magnetic sublevel structure of the ground state structure, which has been neglected so far, and requires a more subtle treatment [12, 13] including optical pumping, light shift and optical lattice due to the counter-propagating beams. Additionally, there is a fundamental limit to the minimum temperature that could be achieved with optical molasses, even in the ideal case with no heating. Assuming an atom has zero velocity at a given time, it will eventually absorb a photon from either beam. The kinetic energy transfer of a single photon sets what is called the recoil temperature and reads

$$T_{\mathrm{rec}} = \frac{\hbar^2 k^2}{m k_{\mathrm{B}}}. \tag{4.14}$$

For ^{87}Rb, this recoil temperature is typically of the order of magnitude of 1 μK.

4.1.2 Zeeman trapping

Doppler cooling, however, does not provide trapping and the atoms can still drift out of the optical molasses, resulting in a very low density. One very elegant way of adding trapping properties to this scheme was first demonstrated in 1987 by Pritchard and co-workers [2] and has since become the standard first stage of neutral atom trapping (with exceptions such as hydrogen [103], for instance). It consists of using the magnetic sublevel structure of the atom to create a position-dependent force. The schematic of the trap is depicted in Fig. 4.5. The excited

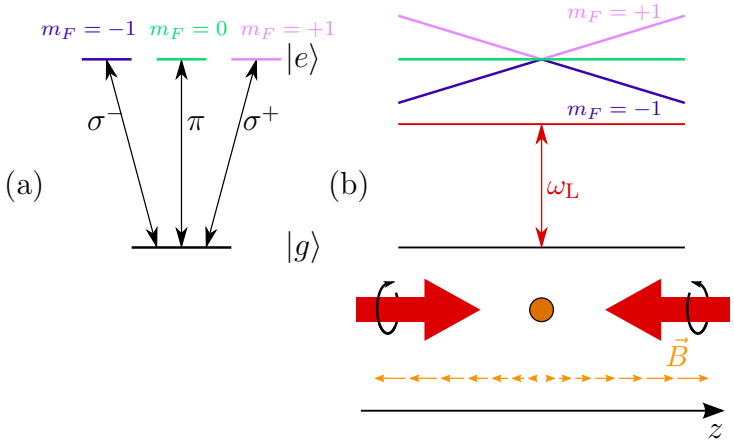

Figure 4.5: Working principle of 1D Zeeman trapping in a two level atom. The spatially varying magnetic field, along with the light beam polarisation, leads to a position dependent force that traps atoms around the magnetic field minimum.

state $|e\rangle$ is assumed to have total angular momentum $F = 1$ such that it is made up of three Zeeman sublevels ($m_F = -1, 0, +1$), normally degenerate in the absence of a magnetic field, and only transitions from a ground state with spin projection $m_F = 0$ are considered. Of course, this view is oversimplified compared to the real structure of ^{87}Rb but it is enough to understand the working principle in simple terms. Suppose there is a magnetic field applied that acts as a quantization axis, the excited state sublevels split with the following energy difference [104]:

$$\Delta E = g_F \mu_B m_F B, \tag{4.15}$$

where g_F is the Landé g-factor for the given state with total angular momentum F, μ_B is the Bohr magneton and B is the amplitude of the static magnetic field. For the present case, we suppose that g_F takes a positive value. The total angular momentum of the atom in the Zeeman sublevel $m_F = +1$ precesses around the local magnetic field and its projection along the magnetic field is anti-aligned with it [105], making this state a low-field seeker. Symmetrically, the angular momentum of an atom in the $m_F = -1$ sublevel precesses in the other direction and is high-field seeking, as its angular momentum projection is aligned, this time, with the magnetic field. Atoms in state $m_F = 0$ are insensitive the to magnetic

field in the sense that their angular momentum is orthogonal to the magnetic field. Due to the conservation of angular momentum, transition probabilities are highly sensitive to the polarisation of light. The state $m_F = +1$ can only be excited (from ground state with $m_F = 0$) with a photon which spin projection along the quantization axis direction is $m_S = +1$, where S denotes the spin of a photon. This corresponds, for beam propagation parallel to the magnetic field vector, to a left circularly polarised photon. Similarly, excitation to state $m_F = -1$ requires a right circularly polarised photon (with spin projection $m_S = -1$), whilst excited state $m_F = 0$ can only be reached with a linearly polarised photon (i.e. polarised along the magnetic field direction with $m_S = 0$). This last case is not possible for beam propagation parallel to the magnetic field orientation. Transitions from ground state to excited sublevels $m_F = -1$, $m_F = 0$ and $m_F = +1$ are respectively called σ^-, π and σ^+, as indicated in Fig. 4.5(a). It is very important to keep in mind these names refer to atomic transitions and not to light polarisation, as they are often mistaken. Although a correspondance can be made for light propagation along the magnetic direction as in a 6-beam MOT, one needs to be careful and first project the light polarisation before considering excitation on the three different channels [106], as will be emphasized later in Sec. 4.2.1 for the 4-beam MOT case.

Let us consider the simple one-dimensional case of Fig. 4.5(b). A linearly varying static magnetic field $\vec{B}$ is applied, with the field vector pointing along z. The position where the field amplitude vanishes is set to be $z = 0$. According to Eqn. 4.15, the energy difference, relative to the ground state, of the $m_F = +1$ ($m_F = -1$) sublevel increases (decreases) when the amplitude of $\vec{B}$ increases. Two red-detuned counter-propagating laser beams, with respective wave vector $\vec{k}_{\text{left}}$ and $\vec{k}_{\text{right}} = -\vec{k}_{\text{left}}$, are shone on the atoms. Their polarisation have the same handedness, i.e. for each beam, the electric field vector rotates in the same direction when looking in the direction of the beam wave vector. Circular polarisations are set such that as it propagates, each laser couples only to $m_F = -1$ ($m_F = +1$) via σ^- (σ^+) transitions before (after) crossing the position of the magnetic field minimum. For an atom on the left side ($z < 0$), photons coming from the left can only induce σ^- transitions and excite the atom to state $m_F = -1$, which is brought closer to resonance with the laser frequency while

state $m_F = +1$, reachable only by absorption from a right laser photon, is being taken further away from resonance. The probability is higher to absorb a left-coming photon than a right-coming photon, and the resulting imbalance in radiation pressure pushes the atom towards the magnetic field minimum, where absorption from both laser is equal and therefore is the trap center.

The force exerted from one beam drives σ^+ or σ^- transitions only, depending on which side of the magnetic field minimum the beam is acting, as depicted in Fig. 4.5, and should be treated accordingly. However $m_F = -1$ states on one side and $m_F = +1$ states on the other side of the magnetic field zero point shift with the same slope and it is justified to consider, in this simple case, that one beam couples the ground state with an excited state with an energy shift which varies linearly relative to position, and with a respectively positive or negative gradient for the left or right coming laser beam. Starting from the scattering force given by Eqns. 4.3, 4.7 and 4.8, the force exerted from the left-coming (right-coming) beam can be therefore calculated by making the substitution $\Delta \rightarrow \Delta + \mu b_1 z$

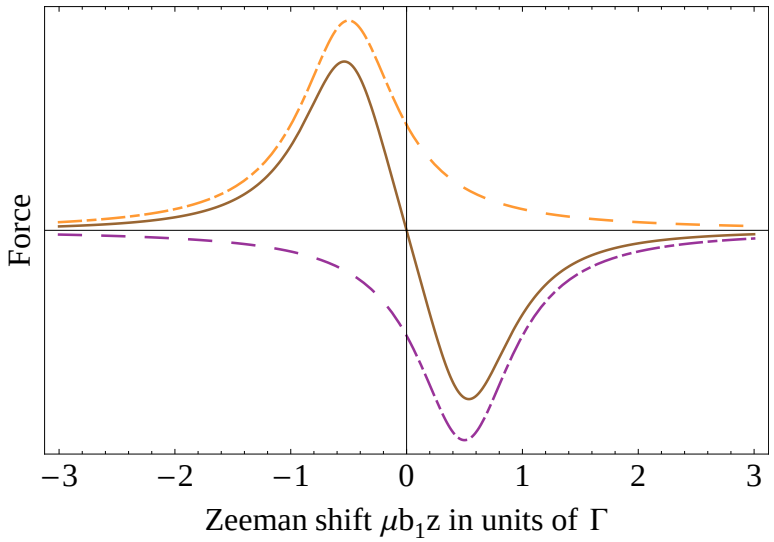

Figure 4.6: Scattering force exerted from two red-detuned counter-propagating lasers as a function of position on an atom at rest with natural linewidth Γ. The laser detuning is $\Delta = -\Gamma/2$ and the magnetic field gradient is $b_1 = \Gamma/2\mu z$. The orange and purple lines show the force from the two individual lasers whereas the brown solid line is the contribution from both. Dashed and dot-dashed parts correspond respectively to σ^+ and σ^- transitions.

($\Delta \to \Delta - \mu b_1 z$) where $\mu = g_F \mu_B m_F$ is the magnetic moment of state m_F and $b_1 > 0$ is the magnetic field gradient:

$$F_{\text{Zeeman}}^{\text{left/right}} = \hbar k \, \frac{\Gamma}{2} \, \frac{I/I_{\text{sat}}}{1 + I_{\text{tot}}/I_{\text{sat}} + 4(\Delta \pm \mu b_1 z)^2/\Gamma^2} \, . \tag{4.16}$$

An example of the force from each individual beam, as well as the resulting restoring force that provides trapping at the magnetic field minimum, is shown in Fig. 4.6.

4.1.3 sub-Doppler cooling

Usually, in experimental physics, things never go as they should. They go worse. However, sub-Doppler cooling is a good counterexample that Murphy's law doesn't apply all the time. Soon after the realisation of the first optical molasses [1] and magneto-optical trap [2], temperatures well below the limit predicted by the Doppler theory were measured [11], that is 43±20 μK instead of the 240 μK expected for sodium atoms. The understanding of the underlying mechanisms in atom trapping and cooling and the experimental achievement of cold gases eventually led in Bill Phillips, Steven Chu and Claude Cohen-Tannoudji getting the Physics Nobel prize in 1997 [15, 16, 17].

The problem with the Doppler cooling theory is that is assumes a two level system and hence cannot deal with variations in polarisation and coupling. In optical molasses, the beams coming from different directions result in a rather complicated optical lattice, with a local polarisation changing in space. Assume atoms with an $F \to F + 1$ transition and red-detuned light, as it is the case with the MOT cooling and trapping laser between the $F = 2$ and $F = 3$ states in ^{87}Rb. In this situation, the hyperfine state with larger ac-Stark shift (hence the lowest energy state) is always the one where optical pumping puts most of the atomic population in [107]. As the atoms move through the optical lattice (i.e. they have a non-zero kinetic energy), they see a slightly different local polarisation of the light. This implies that the coupling, and thus the energy shift of the different hyperfine levels changes. The atoms, that were initially mostly populating the lower energy state, see an increasing potential as the coupling of that state reduces, and

therefore part of their kinetic energy is converted into internal energy. The atomic population is then redistributed with optical pumping such that the state that has now the larger ac-Stark shift is the most populated. During this process, the kinetic energy that was converted into internal energy when the atoms had to "climb" the potential hill is carried away by the emitted photon as the atoms tend to revert to the most ac-Stark shifted level, effectively reducing the kinetic energy spread, hence the temperature, of the atomic ensemble. As sub-Doppler cooling relies of the change of the light polarisation in the optical lattice, it is often referred to as polarisation gradient cooling [12]. Optical pumping that puts an atom into a lower energy ground state takes a finite time. If the atoms have a too high speed, they will travel too quickly through the optical lattice before absorbing a photon. Typically, the lattice polarisation is periodic every at most $\lambda/2$, and the optical pumping time takes a few excitation cycles, such that we can reasonably assume that it is not smaller than $\sim 10\tau$, where τ is the natural decay time from the excited state. Thus, if the velocity is larger than $v_{\max} \sim \lambda/20\tau$, the atoms don't have the time to absorb photons (and hence being redistributed amongst the lower energy states) before they reach the top of the potential. This implies a much narrower velocity capture range than for Doppler cooling such that it is realistically not possible to directly sub-Doppler cool atoms at room temperature, and a first cooling stage, such as a MOT, is necessary. The final achievable temperature is mainly given by the potential hill that the atoms have to climb, that is by the amplitude of the ac-Stark shift, proportional to I/Δ [85]. More precisely, the sub-Doppler temperature is given by [107]

$$T_{\mathrm{s-D}} \approx \frac{\hbar\Gamma^2}{4k_{\mathrm{B}}|\Delta|}\,\frac{I}{I_{\mathrm{sat}}}. \tag{4.17}$$

Experimentally, very low temperature optical molasses (ultimately limited by the recoil energy) is achieved by increasing the light detuning and reducing its intensity. Temperatures as low as 2.5 μK were measured in caesium [108], whereas the Doppler theory predicts a limit at 120 μK. Sub-Doppler cooling has proven to be a critical step in the achievement in very cold atomic samples, without which alkali gases below quantum degeneracy might has not been possible to produce.

4.2 Four beam configuration

The common way of implementing magneto-optical traps in three dimensions uses two current coils in an anti-Helmholtz configuration to generate a quadrupole magnetic field and three pairs of counter-propagating beams, as depicted in Fig. 4.7. Although the field from anti-Helmholtz coils is fully described using elliptical integrals (see Sec. 6.1.2 for the complete expression), in the central region it can be approximated to vary linearly in all three dimensions [109]. Assuming circular coils of diameter d and spacing s, the magnetic field in the central region, where $\{x, y, z\} \ll \{s, d\}$ is

$$\vec{B}_{\text{quad}} = B_1\{x, y, -2z\}, \tag{4.18}$$

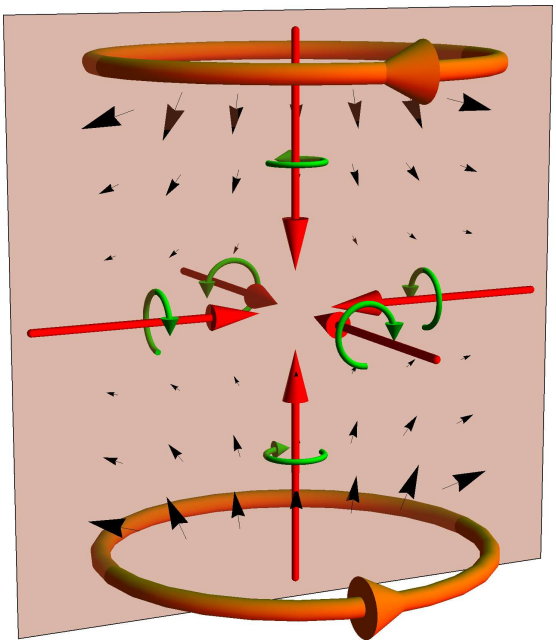

Figure 4.7: Six beam MOT configuration showing the anti-Helmholtz coils (orange) and the different beams (red) with their respective electric field polarisation (green). The vector field shows radial and axial behaviour of the magnetic field.

where the magnetic field gradient B_1 is given by

$$B_1 = \frac{48\mu_0 N I d^2 s}{(4d^2 + s^2)^{5/2}}, \tag{4.19}$$

and N is the number of turns in each coil, I is the electric current and μ_0 is the vacuum permeability. The coil axis is oriented along the z direction. Polarisation of each pair of counter-propagating beams has the same handedness, and it is inverted for the beams propagating along z compared to those propagating in the $x - y$ plane, due to the reversed sign of the magnetic field along the coil axis in Eqn. 4.18. In each orthogonal direction, the situation is similar to the one dimensional case described above, since the beams propagate parallel to the local magnetic field vector. However, the minimum number of beams required to trap and cool in a three dimensional space can be reduced. In 1D, one needs two opposite beams as already explained. In 2D, three beams are required, coming along the bisection angle of an equilateral triangle and the situation extends to four beams for the three dimensional case. This can be seen as if, starting for the 1D case, each time a dimension is "added", a new beam is required to provide the cooling/restoring force to avoid atoms escaping in the new dimension. Thus, one needs $N + 1$ beams to trap and cool in N dimensions. Fig. 4.8 summarizes the $N = \{1, 2, 3\}$ case. It is then possible to reduce the number of beams required

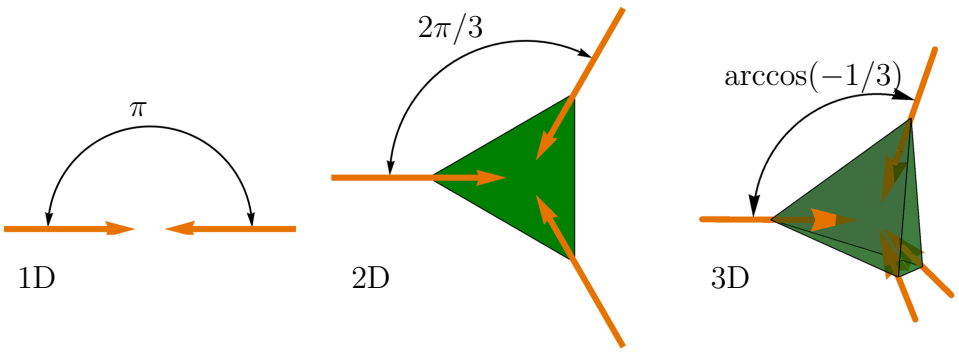

Figure 4.8: Minimum number of beams in one, two and three dimensions with each beam providing the same force. In 2D/3D, the beams follow the medians of the regular polygon/polyhedron with the lowest number of edges/faces, hence a equilateral triangle/regular tetrahedron (depicted in green).

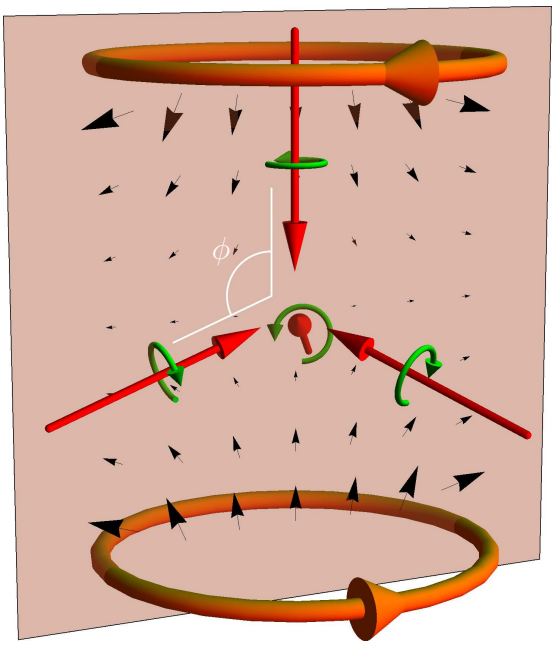

Figure 4.9: Four beam MOT configuration showing the anti-Helmholtz coils (orange) and the different beams (red) with their respective electric field polarisation (green). The vector field shows radial and axial behaviour of the magnetic field.

to trap atoms and the first four beam MOT was demonstrated by Shimizu and co-workers in 1991 [31, 110]. We consider here only the case of collimated laser beams, thus producing a force along their direction of propagation. Indeed, it is also possible to trap atoms with two counter-propagating focused beams [111]. In this case, one uses the transverse component of the wave vectors of the beam being focused to provide trapping and cooling in the other two directions.

In the four beam MOT of the present work, we assume that the coils axis is vertically oriented, relative to the laboratory frame, and one beam follows this axis, propagating towards the bottom coil, such that its wave vector $\vec{k}$ is along the z axis and points towards negative z. The other three beams come from the bottom with an angle ϕ compared to the coils' main axis, as depicted in Fig. 4.9. The laser system used for MOT and optical molasses operations are usually the same one. Although MOTs have proven to be very robust, regarding beam intensity imbalance, optical molasses are more sensitive to that. Balanced optical molasses occur when the force from all beams of intensities I_n and wave

vectors $\vec{k}_n$ cancel such that there is no net force towards one specific direction:

$$\sum_n I_n \vec{k_n} = \vec{0}, \tag{4.20}$$

with the requirement, as outlined previously, that there are components in all three dimensions amongst the entire set of wave vectors $\vec{k}_n$. For four beams with similar intensities I_n, the above condition is verified notably if the beams come along the medians of a regular tetrahedron, with an angle between beams $\arccos(-1/3)$. This special case has the advantage of giving spherically symmetric molasses (with similar cooling forces in each direction). It is worth noting that, to translate to the 2D case, the three beams must follow the medians of an equilateral triangle. This geometric configuration of the beams for balanced molasses can be seen in Fig. 4.8.

4.2.1 Trapping and cooling force

If balanced molasses can be easily achieved with a four beam MOT, understanding how Zeeman trapping is achieved requires more work. Indeed, contrary to the six beam case, the upgoing beams make an angle with the coil axis and it is no longer possible to consider each orthogonal direction independently. For each beam, one needs to project the light polarisation along the local quadrupole field to work out the amount of light that excites each of the σ^+, σ^- and π transitions [106, 112]. Consider a magnetic field pointing along z and a circularly polarised beam, propagating with an angle φ between its wave vector $\vec{k}_j$ and the local field $\vec{B}$, such that $\cos\varphi = \frac{\vec{k}_j \cdot \vec{B}}{|\vec{k}_j|\ |\vec{B}|}$, as depicted in Fig. 4.10. The electric field can be written as

$$\vec{E} = \frac{E_j}{\sqrt{2}} \begin{Bmatrix} 1 \\ e^{is\frac{\pi}{2}} \cos\varphi \\ e^{is\frac{\pi}{2}} \sin\varphi \end{Bmatrix}, \tag{4.21}$$

where E_j is the amplitude of the field and s denotes the handedness of the polarisation direction, relative to the propagation direction, hence a left or right polarised light corresponds respectively to $s = 1$ or $s = -1$. Solving the following

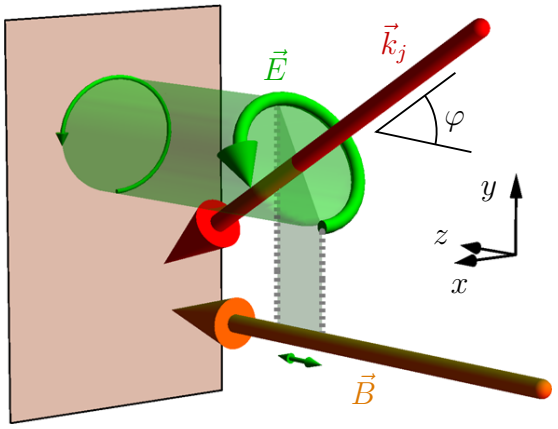

Figure 4.10: Circular polarisation projection on the local magnetic field. Component along the magnetic field vector excites π transitions while projection in the orthogonal plane can be expressed in terms of σ^+ and σ^- transistions.

equation, using the projection of $\vec{E}$ in the plane orthogonal to $\vec{B}$,

$$\vec{E}_\perp = \frac{E_j}{\sqrt{2}} \begin{Bmatrix} 1 \\ e^{is\frac{\pi}{2}} \cos\varphi \\ 0 \end{Bmatrix} = \frac{E_{\sigma^+}}{\sqrt{2}} \begin{Bmatrix} 1 \\ e^{i\frac{\pi}{2}} \\ 0 \end{Bmatrix} + \frac{E_{\sigma^-}}{\sqrt{2}} \begin{Bmatrix} 1 \\ e^{-i\frac{\pi}{2}} \\ 0 \end{Bmatrix}, \tag{4.22}$$

gives the amount of electric field that contributes to σ^+ and σ^- transitions and the projection onto the magnetic field gives the π contribution. Finally, the decomposition of light intensities on the π, σ^+ and σ^- transitions are

$$\begin{aligned} I_0 &= I_j \frac{\sin^2\varphi}{2}, \\ I_{+1} &= I_j \left(\frac{1 - s\cos\varphi}{2}\right)^2, \\ I_{-1} &= I_j \left(\frac{1 + s\cos\varphi}{2}\right)^2, \end{aligned} \tag{4.23}$$

where $I_j = \frac{1}{2} c\,\varepsilon_0\, E_j^2$ is the total light intensity.

The total force is derived by considering the cumulative effect of the three

different transitions and reads, using Eqns. 4.9 and 4.16,

$$\vec{F_j} = \hbar\vec{k_j}\ \frac{\Gamma}{2}\ \frac{I_j}{I_{\rm sat}} \sum_{n=-1,0,1} \frac{\eta_n}{1+\frac{\sum_j I_j}{I_{\rm sat}} + 4\frac{(\Delta-\vec{k_j}\cdot\vec{v}-\mu_F n|\vec{B}|)^2}{\Gamma^2}}, \tag{4.24}$$

where $\eta_n = I_n/I_j$ with $n = -1, 0, +1$ and $\mu_F = g_F\mu_{\rm B}$. For $\{|\vec{k_j}\cdot\vec{v}|, \mu_F|\vec{B}\} \ll \{\Gamma, \Delta\}$, the above equation can be Taylor expanded:

$$\vec{F_j} \approx \hbar\vec{k_j}\ \frac{\Gamma}{2}\ \frac{I_j}{I_{\rm sat}} \sum_{n=-1,0,1} \eta_n \left(K + C(\vec{k_j}\cdot\vec{v} + \mu_F n|\vec{B}|)\right), \tag{4.25}$$

where $K = (1 + \frac{\sum_j I_j}{I_{\rm sat}} + 4\Delta^2/\Gamma^2)^{-1}$ and $C = 8\frac{\Delta}{\Gamma^2}K^2$. Substituting η_n from the expressions of Eqn. 4.23 gives

$$\vec{F_j} \approx \hbar\vec{k_j}\ \frac{\Gamma}{2}\ \frac{I_j}{I_{\rm sat}} \left(K + C(\vec{k_j}\cdot\vec{v} - \mu_F|\vec{B}|s\cos\varphi)\right). \tag{4.26}$$

For a quadrupole magnetic field like Eqn. 4.18, the handedness required in a six beam configuration is $s = 1$ for the beams along z and $s = -1$ for those in the $x-y$ plane. In this approach, the total force from a conventional six beam MOT in cylindrical coordinates can be expressed as

$$\vec{F}^{\rm tot}_{\rm 6beams} \approx F_{\rm max}\frac{I}{I_{\rm sat}} 2C\left(\mu_F B_1\{r, 2z\} + k\{v_r, v_z\}\right), \tag{4.27}$$

where $F_{\rm max} = \hbar k\Gamma/2$ is the maximal force that a single beam can exert, $k = 2\pi/\lambda$ with λ the wavelength of the light and all beams are assumed to have the same intensity I. The trapping force has a cylindrical symmetry, resulting from the anisotropy of the quadrupole field and consequently atoms in such trap are distributed within a sphere flattened in the z direction [1].

For our four beam MOT, we will consider the case where one of the beams propagates vertically along the coil main axis with the correct handedness that provide the full trapping force, hence with $s = 1$. This beam is similar to one of the "z beams" of the six beam configuration. The three other beams are set with the opposite handedness $s = -1$, make an angle ϕ with the vertical beam and are distributed symmetrically around the z axis, their projection in the radial

plane making therefore an angle $2\pi/3$ between beams, as depicted in Fig. 4.9. The change in polarisation handedness corresponds to the vertical beam being reflected simply off a metallic surface –contrary to a standard six beam MOT where a quarter waveplate is put before a mirror to keep the same handedness–, as will be emphasized in the next chapter on the experimental realisation of the four beam MOT. Balanced optical molasses requires that the net radiation pressure from the combination of all beam vanishes with the condition given by Eqn. 4.20. As already outlined, this is obtained for beams in a perfect tetrahedral configuration, however we propose to investigate the general case with variable intensity beams at any angle ϕ. Radial cooling and trapping is achieved with only the upgoing beams. Thus, the above condition is always verified radially due to the symmetry of the problem, as long as all upgoing beams have the same intensity, which we will assume in all the following. Axially however, balanced cooling requires than the intensity of the upgoing beams is multiplied by a factor $-(3\cos\phi)^{-1}$. Including this, the total force in the four beam case is

$$\vec{F}^{\text{tot}}_{\text{4beams}} \approx F_{\max}\frac{I}{I_{\text{sat}}}2C\left(\mu_F B_1\{\gamma_r r, \gamma_z z\} + k\{\kappa_r v_r, \kappa_z v_z\}\right), \tag{4.28}$$

where

$$\begin{aligned}\gamma_r &= \kappa_r = -\frac{1}{4}\sin\phi\tan\phi,\\ \gamma_z &= 1+\cos\phi,\\ \kappa_z &= \sin^2\frac{\phi}{2},\end{aligned} \tag{4.29}$$

which is depicted in Fig. 4.11 as the angle ϕ between the upgoing beams and the vertical is varied. The case $\phi = \pi$ corresponds to all three beams propagating upwards vertically, and therefore no radial cooling nor trapping is achieved. Axial cooling is maximal and axial trapping vanishes completely since the polarisation handedness of the upwards beams is the opposite to the one required in the one dimensional case. As ϕ decreases from π, the upwards beams start to have a radial component providing trapping/cooling in this direction and radial trapping increases as well. For $\phi = \pi/2$, the "upwards" beams are situated in the radial plane, where radial trapping and cooling is maximised while no axial

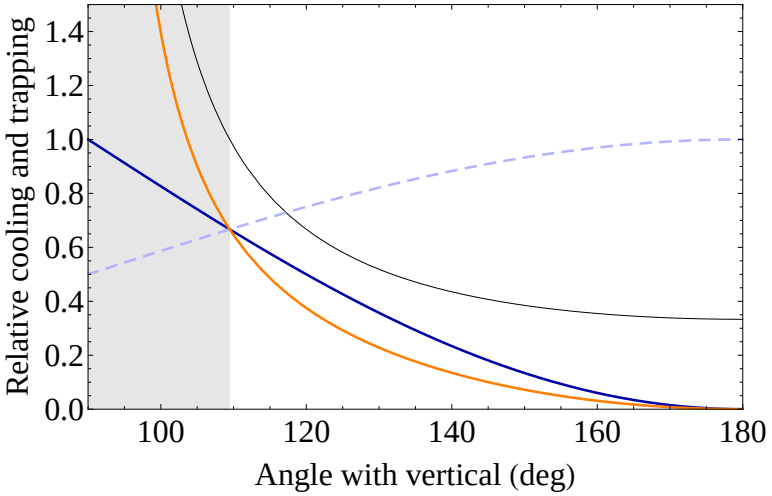

Figure 4.11: Radial trapping/cooling (orange), axial trapping (blue) and cooling (dashed blue) in a four beam MOT as a function of the angle between upgoing and vertical beams, and expressed relative to the radial restoring/damping constant in the six beam configuration. The black line depicts the coefficient factor required on the upgoing beams intensity to achieve balanced optical molasses. The gray area for angles $\phi < \arccos(-1/3)$ denotes the region where amplification of these beams is required.

force can counterbalance the vertical beam. In Fig. 4.11 however, axial cooling doesn't vanish for $\phi = \pi/2$ and trapping becomes maximal! This behaviour is due to the amplification of the upwards beams by the factor $-(3\cos\phi)^{-1}$ which tends to infinity as ϕ approaches $\pi/2$ and therefore represents a theoretical artifact, impossible to realise in real experiments. The same argument explains the asymptotic increase in radial trapping and cooling. Trapping and cooling become spherically symmetric for $\phi = \arccos(-1/3)$, which is the perfect tetrahedral configuration where no amplification or attenuation of the upwards beams is needed. It is worth noting that this nice feature of the four beam MOT results only because of the lucky anisotropy of the quadrupole field. In real experimental cases, as will be presented in Chapter 5, we use a reflective or diffractive element to create the three upgoing beams from a single incident beam. It is thus easy to make configurations where attenuation in the upwards beam is required ($\phi > \arccos(-1/3)$), as this comes free from losses at reflection, for instance. Obtaining MOTs with $\phi < \arccos(-1/3)$ is more challenging, since active beam

amplification is not realistically achievable. The solution might be to attenuate the downwards beam at places across its transverse plane where it reaches the trapping region only without changing its intensity in the region of space that will be reflected or diffracted.

4.2.2 Full force calculation

The reader might wonder how axial trapping is achieved, given that the upwards beams have the exact wrong polarisation handedness ($s = -1$) required for this in the 1D case. Indeed, radial trapping is easy to understand as the handedness matches the expected one. We will see in the following that axial trapping is achieved thanks to the π contribution of the force. Furthermore, we have dealt so far with an approximation of the force valid only at the trap centre and for small velocities, and imposing balance molasses at the magnetic field minimum. We will perform a full force calculation that allows us to investigate the effect of

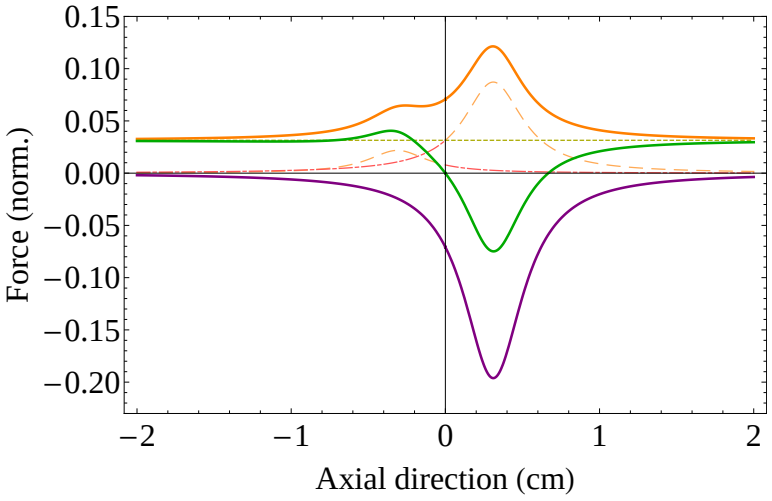

Figure 4.12: Axial trapping force in the tetrahedral configuration. Total force is shown in green, the purple and solid orange lines depicts respectively the effects of the vertical downwards beam and the combination of upwards beams. σ^+ (dot-dashed red), σ^- (dashed orange) and π (dotted yellow) components of the upwards force are shown to illustrate the trapping mechanism. All force are expressed relative to $F_{\max}$. For this simulation, $\Delta/\Gamma = -1.43$, $I/I_{\text{sat}} = 0.91$ and $B_1 = 10$ G/cm.

arbitrary beam angle and intensity imbalance. We start from Eqn. 4.24 to write the total force as

$$\vec{F}^{\text{tot}}_{\text{4beams}} = \vec{F}_{\text{down}} + \sum_{j=1}^{3} \vec{F}_j, \tag{4.30}$$

where the wave vector for beam j is $\vec{k_j} = -\{\cos\left(j\frac{2\pi}{3}\right)\sin\phi, \sin\left(j\frac{2\pi}{3}\right)\sin\phi, \cos\phi\}$. For the tetrahedral case, simulations of the trapping force with typical experimental parameters are shown in Figs. 4.12 and 4.13 respectively along the axial and radial directions. Axially, as already outlined, the force is much greater after the beam passes through the trap centre, as can be seen from the position maximum of the upwards force (orange curve) in Fig. 4.12. However, this force is, in amplitude, still smaller at its maximum than the one exerted from the downwards beams, which allows the total force to be still pointing towards the trap centre above the trap centre location. Trapping is finally achieved thanks to the π component of the force, independent of the magnetic field amplitude and only

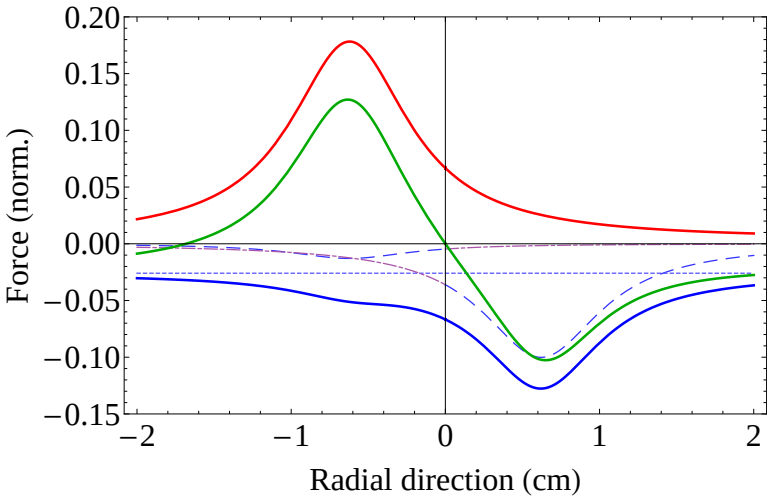

Figure 4.13: Radial trapping force in the tetrahedral configuration taken in the plane where one upwards beam propagates towards the right. Total force is shown in green, the red and solid blue lines depicts respectively the effects of the rightwards beam and the combination of the two other upwards beams. σ^+ (dot-dashed purple), σ^- (dashed blue) and π (dotted light blue) components of the "leftwards" force are shown to illustrate the trapping mechanism. All force are expressed relative to F_{max}. For this simulation, $\Delta/\Gamma = -1.43$, $I/I_{\text{sat}} = 0.91$ and $B_1 = 10$ G/cm.

resulting from the angle between the field and the wave vectors. This provides a force component therefore constant with position, finally allowing the upwards force to counterbalance the downwards force at the magnetic field minimum, as shown by the green curve in Fig. 4.12.

Radial trapping is shown in Fig. 4.13 and is much closer to the usual view of how Zeeman trapping works. The force exerted by the beams coming from the right (blue curve) has its maximum before the magnetic field minimum and therefore counterbalance the force from the left-coming beam. However, it is worth noting the π component that allows, again, the formation of the trap at the magnetic field minimum and provides a high restoring constant.

4.2.3 Critical beam angle and intensity unbalance

According to the principle of the "flow on a line" [80], an equilibrium point corresponds to a position in phase space where a force vanishes, and this equilibrium is stable or unstable if the slope of the force at this position is negative or positive. The simulations of Fig. 4.12 and 4.13 show that, in addition to the stable equilibrium point at the magnetic field minimum, there exists another equilibrium

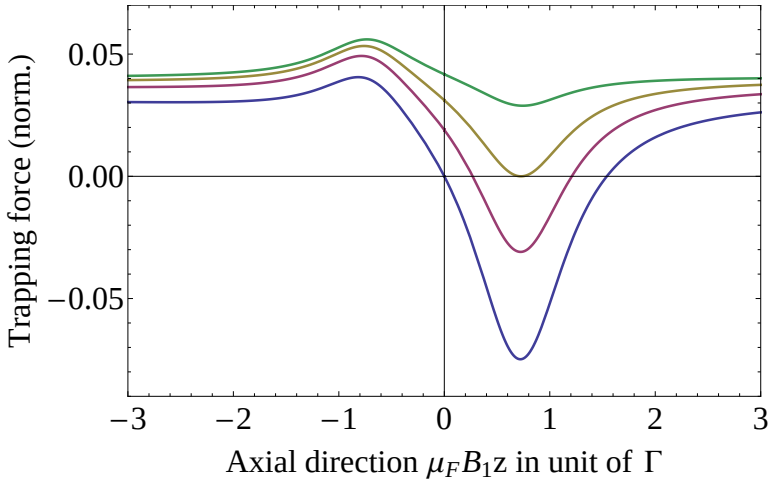

Figure 4.14: Axial trapping force for $\phi = \arccos(-1/3) \approx 109.47°$, $\phi = 115°$, $\phi \approx 118.67°$ and $\phi = 122°$ (from bottom to top) showing the bifurcation that prevent MOT formation for angles $\phi > 118.67°$. Other parameters are similar to those used for Fig. 4.12.

position, unstable this time, as the green curves on these two graphs cross the zero force axis in the other direction on the right. The first consequence is a limitation of the trapping region and therefore of the atom number, as all atoms reaching an unstable point will be pushed away from the trap. Also, until now the intensity of the upwards beams has been set such that for any angle, balanced molasses are possible at the magnetic field centre. Thus, it has been shown that a MOT can always form, as illustrated by Fig. 4.11. One might wonder what happens if all beams keep the same intensity, whatever the angle. The presence of two equilibria in Fig 4.12 implies the possibility that a bifurcation can happen at a given set of parameters. Fig. 4.14 shows the trapping force as the angle ϕ is varied from $\arccos(-1/3) \approx 109.47°$ (lower curve) to 122° (upper curve). As the angle is increased, a saddle-node bifurcation happens at $\phi \approx 118.67°$ where the two stable and unstable equilibrium points merge and disappear, thus preventing axial trapping for any angle larger than this limit. This phenomenon can be understood as larger angles mean that the upwards beams become more anti-trapping, with the limit that eventually the vertical beams have the exact wrong handedness for 1D trapping, and therefore there has to be a threshold for trapping. This is because the $-(3\cos\phi)^{-1}$ doesn't weaken the upwards beam anymore. The positions of both equilibrium points as a function of beam angle

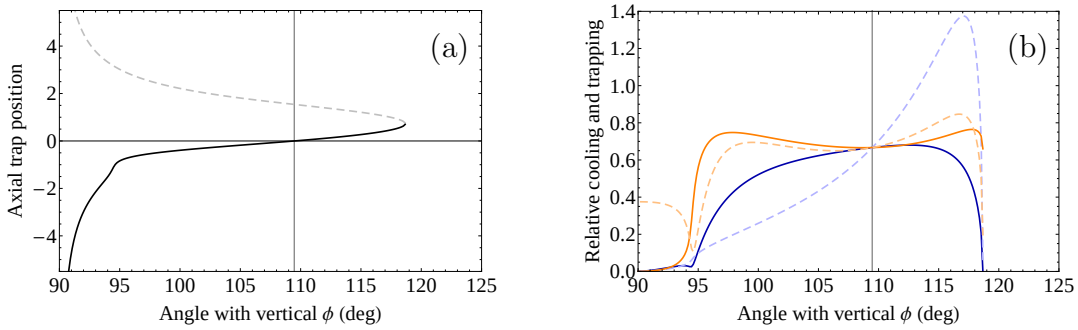

Figure 4.15: (a) Trap position (solid) and unstable equilibrium point (dashed) showing the saddle-node bifurcation. (b) Axial (blue) and radial (orange) trapping (solid) and cooling (dashed) force, relative to 6-beam radial trapping force, as a function of beam angle. All beams have the same intensity. Other parameters are similar to those used for Fig. 4.12. The vertical line corresponds to the tetrahedral configuration.

is shown in Fig. 4.15(a) while the trapping and cooling forces at the trap position appear in Fig. 4.15(b). Radially, trapping and cooling is always achieved, once again thanks to the cylindrical symmetry, by the upwards beams and it can be shown that this is true for any angle smaller than π and at any position along the vertical axis. However, no force is shown for angles above the threshold value, even for the radial components, as the MOT can not form anyway due to the disappearance of axial trapping. Trapping and cooling nearly vanish for angles smaller that $\sim 94.5°$, as this corresponds to the MOT forming where the σ^+ transition is resonant with the atoms, that is where $z = \Delta/(\mu_F 2B_1)$. Below this limit, trapping is mainly provided by π transitions, hence the absence of gradient in the force and the acceleration in the drift of the trap position towards the bottom in Fig. 4.15(a). Small cooling and trapping forces and high magnetic field (thus preventing sub-Doppler mechanisms) make these regions inappropriate for high atom number and cold MOTs.

A similar bifurcation can happen if, this time, we vary the intensity ratio of the upwards beams, while keeping the beam angle constant to $\phi = \arccos(-1/3)$. Fig. 4.16(a) shows the merging of the two equilibria points for $I_j/I_{\text{vert}} \approx 1.54$ in the tetrahedral configuration, where I_j and I_{vert} are respectively the intensities of one upwards beam and of the downwards vertical beam. Too much intensity in the

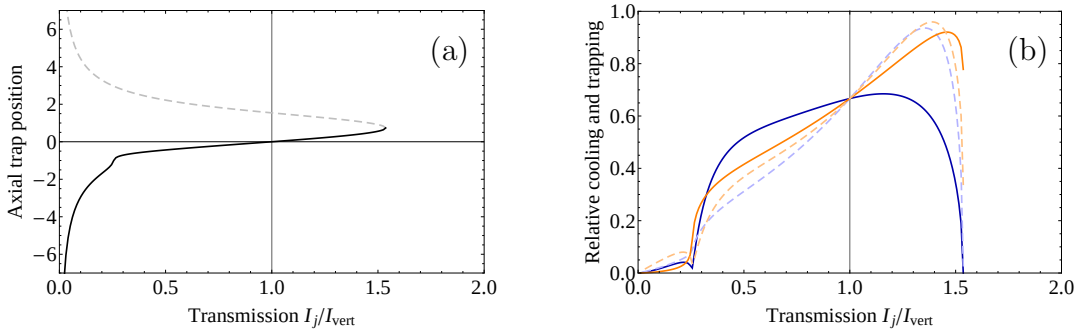

Figure 4.16: (a) Trap position (solid) and unstable equilibrium point (dashed) showing the saddle-node bifurcation. (b) Axial (blue) and radial (orange) trapping (solid) and cooling (dashed) force, relative to 6-beam radial trapping force, as a function of intensity ratio I_j/I_{vert} in the tetrahedral configuration ($\phi = \arccos(-1/3)$). Other parameters are similar to those used for Fig. 4.12. The vertical line corresponds to balanced molasses.

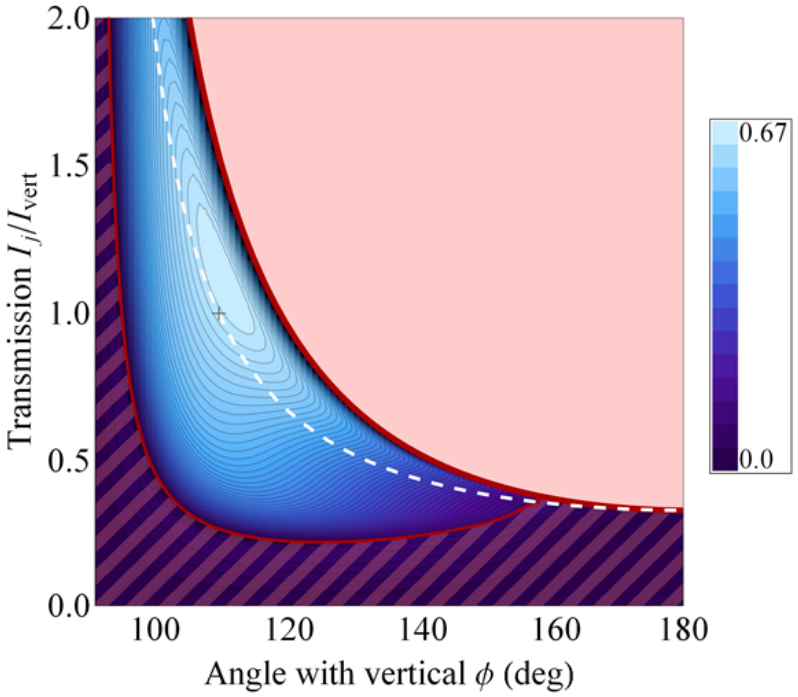

Figure 4.17: Axial trapping force, relative to the radial 6-beam MOT trapping constant, as a function of beam angle and intensity ratio. No MOT can form in the pink top-right region due to the absence of stable trapping point. The lower hatched part shows regions where trapping becomes very low (thin red line is the 0.1 isoline) and thus where MOT operations are not desirable. Balanced optical molasses can be achieved for parameters sitting on the white dashed line, where upwards beams intensity amplification is $-(3\cos\phi)^{-1}$. The tetrahedral configuration is indicated by the cross.

upwards beams creates a situation where the exerted radiation pressure cannot be counterbalanced by the downwards vertical beam, hence the disappearance of a stable trap position. Fig. 4.16(b) shows the trapping and cooling forces when the intensity ratio is varied.

The allowed set of beam angles/intensity ratios is summarised in Fig. 4.17, representing the axial trapping constant for beam angles ϕ varying from $\pi/2$ to π and intensity ratios I_j/I_{vert} between 0 and 2. MOTs cannot form in the pink region, due to the absence of stable equilibrium point above the bifurcation. They can still form in the diagonally hatched region however, but the related trapping

constants become too small for realistic MOT operations to be considered.

4.2.4 Polarisation of upwards beams

Another phenomenon that is interesting to look at is the depolarisation of the upwards beams, since this is directly connected to the experimental investigation. In Chap. 5, we will describe in details the apparatuses used to achieve a four beam MOT. One of them includes three gratings to split and steer a single normally incident beam into the three required upwards beams with the correct angle. The incident beam has a very carefully checked circular polarisation with the right handedness ($s = +1$), but gratings are known for being extremely polarisation sensitive. They usually have different efficiencies for the P and S polarisation components, respectively parallel and orthogonal to the plane of incidence, and can induce a phase delay between these components. These cumulated effects can significantly modify the polarisation after diffraction, thus changing the trapping constants. Fig. 4.18 shows an example of reduced trapping, with linearly polarised upwards beam. Cooling is not perturbed though, since the process does not depend on light polarisation. The polarisation vector of each upwards beam j can be expressed in terms of a decomposition on the two opposite circular polarisations:

$$\frac{\vec{E}}{E_j} = \left\{ \begin{array}{c} \sqrt{\beta_{\mathrm{SP}}} \\ \sqrt{1-\beta_{\mathrm{SP}}}\, e^{i\delta_{\mathrm{SP}}} \end{array} \right\} = \sqrt{\frac{\zeta_1}{2}} \left\{ \begin{array}{c} 1 \\ -i \end{array} \right\} e^{i\delta_1} + \sqrt{\frac{\zeta_{-1}}{2}} \left\{ \begin{array}{c} 1 \\ i \end{array} \right\} e^{i\delta_{-1}}, \quad (4.31)$$

where the intensities of the S and P components are, respectively, $I_S = \beta_{\mathrm{SP}}\, I_j$ and $I_P = (1-\beta_{\mathrm{SP}})\, I_j$, and δ_{SP} is the phase shift between these two components. The relative circular polarisation with handedness s has a relative intensity $\zeta_s = I_s/I_j$ and relative phase δ_s. The "ideal" case considered so far, with upwards beams with handedness $s = -1$, corresponds to $\zeta_{-1} = 1$, $\beta_{\mathrm{SP}} = 1/2$ and $\delta_{\mathrm{SP}} = \pi/2$. One can thus express the relative intensities of the circular polarisations as

$$\zeta_s = \frac{1 - 2s\sqrt{\beta_{\mathrm{SP}}(1-\beta_{\mathrm{SP}})}\sin\delta_{\mathrm{SP}}}{2}. \quad (4.32)$$

One should notice that the trap centre doesn't moves as the polarisation changes.

The force exerted at the magnetic field zero is independent on the light polarisation, since there is no quantisation axis at this location. The upwards beams can thus still counter-balance the force from the downwards beam and the MOT still forms (if the forces don't vanish completely) at the magnetic field zero, as depicted on Fig. 4.18. We can thus use the formalism of Sec. 4.2.1 and express the force from each beam j, using Eqn. 4.26, such that

$$\vec{F_j} \approx \hbar \vec{k_j} \frac{\Gamma}{2} \frac{I_j}{I_{\text{sat}}} \sum_{s=-1,1} \zeta_s \left(K + C(\vec{k_j} \cdot \vec{v} - \mu_F |\vec{B}| s \cos\varphi) \right). \tag{4.33}$$

The relative radial and axial trapping constants, denoted by respectively $\tilde{\gamma}_r$ and $\tilde{\gamma}_z$, are then modified, compared to the ones of the correctly polarised beams given by Eqn. 4.29. If we impose balanced optical molasses, these relative trapping constants now read

$$\begin{aligned} \tilde{\gamma}_r/\gamma_r &= \zeta_{-1} - \zeta_1 = 2\sqrt{\beta_{\text{SP}}(1-\beta_{\text{SP}})}\sin\delta_{\text{SP}}, \\ \tilde{\gamma}_z/\gamma_z &= 1 - \frac{2\zeta_1 \cos\phi}{1+\cos\phi} = \frac{1 + 2\sqrt{\beta_{\text{SP}}(1-\beta_{\text{SP}})}\sin\delta_{\text{SP}}\cos\phi}{1+\cos\phi}, \end{aligned} \tag{4.34}$$

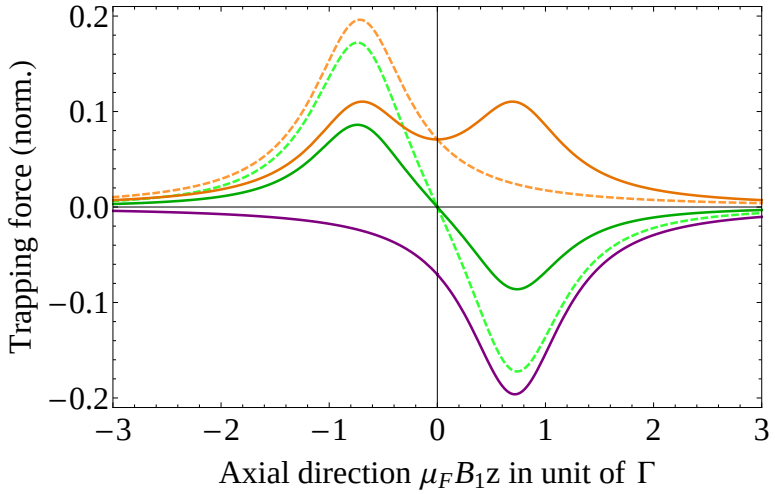

Figure 4.18: Axial trapping force in the 1D case with counter-propagating circularly (purple) and linearly (solid orange) polarised beams. The total force is shown in green, the dashed lines correspond to the configuration with two correctly polarised beams. All force are expressed relative to F_{max}. For this simulation, $\Delta/\Gamma = -1.43$, $I/I_{\text{sat}} = 0.91$ and $B_1 = 10$ G/cm.

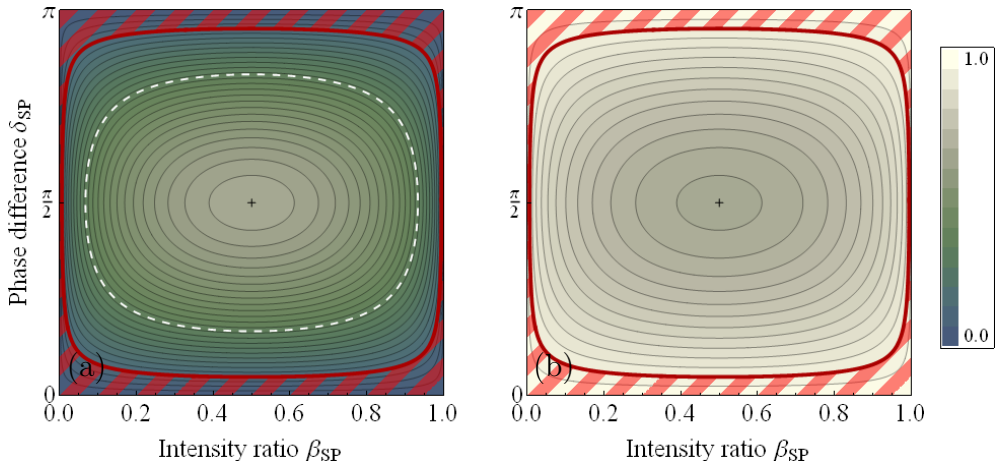

Figure 4.19: Radial (a) and axial (b) trapping constants, relative to the radial 6-beam MOT trapping constant, as a function of the relative intensity $\beta_{\mathrm{SP}} = I_S/(I_S + I_P)$ and phase difference δ_{SP} between the S and P components of the upwards beams. The beams are in the tetrahedral configuration. The red hatched region shows the range of parameters where the radial trapping becomes lower than 1/10 of the one in a 6-beam MOT configuration. The white dashed contour line corresponds to a reduction of the radial trapping of 1/2, compared to the maximum in the tetrahedral configuration.

where, as previously, ϕ is the angle between the vertical and the upwards beams. As the polarisation changes from optimal, radial trapping decreases while axial trapping increases, as shown in Fig. 4.19. This behaviour was expected, since upwards beam with handedness $s = +1$ are radially trapping and axially "anti-trapping", and reciprocally. The beam polarisation is extremely forgiving, since even $I_P/I_S = 0.07$ (or equivalently $I_S/I_P = 0.07$) with $\delta_{\mathrm{SP}} = \pi/2$ yields about half the maximum radial trapping in the tetrahedral configuration.

4.3 Conclusion

The four beam magneto-optical trap configuration was investigated theoretically, proving that trapping is possible with downwards and upwards beam having opposite polarisation handedness. It is thus relatively simple and compact to realise experimentally, since a single incident beam can be split and steered by e.g. mirrors to create all beams and no wave-plates are required after reflection.

The tetrahedral configuration naturally leads to a spherically symmetric MOT and balanced optical molasses. For other angles, these are obtained by changing the intensity of the upwards beams. The trapping and cooling forces are slightly reduced compared to the standard six beam MOT, because the beams don't all propagate along the magnetic field main axes, which reduces the amount of light that induce "trapping" σ^- transitions. The four beam MOT is radially trapping, due to the correct light polarisation along this plane, and axial trapping is explained by the contribution of the magnetically insensitive π contribution of the upwards beams. The present scheme works for a given range of parameter for the beam intensity imbalance and angle, since a bifurcation can happen if the force provided by the upwards becomes too large. Finally, it was shown that the four beam MOT is relatively robust to changes in the polarisation of the upwards beams.

Chapter 5

"Towards a micro-MOT" : experimental realisation

This chapter presents the experimental implementation of the four beam MOT described theoretically in Chap. 4. The work focuses on single incident beam traps, from which different parts are reflected or diffracted in different directions to create all required beams. The aim is clearly to progress towards the realisation of micro-fabricated atom "chip" traps. Very precise and compact time references are achieved with atomic clocks [92, 113]. Furthermore, atoms allows very accurate magnetic field measurements [21] with compact experimental setups. Thus, one can rely on Coherent Population Trapping [20] or Spin Exchange Relaxation-Free [94] to create micro-size magnetometers [24], hence obtaining portable devices. For instance, in the field of biomagnetism [114], atom based magnetometers [84] are an inexpensive and compact alternative to the heavily used Superconducting QUantum Interference Device (SQUID) sensors [115, 116] that requires cryogenic operation.

In surface atom chips, the very strong magnetic field gradients produced by the micron-sized conductive wires [30, 117, 118, 119, 120] or by permanent magnets [121, 122] provides very tight confinement for accurate manipulation of magnetically trapped atoms. Bose-Einstein condensates can be obtained very quickly given the high trapping frequencies leading to a dramatic increase of the evaporative cooling stage efficiency, and therefore experiment time can be greatly

reduced. Furthurmore, atom interferometry [32] on atom chips [123] with quantum gases allows high sensitivity measurements of e.g. inertial or gravitational effects.

The standard first stage of cold atom trapping is very often a MOT and therefore most of the above applications require such apparatus. The usual MOT configuration, with three pairs of orthogonal counter-propagating beams, is not particularly well suited for compact application, even in the case of back-reflected beams. For surface atom chips, the geometry further reduces the available space to shine MOT (or other) beams and people often use the so-called mirror-MOT [30]. However, this configuration still needs three independent beams. Another very attractive way to magneto-optically trap atoms on a chip is achieved using micro-mirrors [125] etched in a 4-sided pyramidal shape [29] and cooling atoms in a MOT [124, 126]. The schematics of Fig. 5.1(a) illustrates the working principle: a single vertically incident beam hits the four inner sides of a hollow pyramid (as seen in Fig. 5.1(b)) that deflects the beam horizontally and, after the second reflection, vertically such that it is counter-propagating with the incident beam, providing in total the six required beams for cooling in a cubic geometry. A MOT is achieved with vertically aligned quadrupole coils. Since the handedness of polarisation reverses upon reflection, all "planar" beams have

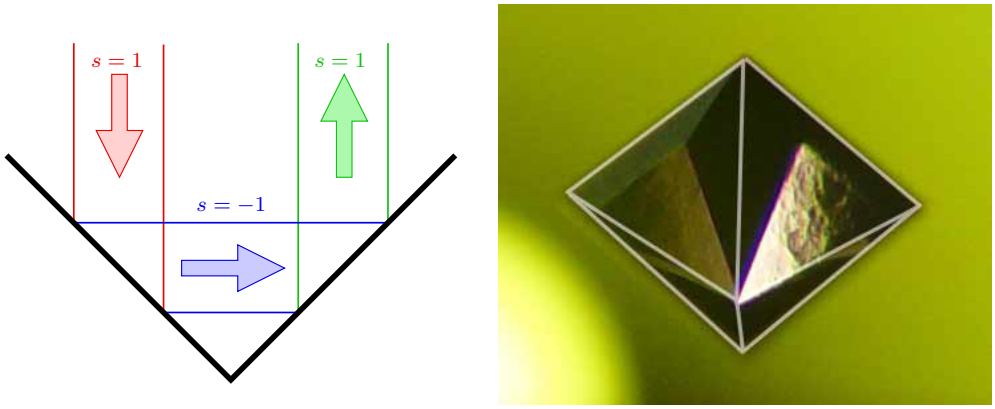

Figure 5.1: (a) Working principle of the four sided hollow pyramid MOT. Opposite circular polarisation handedness are represented by $s = 1$ and $s = -1$. (b) Picture of a hollow pyramid etched in a silicon wafer made at the Imperial College group, taken from Ref. [124].

the (same) opposite circular polarisation and handedness of the twice reflected vertical beam is reverted back to what it was originally. The pyramid constitutes an ideal technique for generating e.g. slow atomic beams [127] but the geometry of the device dictates that the MOT is situated within the volume of the pyramid. Hence, any further manipulation of the cold atoms is strongly limited by the absence of any direct optical access.

5.1 Four beam MOT using pyramid mirrors and gratings

We present here the experimental realisation of our new four-beam pyramid MOT theoretically investigated in Chap. 4. Two different configurations are discussed: using mirrors and diffraction gratings to split and steer a single incident vertical laser beam into three upwards beams, referred to as Pyramid mirror MOT (PMOT) and Grating MOT (GMOT). Theoretical aspects that also connect directly to the experiment are investigated, e.g. the overlap capture volume that can limit the atomic number in a MOT. The realisation of MOTs in the two configurations is discussed, along with a detailed description of the experimental setup. Finally, work that results in sub-Doppler cooled atoms in a GMOT is presented. The scheme presented here has many advantages compared to the traditional six beam pyramid MOT. First, the overlap volume extends above the mirrors or gratings, offering a large optical access and thus, easy optical manipulation of the atoms. In a six beam pyramid MOT, this results in "ghost" MOT images that are due to reflections of the cloud on the pyramid mirrors. In addition, the supra-plane overlap volume allows one to place the reflective or diffractive element either in- or ex-vacuo. Finally, the principle of the grating MOT implies a totally flat diffractive element and is therefore very well suited for micro-fabrication. No etching is required as one can directly "print" the diffractive pattern on a flat surface using e.g. focused ion beam or electron beam lithography. One could then easily embed a GMOT for the MOT stage of an atom chip experiment.

5.1.1 Pyramid mirror MOT: reflective element

The first idea to implement the four beam MOT with a single incoming beam was simply to use a set of reflective elements to create the three upwards beams. The laws of electromagnetism state that the component of the electric field parallel to the surface of an uncharged ideal conductor is zero. For a circularly polarised incident wave, this translates as its polarisation handedness being reversed (i.e. $s \rightarrow -s$) due to the reversal of the wave vector, as shown in Fig. 5.2(b). It is important to point out that, contrary to a standard six beam MOT where each retro-reflected beam passes through a quarter-wave plate to conserve handedness and ensure optimal trapping in each independent direction, here the exact opposite behaviour at reflection is required, to supply radial trapping, in agreement with the theoretical investigations of Sec. 4.2.4. Therefore, no quarter-wave plate is required for the four beam MOT to work as long as the reflection reverses polarisation handedness, resulting in an easy implementation of this scheme, for example in an in-vacuo micro-fabricated version. Such reflections can be ideally achieved using metallic mirrors, and the artist view of Fig. 5.2(a) shows an example of a mirror pyramid created by gold plating of an etched pyramid. Each facet of the mirror pyramid makes a declination angle $\theta = (\pi - \phi)/2$ with the horizontal plane, where ϕ is the angle between an upwards beam and the vertical, as defined in the previous chapter. A cut through the pyramid is shown in Fig. 5.2(b).

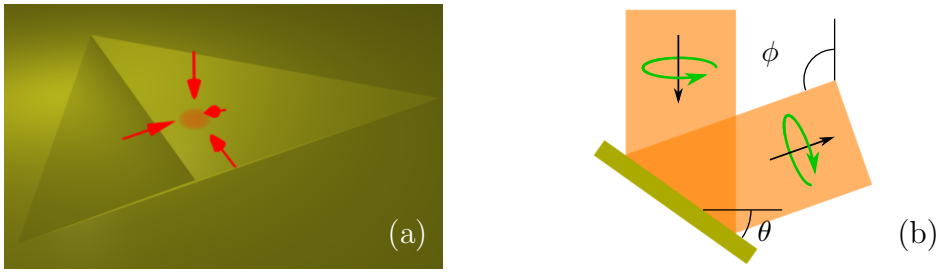

Figure 5.2: (a) Artist view of a micro-fabricated reflective mirror pyramid etched into a metallic material. (b) Side view of one of the mirrors of (a) taken in the plane orthogonal to the mirror and the top flat surface, showing the polarisation handedness reversal. Both views correspond to the tetrahedral configuration ($\phi = \arccos(-1/3)$).

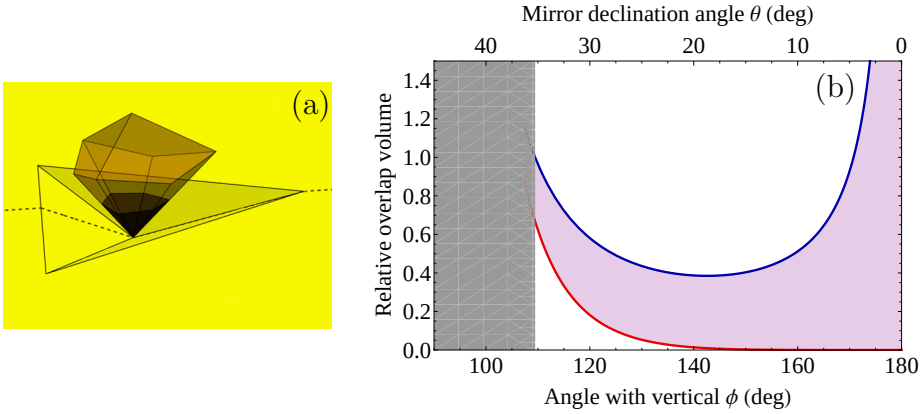

Figure 5.3: (a) Schematic showing the shape of the overlap volume for declination angle $\theta = 22.5°$. (b) Evolution of the total overlap (blue) and sub-plane (red) volumes as a function of beam angle/declination angle. Optimum optical access is available when the MOT forms within the supra-plane volume (purple filling).

One very important point of the present trap configuration is, as already outlined, the optical overlap region that extends above the top surface of the pyramid. Direct optical access is possible, and thus any manipulation or imaging of the atomic cloud is eased. The overlap volume of the four beams determines the number of atoms in the MOT , and is the intersection of two triangular pyramids (the lower pyramid fills the mirror pyramid) in the case of a pure tetrad. More generally the overlap volume is the intersection of a hexagonal pyramid and a triangular pyramid, as depicted in Fig. 5.3(a). To find the overlap volume, one needs to find the intersection points of the different planes that defines the beams volumes. By doing so, one finds that the total and sub-plane capture volumes V_{tot} and V_{sub} have the simple trigonometric relation:

$$\begin{aligned} V_{\text{tot}} &= \frac{a^3}{18}\,\frac{1}{\sin 2\phi\,(3\cos\phi - 1)}, \\ V_{\text{sub}} &= -\frac{a^3}{384}\,\frac{\sin^4\phi\tan\phi}{\sin^8\frac{\phi}{2}}, \end{aligned} \tag{5.1}$$

where a is the length of one side of the equilateral triangle that defines the outer limit of the pyramid when seen from the top. Both total and sub-plane volumes

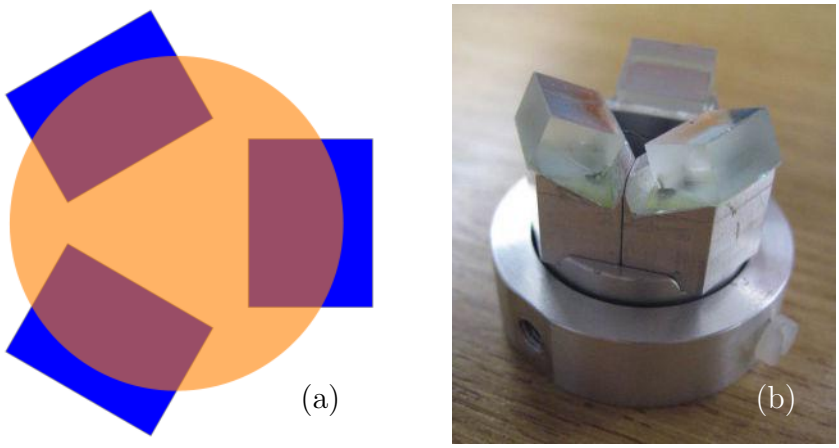

Figure 5.4: Schematics and photograph of the reflective element. (a) Top view (along vertical 1 inch beam propagation axis, denoted by the orange disk). (b) Photograph of the actual reflective element with the three 8×12 mm. dielectric mirrors.

are shown in Fig. 5.3(b). For angles ϕ smaller than $\arccos(-1/3)$, some part of the upwards beams undergo a second reflection that further limits the overlap region, as these double-reflected beams have the wrong polarisation handedness for radial trapping. By applying an appropriate constant magnetic field vector in addition to the magnetic quadrupole, it is possible to form a MOT anywhere within the beam overlap volume. Comparing this with the theoretical predictions of the previous chapter means it is more advantageous to choose a beam angle close to the tetrahedral configuration. A larger angle ϕ increases the overlap volume as well as the supra-plane volume $V_{\text{tot}} - V_{\text{sub}}$ (and so does optical access). However, the trapping and cooling constants are reduced and, depending on the intensity of the upwards beams, this may lead to a situation where the MOT can't form.

The four beam MOT is demonstrated with the mirror triplet presented in Fig. 5.4. Because the main aim of the present work is to prove the feasibility of the pyramidal four beam MOT and not its implementation on a micro-fabricated scale, it has been decided to use an extra-vacuo element, as this would facilitate setting-up and tuning the experiment and demonstrate the robustness and ease of implementation of the principle. The angle of the mirrors with respect to the horizontal plane were set to 22.5°, more acute than the ideal tetrahedral

case, in order to form a MOT with a larger supra-plane capture volume and allow for the thickness of the vacuum chamber glass plate. This non-optimal angle normally prevents MOT formation (for balanced beams, see Fig. 4.17), however we shall see in Sec. 5.2 —which details the experimental setup— that the upwards beams intensity is reduced such that the parameters are still in the range of possible values for MOT formation. Also, even if metallic mirrors are ideally better to conserve polarisation, we used dielectric mirrors as they usually have a higher reflection coefficient. A drawback of the multi-coating process is the unknown phase delay induced between the polarisation components at reflection. Indeed, these dielectric mirrors work very well as long as the polarisation of the incident wave is linear and either in the plane of incidence (P polarisation, from German *paralleler*) or orthogonal to it (S polarisation, from German *senkrecht*). However, for other configurations (i.e. non S or P linear or circular) at non-zero incidence, polarisation of the reflected wave is not guaranteed due to this phase delay. Different mirrors were tested at 22.5° incidence angle, and the triplet was made of a 1 inch high-reflection mirror cut into three pieces with almost no change in polarisation after reflection, and with no notable effect from the rubidium cell glass plates.

5.1.2 Grating MOT: diffractive element

As previously outlined, the GMOT configuration allows one to get a MOT with a totally flat element and would fit perfectly in atom chip experiments. For a wave coming with an incidence angle α_1 on a grating with groove spacing d, the allowed diffracted angle arising from constructive interference in the given direction, are given by the Bragg relation

$$d\ (\sin\alpha_1 + \sin\alpha_m) = m\lambda, \tag{5.2}$$

where the integer m is the diffraction order, α_m the diffraction angle and λ the wavelength of light. For a normally incident beam, α_1=0 as in Fig. 5.5, there exists a certain number of diffracted orders that depends on λ and d (where m=0 is just reflection from the surface), and positive and negative order are symmetric compared to the vertical axis. By taking diffracted orders from many

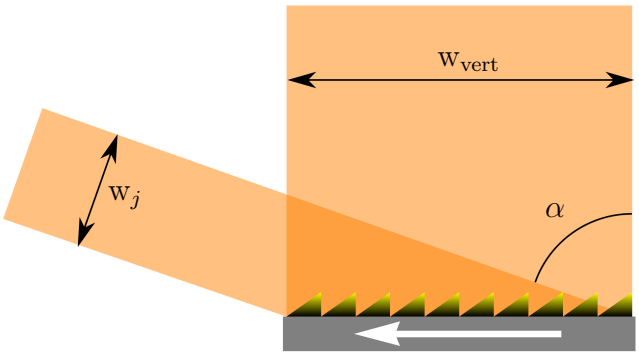

Figure 5.5: Diffraction of a vertically incident beam off a grating illustrating intensity compression. Here $\alpha = \arcsin \lambda/d$ is the first order diffraction angle, w_{vert} and w_j are respectively the sizes of the incident and diffracted beams.

gratings, one can create a "flat" version of the mirror pyramid MOT, as all the "reflective" elements are in a plane orthogonal to the vertically incident beam. Such a scheme is presented in Fig. 5.6(a), with three gratings, each providing one of the upwards beams. For a Rb MOT with 780 nm light, gratings with between ∼641 and ∼1282 grooves/mm can be used; groove density above the maximum leads to no allowed diffracted first order while density below the minimum results in the appearance of a second order, thus changing the trapping and cooling forces of what now becomes a seven beam MOT. Consequently, in theory all

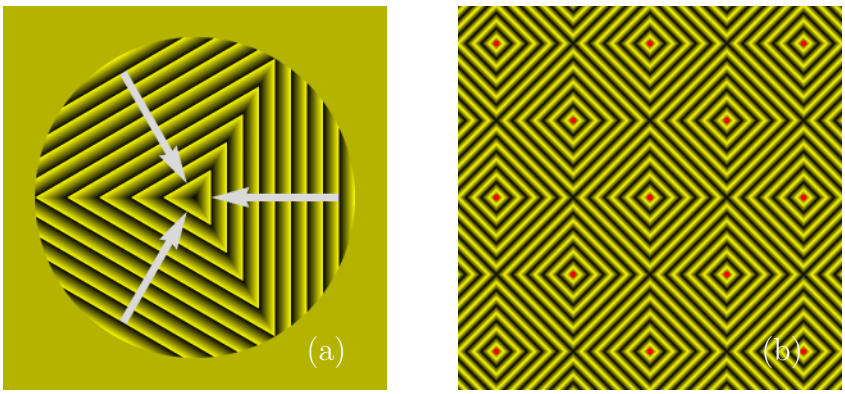

Figure 5.6: (a) Schematic view of a micro-fabricated four beam grating MOT. The arrows indicates blazing direction. (b) Possible implementation of an array of five-beam MOTs using symmetric first orders of non-blazed gratings. MOTs are shown by red dots.

diffraction angles between 30° and 90° (i.e. angles with vertical of 150° and 90°) are achievable, and $d \approx 1208.7$ mm gives the tetrahedral configuration. One major difference compared with the reflective pyramid MOT is due to the fact that gratings spatially compress beams with a corresponding intensity increase (Fig. 5.5). The relationship between the intensities I_{vert} and I_1 of the vertical incident beam and the first-order diffracted beam, respectively, is determined by the corresponding beam widths w_{vert} and w_1 and the first-order diffraction efficiency R_1:

$$\frac{I_1}{I_{\text{vert}}} = R_1 \, \frac{w_{\text{vert}}}{w_1} = \frac{R_1}{\cos\alpha}, \tag{5.3}$$

where $\alpha = \pi - \phi$ is the diffraction angle and we assume that the beams have spatially uniform intensities. If we consider the configuration depicted in Fig. 5.6(a), where all but one beam are provided by diffraction from n symmetrically positioned identical gratings, then the condition for balanced optical molasses Eqn. 4.20 is radially always satisfied, given the symmetry of the problem. Axially, balanced optical molasses is obtained when

$$I_{\text{vert}} = n I_1 \cos\alpha. \tag{5.4}$$

Injecting Eqn. 5.3 into Eqn. 5.4 yields the very simple condition:

$$R_1 = 1/n, \tag{5.5}$$

which is completely independent of diffraction angle and, hence, grating period. For three beams, this corresponds to a first-order diffraction efficiency of $R_1 = 1/3$. One can see in Fig. 5.6(a) that, if present, light in the zeroth order (a retro-reflection with efficiency R_0) has to be considered as it is present in the beam overlap volume. The balanced optical molasses condition is modified in the following way:

$$R_1 = \frac{1 - R_0}{n}, \tag{5.6}$$

but trapping and cooling forces are perturbed —since reflected light is anti-trapping— with a possible bifurcation if R_0 is too large, i.e. the upwards beam become too intense. A possible implementation of an array of MOT is pre-

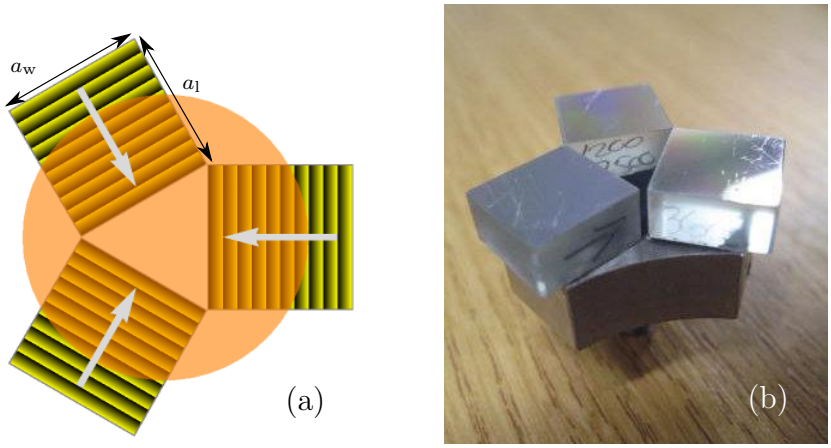

Figure 5.7: Schematics and photograph of the diffractive element. (a) Top view (along vertical 1 inch beam propagation axis, denoted by the orange disk). (b) Photograph of the actual refractive element with the three 12.7×12.7 mm. gratings. The arrow on the leftmost grating indicates the blazing direction.

sented in Fig. 5.6(b). Each MOT is created by the contribution from five beams, four of them being diffracted, and one can gain compactness by using the two first orders, each providing a beam to a different MOT. In this case, one wants a diffraction efficiency of $R_1 = 1/4 = 25\%$ in each order, assuming there is no

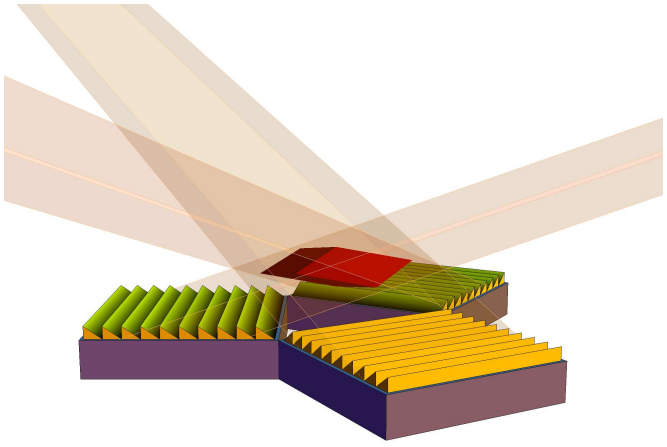

Figure 5.8: Schematics of the GMOT with the three gratings, the beam overlap region (rhombohedron) and the diffracted beams. The vertical downwards beam is not shown, for clarity.

back-reflected light ($R_0 = 0$). The prototype used for experimental investigation is presented in Fig. 5.7. Each grating is a blazed NT43-752 from Edmund Optics. These 1200 grooves/mm gratings deflect a normally incident 780 nm beam at an angle ∼69.4°, close to the ideal tetrahedron angle (arccos(1/3) ≈ 70.5°). A critical point in the achievement of a tetrahedral magneto-optical trap is the circular polarization of the first-order diffracted beams. Grating efficiency is usually specified in terms of S and P polarization and can vary dramatically with wavelength and polarization. However, the difference in phase accumulation between S and P components also has to be taken into consideration and this might lead to reduced trapping as theoretically investigated in Sec. 4.2.4. The efficiency of the gratings for a circularly polarised incident beam is R_1=45.3%, of which 90% has the correct circular handedness. If we consider the ensemble made of the grating and the quartz plate of the vacuum chamber, overall diffraction efficiency drops to a near-optimal R_1=32.2%, with 85% having the correct handedness. Contrary to the case of Fig. 5.6(a), the gratings don't fill the centre of the trap, and a black piece of cardboard ensures that there is no zeroth order reflection

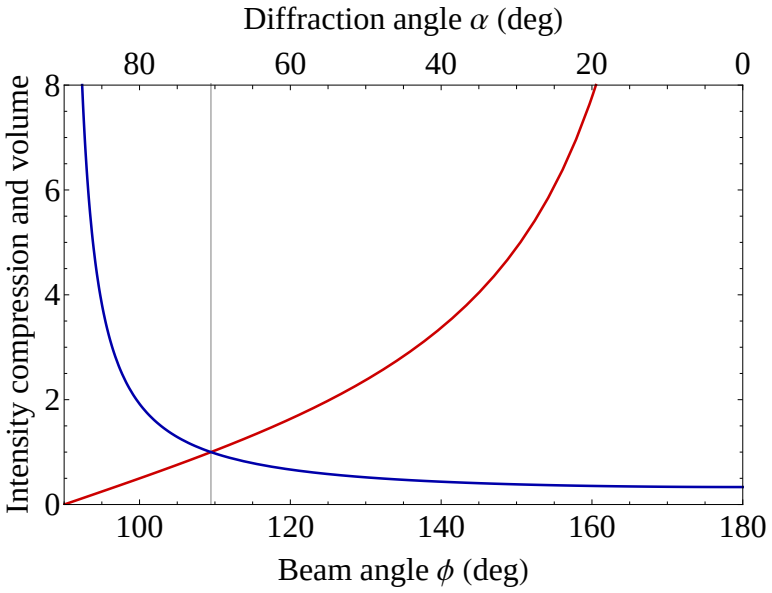

Figure 5.9: Intensity compression (blue) and capture volume (red) for a three grating GMOT, expressed relative to the tetrahedral configuration with $R_1 = 1/3$ and $R_0 = 0$.

that would complicate experimental achievement of the four beam grating MOT. The beam overlap volume is considered for the experimental configuration, that is as in Fig. 5.7(a). The volume is a rhombohedron, as can be seen in Fig. 5.8, which is a function of beam angle ϕ and the grating length a_l. In a similar way as for the PMOT volume, one finds

$$V = \frac{2a_\mathrm{l}^3}{3\sqrt{3}\tan\phi}. \tag{5.7}$$

If the grating width a_w becomes smaller than $\sqrt{3}a_\mathrm{l}/2$, the above volume is further reduced as the beams width turn the rhombohedron into a more complicated shape. The overlap volume, non-limited by beam width, is shown in Fig. 5.9. In practice, the overlap volume is not limited by beam width but is not a simple geometric shape though, since the vertical 1 inch beam doesn't fill the whole grating surface, and there is a bit of curvature on the top surface of the diffracted beams. This results in a overlap looking as an $\sim$ 60 mm^3 approximate rhombohedron located entirely above the vacuum chamber bottom plate.

5.2 Experimental setup

This section describes the experimental system used to implement the PMOT and GMOT. The schematics of Fig. 5.10 gives a general overview of the apparatus.

5.2.1 Laser system

Laser diodes are either GH0781JA2C or GH07P28A1C, both manufactured by Sharp, with a wavelength spectrum centred around 784 nm at room temperature. They are respectively rated at 120 and 150 mW maximum optical power. The laser diode is set in a External Cavity Diode Laser configuration using a home-made design [128]. The diode sits in a Thorlabs collimation tube and a

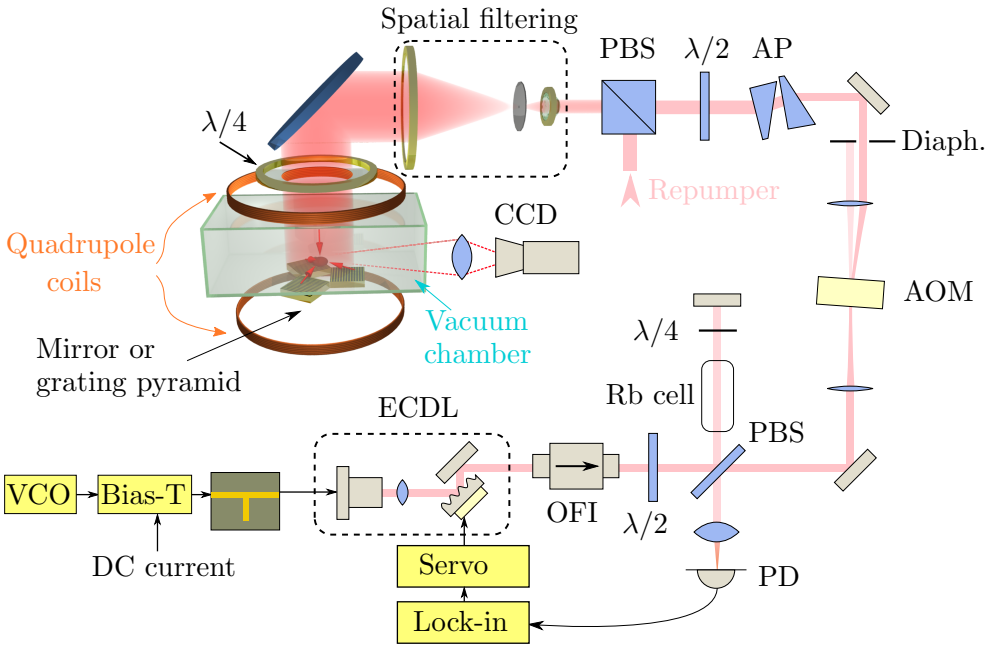

Figure 5.10: Schematics of the pyramid MOT setup. VCO: Voltage Controlled Oscillator. ECDL: External Cavity Diode laser. PBS: Polarising beam-splitter. PD: Photodiode. OFI: Optical Faraday isolator. $\lambda/2$: half waveplate. $\lambda/4$: quarter waveplate. Diaph: Diaphragm. AOM: Acousto-Optic Modulator. CCD: Charge-Coupled Device camera. Either current modulation or an independent laser is used to create the repumping light. Independent repumper is overlapped with trapping laser on the PBS before spatial filtering.

1800 grooves/mm blazed grating in Littrow configuration reflects about 20 % of the output power back into the semiconductor device, reducing the naturally broad spectrum of the free running diode ($\sim$ 500 MHz) to below 100 kHz [54]. The grating has 1800 grooves/mm, and the first negative order is counter-propagating with the incident beam for angle of about 45°, which allows an easy optical setup, as depicted in Fig. 5.11. A steering mirror connected to the grating can be added to cancel beam position shifts when the cavity length is changed. Also, optical feedback increases the optical power inside the semiconductor cavity, and this subsequently reduces the maximum available output by the same diffraction efficiency. Ideally, one wants a low efficiency diffraction element, just high enough to provide optical feedback, that is about 5 %. An Optical Faraday Isolator (OFI) ensures that no light returns into the ECDL, which would perturb the stability of the laser. Unfortunately, the higher power GH07P28A1C diode offers poor modulation efficiency in the microwave range, and they are only used for dual laser operations. The lower power and unfortunately obsolete GH0781JA2C is used with radio-frequency modulation for single laser mode, with simultaneous trap and repump light.

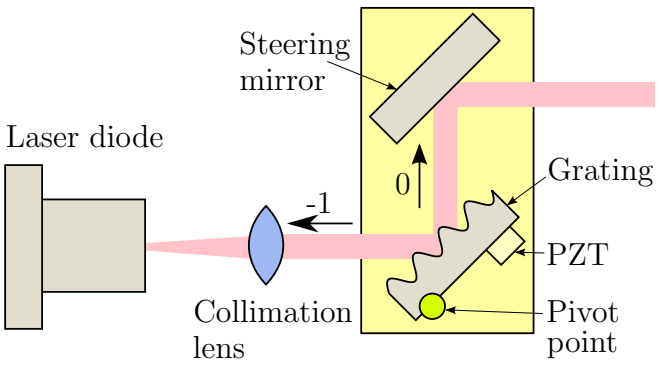

Figure 5.11: Schematics of the External Cavity Diode Laser (ECDL). PZT (Lead Zirconate Titanate): Piezoelectric actuator. The first negative order (-1) from the grating is reflected back into the laser diode while the reflection (0) serves as the output beam. The grating and the steering mirror are mounted together such that adjusting the grating does not change the output beam angle.

5.2.2 Saturated absorption

A thermally stabilised laser is never perfect and the laser frequency always drifts over time, changing the detuning of the trapping laser or shifting away the repumper from resonance and one needs frequency stabilisation to maintain the parameters constant over the time of an experiment, typically from a few tens of seconds to a minute. By passing the laser beam through a rubidium cell, one can expect to obtain a frequency reference to which the laser can be locked. However, a single pass scan gives only a broadened spectrum due to the Doppler effect making all velocity classes resonant with the laser, and the hyperfine structure peaks, with spacing and width are much smaller than the Doppler background, are hence washed away. One very standard way to retrieve these hyperfine peaks is to send two collimated, overlapping, counter-propagating beams, derived from the same laser, through the cell, and this method is known as saturated absorption [129]. Consider the simple case of a single hyperfine transition broadened by the Doppler effect. One beam is much more intense, the pump beam, and mainly interacts with the atoms with velocity class (taken along the beam propagation direction) such that they are resonant with the light to cycle between their ground and excited states. The Doppler-shifted frequency seen by atoms with velocity $\vec{v}$ is

$$\omega_{\mathrm{Dop}} = \omega - \vec{k} \cdot \vec{v}, \tag{5.8}$$

where ω is the angular frequency of the light with wave vector $\vec{k}$ in the laboratory frame. The other beam is less intense, it is called the probe beam, and is the one from which transmission through the cell is recorded. The probe senses atoms with $\vec{v}_{\mathrm{probe}}$ such that $\vec{k} \cdot \vec{v}_{\mathrm{probe}} = -\vec{k} \cdot \vec{v}_{\mathrm{pump}}$ due to the change in $\vec{k}$ as the two beam propagate in opposite directions. If the laser frequency is not resonant with the atomic transition, the two lasers don't talk to the same velocity classes, and transmission of the probe just shows the Doppler-broadening. However, on resonance, the probed atoms are those with velocity such that $\vec{k} \cdot \vec{v} = 0$, resonant with both beams. The pump beam saturates the absorption and thus frees the way for the probe beam, that undergoes less absorption than in the absence of the pump, and the spectrum shows this Doppler-free hyperfine structure. The 7.5 cm long cell contains about 10^{-7} Torr of rubidium at room temperature and

about 100 μW is taken from the laser, reflected after the cell and focused on a photodetector, as pictured in Fig. 5.10. This way, the same beam acts as both pump and probe. Fig. 5.12 shows the spectra obtained from saturated absorption technique when the laser is scanned across the $F = 2 \rightarrow F' = 1, 2, 3$ (Fig. 5.12(a)) and $F = 1 \rightarrow F' = 0, 1, 2$ (Fig. 5.12(c)) sets of transitions in ^{87}Rb. The hyperfine splitting for the ground manifold $5S_{1/2}$ is about 6.8 GHz [130]. The hyperfine levels of the excited state $5P_{3/2}$ occupy about 500 MHz [131], where each level undergoes a Doppler broadening of about 0.5 GHz Full Width Half Maximum at room temperature. For this reason, the Doppler effect only affects transitions that happen from one of the hyperfine ground states (with $F = 1$ or $F = 2$) to the excited states. Due to the conservation of angular momentum between the atom and a photon, only transitions with $\Delta F = \pm 1, 0$ are allowed. Strictly speaking, saturated absorption is a two-level process which can explain the $F = 1 \rightarrow F' = 0$

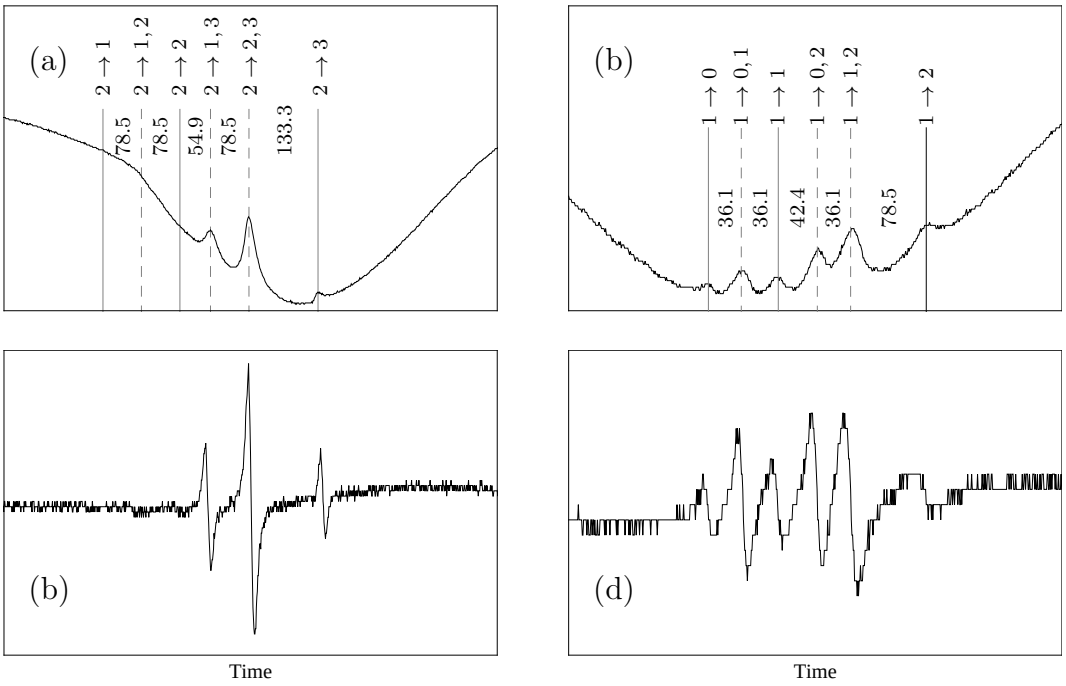

Figure 5.12: Saturation absorption spectra for the (a) $F = 2 \rightarrow F'$ (trapping) and (b) $F = 1 \rightarrow F'$ (repumping) transitions in ^{87}Rb. Corresponding demodulated (derivative) signals are shown in (c) and (d). The numbers between the peaks are the frequency difference (in MHz).

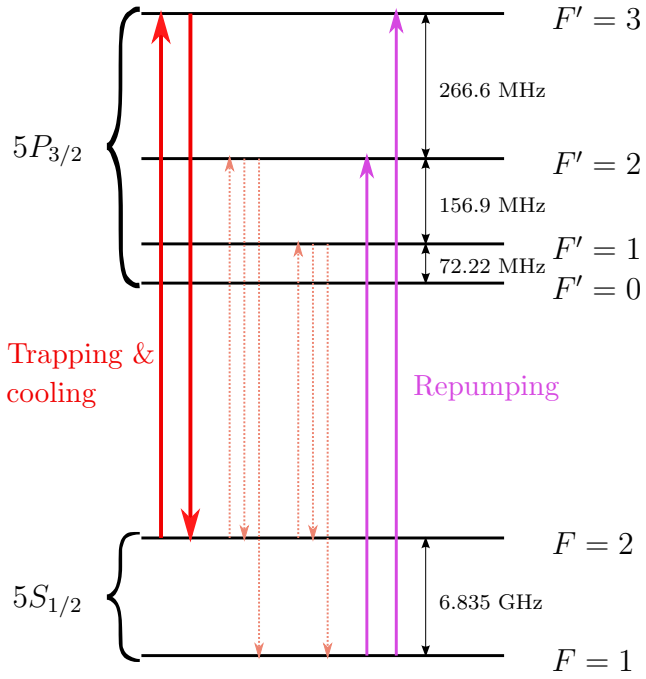

Figure 5.13: Energy level diagram of the $5S_{1/2}$ and $5P_{3/2}$ manifolds in ^{87}Rb. Cooling and trapping is achieved using the $F = 2 \rightarrow F' = 3$ transition. Pumping to levels $F' = 1$ and $F' = 2$ and the associated decay channels are shown with dashed arrows. Atoms optically pumped into the non-resonant $F = 1$ ground state can be repumped to either $F' = 1$ or $F' = 2$ excited states to regenerate the cooling/trapping cycle.

and $F = 2 \rightarrow F' = 3$ peaks only. The $F = 1 \rightarrow F' = 1$, $F = 1 \rightarrow F' = 2$, $F = 2 \rightarrow F' = 1$ and $F = 2 \rightarrow F' = 2$ peaks mainly result from optical pumping by the pump beam of the population into another ground state. Atoms in a non-zero longitudinal velocity class can be resonant with both counter-propagating lasers and this leads to the cross-over peaks, visible in Fig. 5.12, at frequencies $\frac{\omega_i+\omega_j}{2}$, where ω_i and ω_j are two different atomic transitions.

For optimum MOT operation, the trapping transition is chosen to be the $F = 2 \rightarrow F' = 3$, as atoms pumped into the excited state $F' = 3$ can only decay onto $F = 2$, hence favoring a closed cycle of transitions between these two states. The two hyperfine excited states with $F' = 2$ and $F' = 3$ are separated by ~ 266 MHz [131] and the natural linewidth is $\Gamma \approx 6$ MHz [132]. Thus even for an about 10 MHz red-detuned light, there is a non-zero probability that an atom

jumps to $F' = 2$ where it can decay back to either hyperfine ground states. All atoms ending in the $F = 1$ ground state cannot enter the cooling cycle, as the separation between ground state is much larger, and a repumper laser is required between the states $F = 1$ and $F' = 2$ or $F = 1$ and $F' = 1$ to regenerate the cooling cycle. The energy level diagram for the $5S_{1/2}$ and $5P_{3/2}$ manifolds of Fig. 5.13 show the cooling and trapping transition, as well as the possible decay channels and the two options for the repumping light.

5.2.3 Feedback electronics

A laser cannot be locked to a saturated absorption peak, as electronics servos need an odd error signal, proportional, in a small range, to the frequency difference with the reference. A convenient way to get such an error signal is to obtain the derivative of the saturated absorption signal. This can be achieved by applying a frequency modulation on the laser and demodulate the recorded saturated absorption spectrum [133]. The absorption signal I_{abs} is a function of the laser frequency ω such that $I_{\text{abs}} = f(\omega)$. In our case with saturated absorption peaks, $f(\omega)$ is a Lorentzian function. Assume now that the laser is frequency modulated with modulation frequency ω_{m} and modulation depth δ. We can write the absorption signal as

$$I_{\text{abs}} = f\left(\omega + \delta \sin \omega_{\text{m}} t\right). \tag{5.9}$$

The above expression can be Taylor-expanded around the frequency ω:

$$I = f(\omega) + (\delta \sin \omega_{\text{m}} t)\, f^1(\omega) + \frac{\delta^2 \sin^2 \omega_{\text{m}} t}{2!} f^2(\omega) + \frac{\delta^3 \sin^3 \omega_{\text{m}} t}{3!} f^3(\omega) + \cdots, \tag{5.10}$$

where the notation $f^k(\omega) = \mathrm{d}^k f(\omega)/\mathrm{d}\omega^k$ is used for clarity. Demodulation using the modulation signal $\sin \omega_{\text{m}} t$ brings only the terms oscillating at ω_{m} in Eqn. 5.10 in baseband and the high frequency components can always be filtered out. One can show, by expanding the terms $\sin^k \omega_{\text{m}} t$, that the amount of intensity that

oscillates at $\omega_{\mathrm{m}}t$ in Eqn. 5.10 is

$$\begin{aligned}\sin\omega_{\mathrm{m}}t &\rightarrow \sum_{u=0}^{\infty}\frac{1}{4^u(2u+1)!}\begin{pmatrix}2u+1\\u\end{pmatrix}\delta^{2u+1}f^{2u+1}(\omega),\\ &\rightarrow \delta^1 f^1(\omega)+\frac{\delta^3}{8}f^3(\omega)+\frac{\delta^5}{192}f^5(\omega)+\cdots\ .\end{aligned} \tag{5.11}$$

Thus, the demodulated signal is made of a constant part, given by the above expression, and terms that oscillate at frequencies $n\omega_{\mathrm{m}}$ with $n > 1$. These unwanted terms can be removed by adequately low-pass filtering the demodulated signal. The non-saturated Lorentzian absorption structure is supposed to have the simple shape

$$f(\omega) = \frac{\Gamma^2}{\Gamma^2+4\omega^2}, \tag{5.12}$$

where Γ is the FWHM of the transition and the transition is assumed to be at the zero frequency, for simplicity. A dimensional analysis imposes that the successive derivatives of the above function, with respect to ω, have an amplitude that varies as

$$\frac{\mathrm{d}^k f(\omega)}{\mathrm{d}\omega^k} \propto \frac{1}{\Gamma^k}. \tag{5.13}$$

This implies that the amplitude of the k^{th} derivative that made up the demodulated signal of Eqn. 5.11 is proportional to $\left(\frac{\delta}{\Gamma}\right)^k$. Thus, for $\delta \ll \Gamma$, the high order derivatives (with $k \geq 3$) are strongly damped and the demodulated signal is mainly proportional to the first derivative. Since the Lorentzian is an even function (relative to its maximum), its first derivative is odd and constitutes an ideal error signal. One notices that, even if the condition $\delta \ll \Gamma$ is not strictly verified, contributions from higher order derivatives are not detrimental since these are all odd functions as well. It is worth noting that it is also possible to demodulate on higher harmonics [134], i.e. using $\sin k\ \omega_{\mathrm{m}}t$ with $k > 1$. It can be shown in a similar way that the resulting error signal is mainly proportional to the k^{th} derivative of the absorption structure with only limited contributions from higher order derivatives [135]. Finally, the above treatment doesn't include dispersion, but it is also possible to demodulate in quadrature and obtain the derivatives of the dispersion, that is an odd signal for even k. Error signals are

shown in Fig. 5.12(b) and Fig. 5.12(d) for the trapping and repumping transitions. The laser frequency is modulated or scanned via a piezoelectric actuator (PZT) that acts on the ECDL feedback grating to control the cavity length, and therefore the laser frequency. The modulation frequency is $\omega_{\mathrm{m}} = 50$ kHz with a depth $\delta \approx 1$ MHz, that is smaller than the natural line width $\Gamma \approx 6$ MHz but high enough to yield relatively large amplitude error signal.

With a valid error signal, one needs some way to correct in real time the laser frequency as it drifts away from the desired operation point. This is achieved with an electronic feedback circuit, or servo that is fed with the error signal and acts by some way on the laser frequency to lock it. Usually, servos have a relatively high gain in DC, in order to correct mainly slow drifts in the laser frequency, and subsequently integrators are usually used. In a closed feed-back system, the role of the servo is to maintain its input, the error signal, at zero, and, in order to do so, it adjusts the level of its output signal. The output of an integrator with zero input signal doesn't change, but once there is a drift in the frequency, e.g. the error signal varies, the circuit integrates the error and changes its output, only stabilising when the error signal goes back to zero. More information on electronics feedback theory can be found, for example, in [136]. The frequency capture range where the feedback operates is roughly limited to the natural linewidth of the peak, that is 6 MHz in Rb. The slope of the error signal is of primary importance, since the locking electronics needs to be fed with a signal that gives an information of how far the frequency is from the reference. With the opposite slope to the one required, the normally wanted negative feedback becomes positive and the system shoots away from the desired locking point.

As previously outlined, integrators are advantageous for the servo system as they offer a (theoretically) infinite gain at DC, and therefore slow drifts in the laser frequency are better corrected. The simplified schematics of the locking electronics in Fig. 5.14 shows the lock-in amplifier and servo. The 50 kHz modulation is generated by the lock-in amplifier and subsequently sent to the laser piezoelectric actuator (PZT). In open loop operation, a ramp is added to the modulation sent to the laser PZT to allow one to scan across the different saturated absorption peaks and coarsely position the laser frequency within the desired peak capture range. The error signal is accessible at the output E of the lock-in amplifier for

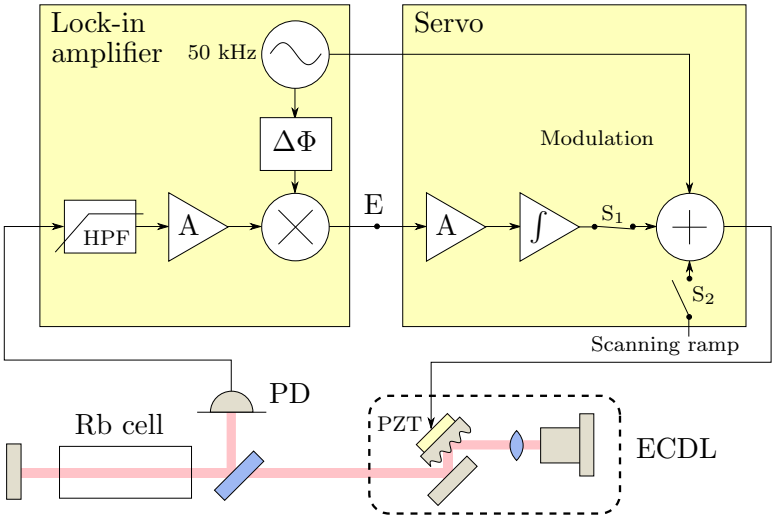

Figure 5.14: Schematics of the locking electronics showing the lock-in amplifer (left) and servo (right). A: Amplifier. HPF: High-Pass Filter. $\int$: Integrator. $\Delta\Phi$: Phase shifter. +: Adder. $\times$: Demodulator. S: Swith. PD: Photodetector. PZT (Lead Zirconate Titanate): Piezoelectric actuator.

monitoring. The set of switches S_1 and S_2 disconnect the scan, close the feedback loop and effectively lock the laser frequency to the reference. Exact electronics circuits can be found in [109] and [137].

For single beam operations, the same laser, modulated at radio frequencies, contains both trapping and repumping wavelengths, as seen in 2.2. As these two wavelengths are close to saturated absorption peaks, the error signal containing both contributions is distorted and the locking point might be modified. Experimentally, as the intensity in the repumping sideband is much smaller than the trapping one, the error signal is pretty much unchanged. In addition, depending on the RF modulation frequency chosen, the peaks arising from the repumper light sit many natural linewidth away from the desired locking peak and we didn't notice any perturbation while the laser was locked.

The trapping laser needs to be ∼10 MHz red-detuned from the cooling transition $F = 2 \rightarrow F' = 3$. As there are no efficient options to frequency shift *only* by this small amount, the laser is locked on the $F = 2 \rightarrow F' = 2, 3$ peak and the acousto-optical modulator (AOM) then shifts the frequency by about 120 MHz to reach the desired detuning. AOMs operating between 40 and 200 MHz are

widely available, they have a wide bandwidth (±20-40 MHz) with high deflection efficiency (∼85 % in first order) that allows one to change the detuning without sacrificing too much optical power. In addition, the cross-over peaks have a higher amplitude, and so do the error signal slope, usually resulting in a tighter lock [138]. In two beam operation mode, the repumper frequency is locked directly to the repuming transition peak $F = 1 \rightarrow F' = 2$ and independent locking electronics are required for each laser. The two beams are spatially overlapped with a polarising beam splitter before being sent through to the vacuum cell.

5.2.4 Beam shaping and Rubidium vacuum cell

The reflecting or diffracting element that creates the three beams is positioned underneath the bottom plate of the quartz vacuum cell and the incoming 1 inch beam is sent vertically from the top of the cell, as can be seen on Fig. 5.15. A

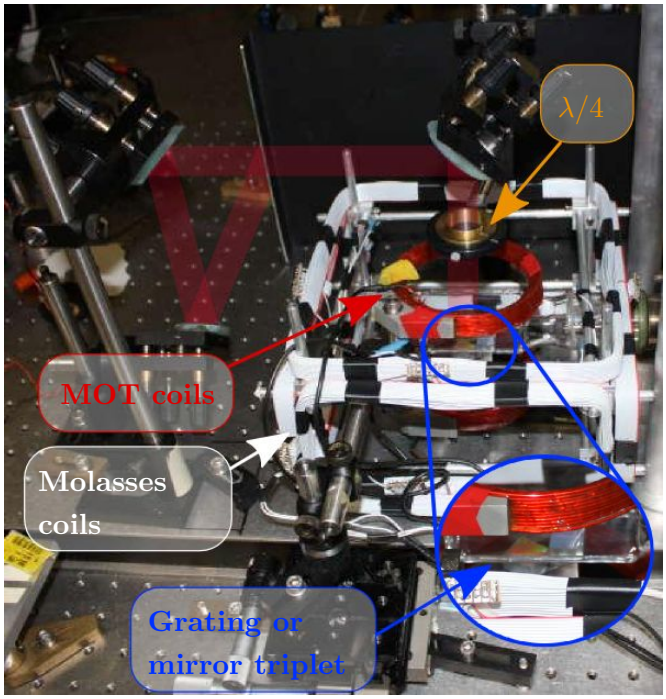

Figure 5.15: Photograph of the vacuum chamber with MOT and molasses coils, $\lambda/4$ wave plate and diffracting triplet, and showing the beam path after spatial filtering and expansion.

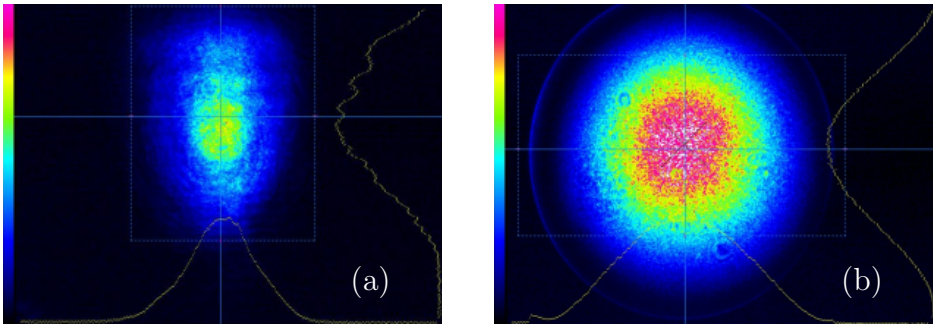

Figure 5.16: Beam profile (a) before and (b) after anamorphic prisms and spatial filtering.

single quarter-wave plate constitutes the last element before the beam enters the vacuum chamber and turns the linearly incoming polarisation (set by the beam splitter that combines trapping and repumping light) into the correct circular one (see Fig. 5.10 for a clearer view of the actual experimental setup). One of the critical aspects in the four beam pyramid MOT is intensity imbalance between the incoming beam and the three (or more) reflected or diffracted components. Thus, one wants to get an intensity profile as flat as possible before reaching the vacuum cell. A 30 μm pinhole spatially filters the incident beam to remove spatial high frequency components. The active region in a semiconductor laser is usually transversely wider in one direction and this causes beam ellipticity in a ratio about 2:1. A set of two anamorphic prisms before the spatial filtering expands the beam in one direction, to maximise coupling through the pinhole, resulting in a beam size ($1/e^2$ radius of the intensity profile) of 1.5 mm. After the pinhole, the beam is expanded by a factor ~ 20 and collimated, such that it becomes much larger than the 1 inch optics. This yields a limited curvature on the transverse Gaussian profile. At the price of reduced intensity, one can this way ensure balanced beam intensities. The effect of the beam shaping is shown in Fig. 5.16. Any changes in polarisation can result in imbalanced cooling forces, and special care was taken to ensure that the trapping light is well linearly polarised before it reaches the quarter-wave plate. Therefore, all reflections after the last polarising beam splitter are operated at 45° incidence angle (which is the nominal angle for these mirrors) such that polarisation is always S or P, relative to the mirrors, to avoid any phase delays induced between the two crossed components

that could perturb the linear polarisation. The telescope around the pinhole is actually made up of three lenses, one of which is diverging, to gain compactness. This technical detail was needed because of the limited optical path available for the telescope, and to make sure the beam was well collimated before it reaches the following mirror and therefore limit any possible change in polarisation at reflection. Finally, it is worth checking the quality of the circular polarisation between the wave plate and the chamber with an analyzer. We obtained an almost pure circular polarisation, only limited by the extinction ratio of the polarising beam splitter. Starting from about 50 mW of optical power off the grating of the ECDL, typically 16 mW are left passing through all optical elements. This translates into between $\sim$1 and $\sim$2 mW/cm^2 of optical intensity in the vertical beam in the vacuum chamber. The quadrupole magnetic field is provided by two circular 56 turns 8 cm diameter coils, spaced by 7 cm in an anti-Helmholtz configuration. Coils are mounted on translation stages for fine positioning relative to the beam overlap, as will be explained later. A set or three orthogonal pairs of Helmholtz coils surround the whole vacuum chamber and the quadrupole coils to cancel external static magnetic field at the MOT location to allow sub-Doppler mechanisms to takes place correctly. Science experiments are finally performed in a 70$\times$25$\times$25 mm^3 quartz vacuum chamber with a 10^{-10} - 10^{-9} Torr vacuum provided by a Varian ion pump.

5.3 Pyramid mirror MOT: implementation

In order to create a mirror PMOT, a few critical points have to be fulfilled:

- Vertical beam should have a radially symmetric intensity profile.
- Mirror triplet should be centred in the vertical beam.
- Polarisation should be as circular as possible.
- Magnetic field minimum should be located within the beam overlap volume.

A careful positioning of the vertical beam through the cell allows one to achieve the first two criteria. The beam intensity in parts of the vertical beam which

will generate the vertical and upwards beams was checked just before the beams enter the vacuum chamber, and also directly on the three reflected beams. This measurement is tricky because the reflected beams cross the chamber twice before their intensities can be checked, which will cause an absorption possibly different for each beam as they all reach the glass plates with different incidence angle. One can either take into consideration these attenuations but the best way to circumvent this is to do the intensity measurement whilst the vacuum chamber is not present. Also, as the upwards beams come with a 45° angle compared to the vertical, a MOT shouldn't be allowed to form since —according to the conclusions of Sec. 4.2.3— for this angle, total upwards intensity is higher than the critical point. This issue is addressed by controlling the vertical beam profile with the telescope lenses, that is allowing a given amount of curvature in the profile such that the intensity of the outer part of the beam, which will be reflected by the mirrors, is lower than in the central region. By doing so, intensities in vertical and reflected beams at the trap position are calculated (by measuring intensities without the vacuum chamber and including absorption by the glass plates) to be respectively 2.3 mW/cm^2 and 1.2 ($\pm$0.2) mW/cm^2. The third point of the list was already discussed in Sec. 5.2.4 as it is a known key point in any MOT. The beam overlap volume is about 1 cm^3 and therefore the magnetic field minimum needs to be carefully centred. The coils then require to be mounted on translation stages for fine positioning. A control along three axes is ideal but, for space limitation reasons, we used only two controls, in the radial directions, and fine vertical positioning was done by running different current through the coils. Final positioning is done with the laser(s) locked by scanning the overlap volume with the expected magnetic field minimum until evidence of a MOT appears. Then the cloud is moved to the very center of the overlap region with two cameras looking from orthogonal directions, and fluorescent light from the reflected beam is used to define the boundaries of the overlap. Finally, scattered photons from the MOT are collected with a Costar SI-M350 CCD camera. An example of a monitoring image of the pyramid MOT is shown in Fig. 5.17. In this experiment, the aim was to demonstrate single laser single beam magneto-optical trapping, and the repumping light is generated via direct modulation of

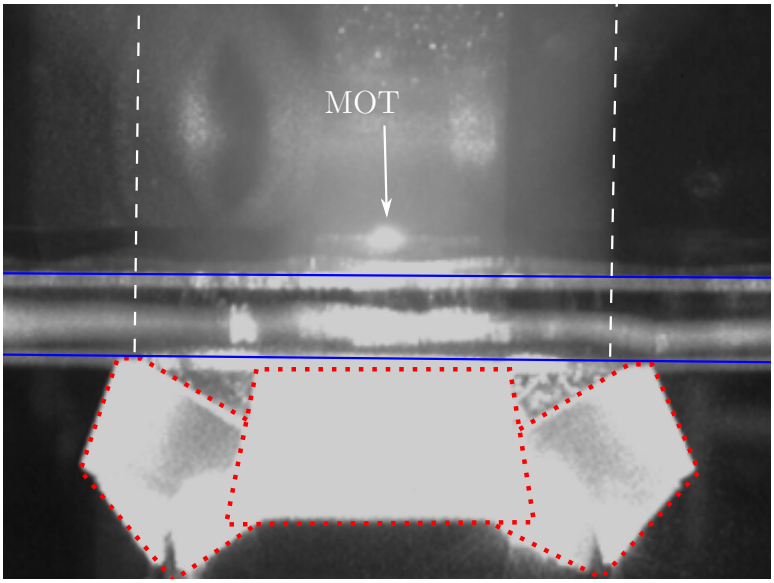

Figure 5.17: Photographs of pyramid mirror MOT. The blue lines denote the glass plate at the bottom of the vacuum cell. The red dotted overlaying lines indicate the position of the mirrors.

the injection current in the trapping laser, as described in Chap. 2, and high-frequency boards, relaxation oscillations resonance and optimum external cavity size were used to maximize the repump light generation efficiency. The energy splitting between the ground states is roughly 6.835 GHz, and a 13 dBm output 6.5 GHz VTO-8650 Voltage Controlled Oscillator from Avantek/PhaseMatrix was used to scan the two repumping transitions $F = 1 \rightarrow F' = 1$ and $F = 1 \rightarrow F' = 2$. Using the pyramid in conjunction with independent cooling and repumping lasers, fluorescence measurements indicated that $1.3{\times}10^6$ atoms were trapped. Fig. 5.18 shows the number of atoms in the MOT using the current modulation. The amount of repump light generated is of the order of 0.5 mW, enough to get a maximum of $1.1{\times}10^6$ atoms. The two peaks correspond to the repumping transitions $F = 1 \rightarrow F' = 1$ and $F = 1 \rightarrow F' = 2$. The positions of the maxima are in accordance with the expected values for a detuning of the cooling light of 8.3 MHz from the $F = 2 \rightarrow F' = 3$ transition. Note also that using the $F = 1 \rightarrow F' = 2$ transition to repump the atoms is more efficient than the $F = 1 \rightarrow F' = 1$ transition. This is to be expected as the branching ratio to the $F = 2$ level is more favorable via decays from $F' = 2$ rather than the $F' = 1$

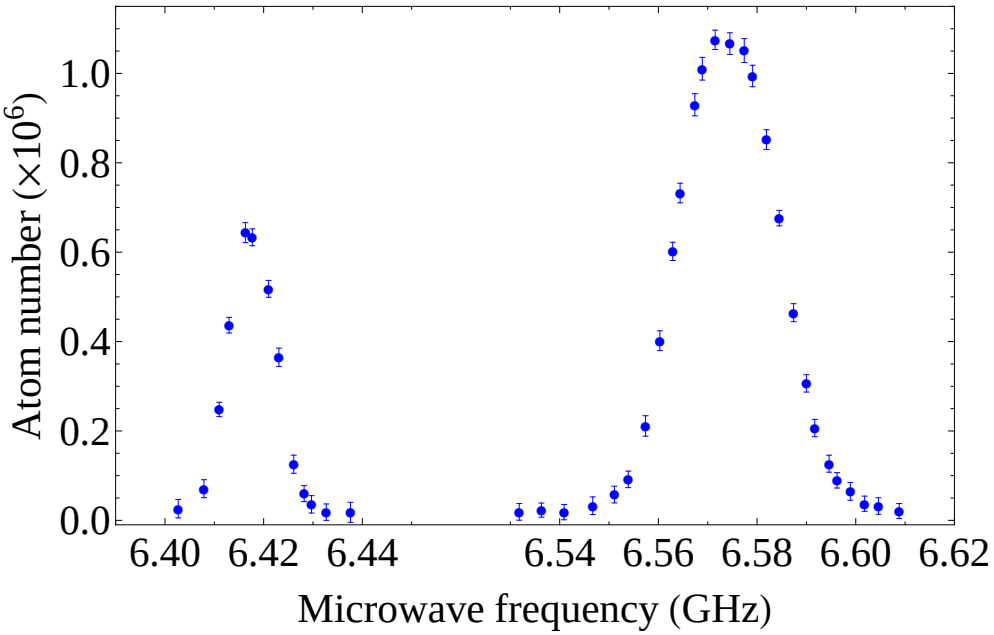

Figure 5.18: Atom number as a function of microwave frequency scanning the $F = 1 \rightarrow F' = 1$ (left) and $F = 1 \rightarrow F' = 2$ (right) repumping transitions. Each point in an average of five measurements for a given VCO frequency.

level, and the $F = 1 \rightarrow F' = 1$ transition is weaker than the $F = 1 \rightarrow F' = 2$ one [86].

The relatively small number of atoms in the MOT is due mainly to the small capture volume ($\sim$400 mm^3) of our demonstration setup. For comparison, in a separate experiment in the same cell, an 8000 mm^3 6-beam MOT collects 2×10^8 atoms. As the atom number N for a MOT with capture volume V scales approximately as $N \propto V^{1.2}$ [139], one must only account for a factor of four in atom number reduction. This reduction can be attributed to our experiment currently operating far from the optimal cooling/trapping regime of the pure tetrad configuration, and to a lesser extent due to the reduced cooling and trapping of a 4-beam MOT compared to a 6-beam MOT. For smaller traps, uniform intensity beams and small velocity/position changes imply a deceleration linear in velocity, $a = -\alpha v$, leading to a capture velocity $v_c = \alpha d$ for beam diameter d. The atom number scales as $N \propto d^2 v_c^2$ [139] and thus $N \propto d^6$, i.e $N = k_V V^2$. As our design

obviates some of the constraints placed on the very first integrated atom-chip pyramid MOT [124, 126], we predict the experimental proportionality constant k_V can be increased. For smaller MOTs optimal detuning decreases ($\Delta/\Gamma \approx 1.4$ in the present case), and one can estimate the rapid scaling with trap volume begins at pyramid sizes around $v/\alpha = 0.6$ mm since the damping is then linear for speeds $|v| < 3$ m/s and $\alpha = 5000$ s^{-1}). To circumvent the low background vapour loading rate for small pyramids, the use of loading mechanisms with low 3D spatial and velocity spreads and zero final center-of-mass velocities could be used: e.g. magnetic transport [140, 141] or magnetic lensing/optical guiding [142] of launched atoms.

5.4 Grating MOT: implementation

The experimental realisation of the grating MOT mainly recycles the same points as the mirror pyramid MOT. However, the upwards beams in the grating MOT come with an angle ($\phi \approx 110.6°$) much closer to the tetrahedral configuration ($\phi \approx 109.5°$). Given that the total diffraction efficiency, including absorption from the quartz plates, is about 32.2 %, that is close to ideal (according to Eqn. 5.5), the vertical beam had to be expanded, compared to the PMOT configuration, in order to flatten its intensity profile and obtain similar intensities in diffracted beams after compression from the gratings. Due to the smaller beam overlap volume in this case, quadrupole field positioning is even more critical. This experiment was set up starting from a PMOT, changing the optical triplet and expanding the vertical beam, to keep knowledge of the magnetic field minimum position. Given the initial difficulties to obtain trapped atoms, the gratings were first slightly tilted by lifting their side directed towards the centre to get more acute diffraction angles and maximise the overlap volume. After evidence of a MOT was seen with this configuration, the gratings were once again put on a flat surface with all other experimental parameters kept constant. A photograph of a MOT obtained with totally flat planar diffractors is shown in Fig. 5.19, where the rightmost grating diffracts the beam orthogonally to the viewing direction with a $\sim$69° angle compared to vertical. The numbers of atoms is the GMOT as a function of quadrupole field gradient and trapping laser detuning are shown in Fig. 5.20.

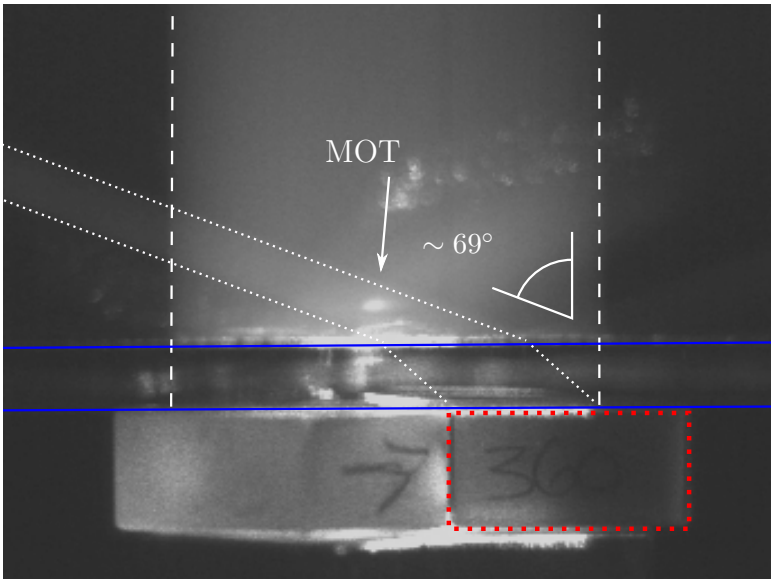

Figure 5.19: Photographs of the grating MOT. The blue lines denote the glass plate at the bottom of the vacuum cell. The red dotted overlaying lines indicate the position of the rightmost grating. The white dotted lines show the ∼69° diffracted beam from a 1200 grooves/mm grating.

The lower values, compared to the PMOT, are due to the smaller overlap volume, which is evaluated to be about 60 mm^3 for the GMOT, that is 15 % of the one of the PMOT. This results in a reduction in the atom number [139] of 0.15. Although the number in the GMOT is only reduced by one order of magnitude

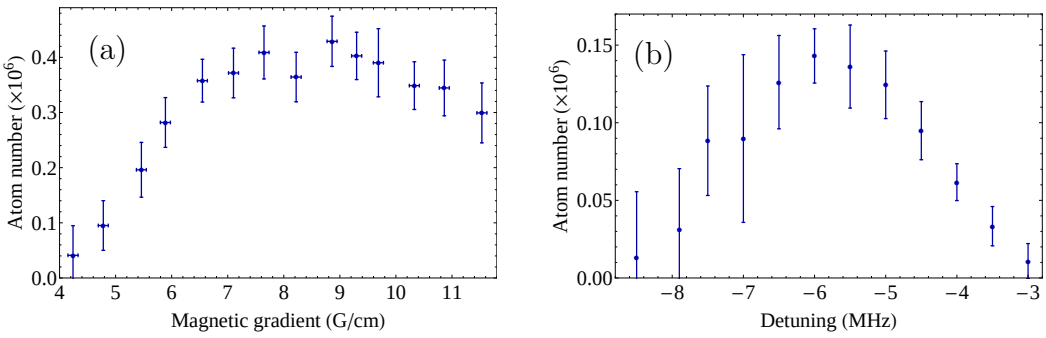

Figure 5.20: (a) Atom number as a function of MOT magnetic field. Detuning is -6.6 MHz. (b) Atom number as a function of trapping laser detuning. Magnetic field gradient is ∼5 G/cm. For both measurements, beam intensities are about 0.64 mW/cm^2.

compared to the PMOT, the experimental parameters (magnetic gradient, beam intensities and detuning) are not strictly similar but the trend is in the expected direction.

5.4.1 Sub-Doppler cooling in the grating MOT

Sub-Doppler cooling theory states that the final temperature is proportional to the ratio of light intensity over detuning (I/Δ), since this quantity defines the amplitude of the optical lattice [12, 13], and one can play on either or both parameters to achieve temperatures typically one order of magnitude lower than the ones predicted by Doppler theory [11], that is about 140 μK for rubidium. Also, any remanent magnetic field at the trap location will induce an asymmetry between magnetic sub-levels and further inhibit sub-Doppler mechanisms, and usually three orthogonal pairs of Helmholtz coils cancel stray magnetic fields. There are several ways of measuring temperature [1, 11], and we used Time-Of-Flight (TOF) imaging. The cloud is let to freely evolve in the absence of light for a known duration, its size is measured and compared at two different times from which it is possible to extract the temperature information. Cold atoms in MOTs and optical molasses have both position and velocity distributions following a normal distribution [85] (although the distribution in not Maxwell-Boltzmannian, since a MOT is not a conservative trap, but results coincidentally from the combination of trapping and cooling forces in a MOT) and the cloud width $\langle x^2 \rangle$ after a time evolution t relates to the initial width $\langle x_0^2 \rangle$ by [14]

$$\langle x^2 \rangle = \langle x_0^2 \rangle + \frac{k_\mathrm{B} T}{m} t^2. \tag{5.14}$$

The experimental modifications needed to implement sub-Doppler cooling from the setup used for four beam magneto-optical trapping are presented in Fig. 5.21 while the timings associated with each signal that controls one part of the experiment are shown in Fig. 5.22. All triggers are generated from a single computer which also programs the different functions generated (as described later) and camera, and processes data afterwards. The two key points to achieve sub-Doppler cooling are the decrease of I/Δ and the magnetic field extinction.

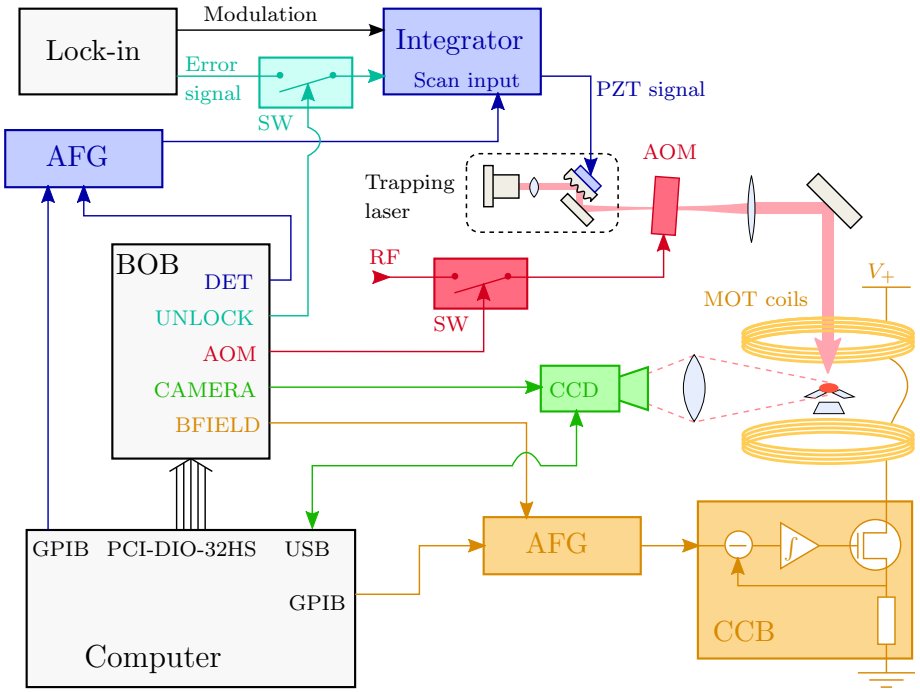

Figure 5.21: Schematics of the sub-Doppler experiment showing only timed elements and using the same color scheme and names for the five triggers as in Fig. 5.22. GPIB: General Purpose Interface Bus. USB: Universal Serial Bus. PCI-DIO-32HS: National Instrument Digital Input-Output Card. BOB: Break-Out Box. CCB: Coil Control Box. AFG: Arbitrary Function Generator. SW: Switch. RF: AOM Radio-Frequency signal.

The equipment and signals related to these two concepts are respectively shown in (dark and light) blue and orange. Elements related to light switching are shown in red, and green refers to the camera and its timings. A experimental run consists of five phases. First, the MOT is loaded for 3 s. Secondly, the trapping laser frequency is unlocked and further red-detuned during the Extra-Detuned MOT (EDM) phase. In the Reduced B-field MOT (RBM) phase, the MOT quadrupole field is decreased. Optical molasses is achieved when the MOT quadrupole field totally vanishes. The EDM and RBM phase durations are typically a few tens of ms long. Atoms are then left to freely evolve without magnetic fields or light for Time-Of-Flight (TOF), at the end of which an image is taken. The laser fre-

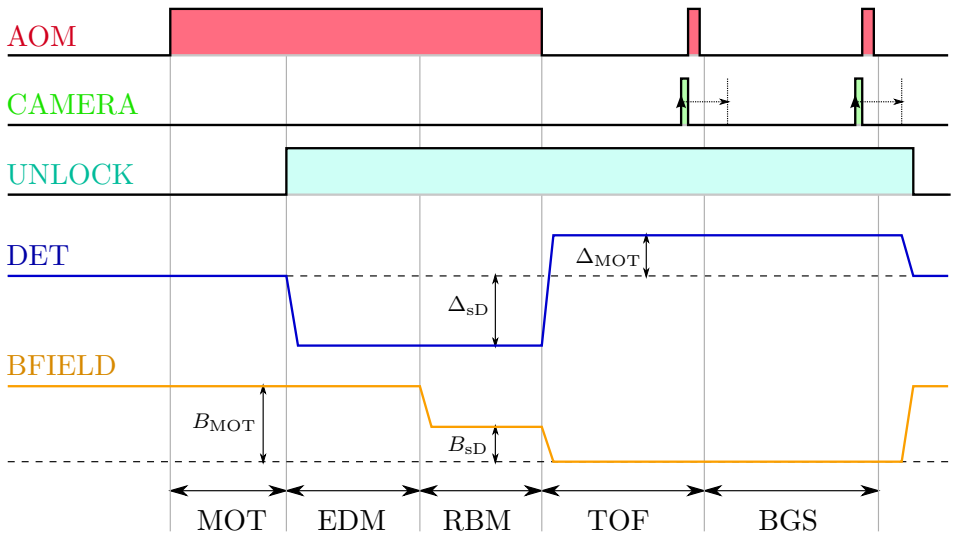

Figure 5.22: Timing diagram for sub-Doppler cooling including five phases. MOT: MOT loading. EDM: Extra-Detuned MOT. RBM: Reduced B-field MOT. TOF: Time Of Flight. BGS: BackGround Substraction imaging. The three top lines are digital signals for the AOM switch, CCD camera and laser unlock. Two extra pulses (not shown) at the beginning of EDM and SDM phases respectively trig the function generators to output the programmed detuning (DET) and magnetic field (BFIELD) signals. Horizontal arrows for the CAMERA trigger indicate the camera exposure time. Dashed lines for Detuning and Magnetic field represent the reference.

quency is then brought to resonance to maximise photon scattering and therefore Signal to Noise (S/N). A short pulse of light (450 μs) is sent 100 μs after the camera has started acquiring. Exposure time is set to 1 ms, and this way the actual signal duration is directly defined by the pulse duration. Finally, an extra image is required for Background Substraction (BGS). Since at least two cloud sizes are required to extract temperature information, the experiment is repeated with different TOF durations. This last phase lasts for about 100 ms, allowing for atoms to leave the imaging region and for the camera to take a second image. A resonant light pulse can be sent before the second image to heat the remaining atoms and thus actively clean the region.

In order to achieve temperatures well below the Doppler limit, one can either detune the frequency of the trapping laser or reduce its intensity, or combine both.

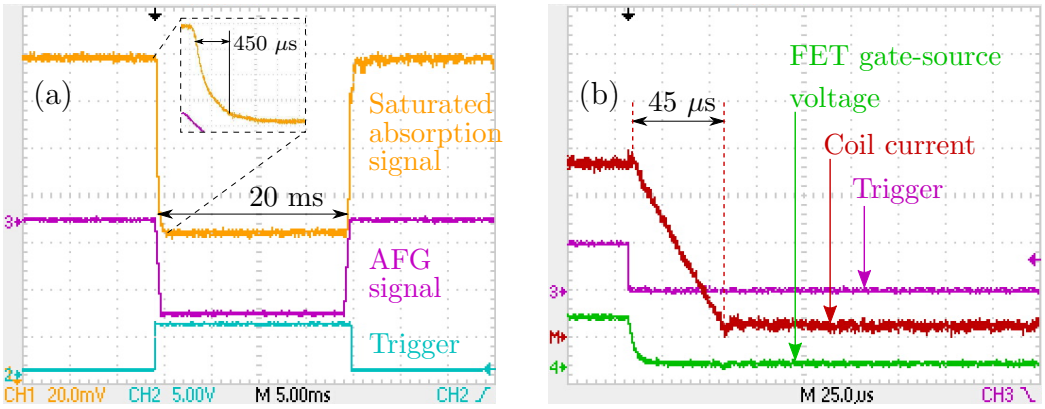

Figure 5.23: (a) Saturated absorption signal recorded during detuning signal applied on scan input. The laser frequency shift set by the signal is about 20 MHz. (b) Current in MOT coils as the FET is switched off with 1 μs time constant low pass filtering applied to the trig signal.

In all the following, only the detuning is changed, to simplify the experimental setup, since no improvement was found by using a combination of both methods. The detuning is increased by acting on the PZT of the trapping laser cavity. A digital switch disconnects the error signal sent by the lock-in amplifier to the integrator (as done initially for the MOT setup depicted by Fig. 5.14) and, while the laser is thus let free-running, a signal connected to the scan input of the integrator shifts the laser frequency by a few MHz during optical molasses and imaging before the lasers relocks to its original point. Such a scheme is relatively easy to implement but the downside is that the frequency of the unlocked laser can drift in uncontrolled ways. Fig. 5.23(a) shows the saturated absorption signal as the PZT signal is changed in a region where absorption varies roughly linearly with frequency. The laser frequency is pulled by ∼35 MHz for 20 ms and no significant drifts can be observed, even for much longer (∼200 ms) free-running times corresponding to typical experimental durations. It was first seen that a rapid signal applied to the scan input would excite resonances in the PZT transducer around 2.5 kHz and this can be circumvented by low-pass filtering the scan signal and clean frequency switching is then achieved within typically 1 ms. In the present case, this scan signal is generated by an Arbitrary Function Generator (AFG) DS345 from Stanford Research Systems, itself being remotely

programmed via a General Purpose Interface Bus (GPIB) by the computer prior to experimental runs. Fig. 5.23(a) also shows time traces of the AFG trigger and the (programmed) generated scan signal. Therefore, the laser is unlocked and frequency shifted from the beginning of the EDM phase to the end of the current experimental run.

The MOT magnetic field has to be changed in a time no longer than 1 ms, the optical molasses phase typically lasting for a few tens of ms. Also, one wants a monotonic decrease and oscillations should be avoided as it means the magnetic field may change direction and the force becomes repulsive, pushing atoms away from the trap centre. The magnetic field, or rather the coil current, is controlled via a Metal-Oxide Semiconductor Field Effect Transistor (MOSFET) PHP125N06T in series with the coils that acts as a switch or a regulator. The current across the drain and the source (i.e. the resistance between these two points), although strongly non-linear, is a monotonic function of the gate voltage and one can easily switch on or off the current by applying gate voltage much lower or higher than the threshold voltage.

The magnetic field is a function of the current *inside* the coils. During transients, the external current, as the one flowing through the MOSFET, can differ, since there can be current exchange between the coils and their parasitic capacitance. However, the external current is the only thing one one can easily control, and the magnetic field can be checked by using a magnetic probe.

A typical current switch off is displayed in Fig. 5.23(b), starting from $I_{\text{coils}} = 3.5$ A. At switch on (not shown), the current rises with the typical fashion of the first order circuit defined by the time constant $\tau = L/R \approx 2.5$ ms where $L = 800$ μH is the inductance of the anti-Helmholtz coils pair and $R = 0.3$ Ω is the resistance of the coils wires. One might then expect the same behaviour at switch off; the linear decay is due to the presence of a Zener diode across the drain and the source of the MOSFET, used to prevent high voltages that could damage the component. When the transistor is shut off quickly, the back electromotive force from Lenz's law $V_{\text{EMF}} = -\mathrm{d}\phi/\mathrm{d}t$ becomes larger than the Zener diode breakdown voltage ($V_{\text{Zener}} = 55$ V for PHP125N06T). Therefore, the voltage across the coils is mainly equal to V_{Zener} and the current slew rate is given by $\mathrm{d}I_{\text{coils}}/\mathrm{d}t = V_{\text{Zener}}/L = 69$ kA/s and the predicted switch off duration

from initial current $I_{\text{coils}} = 3.5$ A (as in Fig. 5.23(b)) is $\sim$50 μs. In experimental conditions, the current is always lower than 7 A, that is the maximum switch off time is always fast enough, i.e. $<$100 μs. Ripples were first observed on the current, due to a rapid gate signal, but a simple 1 μs low-pass filter can remove them. In addition, a feedback circuit (CCB in Fig 5.21) (for which detailed schematics can be found in [109]) is used to accurately set the MOT magnetic field for investigation in a sub-Doppler MOT. The CCB is in turn controlled by an AFG DS345 remotely programmed via GPIB on the computer, as for the detuning signal.

Due to the very low atom number (typically a few 10^5 as shown in Fig.5.20) obtained in the tetrahedral grating MOT, the initial SI-M350 camera had to by changed for an Andor Luca-R. This Electron Multiplying Charge-Coupled Devide (EMCCD) comprises an extra register (the electron multiplying register) that amplifies the signal in each potential well before charges are read-out, increasing the S/N ratio since the read-out conversion process adds noise per site. These cameras thus allow accurate imaging in a low light environment. The computer controls the camera parameters (e.g. exposure time) and reads images via a Universal Serial Bus (USB) connection.

All digital signals: AOM and unlock switches, as well as the triggers for the camera and the two AFGs for detuning and magnetic field are generated by a digital input/output card PCI-DIO-32HS from National Instrument in the main computer. A Break-Out Box (BOB) offers handy BNC connections to these inputs and outputs. All hardware equipments connected to the computer are accessed via the LabVIEW code that controls all the experiment.

For either MOT or sub-Doppler MOT operating conditions (i.e depending on the light detuning), the temperature measured vertically was always half of the horizontal one. Although, temperatures can be slightly different along different directions [106], such a difference is unlikely, given the relatively balanced beam intensities, and we concluded the difference was an optical artefact due to the MOT being very close to the glass bottom plate: part of the scattered light is blocked or deflected by the plate and imaging gives a biased information along the vertical axis. Also, the overlap region is roughly a flattened rhombohedron that extends $\sim$10 mm horizontally but only $\sim$2.5 mm vertically, thus the vertical

cloud size may appear smaller than it actually is since atoms reaching the beam boundaries scatter less photons during imaging. Therefore all temperatures are measured horizontally in the following, and this is likely to consist in a higher limit.

We initially thought that obtaining optical molasses would be a straightforward step, due the relative ease of implementation and robustness once timed parameters are well controlled. Although temperatures in standard MOT conditions agreed with the expected values, once the magnetic field was removed, we observed an increased of the expansion rate, that is the temperature, of the cloud in optical molasses. Much work has been done to check every single experimental parameter, and especially the ones that are critical for efficient optical molasses, that is the intensity balance between each beam and the cancellation of the magnetic field [107]. Typically, sub-Doppler cooling works well with stray magnetic fields not higher than a few tens of mG [14, 143] at the atoms' location.

For larger fields, ground levels each feel a significant Zeeman shift that strongly reduces redistribution of the atomic population through optical pumping. The usual way to cancel magnetic fields is to check the expansion of the cloud while the MOT field is decreased, and from this observation the field was inferred to be not larger than 50 mG, that is small enough for sub-Doppler cooling to take place. However, even in these carefully checked experimental conditions, we still observed a dramatic increase of the atomic temperature when the magnetic field is switched off completely. It is nevertheless possible to obtain sub-Doppler temperatures without extinguishing the quadrupole field and subsequent work focused on this direction, given the difficulty to get optical molasses. Possible reasons for this behaviour are discussed later on in the text. The temperature in a MOT decreases with atom number [144] and one can observe evidence of sub-Doppler cooling for small enough MOTs [145, 146]. In these configurations, atoms stay near the magnetic field minimum, effectively reproducing the conditions of optical molasses. The EDM phase shown in the timing diagram of Fig. 5.22 is indeed used in this purpose; the detuning is increased whilst the magnetic field is kept constant.

The atomic density profile typically shows a bimodal distribution and thus can be accurately fit only with two Gaussians, as seen in Fig. 5.24(a). This indicates

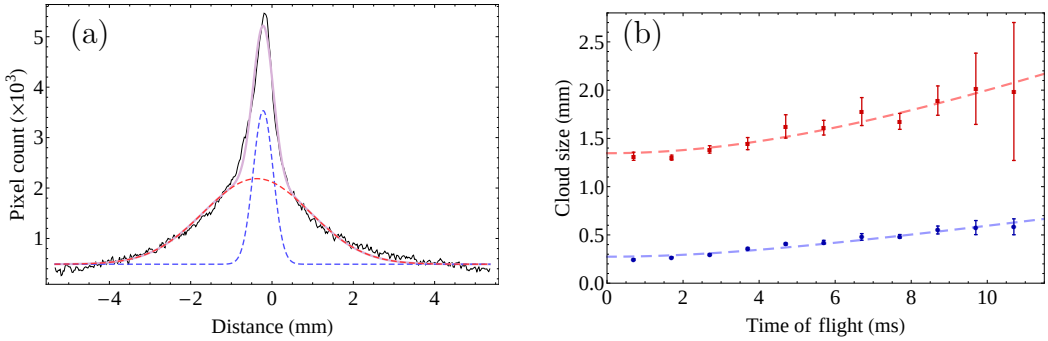

Figure 5.24: (a) Cloud density profile integrated horizontally showing the bimodal distribution. Blue and red dashed curves are Gaussian fits to cold and hot fractions. Solid purple line is the bimodal fit to experimental data points. (b) Size of the cold (blue squares) and hot (red disks) cloud components for different times of flight. Dashed lines are fits using Eqn. 5.14 that gives temperatures of $T_{\rm cold} = 29^{+7}_{-4}$ μK and $T_{\rm hot} = 228^{+300}_{-228}$ μK.

the presence of two atomic fractions with different temperatures [14, 147]. Some of the atoms that stay near the trap centre, typically those with low kinetic energies fitted by the smaller Gaussian in Fig. 5.24(a), effectively felt no magnetic field. The cloud sizes of the two fractions as a function of time of flight is displayed in Fig. 5.24(b). As expected in such cases, the cold fraction ($T \approx 29$ μK) undergoes sub-Doppler cooling mechanisms whilst the hotter atoms ($T \approx 228$ μK) are still in a Doppler cooling phase. For the results of Fig. 5.24, the magnetic field is 20 G/cm, light intensity is 1.24±0.07 mW/cm^2, initial MOT detuning of -8.7 MHz is ramped down to -18 MHz within 2 ms and thereafter these conditions are kept constant for 18 ms before TOF and imaging. For larger times of flight, the cloud expands and becomes flatter, the number of photons collected by the camera per site decreases, and S/N decreases. This is particularly true whenever one wants to extract information on the hot atomic fraction, by nature occupying a larger volume, and this is seen in the very large uncertainties in the measure of the temperature, with $T_{\rm hot} = 228^{+300}_{-228}$ μK.

The cloud comprises typically a few 10^4 atoms, of which about one third is sub-Doppler cooled. Temperature and relative atomic number as a function of EDM detuning with no reduction of magnetic field are shown, for the cold fraction, in Fig. 5.25. The initial point, for a laser detuning of -8.7 MHz, corresponds to the

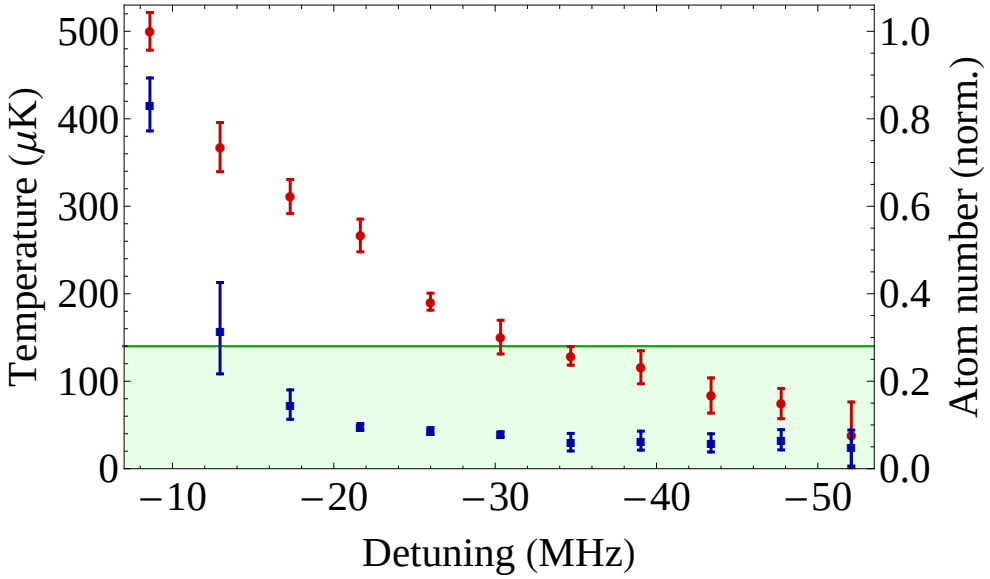

Figure 5.25: Temperature (blue squares) and relative atom number at 0 ms TOF (red disks) as a function of EDM detuning. Quadrupole magnetic field is kept constant at 20 G/cm. The date refers to the cold atom fraction, and the green region denotes sub-Doppler temperataures. The atom number is normalised against its value in the cold fraction at a -8.6 MHz.

normally operating MOT conditions, cooling is dominated by Doppler mechanism and effectively no bimodal distribution is observed. As the laser frequency is brought further away from resonance, the phenomenon described above becomes more and more apparent and there is effectively a part of the atomic cloud in a sub-Doppler regime, with a saturation of the temperature around 40 μK reached for detuning larger than $\sim$20 MHz. We infer the reduction in the sub-Doppler cooled atomic fraction to the fast change in detuning at the beginning of the EDM phase. Indeed, the velocity capture range for sub-Doppler cooling varies as the inverse of the detuning squared [12] (for detunings much larger than the natural linewidth), and for larger EDM detuning, less and less atoms, only those with the smallest kinetic energies, can be sub-Doppler cooled. By ramping the detuning more slowly and keeping the same final value, we observed that more atoms can be caught by the sub-Doppler cooling mechanism. It has been outlined previously that optical molasses could not be achieved, and Fig. 5.26 presents the cloud size when the RBM phase is added to the experimental sequence, that is the magnetic

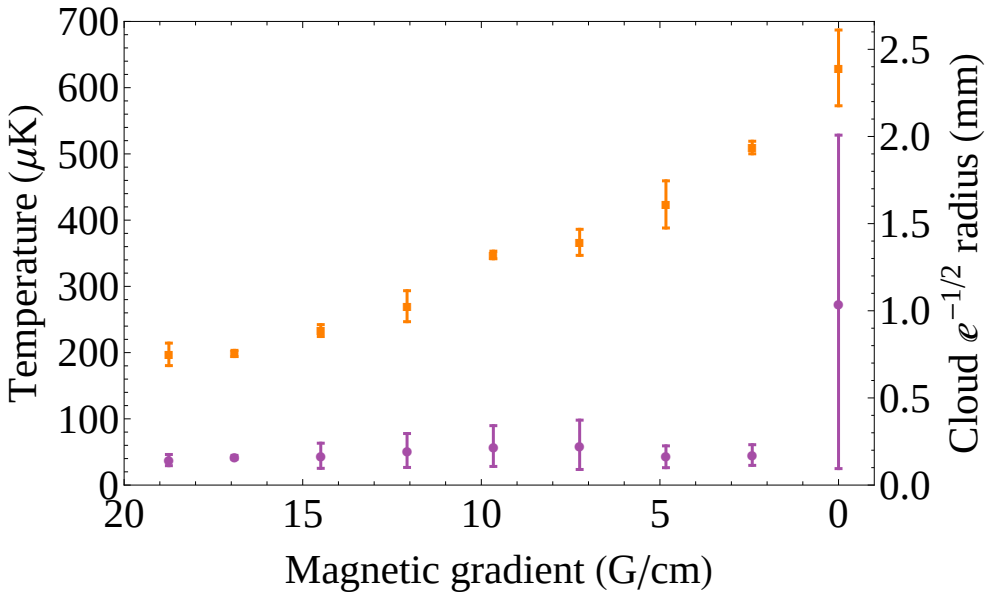

Figure 5.26: Cloud $e^{-1/2}$ radius at 0 ms TOF (orange squares) and temperature (purple disks) as the magnetic field is reduced during RBM phase. Detuning is -30 MHz.

field is reduced, after EDM[1]. The detuning used for EDM is -30 MHz and kept constant during the 10 ms of the RBM phase. Optical molasses is therefore achieved when the magnetic field during RBM is completely switched off. As the quadrupole field is reduced, the magneto-optical trapping force decreases and the cloud becomes larger as atoms can more freely diffuse. Although the temperature remains approximately constant, as the final magnetic field gradient reaches zero, the $1/e$ diameter of the Gaussian cloud prior to time-of-flight imaging reaches a size ($\sim$4 mm) comparable with the beam-overlap volume. It appears that deeper molasses cooling is largely prevented by spatial intensity variation in our small beam overlap volume, particularly near the edge of the cloud. Future experiments would be better performed in an optimized setup with larger beam overlap and less dramatic diffracted beam compression. Both goals can be achieved using diffraction gratings with a larger groove period.

[1]Evidence of sub-Doppler cooled optical molasses has been seen, but it was afterwards impossible to reproduce this experimental observation

5.5 Conclusion

We have experimentally realised a four-beam MOT based on the theory developed in Chap. 4 by using a triplet of either mirrors (PMOT) or diffraction gratings (GMOT) to split and steer and single incident beam, thus making this scheme ideal for low cost and compact applications. We have captured about 10^6 atoms in the PMOT, limited by the small overlap volume that dictates the atom number, with a single laser setup. The repumping frequency was generated by direct modulation of the semiconductor laser current, resulting in an even more compact and inexpensive system. In-MOT sub-Doppler cooling was achieved with a the completely planar diffractor element, using only commercially available gratings. The extra-vacuo configuration of the system limits the atom number and an accurate control of the intensities of the upwards beams cannot be made. However, next generation grating MOTs are currently being designed, for an in-vacuo system that maximises that atom number and allow for precise adjustment of the key parameters, and we hope to get sub-Doppler cooled optical molasses with this scheme. The present experimental work led to two publications for the PMOT [112] and GMOT [148].

Chapter 6

Inductively coupled ring trap using dressed state potentials

This chapter presents theoretical results on toroidal ring trap geometries that could be used for thermal or quantum gases. Ring traps are of special interest since they are readily usable for atom interferometry in a Sagnac configuration [149], where the two counter-propagating waves use the same paths and this scheme benefits from common noise rejection. One gains sensitivity by using atoms instead of photons; for example, in a rotating Sagnac interferometer that measures inertial effect, the phase difference between the two paths is given by [150]

$$\delta\phi = A\Omega\frac{4E}{\hbar c^2}, \tag{6.1}$$

where A is the area enclosed by the interferometer and Ω the angular rotation frequency of the interferometer. The sensitivity is directly proportional to the relativistic energy E, which is larger by many orders of magnitude for an atom ($E_{\text{atom}} = mc^2$) compared to a photon ($E_{\text{photon}} = \hbar\omega$). Also, such Sagnac interferometer can measure differences in the gravitational field felt by the atom in each "arm", and this could be used, for instance, as a tool for mineral, oil or water prospecting or to measure density gradients in the crust of Earth. Such a ring trap could be used along with e.g. a totally flat grating magneto-optical trap, as the one of Chap. 5, to make an all-embedded compact sensor.

On the other hand, small size ring traps are useful to investigate interesting

phenomena in low dimensional quantum gases, such as sonic black holes [151], quantised rotation in superfluids [46, 47] and solitons [152, 153].

Ring or stadium [36] shaped traps have been proposed and realised using either static [35, 36, 37] or time averaged [33, 34] magnetic fields. One can make use of the optical dipole force to confine atom with "hollow" Laguerre-Gauss beams [38, 154, 155], to quickly swirl a focus beam [39, 156, 157] –allowing for even more complex geometries– or to plug a magnetic quadrupole trap [158]. Electric forces have also been used to create ring traps for molecules [159] or ions [160]. For purely magnetic traps, if one wants to reduce the size of the system, the current-carrying wires –needed to connect the system to an external electric source– get closer to the trap region, having a non negligible effect on the potential shape since they perturb the rotational symmetry. Furthermore, fragmentation of atomic clouds has been seen for magnetically trapped gases lying close to current carrying wires in atom chips [161, 162, 163, 164]. This was attributed to corrugations in the conductor that deflect the current from the desired path. One way to circumvent this is the use of alternating current to "average" the defects to zero [165]. More recently, new designs have been suggested to create toroidal ring traps [40, 41, 42, 43, 44, 45] using radio-frequency adiabatic potentials as primarily investigated by Oliver Zobay and Barry Garraway [49], offering extended flexibility for the trap design. This chapter first presents the magnetically induced ring trap [48], currently being experimentally implemented at the University of Strathclyde, then focuses on a possible way to create a micro-fabricated toroidal ring trap for quantum gases, recycling the same (but reduced) apparatus of Ref. [48] but in a dressed state approach.

6.1 Macroscopic magnetically induced ring trap

A schematic of the experimental setup of the magnetically induced ring trap is shown in Fig. 6.1. A homogenous alternating magnetic field $B_{\mathrm{ac}}(t)$, generated by a pair of Helmholtz coils, induces a current in a small conductor ring. This current flows through the ring, creating in turn a second alternating magnetic field $B_{\mathrm{ring}}(r, z, t)$. We shall see that the combination of these two fields results in a ring of zero magnetic field, the radius of which varies in time. By averaging

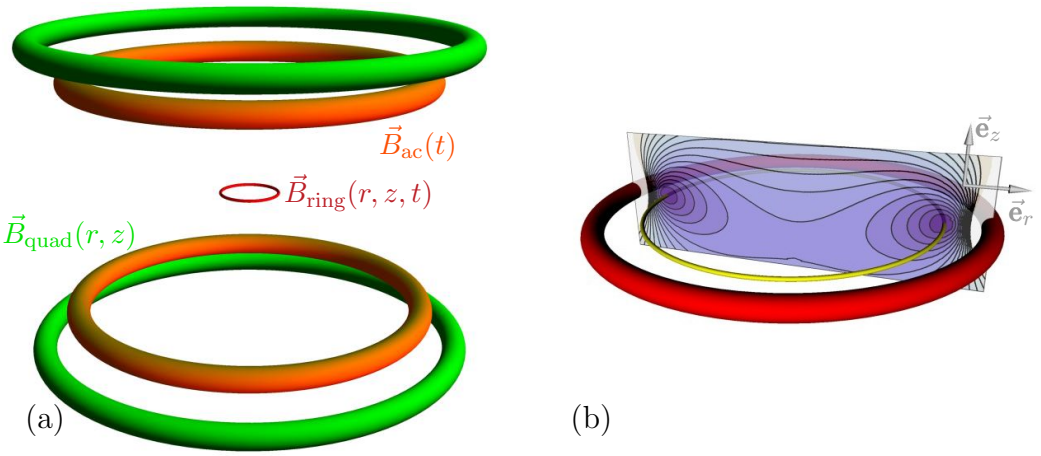

Figure 6.1: (a) Schematics showing the magnetically induced ring (red), the ac-Helmholtz coils (orange) and the anti-Helmholtz quadrupole coils (green). (b) Close-up view on the induced ring illustrating the potential in a cut through the ring and the position of the toroidal potential minimum (yellow).

over one cycle, one gets a toroidal time averaged potential located within the conducting ring, as shown on the close-up view of the induced ring in Fig. 6.1(b). In the following, we will consider a copper inductive ring of radius $r_{\mathrm{ring}} = 1$ cm with a circular cross-section of radius $r_{\mathrm{wire}} = 0.5$ mm.

6.1.1 Induced current through the conductive ring

The electromotive force $E_{\mathrm{emf}}(t)$ in a conductive loop is a function of the magnetic flux $\Phi(t)$ flowing through that loop and its amplitude is given by Faraday's law of induction:

$$E_{\mathrm{emf}}(t) = -\frac{\mathrm{d}\Phi(t)}{\mathrm{d}t}, \tag{6.2}$$

where the negative sign is imposed by Lenz's law. If we make the realistic assumption that the flux from the Helmholtz coils is homogenous through the ring, we can write their associated magnetic field as $B_{\mathrm{ac}}(t) = B_0 \cos \omega t$ with B_0 the field amplitude and ω the driving frequency in the harmonic regime. The flux then reads $\Phi(t) = sB_{\mathrm{ac}}(t)$ where $s = \pi\, r_{\mathrm{ring}}^2$ is the area of the ring. On the other hand, a conductive ring is an electric circuit that can be idealised with a corresponding inductance L and a resistance R in series, responsible for Ohmic

losses in the never perfect conductor. Thus, $E_{\mathrm{emf}}(t)$ relates to the current flowing through the ring $I_{\mathrm{ring}}(t)$ by

$$E_{\mathrm{emf}}(t) = L\frac{\mathrm{d}I_{\mathrm{ring}}(t)}{\mathrm{d}t} + RI_{\mathrm{ring}}(t). \tag{6.3}$$

If the ring size is much larger than conducting region, that is $r_{\mathrm{ring}} \gg r_{\mathrm{wire}}$, the resistance is well approximated by

$$R \approx \frac{2\rho\ r_{\mathrm{ring}}}{r_{\mathrm{wire}}^2}, \tag{6.4}$$

where ρ is the electric resistivity of the material, equals to $1.68{\times}10^{-8}$ $\Omega{\cdot}$m [166] in the case of a copper ring at room temperature. The inductance has a more complex expression and depends on the ring and wire radii [167] that reads

$$L \approx \mu_0\ r_{\mathrm{ring}}\left(\ln\frac{8\ r_{\mathrm{ring}}}{r_{\mathrm{wire}}} - \frac{7}{4}\right), \tag{6.5}$$

which is again valid under the condition $r_{\mathrm{ring}} \gg r_{\mathrm{wire}}$ and where μ_0 is the magnetic permeability of vacuum. By combining Eqns. 6.2 and 6.3, one gets the ring current as a function of the ac field amplitude and frequency B_0 and ω, and the ring physical parameters:

$$I_{\mathrm{ring}}(t) = -\frac{I_{\mathrm{max}}}{\sqrt{1+\Omega_{\mathrm{r}}^{-2}}}\cos(\omega t + \delta_0). \tag{6.6}$$

The above expression is the typical response of a high pass first order system, with the cut-frequency $\omega_0 = R/L$ of an $R-L$ circuit. The current in Eqn. 6.6 is expressed using the relative frequency $\Omega_{\mathrm{r}} = \omega/\omega_0$ and $\delta_0 = \tan^{-1}(1/\Omega_{\mathrm{r}})$ is the phase difference with the inducing ac field $B_{\mathrm{ac}}(t)$. The maximum current $I_{\mathrm{max}} = \pi r_{\mathrm{ring}}^2 B_0/L$ is approached for frequencies well above $\omega_0 = R/L$, while in the other limit, no current couples through the ring, as stated by Faraday's law. Both amplitude and phase shift are shown in Fig. 6.2. For our specific case, the resistance and inductance are, respectively, $R \approx 1.3$ mΩ and $L \approx 42$ nH. The cut-off frequency is $\omega_0/2\pi = 5.1$ kHz and the skin depth at this frequency in copper is $\delta_{\mathrm{sd}} = \sqrt{\frac{2\rho}{\omega\mu_0}} = 0.9$ mm$> r_{\mathrm{ring}}$. For driving frequencies not too far above

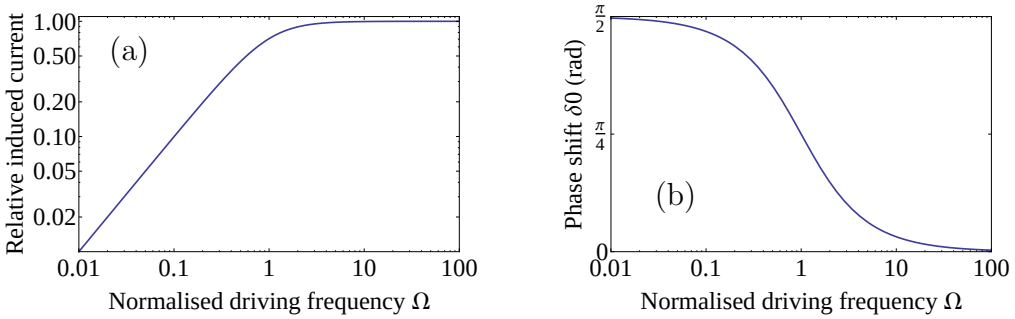

Figure 6.2: Amplitude (a) and phase shift relative to the ac field (b) of the ring current as a function of driving frequency.

ω_0, it can be assumed that the current flows uniformly through the ring, and the expressions for R and L are thus valid in this regime.

6.1.2 Magnetic field emitted by the induced ring

A current I flowing through a conductor radiates a magnetic field which can be found by integrating Biot-Savart law [167]

$$\mathrm{d}\vec{B} = \frac{\mu_0 I}{4\pi} \frac{\mathrm{d}\vec{l} \times \vec{r}}{|\vec{r}|^3}, \tag{6.7}$$

where $\mathrm{d}\vec{l}$ is an infinitesimal segment of the conductor that carries I and $\vec{r}$ is the vector that connects the current segment to the point of interest. Although it is easy to solve this equation, using symmetry arguments, to find the on-axis field emitted by a current carrying loop, the general expression requires the use of elliptic integrals. In cylindrical coordinates, the total field reads [168]

$$\begin{aligned} \vec{B}_{\mathrm{ring}}(r,z,t) = \frac{I_{\mathrm{ring}}(t)\ \mu_0}{2\pi\ r_{\mathrm{ring}}\ \sqrt{Q}} \Bigg\{ \gamma \left(\frac{1+\alpha^2+\beta^2}{Q-4\alpha} E(m) - K(m) \right) \vec{\mathbf{e}}_r \\ + \left(\frac{1-\alpha^2-\beta^2}{Q-4\alpha} E(m) + K(m) \right) \vec{\mathbf{e}}_z \Bigg\}, \end{aligned} \tag{6.8}$$

where r and z are, respectively, the radial and axial coordinates relative to the ring centre and $\vec{\mathbf{e}}_r$ and $\vec{\mathbf{e}}_z$ are unit vectors, as shown in Fig. 6.1. $E(m)$ and $K(m)$ are, respectively, the incomplete elliptic integral of the second kind and complete elliptic integral of the first kind defined as $E(m) = \int_0^{\pi/2} \sqrt{1 - m \sin^2\theta}\ \mathrm{d}\theta$ and $K(m) = \int_0^{\pi/2} \frac{\mathrm{d}\theta}{\sqrt{1-m\sin^2\theta}}$ with $m = 4\alpha/Q$. The normalised spatial parameters α, β, γ and Q are given by $\alpha = r/r_{\mathrm{ring}}$, $\beta = z/r_{\mathrm{ring}}$, $\gamma = z/r$ and $Q = (1+\alpha)^2 + \beta^2$. Strictly speaking, Eqn. 6.8 stands for an infinitesimally small wire radius, and one might need to integrate over the whole wire cross-section to get a more accurate expression for the field generated by the ring. However, such full simulations have shown to give results that agreed to better than 0.5 % with the simplified model used here [48].

6.1.3 Total field and time-averaged potential

The total alternating field is the sum of the spatially uniform inducing field from the Helmholtz coils $\vec{B}_{ac}(t) = B_{ac}(t)\ \vec{\mathbf{e}}_z$ and the field emitted by the ring $\vec{B}_{\mathrm{ring}}(r, z, t)$. It is here assumed that the conducting ring is of much smaller dimension than the Helmholtz coil, and thus the mutual inductance between the difference inductors can be neglected. As stated by Lenz's law, the re-emitted field $\vec{B}_{\mathrm{ring}}(r, z, t)$ within the ring tends to point in the opposite direction compared to the inducing, homogenous one. We consider here only what happens in the plane of the ring (i.e z=0), where all magnetic field vectors have an axial component only. For the present ring geometry, the field $|\vec{B}_{\mathrm{ring}}(0, 0, t)|$ at the ring centre is always smaller, in amplitude, than B_0. Since the amplitude of $\vec{B}_{\mathrm{ring}}(r, z, t)$ increases with r until it diverges at $r = r_{\mathrm{ring}}$ (in the ideal case of an infinitesimally small wire radius), there is a circle of points within the conducting ring where the two fields cancel.

The radius of the zero circle is not a function of B_0. One then wants to have the largest current in the ring, as this will result in tighter traps, which implies to choose driving frequencies ω at least larger than ω_0, or equivalently $\Omega_{\mathrm{r}} > 1$. For the following investigation, the driving frequency is set to $\omega/2\pi = 20$ kHz, and $\Omega_{\mathrm{r}} \approx 3.9$. The ac-Helmholtz field amplitude B_0 is set to 100 G. The fields in the plane are shown in Fig. 6.3 at a time $t = \pi/\omega$. For $\Omega_{\mathrm{r}} \to \infty$, the phase

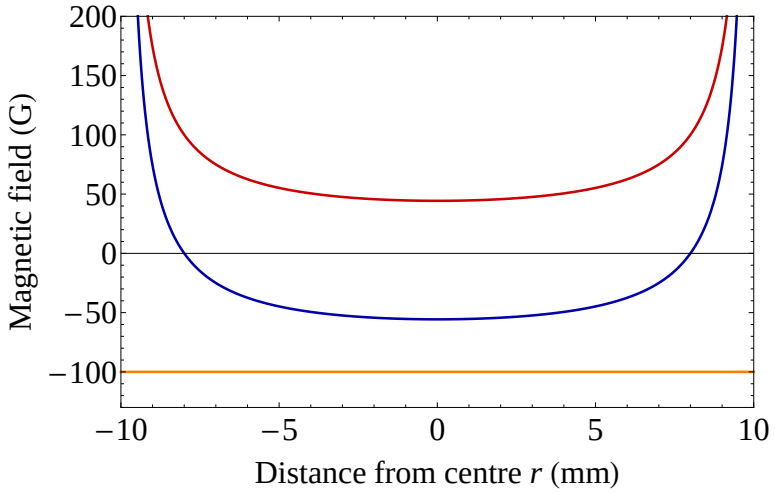

Figure 6.3: Time shot of the axial magnetic field in the plane of the ring at $t = \pi/\omega$. The ac-Helmholtz, ring and total fields are respectively shown in orange, red and blue.

shift $\delta_0 \sim 0$ and the two fields would cancel always at the same position. For the chosen value of Ω_r, the two fields do not oscillate in phase (or more correctly, out of phase, according to Lenz's law), resulting in a circle of zero magnetic field that spans the induced ring area each half period of the oscillating field, starting from the ring centre and eventually "vanishing" in the induced ring at the end of the half period. This behaviour is depicted by the black dots in Fig. 6.4, each representing the zero at one time step, and the arrows, show their direction of motion as time increases.

Particles with a magnetic moment $\vec{\mu}$ couple to a magnetic field $\vec{B}$ through their interaction Hamiltonian [91]

$$\hat{H} = -\vec{\mu} \cdot \vec{B}. \tag{6.9}$$

For atoms with total orbital momentum F, the Zeeman shift ΔE_B arising from this coupling is simply given by

$$\Delta E_B = g_F m_F \mu_B |\vec{B}|, \tag{6.10}$$

where g_F is the Landé g-factor, μ_B the Bohr magneton and m_F the magnetic

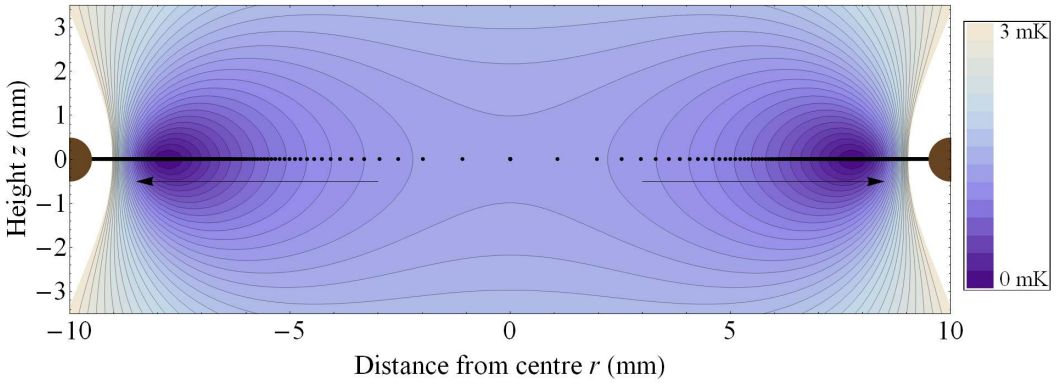

Figure 6.4: Averaged potential in a cut through the induced ring. The potential is expressed in Kelvin and is relative to the value at the trap minimum. Black dots indicate the instantaneous magnetic zero over a half period and the arrows show their direction of motion as time increases.

sub-level considered. The above expression holds for small magnetic fields, i.e. when the Zeeman energy is much smaller than the splitting between bare F levels. Electromagnetism theory state that it is not possible to create a local magnetic field maximum in all three directions of space [169] and the only way to magnetically trap atoms with dc is to use the so-called "low field seeking" magnetic states. For the specific case of ^{87}Rb atoms, only the ground states $|F = 1, m_F = -1\rangle$, $|F = 2, m_F = 1\rangle$ and $|F = 2, m_F = 2\rangle$ states can be trapped, due to the opposite sign in g_F between the $F = 1$ and $F = 2$ levels. In this work, we will consider atoms in the $|F = 2, m_F = 2\rangle$ state only. Different static magnetic field configurations are commonly used to trap atoms [170], such as quadrupole [171] or Ioffe-Pritchard [172] traps.

The spin of trapped atoms in a specific m_F state processes around the local magnetic field $\vec{B}$ at the Larmor frequency

$$\Omega_0 = g_F m_F \mu_B |\vec{B}|/\hbar. \tag{6.11}$$

The spin can adiabatically follow the local magnetic field as long as the field varies slowly (due to an external change of $\vec{B}$ or the atom moving in a inhomogeneous

field) compared to the Larmor frequency [173]. This condition translates as:

$$\dot{\theta} \ll \Omega_0, \tag{6.12}$$

where $\dot{\theta} = \frac{1}{|\vec{B}|}\left|\frac{\mathrm{d}\vec{B}}{\mathrm{d}t}\right|$ is the normalised rate of change of the magnetic field. If the variation is too fast, then the atomic spin is projected to other magnetic sub-levels, leading to Majorana losses [174], since the spin can fall into a high field seeking state. This is particularly evident for a quadrupole trap where the vanishing magnetic field at the trap centre implies that Ω_0 becomes zero as well, and an atom moving across a zero has $\dot{\theta} \to \infty$ In other static trap [175], such as Ioffe-Pritchard, this issue is addressed by making a non-zero minimum, thus greatly reducing spin-flip losses. The giant storage ring at the University of Strathclyde [37] is an other example of such an non-zero minimum trap, used in a toroidal configuration. Another purely magnetic way to circumvent Majorana losses in a quadrupole trap is to quickly swirl the field zero at a rate much higher than the trapping frequencies. Atoms stay where the mean value of the field, over one period, is minimum, but with an appropriate configuration, the instantaneous field minimum never enters the trapping region. Such Time Orbiting Potential (TOP) scheme was indeed used to achieved the first Bose-Einstein condensate [3].

The present toroidal trap design uses the same principle, the atoms feel only the averaged magnetic field, and the resulting potential in shown in Fig. 6.4.

6.1.4 Zero-shifting quadrupole field

As outlined in the previous section, the passing of the magnetic field zero through the atomic cloud induces spin-flip losses. This is clearly the case for the inductive ring trap, as can be seen in Fig. 6.4, the minimum of the average potential forming in the plane of the ring. To avoid these losses, we propose to use an additional static, quadrupole field that shifts the zeros away from the trap formation region. This field can be generated from a pair of coils in anti-Helmholtz configuration, as depicted in Fig. 6.1(a), centred on the induced ring. The following simulations use a quadrupole field $\vec{B}_{\mathrm{quad}}(r,z) = B_{\mathrm{quad0}}(-\frac{r}{2}\vec{\mathbf{e}}_r + z\vec{\mathbf{e}}_z)$ with a gradient $B_{\mathrm{quad0}} =$ 25 G/cm. The trajectory of the magnetic field zero in time is shown in Fig. 6.5. During one half period, the magnetic zero circle spans the region above the ring

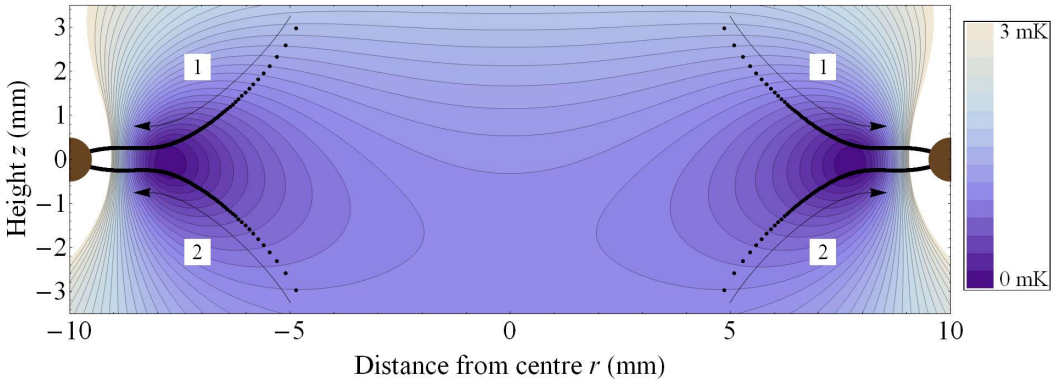

Figure 6.5: Averaged potential in a cut through the induced ring with a static quadrupole field, including gravity. The potential is expressed in Kelvin and is relative to the value at the trap minimum. Black dots indicate the instantaneous magnetic zero over each half period and the arrows show their direction of motion as time increases.

plane (1 in Fig. 6.5), and the lower region (2) during the second half period. As a result, the time averaged minimum still forms in the plane of the ring, but this point never sees a zero magnetic field. For a horizontally orientated ring, the minimum is shifted down because of gravity, and Fig. 6.5 shows this complete potential. The toroidal trap has a radius of 7.8 mm and forms about 0.1 mm below the ring plane. The instantaneous magnetic field at the trap position is always larger than 6.6 G and the Larmor frequency is always at least two orders

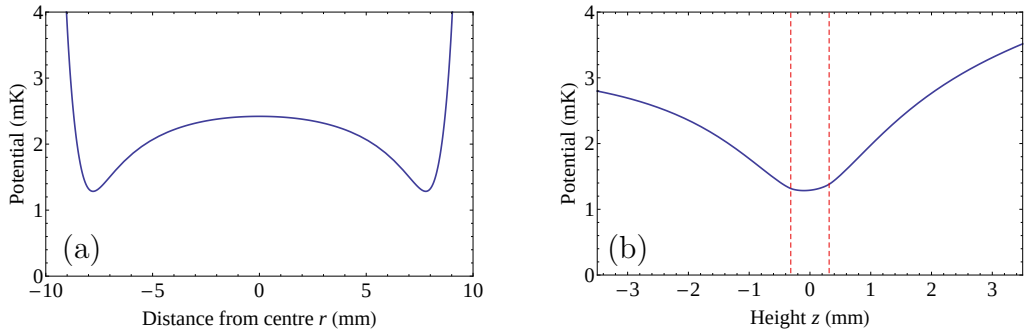

Figure 6.6: Radial (a) and axial (b) potentials around the trap centre. The tilt in (b) indicates the effect of gravity and the two red dashed lines show the effective boundaries of the trapping region, where the vanishing magnetic field induces Majorana losses.

of magnitude larger that the rate of change of the magnetic field at this position. Thus Majorana losses can be neglected, according to Eqn. 6.12. For ^{87}Rb atoms, radial and axial trap frequencies in the average potential are respectively 59 Hz and 51 Hz. For temperatures higher than 1.1 mK, atoms are not confined in a toroidal potential since they reach the ring centre. The maximum trapped temperature is 1.8 mK, atoms hotter than this fall due to gravity. Radial and axial potentials around the trap centre are depicted in Fig 6.6. The effective trapping region is vertically limited, however, by the zero magnetic field passing every period above and below the trap centre. Since gravity shifts the trap position downwards, the lower zero passing point will be predominant in non-adiabatic losses and the effective maximally trapped temperature is 31 μK, but this might be raised to above 100 μK by increasing the quadrupole field amplitude.

6.1.5 Ring scaling

The process of scaling down the ring to stydy e.g. superfluidity in quantum gases, is not as straightforward as one could think at first glance. In the following we will assume a ring with constant geometry, that is the ratio $r_{\text{ring}}/r_{\text{wire}} = 20$ is kept constant. For a 1 cm ring radius, we are well in a time-averaged regime, since $\omega_{\text{trap}} \ll \omega_{\text{drive}} \ll \Omega_0$, where ω_{trap} and ω_{drive} denote respectively the trapping and driving frequencies. One problem is that these three frequencies do not follow the same scaling law with ring radius reduction. Indeed, we found that these parameters vary as

$$\begin{aligned} \omega_{\text{trap}} &\propto \frac{\sqrt{B_0}}{r_{\text{ring}}}, \\ \omega_{\text{drive}} &\propto \frac{1}{r_{\text{ring}}^2}, \\ \Omega_0 &\propto r_{\text{ring}}, \end{aligned} \tag{6.13}$$

where a constant quadrupole field has been assumed in addition. The variation of these three frequencies as the ring is scaled down is shown on the numerical simulations of Fig. 6.7. The striking feature is the dramatic reduction of the quantity $\Omega_0/\omega_{\text{drive}}$, such that these two frequencies become of similar importance

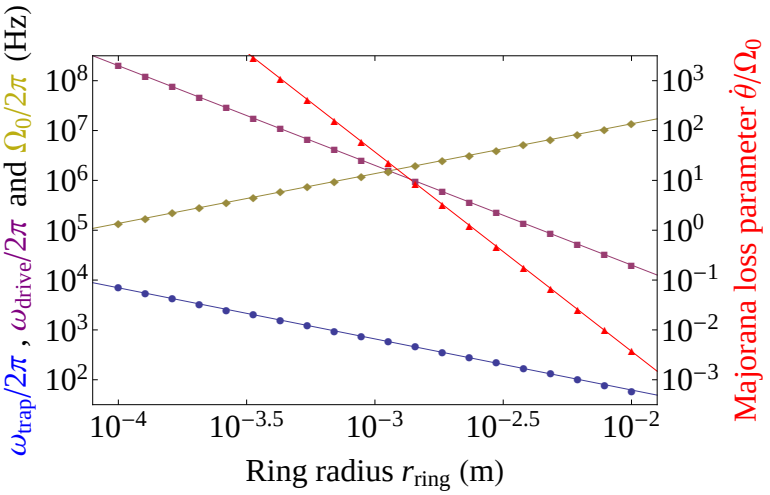

Figure 6.7: Scaling of the trapping (ω_{trap}, blue circles), driving (ω_{drive}, purple squares) and Larmor (Ω_0, gold diamonds) frequencies with ring size reduction. The ac and quadrupole field amplitude are kept constant, along with the ring geometry. The red triangle show the variation of the Majorana loss parameter.

at about $r_{\text{ring}} \approx 1$ mm. In these conditions, the trap can not be considered as time-averaged anymore, since the atomic spins can't follow adiabatically the variation of the local magnetic field. This translates in an large increase of the Majorana losses, shown as well on Fig. 6.7 and we found that the ratio $\dot{\theta}/\Omega_0$ scales as $\dot{\theta}/\Omega_0 \propto B_0\, r_{\text{ring}}^{-4}$. One could think of reducing the driving field amplitude B_0 accordingly to keep the Majorana losses low, but this yields a great decrease in the trapping frequencies, as seen on Eqn. 6.13, resulting in a very loose trap. Rather than trying to stay in a time-averaged regime, the fact that the field and Larmor frequencies becomes of the same order of magnitude favour a dressed state approach of the problem, which is discuss in the next section.

6.2 Time averaged dressed potential for micro-fabricated toroidal trap

Given the difficulties to maintain the adiabatic spin following with large trap frequencies as the ring is scaled down, we present here a way to create a toroidal potential, recycling the same magnetically induced ring principle, but with the

dressed atom approach. Most of the novel small size toroidal traps use these so-called dressed states (or adiabatic) potentials as they allow very flexible trap geometries with large trapping frequencies. It should be noted that the work presented in this thesis is still ongoing, and thus does not give a comprehensive investigation of the whole field of parameters. It focuses on a set of parameters that gives sensible results, where thermal atoms can be trapped in a annular potential, in the limit of the approximations made.

6.2.1 Theory of the dressed atom and application to atom trapping

The dressed atom theory, developed by Claude Cohen-Tannoudji in the 1970's [87], allows one to model the interaction of an atom in a strong near-resonant electromagnetic field. This section gives a short introduction to this theory and reviews the different toroidal traps using dressed potentials.

Let us consider the simple case of a half spin particle of Hamiltonian

$$\hat{H}_{\mathrm{A}} = \hbar(\omega_b|b\rangle\langle b| + \omega_a|a\rangle\langle a|), \tag{6.14}$$

where $\omega_0 = \omega_b - \omega_a > 0$ is defined here as the energy difference between the two states. This atom interacts with a electromagnetic field of Hamiltonian

$$\hat{H}_{\mathrm{F}} = \hbar\omega(\hat{a}^\dagger\hat{a} + 1/2), \tag{6.15}$$

where $\hat{a}^\dagger$ and $\hat{a}$ are respectively the operators that create and annihilate a photon at energy ω. The operators act on a photon state $|n\rangle$, comprising n photons, as follows:

$$\begin{aligned} \hat{a}|n\rangle &= \sqrt{n}|n-1\rangle, \\ \hat{a}^\dagger|n\rangle &= \sqrt{n+1}|n+1\rangle, \end{aligned} \tag{6.16}$$

and $\hat{a}|0\rangle = 0$.

The coupling between the atom and the field is first omitted. The total field + atom Hamiltonian cannot be easily interpreted since the two Hamiltonians have

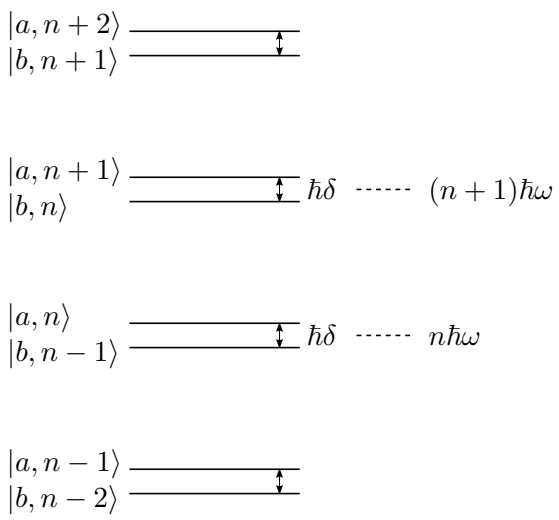

Figure 6.8: Energy structure of the uncoupled states for a positive detuning $\delta > 0$.

different dimensions, the field having an infinite number of modes. However, we can look at the energies of the complete system and we introduce the eigenbasis of the atom + field Hamiltonian

$$\{|a, n\rangle, |b, n\rangle \quad n \in \mathbb{N}\}, \tag{6.17}$$

where $|a, n\rangle = |a\rangle \otimes |n\rangle$. We can easily calculate the energies of the uncoupled system. For example, we take the two states $|a, n\rangle$ and $|b, n-1\rangle$:

$$\begin{aligned} E_{a,n} &= n\hbar\omega + \frac{\hbar}{2}\delta, \\ E_{b,n-1} &= n\hbar\omega - \frac{\hbar}{2}\delta, \end{aligned} \tag{6.18}$$

where $\delta = \omega - \omega_0$ is the detuning between the atomic transition and the field energy. For small detunings compared to the field frequency, that is $|\delta| \ll \omega_0 \sim \omega$, the energy structure of the system looks like the one in Fig. 6.8. The states are organised in doublets with energy separation $\hbar\delta$.

So far we have neglected to coupling between states, which is described by the operator [85]

$$\hat{H}_{\mathrm{C}} = g(\hat{S}_+ + \hat{S}_-)(\hat{a}^\dagger + \hat{a}), \tag{6.19}$$

where g is a coupling constant and $\hat{S}_+$ and $\hat{S}_-$ are the ladder operators. The operators pass from one spin state to the next or previous one. In the more global case of a system with angular momentum J, these are defined as [86]

$$\hat{J}_\pm|J, m_J\rangle = \sqrt{J(J+1) - m_J(m_J \pm 1)}|J, m_J \pm 1\rangle, \tag{6.20}$$

with $\hat{J}_+|J, J\rangle = 0$, $\hat{J}_-|J, -J\rangle = 0$ and where m_J is the component of the angular momentum along the quantisation axis. For the half spin case considered here, these operators act on the states $|a\rangle$ and $|b\rangle$ such that $\hat{S}_+|a\rangle = |b\rangle$ and $\hat{S}_-|b\rangle = |a\rangle$. Each state $|a, n\rangle$ couples to the two states $|b, n+1\rangle$ and $|b, n-1\rangle$:

$$\begin{aligned} \langle a, n|\hat{H}_C|b, n-1\rangle &= g\sqrt{n}, \\ \langle a, n|\hat{H}_C|b, n+1\rangle &= g\sqrt{n+1}. \end{aligned} \tag{6.21}$$

One can show, using second order perturbation analysis [85], the energy shift of state $|a, n\rangle$ due to the coupling with state $|b, n_1\rangle$, where $n_1 = n \pm 1$, goes as

$$\Delta E_{|b,n_1\rangle \to |a,n\rangle} \propto \frac{W^2}{E_{|b,n_1\rangle} - E_{|a,n\rangle}}. \tag{6.22}$$

Here, W is the coupling between the two states and $E_{|a,n\rangle}$ and $E_{|b,n_1\rangle}$ are the energies of the uncoupled states $|a, n\rangle$ and $|b, n_1\rangle$. Therefore, the energy shift caused by the coupling with state $|b, n+1\rangle$ is negligible compared to the one caused by $|b, n-1\rangle$:

$$\Delta E_{|b,n+1\rangle \to |a,n\rangle} \propto \frac{g^2 n}{2\hbar\omega} \ll \frac{g^2 n}{\hbar\delta} \propto \Delta E_{|b,n-1\rangle \to |a,n\rangle}, \tag{6.23}$$

where the assumption $n \gg 1$, corresponding to a strong field, has been done. The above expression is valid as long as the condition $\delta \ll \omega_0$ is verified. We can now neglect the effect of the terms $\hat{S_-}\hat{a}$ and $\hat{S}_+\hat{a}^\dagger$ in the interaction Hamiltonian of Eqn. 6.19, this is the rotating wave approximation that keeps only near resonant terms.

Now the field and interaction Hamiltonians can be reduced to a two dimension space only. We consider the total Hamiltonian for the doublet $|a, n\rangle$ and $|b, n-1\rangle$

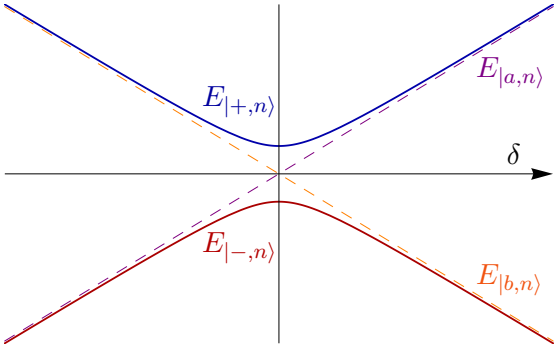

Figure 6.9: Energy difference of the uncoupled and dressed states as a function of detuning. The on-resonance energy difference is $\hbar\Omega_1$.

$$\hat{H}_T = \hat{H}_A + \hat{H}_F + \hat{H}_C = n\hbar w\mathbb{I}_2 + \frac{\hbar}{2}\begin{pmatrix} \delta & \Omega_1 \\ \Omega_1 & -\delta \end{pmatrix}, \tag{6.24}$$

where the Rabi frequency is defined as $\Omega_1 = 2g\sqrt{n}/\hbar$ and $\mathbb{I}_2$ is the two dimension identity matrix. Diagonalisation of this Hamiltonian give the following dressed states:

$$\begin{aligned} |+,n\rangle &= \sin\frac{\theta}{2}|a,n\rangle + \cos\frac{\theta}{2}|b,n-1\rangle, \\ |-,n\rangle &= \cos\frac{\theta}{2}|a,n\rangle - \sin\frac{\theta}{2}|b,n-1\rangle, \end{aligned} \tag{6.25}$$

where the angle θ is defined as $\tan\theta = -\Omega_1/\delta$ and represents the orientation of the dressed states compared to the uncoupled ones. These dressed states have eigenenergies

$$\Delta E_{|\pm,n\rangle} = n\hbar\omega \pm \sqrt{\delta^2 + \Omega_1}. \tag{6.26}$$

The levels in each doublet part from each other, due to the coupling, as depicted in Fig. 6.9. As the detuning (or equivalently the angle θ) is varied from resonance, the dressed states separate with an energy difference given by Eqn. 6.26. Varying δ is equivalent to varying the angle θ; on resonance ($\delta = 0$ or $\theta = \pi/2$), the levels are separated by $\hbar\Omega_1$ and the dressed states comprise a balanced superposition of the uncoupled states. For $\delta \to \infty$ (or $\theta = \pi$), the dressed states $|+,n\rangle$ and $|-,n\rangle$ respectively reduce to the uncoupled states $|a,n\rangle$ and $|b,n-1\rangle$, and symmetrically for $\delta \to -\infty$ (or $\theta = 0$).

6.2 Time averaged dressed potential for micro-fabricated toroidal trap

Oliver Zobay and Barry Garraway proposed a novel way to trap atoms [49, 176], using a Radio Frequency (RF) field to create a coupling between the different magnetic sub-levels $|F, m_F\rangle$ of an hyperfine state with total angular momentum F. First, a static magnetic field is used to separate the different sub-levels. The spin of an atom in a the magnetic level m_F processes around the local magnetic field at the Larmor frequency given by Eqn. 6.11 and the energy difference between each sub-level is $\Delta E_{m_F} = g_F \mu_B |\vec{B}|$. Assume now a near resonant RF field (i.e. the detuning $\delta = \omega_{RF} - \Omega_0$ between the energy of a photon with energy ω_{RF} and the Larmor frequency is small compared with the Larmor frequency). In this case, applying the rotating wave approximation means that an atom in a m_F sub-level can only interact with one circular polarisation of the RF field. This is found by projecting the RF total polarisation along the local magnetic field –which acts as a quantisation axis– and decomposition in terms of σ^+, σ^- and π components, in a similar way to the one used in Sec. 4.2.1. The component π of the RF polarisation along the static field doesn't contribute to coupling between magnetic sub-levels and can therefore be neglected. We define the Rabi coupling as

$$\Omega_{RF} = g_F \mu_B B_{RF} / \hbar, \tag{6.27}$$

where B_{RF} is the amplitude of the component of the RF field that rotates in the same direction as the spin in the magnetic sub-level considered. The energy shift of an atom initially in the sub-level m_F is then given by [177]

$$\Delta E_{m_F}(\vec{r}) = m_F \hbar \sqrt{\delta^2(\vec{r}) + \Omega_{RF}^2(\vec{r})}. \tag{6.28}$$

One can then create a minimum of the potential for low field seeking states by either creating a local minimum of the detuning $\delta(\vec{r})$ or the Rabi coupling $\Omega_{RF}(\vec{r})$.

The proposal of Zobay and Garraway consisted of a homogenous RF field, while the Larmor frequency is position-dependent. This is easily achieved with simple static magnetic such as the ones obtained with quadrupole or Ioffe-Pritchard coils. The local trap minimum forms where the RF field frequency becomes resonant with the local Larmor frequency. For example, in the case of quadrupole coils, the trap minimum corresponds to an iso-surface of magnetic field and looks like an "egg shell" potential. It is assumed here that the coupling stays constant

in space. However, the angle of the local magnetic field varies along the potential minimum, and so does the Rabi coupling since the polarisation projection changes. This leads to "holes" in the potential. It turns out that such potential offers very high trapping frequencies in the direction orthogonal to the shell and therefore allow one to strongly confine atoms and achieve, for instance, 2D Bose-Einstein condensation. RF dressed potentials were experimentally demonstrated by Colombe *et al.* [178] to get such an "egg shell" potential. They were then successfully used on surface atom chip to coherently split and recombine BECs [42, 123] or as way to create state-dependent potentials [179] for quantum metrology [180].

Very recently, there have been several new proposals and realisation of toroidal ring traps using RF dressed state potentials, benefiting from the flexibility and the ease of implementation of the principle. One can with a cylindrically symmetrical "egg shell" and use a dipole trap from either an optical lattice [40] or a light sheet [45] to confine the atoms in the third dimension. Alternatively, the "egg shell" can be quickly moved in space and atoms are trapped in a Time Averaged Adiabatic Potential (TAAP) [44]. This technique, recently demonstrated [181], is very versatile, given the wide variety of trapping geometries it offers, other than a ring potential. Using circular current loops, one can make a quadrupole ring and add the coupling with an axially symmetric RF field [43]. On atom chips, the combination of a quadrupole field with a spatially varying Rabi coupling from neighbouring wires is an other way of creating a micro size ring trap [41].

6.2.2 Horizontal "static" quantisation field

The rest of this chapter presents ongoing work on a way to create a micro-size ring potential, recycling the induced ring described previously, in a dressed-atom approach. It has been shown that there are strong limitations on the scaling down of the time averaged potential of Sec. 6.1, due to adiabatic losses with size reduction and the necessity to maintain relatively high trapping frequencies. In order to "dress" the ring, there are two possibilities: one can think of either using the total alternating magnetic field as the quantisation or the dressing field. The first option is experimentally demanding, it implies an extra dressing field

at a frequency much higher than the ring driving frequency. The other way, investigated in this work, is easier to implement, it requires a static (or quasi-static, as will be outlined later) homogenous magnetic field, dressed by the total field $B_{\mathrm{ac}} + B_{\mathrm{ring}}$. Thus, in the following, this alternating field is called the RF dressing field. The scheme supposes a quasi-static homogenous magnetic field $\vec{B}_{\mathrm{qs}}$, oriented in the plane of the ring, as depicted in Fig. 6.10. We will see that, due to the spatial variation of the amplitude of the RF field, this configuration leads to the potential of Fig. 6.10, which is not cylindrically symmetric. By rotating $\vec{B}_{\mathrm{qs}}$ around the ring axis, one can average this toroidal potential to get a smooth annular ring potential. It is worth noting that the completely symmetric situation with a vertical static field doesn't work. Indeed, all the RF magnetic field vectors are aligned vertically in the plane of the ring and along its axis, and therefore there is no couling at these position and atoms fall along the ring axis with gravity.

Regarding the dressing field, what matters is the amplitude of the circularly polarised components, after projection onto the local static field. It is thus useful to drop the time dependence and adopt Jones' formalism [182], as one would

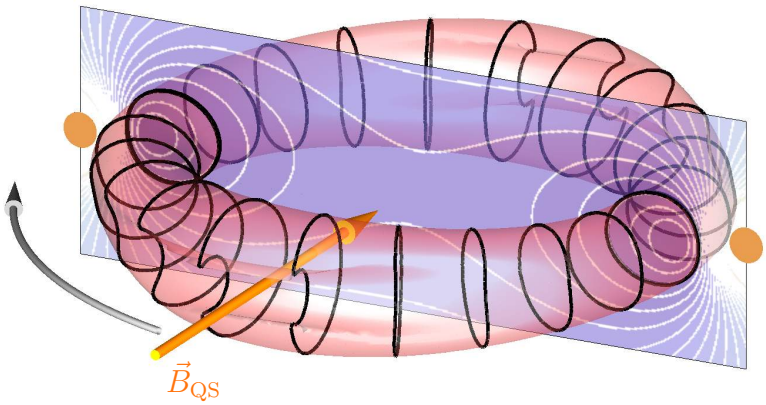

Figure 6.10: Schematic showing the horizontal quasi-static magnetic field $\vec{B}_{\mathrm{qs}}$, the potential in a plane through the ring orthogonal to $\vec{B}_{\mathrm{qs}}$ and the 3D 40 μK iso-potential surface. The ring is not shown, for clarity, but its position is indicated by the brown disks.

do to handle polarisation of electromagnetic wave in the optical domain. Using Laplace transforms [183], one can first rewrite the ring current, given by Eqn. 6.6, as

$$I_{\mathrm{ring}}(\Omega_{\mathrm{r}}) = -I_{\max}\frac{i\Omega_{\mathrm{r}}}{1+i\Omega_{\mathrm{r}}}, \tag{6.29}$$

which is now a complex function of the normalised frequency Ω_{r} only. One can then redefine the equations for the inducing and emitted fields $\vec{B}_{\mathrm{ac}}(r,z,\Omega_{\mathrm{r}})$ and $\vec{B}_{\mathrm{ring}}(r,z,\Omega_{\mathrm{r}})$. In a plane taken orthogonal to the ring and including the ring axis, the total RF field is, as previously, entirely contained in the plane and reads

$$\vec{B}_{\mathrm{tot}} = B_r\ e^{i\delta_r}\ \vec{\mathbf{e}}_r + B_z\ e^{i\delta_z}\ \vec{\mathbf{e}}_z. \tag{6.30}$$

The radial and axial components have complex values, corresponding to their amplitudes B_r and B_z, and relative phases δ_r and δ_z. The frequency and spatial dependence have been dropped for clarity. The quasi-static field $\vec{B}_{\mathrm{qs}}$ is expressed as

$$\vec{B}_{\mathrm{qs}} = B_{\mathrm{qs0}}\ \left(\sin\varphi\ \vec{\mathbf{e}}_r + \cos\varphi\ \vec{\mathbf{e}}_\perp\right), \tag{6.31}$$

where φ is the angle of the quasi-static field in the plane of the ring, and $\vec{\mathbf{e}}_\perp$ is a unit vector such that $\{\vec{\mathbf{e}}_r, \vec{\mathbf{e}}_z, \vec{\mathbf{e}}_\perp\}$ forms an orthonormal basis. It should be noted that rotating either the plane we're looking at or the quasi-static field results to the same. Here, we set the plane and change the orientation angle φ. By varying this angle between 0 and 2π, one can reconstitute the total three-dimensional potential.

To calculate the amount of RF field that contributes to coupling, one has to find the amplitude in the correct circular polarisation relative to the quasi-static field. The total RF field of Eqn. 6.30 is first projected into the new orthonormal basis $\{\vec{\mathbf{e}}_{\perp 1}, \vec{\mathbf{e}}_{\perp 2}, \vec{\mathbf{e}}_\parallel\}$ given by

$$\begin{aligned}
\vec{\mathbf{e}}_{\perp 1} &= \cos\varphi\ \vec{\mathbf{e}}_r - \sin\varphi\ \vec{\mathbf{e}}_\perp\ , \\
\vec{\mathbf{e}}_{\perp 2} &= \vec{\mathbf{e}}_z\ , \\
\vec{\mathbf{e}}_\parallel &= \vec{B}_{\mathrm{qs}}/B_{\mathrm{qs0}}\ .
\end{aligned} \tag{6.32}$$

The component of the RF field along the quasi-static quantisation field, given by

$\vec{B}_{\rm tot} \cdot \vec{\mathbf{e}}_{\parallel}$, does not contribute to coupling between sub-level magnetic states. The effective RF field is in the plane orthogonal to $\vec{B}_{\rm qs}$, and simply reads

$$\vec{B}_{\rm tot}^{\rm eff} = B_r \cos\varphi \; e^{i\delta_r} \; \vec{\mathbf{e}}_{\perp 1} + B_z \; e^{i\delta_z} \; \vec{\mathbf{e}}_{\perp 2}. \tag{6.33}$$

This is the Jones' vector that describes the RF polarisation in the frame rotated by the azimuthal angle φ. One can show that the amplitude of the circular components relative to the quantisation axis is

$$B_s = \frac{1}{2}\sqrt{B_r^2 \cos^2\varphi + B_z^2 + 2sB_rB_z \cos\varphi \;\; \sin(\delta_r - \delta_z)} \; , \tag{6.34}$$

where $s = \pm 1$ is the handedness of the polarisation, $s = 1$ corresponding to the right polarisation (clockwise rotation when looking in the direction of the quasi-static field) and *vice versa*. In the case of ^{87}Rb atoms in the $|F = 2, m_F = 2\rangle$ state, and in the limit where the rotating wave approximation is valid, we are only interested in the right polarisation. This spatially varying amplitude of the right polarisation is simply referred to as $B_{\rm RF}(r, z)$, and leads to a spatially varying Rabi coupling, given by Eqn. 6.27 and recalled here:

$$\Omega_{\rm RF}(r, z) = g_F \mu_{\rm B} B_{\rm RF}(r, z)/\hbar. \tag{6.35}$$

The $\{r, z\}$ coordinates have been inserted again to emphasise the spatial dependence. Since the quasi-static magnetic field is homogenous, the Larmor frequency $\Omega_0 = g_F m_F \mu_{\rm B} B_{\rm qs0}/\hbar$ and the detuning $\delta = \omega - \Omega_0$ are also spatially constant. The trapping potential is then given by Eqn. 6.28 and reads

$$U(r, z) = m_F \hbar \sqrt{\delta^2 + \Omega_{\rm RF}^2(r, z)}. \tag{6.36}$$

For the purpose of this work, we assume a copper ring of radius $r_{\rm ring} = 400$ μm and wire radius $r_{\rm wire}$=20 μm. The natural cut-off frequency of such ring is $\omega_0/2\pi = 3.2$ MHz. The driving frequency is chosen to be $\omega/2\pi = 40$ MHz, such that $\Omega_{\rm r} = 12.3$, and the amplitude of the RF field is $B_0 = 8$ G. The quasi-static field amplitude is chosen such that the detuning between the RF and the Larmor frequencies (here constant in space) is $\delta = -1$ MHz, and thus $B_{\rm qs0} \approx 29.3$ G (or

$\Omega_0/2\pi = 41$ MHz). With this value of the detuning, the condition $\delta \ll \omega \sim \Omega_0$ is verified and the rotating wave approximation is valid. The choice of the values of the RF amplitude, RF frequency and detuning will be discussed later on. For the chosen driving frequency, the skin depth is $\delta_{\mathrm{sd}} \approx 10.8$ μm$\sim r_{\mathrm{wire}}/2$ and thus the current density is higher near the ring wire surface than at the centre of the conductor. Strictly speaking, the expressions for the resistance and inductance given by Eqns. 6.4 and 6.5 are no longer valid. They are however still used for the preliminary results of the present work, as the deviations are expected to have a small impact, but a full treatment will be eventually required before any experimental implementation.

In the following we focus on two configurations that illustrate well the working principle: the quasi-static field being orthogonal to the plane of interest ($\varphi = 0$) or contained in it ($\varphi = \pi/2$). A sketch of the overall potential, with $\vec{B}_{\mathrm{qs}}$ doing a complete turn, can be see in Fig. 6.10.

Quantisation field orthogonal to the plane

We set the orientation angle as $\varphi = 0$, such that the quasi-static field is orthogonal to the plane, as shown by the orange arrow in Fig. 6.11. There are two minima of the RF amplitude, which consequently lead to two potential minima, and they

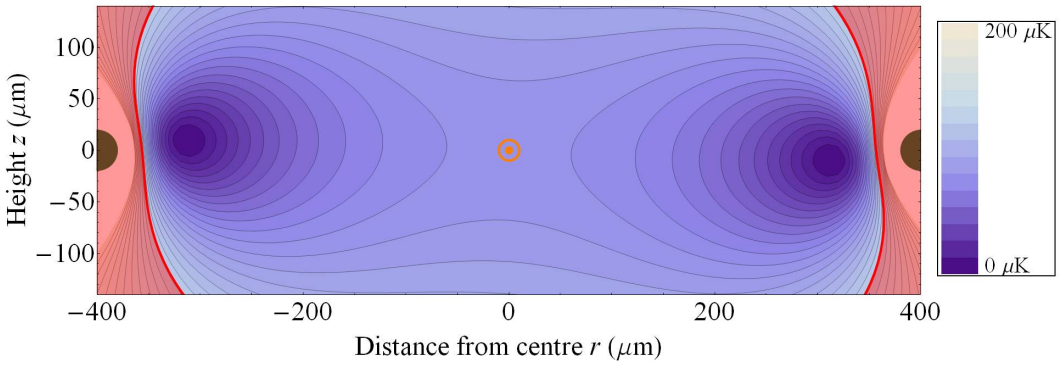

Figure 6.11: Potential in a cut through the induced ring with the quasi-static magnetic field orthogonal to the plane (shown by the orange arrow). The potential is expressed in Kelvin and is relative to the minimum. The red overlayed part shows the region where $\Omega_{\mathrm{RF}}(r, z) > \Omega_0/20$.

are clearly visible Fig. 6.11. These points correspond to an RF field circularly polarised with the incorrect handedness. There are two other points (not shown on graph), where the RF is also purely circularly polarised but with the correct handedness. They are symmetrically positioned compared to the potential minima of Fig. 6.11, taking the ring axis as a symmetry axis.

In this work, we investigate dressed state potentials in the adiabatic regime which is defined by the following criterion [184]:

$$\frac{\Omega_0^2}{\omega} \gg \Omega_{\mathrm{RF}}(r,z). \tag{6.37}$$

In the limit of $\Omega_0 \sim \omega$ of the rotating wave approximation, this reduces to the condition $\Omega_0 \gg \Omega_{\mathrm{RF}}$. It means that the RF field amplitude is considered as a small perturbation of the static magnetic field. It should be noted that atom manipulation in dressed states regimes where this criterion is no longer true [185, 186] is also possible. The red color overlay in Fig. 6.11 shows the region of space where $\Omega_{\mathrm{RF}} > \Omega_0/20$, given for information, and we will discuss this later on for the atoms in the time averaged potential.

It has been said previously that the two potential minima of Fig. 6.11 correspond to a purely circularised RF in the incorrect handedness. This means that

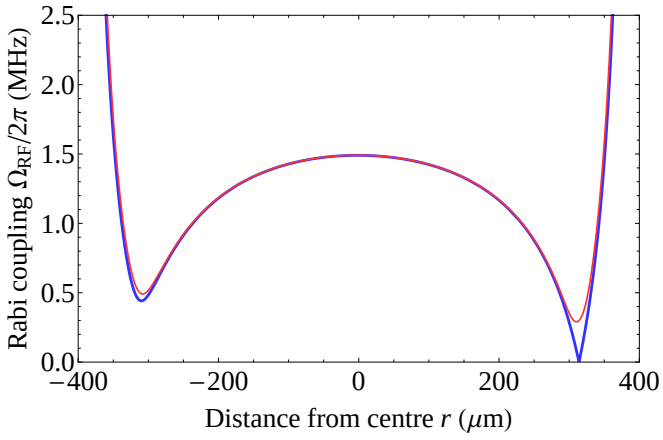

Figure 6.12: Spatial variation of the Rabi coupling at the height of the rightmost minimum for an infitesimaly small (blue) and finite size wire with radius $r_{\mathrm{wire}} = 20$ μm (red).

there is a vanishing coupling at these points, which may lead to "holes" where atoms can leak outside the trap. The horizontal variation of the Rabi coupling at the position of the rightmost minimum is shown in Fig. 6.12. These zero-coupling points happen only in the case of an infitesimally small wire radius, as described by Eqn. 6.8. This configuration is shown by the blue curve in Fig. 6.12. If one assumes a finite size wire and integrate the field generated over the wire area, this leads to a non-zero minimum (red curve in Fig. 6.12) of ∼290 kHz, thus obviating any atomic losses at these points. The simulations including the finite size wire give results that agree to better than 5 % with the simple model regarding the trap frequencies in the time averaged potential. Therefore, numerical results are given assuming the finite wire model but potential graphs are made using the simplier wire model, due to sensibly lower computational times required.

Quantisation field contained in the plane

We look now at the case where the quasi-static in contained in the plane, that is $\varphi = \pi/2$, as depicted by the orange arrow in Fig. 6.13. In the rotated basis $\{\vec{\mathbf{e}}_{\perp 1}, \vec{\mathbf{e}}_{\perp 2}, \vec{\mathbf{e}}_{\parallel}\}$, the RF field has no component along $\vec{\mathbf{e}}_{\perp 1}$, since it is entirely contained in the plane. Only the axial component along $\vec{\mathbf{e}}_{\perp 2} = \vec{\mathbf{e}}_z$ matters, and this means that the quasi-static magnetic field "sees" only a linearly polarised RF.

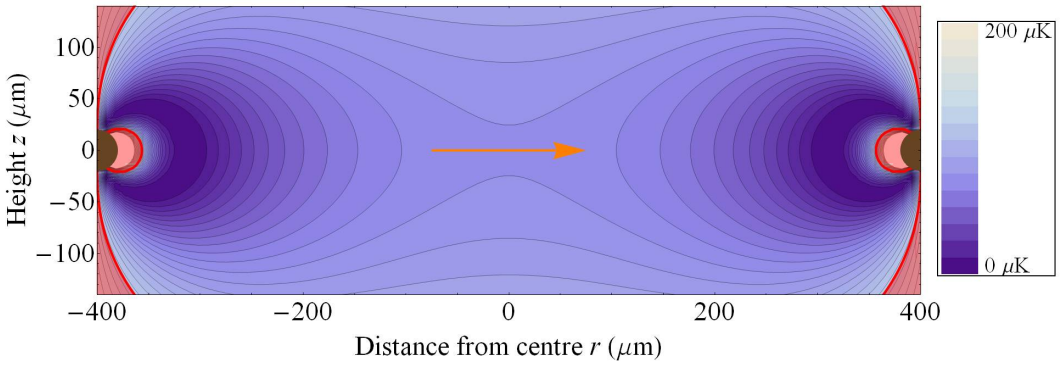

Figure 6.13: Potential in a cut through the induced ring with the quasi-static magnetic field contained in the plane (shown by the orange arrow). The potential is expressed in Kelvin and is relative to the minimum. The red overlayed part shows the region where $\Omega_{\mathrm{RF}}(r, z) > \Omega_0/20$.

This leads to the potential of Fig. 6.13, which is symmetric relative to the ring axis. In this case, there are no zero coupling points (even when assuming an infinitesimally small wire) and the Rabi frequency is roughly constant at ∼300 kHz along the crescent shape that defines that potential minimum.

6.2.3 Time averaged dressed potential

The 3D potential for a given direction of the quasi-static field is shown in Fig. 6.10. One can clearly see that it is not a smooth annular shape. By rotating the quasi-static field over time (hence the name quasi-static!) around the ring axis at a frequency much larger than the trapping frequencies, one gets the toroidal ring potential which cross section is shown in Fig. 6.14. For a field rotating or oscillating in the plane of the ring, there is no magnetic flux crossing the ring area and thus no extra induced current that could somehow perturb the RF magnetic field. The trapping minimum is located around a circle of radius 310 μm and shifted down by 4.5 μK relative to the plane of the induced ring because of gravity. Atoms hotter than 110 μK fall due to gravity but, since such atoms span regions where the condition Eqn. 6.37 that defines the adiabatic regime is violated, a different approach would have to be used. Atoms reach the

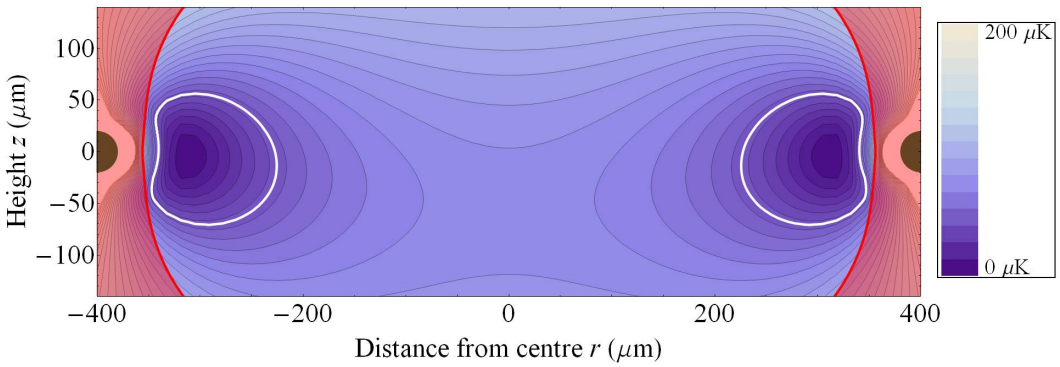

Figure 6.14: Cross section of the time averaged dressed potential including gravity. The potential is expressed in Kelvin and is relative to the minimum. The white line shows the 40 μK iso-potential. The red overlayed part shows the region where $\Omega_{\mathrm{RF}}(r, z)$ is larger than $\Omega_0/20$ at any time during the rotation of the quasi-static field.

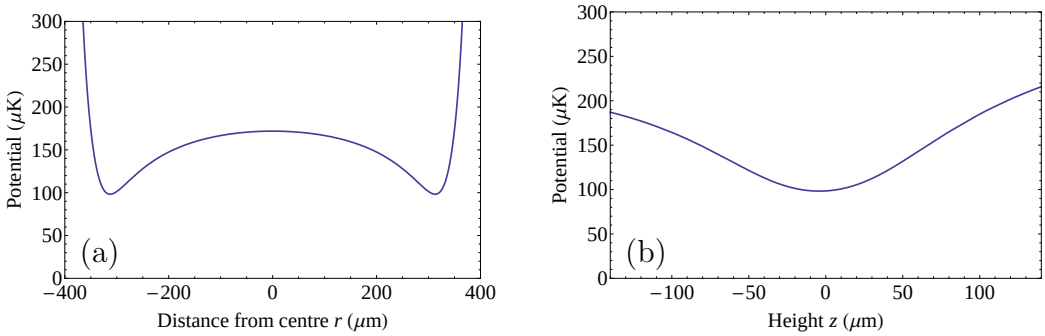

Figure 6.15: Radial (a) and axial (b) potentials around the trap centre. The tilt in (b) indicates the effect of gravity.

centre of the ring for temperatures larger than 70 μK and thus are no longer confined in the toroidal trap. Trapping frequencies are respectively $\omega_r = 335$ Hz and $\omega_z = 234$ Hz along the radial and axial directions. The potentials in these two directions and centrered on the trap minimum are shown in Fig. 6.15. It should be noted that the potential can be considered as harmonic only within a small region that extends a few μm around the trapping minimum, as can be seen in Fig. 6.15, and this is particularly true in the radial direction. Thus, only atoms with very low temperatures, e.g. typically quantum gases, are effectively oscillating at the given trapping frequencies.

For an RF frequency corresponding to the same normalised frequency ($\Omega_\mathrm{r} = 3.9$) as for the time averaged trap of the first section, it was observed that the time averaged dressed potential was axially very flat, leading to small trapping frequencies. Tighter traps are achieved with much higher normalised frequencies and the current parameter ($\omega/2\pi = 40$ MHz or $\Omega_\mathrm{r} = 12.3$) was chosen to offer a tight axial confinement but low enough regarding experimental complication to drive fields at very large RF frequencies.

6.2.4 Landau-Zener losses in the averaged potential

Atoms in the dressed potential are in states described by Eqn. 6.21. They see a different potential as time goes by, either due to their own atomic motion or to the time rotating magnetic field. This can lead to losses as the dressed state can be projected into the high seeking state if the parameters for the detuning

δ or coupling Ω_{RF} vary too quickly. Such Landau-Zener losses are analogous to the Majorana loss mechanism that happens in static magnetic fields and one can show [177, 187] that the condition that minimises these losses is given by

$$|\Omega_{\mathrm{RF}}\ \dot{\delta} - \delta\ \dot{\Omega}_{\mathrm{RF}}| \ll \left(\delta^2 + \Omega_{\mathrm{RF}}^2\right)^{3/2}. \tag{6.38}$$

In our case, since the detuning is kept constant, $\dot{\delta} = 0$ but the coupling changes with space and time. The above equation thus reduces to

$$|\delta\ \dot{\Omega}_{\mathrm{RF}}| \ll \left(\delta^2 + \Omega_{\mathrm{RF}}^2\right)^{3/2}. \tag{6.39}$$

The time derivative of the Rabi coupling can be expressed, in three dimensions, as

$$\dot{\Omega}_{\mathrm{RF}} = \vec{\nabla}\Omega_{\mathrm{RF}} \cdot \vec{v}_{\mathrm{atom}}\ , \tag{6.40}$$

where $\vec{\nabla}$ denotes the gradient operator and $\vec{v}_{\mathrm{atom}}$ is the atomic velocity in the potential. The worst case scenario is reached for maximal values of $\vec{\nabla}\Omega_{\mathrm{RF}}$ and $\vec{v}_{\mathrm{atom}}$, and thus we can investigate the case of $\dot{\Omega}_{\mathrm{RF}}^{\mathrm{max}} = |\vec{\nabla}\Omega_{\mathrm{RF}}| \times |\vec{v}_{\mathrm{atom}}|$. The quantity $|\vec{v}_{\mathrm{atom}}|$ results either from the thermal velocity, given by Eqn. 4.2, in the time averaged potential, or from the variation of the potential itself as the quantisation magnetic field is spinned around the ring axis. In this last case, the atomic velocity is simply given by $|\vec{v}_{\mathrm{atom}}| = r_{\mathrm{trap}} \times \omega_{\mathrm{qs}}$ with $r_{\mathrm{trap}} = 310\ \mu$m and where ω_{qs} is the rotation frequency of the quasi-static magnetic field. The azimuthal variation of the Landau-Zener loss parameter $|\delta\ \dot{\Omega}_{\mathrm{RF}}|/\left(\delta^2 + \Omega_{\mathrm{RF}}^2\right)^{3/2}$ is shown in Fig. 6.16 in the two cases taken separately. We assume here that atoms are located at the trap minimum. The blue curve corresponds to an ^{87}Rb atom at 40 μK in the totally static dressed potential, while the case of an atom at rest seeing the fast variation of the Rabi coupling due to the quantisation field rotation is depicted by the red curve. Here we set the rotation frequency to $\omega_{\mathrm{qs}}/2\pi = 5$ kHz. We clearly see that the second effect is more restrictive as it leads to losses four orders of magnitude higher than those caused by the thermal velocity. There is thus a trade-off in the choice of ω_{qs}. One wants to keep it much larger than the trapping frequencies, such that the final potential can be considered as time averaged, and to have it low enough to minimise Landau-Zener

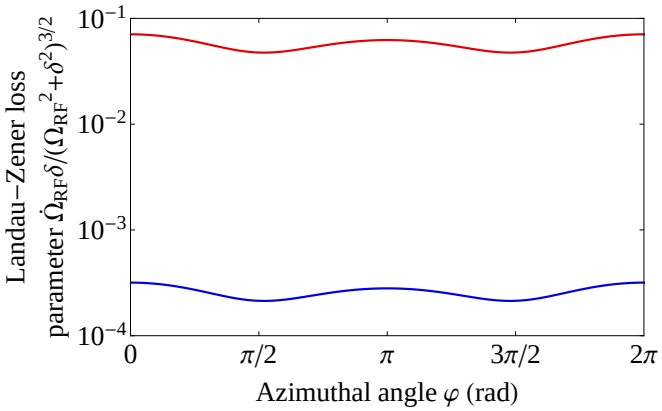

Figure 6.16: Landau-Zener loss parameter as a function of the azimuthal angle φ for atoms at the trapping minimum. The blue curve corresponds to ^{87}Rb atoms at 40 μK in a static potential. The red curve depicts the losses induced by an atom at rest while the quantisation field is rotation at the frequency $\omega_{qs}/2\pi = 5$ kHz.

losses. The current chosen parameters are clearly far from being optimal since $\omega_r/\omega_{qs} \approx 0.07$ and $\delta\ \dot{\Omega}_{RF}/\left(\delta^2+\Omega_{RF}^2\right)^{3/2} \approx 0.05$ at its maximum at $\varphi = 0$. It has been seen that larger detunings significantly reduce the Landau-Zener losses. The potential minimum at the trap position is indeed a (complicated) function that grows monotonically with $|\delta|$, as suggested by Eqn. 6.36. Thus, increasing $|\delta|$ increases the potential minimum but reduces the trapping frequencies. This means that the overall potential seen by the atoms along their azimuthal journey is smoother. Alternatively, by looking at Eqn. 6.39, one can clearly see that increasing δ increases the rightmost part faster than the leftmost one. However, if δ is too large, one can enter the case where $\delta \sim \Omega_0$ and thus violates the rotating wave approximation. Even if both theoretical and experimental investigations have shown that the shape of the trapping potential is not significantly changed in this regime [188], this is beyond the scope of the present work.

6.3 Conclusion

We have presented a novel way to trap atom in annular potentials, using two distinct approaches. The time averaged ring potential of the first section works for macroscopic ring radii and is currently being on the way to being experimentally

implemented at the University of Strathclyde for quantum metrology with bosons or fermions in the quantum degeneracy phase. The dressed state time averaged potential makes advantage of the spatially varying RF field to obtain a ring potential with much smaller dimensions. It offers a smooth potential with no symmetry breaking possibilities other than the induced ring geometry, contrary to the macroscopic time averaged ring which requires two elements (the conductive ring and a quadrupole field) that need to be positioned in combination. Further theoretical investigations of the dressed ring are still necessary to find a range of parameters that allow low loss rate in a "true" time averaged potential. Finally, the loading of the ring was not considered here, as well as evaporative cooling in the ring. These constitute two other main points that should be addressed prior to any experimental realisation of course. Loading could be done by keeping atoms in another magnetic or dipole trap while ramping on the RF and quasi-static fields and evaporative cooling might be possible by switching on a second RF field [189] with atoms loaded in the ring potential.

Chapter 7

Conclusions

In this thesis, we have discussed different aspects to achieve compact and inexpensive atom traps. In Chap. 2, we investigated different ways to obtain high modulation efficiency of an GaAs laser diode operating around 780 nm. It has been shown that there is dependence with the external cavity length and largest sidebands are achieved when the cavity round trip time matches the period of the modulation signal. We presented a technique to increase the amount of microwave power coupled into the laser, since one might expect that the modulation efficiency is a monotonic function of the modulation current. The high frequency complex impedance of the lasers were measured and "stub" matching circuits were fabricated. Although an decrease of the reflection coefficient was observed, no sensible improvement in the sideband amplitude was measured, which can be due to non-linear loss mechanisms within the semiconductor gain medium. Finally, one could take advantage of a resonance with the relaxation oscillations to achieve high efficiency, although this technique seems to be limited to "low frequency" applications since the relaxation oscillations frequencies can correspond to currents that can damage the diode. For a ^{87}Rb application, we managed to get a two frequency laser with large carrier amplitude ($\sim$ 80 mW) and a few mW in the sideband used as repumping light, that is enough to get a descent atom number in the MOT. The investigation on diode laser modulation is ongoing, with perhaps the possibility to get a self-oscillating laser with high sideband amplitude, making use of the principle of Ref. [190], and use that compact system for e.g. CPT magnetometry.

We then presented some early results on magnetic field measurements using CPT spectroscopy in Chap. 3. We saw that this technique is relatively easy to implement and, according to the literature [21], allows very precise measurements that makes it the ideal candidate for all-embedded magnetometers.

The rest of the thesis was focused more precisely on compact traps for cold atoms. We have presented a new magneto-optical trap geometry in Chap. 4, based on a four beam configuration, and have demonstrated its experimental realisation in Chap. 5. Using the results of Chap. 2 on current modulation into a semiconductor laser, we have obtained a single laser, single beam magneto-optical trap with about 10^6 atoms in a extra-vacuo configuration, only limited by the beam size. The grating configuration is a lot more attractive however, since it would be ideal for micro-fabricated apparatus, due to its inherently totally flat nature. Using the PMOT, we trapped a few 10^5 ^{87}Rb atoms that we further cooled to sub-Doppler temperature at about 40 μK with an extra-detuned MOT phase. Repeatable attainment of optical molasses proved elusive, which is a key step in the realisation of any more advanced atomic physics experiment, and we ascribe this to the small beam size, such that the atoms leave too rapidly the beam overlap volume. The next step of the grating MOT is currently being developed, with a custom made diffractor element. The overlap volume will be increased, allowing for more atoms to be trapped and for real optical molasses cooling to take place. We are planning to make an in-vacuo GMOT as a first step to a compact magnetometer where the magnetic field could be probe using CPT spectroscopy during the molasses phase. Following this idea, a micro-fabricated array of GMOTs would also allow one to measure 3D gradient of, e.g. the local magnetic or gravitational fields, as the one depicted on Fig. 7.1.

In the last chapter, we have theoretically investigated two configuration of a toroidal ring trap for cold atom. They both rely on a electrically conductive conductor loop. We first showed that a time alternating magnetic field induces a ac-current in the ring which, in turns, re-emits a cylindrically symmetric magnetic field. From the composition of these two fields, a time-averaged potential can be obtained, and a extra static quadrupole field allows an adiabatic following of the atomic spin in the alternating magnetic field. This ring trap is being implemented at the University of Strathclyde with a ~ 1 cm ring radius, and this experiment

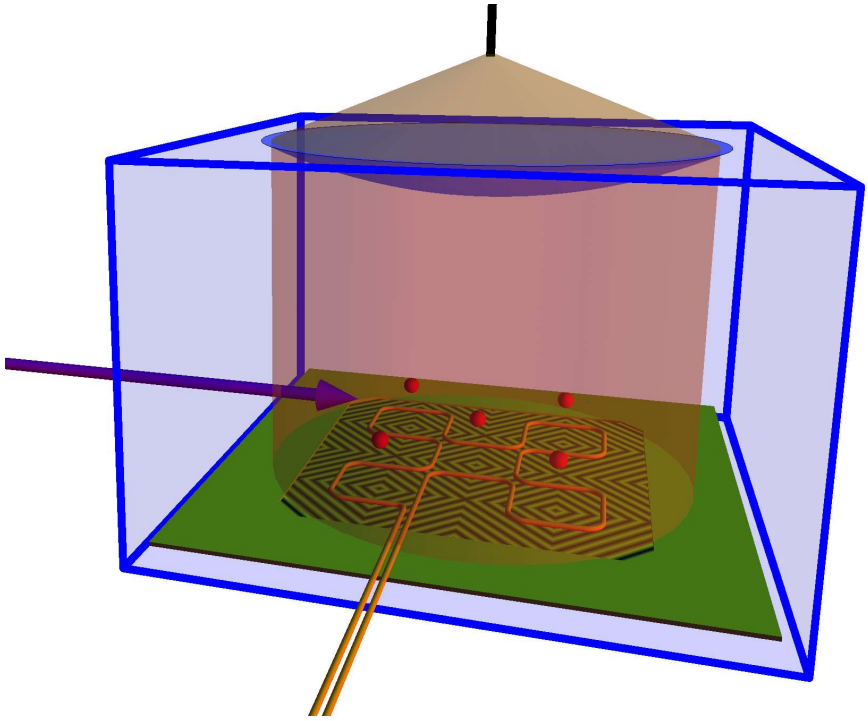

Figure 7.1: Schematics of a compact GMOT gradient sensor. The trapping and repuming light is brought by the fibre above the small vacuum cell and collimated. Five MOTs are formed, allowing for differential measurements. The purple arrow shows a beam probing from the left. The orange wire creates five magnetic zeros (along with a homogenous vertical field, not shown) where the MOTs form. This wire is shown above the gratings in this view, for clarity, although it should be placed underneath them.

will be used for interferometry and gravimetry with rubidium and potassium atoms. We saw, however, that the scaling of the ring to smaller dimensions is not straightforward, since the Majorana losses quickly become detrimental. Following the fact that the Larmor frequency becomes of the same magnitude as the driving frequency for small ring, we developed another ring trap based on dressed state potentials. Thanks to a spatial variation of the rf magnetic field, one can, by applying a horizontal homogenous field, get a torus-like potential. The fast rotation of the horizontal field around the ring axis results in a smooth annular time averaged dressed potential. Such trap could be used as a portable atom interferometer sensor or to study , e.g superfluids in rotation. However,

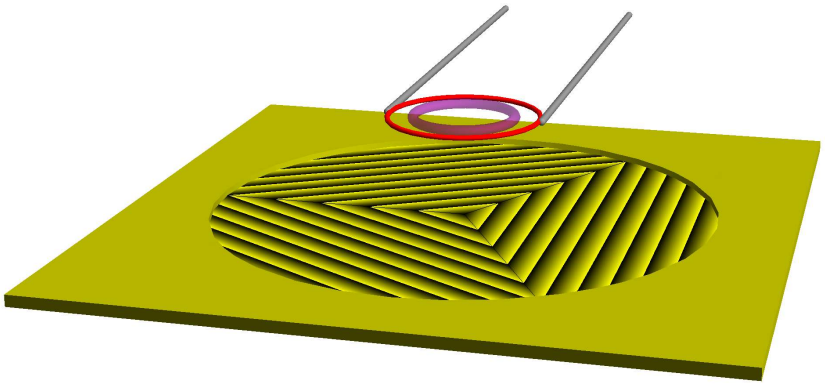

Figure 7.2: Schematics of a micro-fabricated ring trap that uses a planar grating magneto-optical trap as the first stage cooling. The conductor ring is shown in red and the ring potential in transparent purple. The two sticks are used to hold the conductor ring against gravity.

we saw that there is a trade-off between the spin-flip loss rate and the rotation frequency that averages the the instantaneous potential. This work is still ongoing as, in this thesis, only one specific ring geometry was presented, but a more thorough investigation of the range of parameters is on the way. Furthermore, a analysis beyond the rotating wave approximation might be required, as a large detuning would guarantee low spin-flip losses and thus make this scheme ideal for micro-fabrication. Other configurations of the quantisation field will also be considered, such as quadrupole or azimuthal static fields, that could ensure low atom losses, but has the disadvantage of introducing another cylindrically symmetric element, and thus the relative positioning of the induced ring and the static field becomes critical in order to maintain the symmetry.

Finally, we conclude on a possible way to combine the different elements presented in this thesis to get a compact atom interferometer using the time averaged dressed potential on a surface atom chip, as shown in Fig. 7.2, where the first stage cooling is provided by a GMOT along with a single modulated laser.

References

[1] S. Chu, L. Hollberg, J. E. Bjorkholm, A. Cable, and A. Ashkin, *Three-dimensional viscous confinement and cooling of atoms by resonance radiation pressure*, Phys. Rev. Lett. **55**, 48 (1985).

[2] E. L. Raab, M. Prentiss, A. Cable, S. Chu, and D. E. Pritchard, *Trapping of Neutral Sodium Atoms with Radiation Pressure*, Phys. Rev. Lett. **59**, 2631 (1987).

[3] M. Anderson, J. Ensher, M. Matthews, C. Wieman, and E. Cornell, *Observations of Bose-Einstein condensation in a dilute atomic vapor*, Sci. **269**, 198 (1995).

[4] K. B. Davis *et al.*, *Bose-Einstein Condensation in a Gas of Sodium Atoms*, Phys. Rev. Lett. **75**, 3969 (1995).

[5] S. N. Bose, *Plancks Gesetz und Lichtquantenhypothese*, Z. Phys. **26**, 178 (1924).

[6] A. Einstein, *Quantentheorie des einatomigen idealen Gases*, Sitzungsber. Kgl. Preuss. Akad. Wiss. **1924**, 261 (1924).

[7] B. DeMarco and D. S. Jin, *Onset of Fermi Degeneracy in a Trapped Atomic Gas*, Science **285**, 1703 (1999).

[8] M. Greiner, O. Mandel, T. Esslinger, T. W. Hänsch, and I. Bloch, *Quantum phase transition from a superfluid to a Mott insulator in a gas of ultracold atoms*, Nat. **415**, 39 (2002).

[9] J. Billy *et al.*, *Direct observation of Anderson localization of matter waves in a controlled disorder*, Nat. **453**, 891 (2008).

[10] G. Roati *et al.*, *Anderson localization of a non-interacting Bose-Einstein condensate*, Nat. **453**, 895 (2008).

[11] P. D. Lett *et al.*, *Observation of Atoms Laser Cooled below the Doppler Limit*, Phys. Rev. Lett. **61**, 169 (1988).

[12] J. Dalibard and C. Cohen-Tannoudji, *Laser cooling below the Doppler limit by polarization gradients: simple theoretical models*, J. Opt. Soc. Am. B , 2023 (1989).

[13] P. J. Ungar, D. S. Weiss, E. Riis, and S. Chu, *Optical molasses and multilevel atoms: theory*, J. Opt. Soc. Am. B **6**, 2058 (1989).

[14] D. S. Weiss, E. Riis, Y. Shevy, P. J. Ungar, and S. Chu, *Optical molasses and multilevel atoms: experiment*, J. Opt. Soc. Am. B **6**, 2072 (1989).

[15] W. D. Phillips, *Nobel Lecture: Laser cooling and trapping of neutral atoms*, Rev. Mod. Phys. **70**, 721 (1998).

[16] S. Chu, *Nobel Lecture: The manipulation of neutral particles*, Rev. Mod. Phys. **70**, 685 (1998).

[17] C. N. Cohen-Tannoudji, *Nobel Lecture: Manipulating atoms with photons*, Rev. Mod. Phys. **70**, 707 (1998).

[18] E. A. Cornell and C. E. Wieman, *Nobel Lecture: Bose-Einstein condensation in a dilute gas, the first 70 years and some recent experiments*, Rev. Mod. Phys. **74**, 875 (2002).

[19] W. Ketterle, *Nobel lecture: When atoms behave as waves: Bose-Einstein condensation and the atom laser*, Rev. Mod. Phys. **74**, 1131 (2002).

[20] A. Nagel *et al.*, *Experimental realization of coherent dark-state magnetometers*, Europhys. Lett. **44**, 31 (1998).

[21] D. Budker and M. Romalis, *Optical magnetometry*, Nat. Phys. **3**, 227 (2007).

[22] A. Peters, K. Y. Chung, and S. Chu, *Measurement of gravitational acceleration by dropping atoms*, Nat. **400**, 849 (2000).

[23] C. J. Bordé, *Atomic clocks and inertial sensors*, Metrologia **39**, 435 (2002).

[24] P. D. D. Schwindt *et al.*, *Chip-scale atomic magnetometer*, Appl. Phys. Lett. **85**, 6409 (2004).

[25] Q. Bodart *et al.*, *A cold atom pyramidal gravimeter with a single laser beam*, Appl. Phys. Lett. **96**, 134101 (2010).

[26] A. Douahi *et al.*, *Vapour microcell for chip scale atomic frequency standard*, Electron. Lett. **43**, 33 (2007).

[27] C. J. Myatt, N. R. Newbury, and C. E. Wieman, *Simplified atom trap by using direct microwave modulation of a diode laser*, Opt. Lett. **18**, 649 (1993).

[28] S. Knappe *et al.*, *A chip-scale atomic clock based on 87Rb with improved frequency stability*, Opt. Express , 1249 (2005).

[29] K. I. Lee, J. A. Kim, H. R. Noh, and W. Jhe, *Single-beam atom trap in a pyramidal and conical hollow mirror*, Opt. Lett. **21**, 1177 (1996).

[30] J. Reichel, W. Hänsel, and T. W. Hänsch, *Atomic Micromanipulation with Magnetic Surface Traps*, Phys. Rev. Lett. **83**, 3398 (1999).

[31] F. Shimizu, K. Shimizu, and H. Takuma, *Four-beam laser trap of neutral atoms*, Opt. Lett. **16**, 339 (1991).

[32] A. D. Cronin, J. Schmiedmayer, and D. E. Pritchard, *Optics and interferometry with atoms and molecules*, Rev. Mod. Phys. **81**, 1051 (2009).

[33] A. S. Arnold, *Adaptable-radius, time-orbiting magnetic ring trap for Bose-Einstein condensates*, J. Phys. B **37**, L29 (2004).

[34] S. Gupta, K. W. Murch, K. L. Moore, T. P. Purdy, and D. M. Stamper-Kurn, *Bose-Einstein Condensation in a Circular Waveguide*, Phys. Rev. Lett. **95**, 143201 (2005).

[35] J. A. Sauer, M. D. Barrett, and M. S. Chapman, *Storage Ring for Neutral Atoms*, Phys. Rev. Lett. **87**, 270401 (2001).

[36] S. Wu, W. Rooijakkers, P. Striehl, and M. Prentiss, *Bidirectional propagation of cold atoms in a "stadium"-shaped magnetic guide*, Phys. Rev. A **70**, 013409 (2004).

[37] A. S. Arnold, C. S. Garvie, and E. Riis, *Large magnetic storage ring for Bose-Einstein condensates*, Phys. Rev. A **73**, 041606 (2006).

[38] S. E. Olson, M. L. Terraciano, M. Bashkansky, and F. K. Fatemi, *Cold-atom confinement in an all-optical dark ring trap*, Phys. Rev. A **76**, 061404 (2007).

[39] N. Houston, E. Riis, and A. S. Arnold, *Reproducible dynamic dark ring lattices for ultracold atoms*, J. Phys. B **41**, 211001 (2008).

[40] O. Morizot, Y. Colombe, V. Lorent, H. Perrin, and B. M. Garraway, *Ring trap for ultracold atoms*, Phys. Rev. A **74**, 023617 (2006).

[41] I. Lesanovsky *et al.*, *Adiabatic radio-frequency potentials for the coherent manipulation of matter waves*, Phys. Rev. A **73**, 033619 (2006).

[42] S. Hofferberth, I. Lesanovsky, B. Fischer, J. Verdu, and J. Schmiedmayer, *Radiofrequency-dressed-state potentials for neutral atoms*, Nat. Phys. **2**, 710 (2006).

[43] T. Fernholz, R. Gerritsma, P. Krüger, and R. J. C. Spreeuw, *Dynamically controlled toroidal and ring-shaped magnetic traps*, Phys. Rev. A **75**, 063406 (2007).

[44] I. Lesanovsky and W. von Klitzing, *Time-Averaged Adiabatic Potentials: Versatile Matter-Wave Guides and Atom Traps*, Phys. Rev. Lett. **99**, 083001 (2007).

[45] W. H. Heathcote, E. Nugent, B. T. Sheard, and C. J. Foot, *A ring trap for ultracold atoms in an RF-dressed state*, New J. Phys. **10**, 043012 (2008).

[46] E. Nugent, D. McPeake, and J. F. McCann, *Superfluid toroidal currents in atomic condensates*, Phys. Rev. A **68**, 063606 (2003).

[47] C. Ryu *et al.*, *Observation of Persistent Flow of a Bose-Einstein Condensate in a Toroidal Trap*, Phys. Rev. Lett. **99**, 260401 (2007).

[48] P. F. Griffin, E. Riis, and A. S. Arnold, *Smooth inductively coupled ring trap for atoms*, Phys. Rev. A **77**, 051402 (2008).

[49] O. Zobay and B. M. Garraway, *Two-Dimensional Atom Trapping in Field-Induced Adiabatic Potentials*, Phys. Rev. Lett. **86**, 1195 (2001).

[50] R. Pallás-Areny and J. G. Webster, *Analog Signal Processing* (Wiley-Interscience Publication, 1999).

[51] P. Feng and T. Walker, *Inexpensive diode laser microwave modulation for atom trapping*, Am. J. Phys. **63**, 905 (1995).

[52] J. N. Dodd, W. N. Fox, G. W. Series, and M. J. Taylor, *Light Beats as Indicators of Structure in Atomic Energy Levels*, Proc. Phys. Soc. **74**, 789 (1959).

[53] W. E. Bell and A. L. Bloom, *Optically Driven Spin Precession*, Phys. Rev. Lett. **6**, 280 (1961).

[54] C. E. Wieman and L. Hollberg, *Using diode lasers for atomic physics*, Rev. Sci. Instrum. **62**, 1 (1991).

[55] J. R. Barry, E. A. Lee, and D. G. Messerschmitt, *Digital communication* (Springer, 2004).

[56] D. A. Shaddock, *Advances Interferometry for Gravitational Wave Detection*, PhD thesis, The Australian National University, 2000.

[57] F. W. J. Olver, *Bessel Functions of Integer Order*, in *Handbook of Mathematical Functions with Formulas, Graphs and Mathematical Tables*, Dover Publications, 1965.

[58] N. B. Colthup, S. E. Wiberly, and L. H. Daly, *Introduction To Infrared And Raman Spectroscopy* (Academic Press, 1980).

[59] M. Fleischhauer, A. Imamoglu, and J. P. Marangos, *Electromagnetically induced transparency: Optics in coherent media*, Rev. Mod. Phys. **77**, 633 (2005).

[60] E. Arimondo, *Coherent population trapping in laser spectroscopy*, Prog. Opt. **35**, 257 (1996).

[61] J. R. Kuklinski, U. Gaubatz, F. T. Hioe, and K. Bergmann, *Adiabatic population transfer in a three-level system driven by delayed laser pulses*, Phys. Rev. A **40**, 6741 (1989).

[62] H. N. Rutt, *A heterodyne frequency offset locking technique for pulsed or CW lasers*, J. Phys. E **17**, 704 (1984).

[63] R. Steele, *Optical phase-locked loop using semiconductor laser diodes*, Electron. Lett. **19**, 69 (1983).

[64] B. E. Unks, N. A. Proite, and D. D. Yavuz, *Generation of high-power laser light with Gigahertz splitting*, Rev. Sci. Instrum. **78**, 083108 (2007).

[65] M. Bashkansky *et al.*, *Slow-light dynamics of large-bandwidth pulses in warm rubidium vapor*, Phys. Rev. A **72**, 033819 (2005).

[66] S. Kobayashi and T. Kimura, *Injection locking in AlGaAs semiconductor laser*, J. Quant. Electron. **17**, 681 (1981).

[67] S.-Q. Shang and H. J. Metcalf, *Narrowband, high power light from diode lasers*, Appl. Opt. **28**, 1618 (1989).

[68] M. J. Snadden, R. B. M. Clarke, and E. Riis, *Injection-locking technique for heterodyne optical phase locking of a diode laser*, Opt. Lett. **22**, 892 (1997).

[69] A. Yariv, *Optical Electronics* (Holt, Rinehart and Winston, Inc., 1985).

[70] J. Osterwalder and B. Rickett, *Frequency modulation of GaAlAs injection lasers at microwave frequency rates*, J. Quant. Electron. **16**, 250 (1980).

[71] A. Waxman, M. Givon, G. Aviv, D. Groswasser, and R. Folman, *Modulation enhancement of a laser diode in an external cavity*, Appl. Phys. B **95**, 301 (2009).

[72] D. M. Pozar, *Microwave Engineering* (Wiley, 2005).

[73] A. K. Bliskavitskiĭ, Y. K. Vladimirov, and S. K. Taktashov, *Microwave impedance matching of a laser diode to a microstrip line with a 50-Ω characteristic impedance*, J. Quant. Electron. **23**, 251 (1993).

[74] P. Biernacki and A. Mickelson, *Impedance matching of laser diodes using packaged microstrip lines: active and passive*, in *Proc. Las. Elect. Opt. Soc. Ann. Meet.*, volume 1, pp. 238 –239, 1995.

[75] P. H. Smith, *Transmission Line Calculator*, Electronics **12**, 29 (1939).

[76] P. H. Smith, *An Improved Transmission Line Calculator*, Electronics **17**, 130 (1944).

[77] P. W. Milonni, M.-L. Shih, and J. R. Ackerhalt, *Chaos in laser-matter interactions* (World Scientific, 1987).

[78] A. E. Siegman, *Lasers* (University Science Books, 1986).

[79] H. Haug and S. W. Koch, *Quantum Theory of the Optical and Electronic Properties of Semiconductors* (World Scientific, 1993).

[80] S. H. Strogatz, *Nonlinear dynamics and chaos* (Westview Press, 2000).

[81] B. Mroziewicz, M. Bugajski, and W. Nakwaski, *Physics of Semiconductor Lasers* (North-Holland Publishing Company, 1991).

[82] L. Figueroa, C. Slayman, and H.-W. Yen, *High-Frequency Characteristics of GaAlAs Injection Lasers*, IEEE Trans. Micro. Th. Tech. **30**, 1706 (1982).

[83] P. N. Melentiev, M. V. Subbotin, and V. I. Balykin, *Simple and Effective Modulation of Diode Lasers*, Laser Phys. **11**, 1 (2001).

[84] G. Bison *et al.*, *A room temperature 19-channel magnetic field mapping device for cardiac signals*, Appl. Phys. Lett. **95**, 173701 (2009).

[85] G. Grynberg, A. Aspect, and C. Fabre, *Introduction to Quantum Optics* (Cambridge University Press, 2010).

[86] J.-L. Basdevant and J. Dalibard, *Mécanique quantique* (Ecole polytechnique, 2006).

[87] C. Cohen-Tannoudji, J. Dupont-Roc, and G. Grynberg, *Atom-Photon Interactions* (Wiley-Interscience, 1992).

[88] L. Brillouin, *Wave Propagation and Group Velocity* (Academic Press, 1960).

[89] L. V. Hau, S. E. Harris, Z. MDutton, and C. H. Behroozi, *Light speed reduction to 17 metres per second in an ultracold atomic*, Nat. **397**, 594 (1999).

[90] J. Oreg, F. T. Hioe, and J. H. Eberly, *Adiabatic following in multilevel systems*, Phys. Rev. A **29**, 690 (1984).

[91] C. J. Foot, *Atomic Physics* (Oxford University Press, 2005).

[92] J. Vanier, *Atomic clocks based on coherent population trapping: a review*, Appl. Phys. B **81**, 421 (2005).

[93] M. Stähler, S. Knappe, C. Affolderbach, W. Kemp, and R. Wynands, *Picotesla magnetometry with coherent dark states*, Europhys. Lett. **54**, 323 (2001).

[94] I. K. Kominis, T. W. Kornack, J. C. Allred, and M. V. Romalis, *A subfemtotesla multichannel atomic magnetometer*, Nat. **422**, 596 (2003).

[95] E. Arimondo, M. Inguscio, and P. Violino, *Experimental determinations of the hyperfine structure in the alkali atoms*, Rev. Mod. Phys. **49**, 31 (1977).

[96] M. Stähler *et al.*, *Coherent population trapping resonances in thermal* ^{85}*Rb vapor:* D_1 *versus* D_2 *line excitation*, Opt. Lett. **27**, 1472 (2002).

[97] A. Millett-Sikking, I. G. Hughes, P. Tierney, and S. L. Cornish, *DAVLL lineshapes in atomic rubidium*, J. Phys. B **40**, 187 (2007).

[98] J. R. Carson, *Notes on the theory of modulation*, Proc. IRE **10**, 57 (1922).

[99] R. Wynands and A. Nagel, *Precision spectroscopy with coherent dark states*, Appl. Phys. B **68**, 1 (1999).

[100] H. S. Moon, S. E. Park, Y.-H. Park, L. Lee, and J. B. Kim, *Passive atomic frequency stadard based on coherent population trapping in* ^{87}*Rb using injection-locked lasers*, J. Opt. Soc. Am. B **23**, 2393 (2006).

[101] S. J. Park, H. Cho, T. Y. Kwon, and H. S. Lee, *Transient coherence oscillation induced by a detuned Raman field in a rubidium* Λ *system*, Phys. Rev. A **69**, 023806 (2004).

[102] C. Kittel and H. Kroemer, *Thermal Physics* (Wiley, 1980).

[103] D. G. Fried *et al.*, *Bose-Einstein Condensation of Atomic Hydrogen*, Phys. Rev. Lett. **81**, 3811 (1998).

[104] C. Cohen-Tannoudji, B. Diu, and F. Laloë, *Quantum Mechanics, volume one* (Wiley-Interscience, 1977).

[105] R. N. Zare, *Angular Momentum* (Wiley-Interscience, 1988).

[106] A. S. Arnold, *Cool Things you can do with Lasers*, Master's thesis, University of Otago, 1996.

[107] C. S. Adams and E. Riis, *Laser cooling and trapping of neutral atoms*, Prog. Quant. Electron. **21**, 1 (1997).

[108] C. Salomon, J. Dalibard, W. D. Phillips, A. Clairon, and S. Guellati, *Laser cooling of cesium atoms below 3 μK*, Europhys. Lett. **12**, 683 (1990).

[109] A. S. Arnold, *Preparation and Manipulation of an ^{87}Rb Bose-Einstein Condensate*, PhD thesis, University of Sussex, 1999.

[110] Z. Lin, K. Shimizu, M. Zhan, F. Shimizu, and H. Takuma, *Laser Cooling and Trapping of Li*, Jap. Jour. Appl. Phys. **30**, 1324 (1991).

[111] C. Chesman, E. G. Lima, F. A. M. de Oliveira, S. S. Vianna, and J. W. R. Tabosa, *Two- and four-beam magneto-optical trapping of neutral atoms*, Opt. Lett. , 1237 (1994).

[112] M. Vangeleyn, P. F. Griffin, E. Riis, and A. S. Arnold, *Single-laser, one beam, tetrahedral magneto-optical trap*, Opt. Express **17**, 13601 (2009).

[113] K. Beloy, A. Derevianko, V. A. Dzuba, and V. V. Flambaum, *Micromagic Clock: Microwave Clock Based on Atoms in an Engineered Optical Lattice*, Phys. Rev. Lett. **102**, 120801 (2009).

[114] M. Hämäläinen, R. Hari, R. J. Ilmoniemi, J. Knuutila, and O. V. Lounasmaa, *Magnetoencephalography—theory, instrumentation, and applications to noninvasive studies of the working human brain*, Rev. Mod. Phys. **65**, 413 (1993).

[115] S. N. Erné, H.-D. Hahlbohm, and H. Lübbig, *Theory of rf-biased superconducting quantum interference device for nonhysteretic regime*, J. Appl. Phys. **47**, 5440 (1976).

[116] D. Drung, S. Bechstein, K.-P. Franke, M. Scheiner, and T. Schurig, *Improved direct-coupled dc SQUID read-out electronics with automatic bias voltage tuning*, IEEE Trans. Appl. Supercond. **11**, 880 (2001).

[117] J. Denschlag, D. Cassettari, and J. Schmiedmayer, *Guiding Neutral Atoms with a Wire*, Phys. Rev. Lett. **82**, 2014 (1999).

[118] H. Ott, J. Fortagh, G. Schlotterbeck, A. Grossmann, and C. Zimmermann, *Bose-Einstein Condensation in a Surface Microtrap*, Phys. Rev. Lett. **87**, 230401 (2001).

[119] W. Hänsel, P. Hommelhoff, T. W. Hänsch, and J. Reichel, *Bose-Einstein condensation on a microelectronic chip*, Nature **413**, 498 (2001).

[120] J. Estève *et al.*, *Realizing a stable magnetic double-well potential on an atom chip*, Eur. Phys. J. **35**, 141 (2005).

[121] C. D. J. Sinclair *et al.*, *Bose-Einstein condensation on a permanent-magnet atom chip*, Phys. Rev. A **72**, 031603 (2005).

[122] A. Shevchenko *et al.*, *Trapping atoms on a transparent permanent-magnet atom chip*, Phys. Rev. A **73**, 051401 (2006).

[123] T. Schumm *et al.*, *Matter-wave interferometry in a double well on an atom chip*, Nat. Phys. **1**, 57 (2005).

[124] S. Pollock, J. P. Cotter, A. Laliotis, and E. A. Hinds, *Integrated magneto-optical traps on a chip using silicon pyramid structures*, Opt. Express **17**, 14109 (2009).

[125] M. Trupke *et al.*, *Pyramidal micromirrors for microsystems and atom chips*, Appl. Phys. Lett. **88**, 071116 (2006).

[126] G. Lewis *et al.*, *Fabrication of Magnetooptical Atom Traps on a Chip*, J. MEMS **18**, 347 (2009).

[127] J. J. Arlt, O. Maragò, S. Webster, S. Hopkins, and C. J. Foot, *A pyramidal magneto-optical trap as a source of slow atoms*, Opt. Comm. **157**, 303 (1998).

[128] A. S. Arnold, J. S. Wilson, and M. G. Boshier, *A simple extended-cavity diode laser*, Rev. Sci. Instrum. **69**, 1236 (1998).

[129] S. Haroche and F. Hartmann, *Theory of Saturated-Absorption Line Shapes*, Phys. Rev. A **6**, 1280 (1972).

[130] S. Bize *et al.*, *High-accuracy measurement of the ^{87}Rb ground-state hyperfine splitting in an atomic fountain*, Europhys. Lett. **45**, 558 (1999).

[131] J. Ye, S. Swartz, P. Jungner, and J. L. Hall, *Hyperfine structure and absolute frequency of the 87Rb 5P3/2 state*, Opt. Lett. **21**, 1280 (1996).

[132] U. Volz and H. Schmoranzer, *Precision lifetime measurements on alkali atoms and on helium by beam–gas–laser spectroscopy*, Physica Scripta **1996**, 48 (1996).

[133] G. C. Bjorklund, *Frequency-modulation spectroscopy: a new method for measuring weak absorptions and dispersions*, Opt. Lett. **5**, 15 (1980).

[134] A. J. Wallard, *Frequency stabilization of the helium-neon laser by saturated absorption in iodine vapour*, J. Phys. E **5**, 926 (1972).

[135] M. Vangeleyn, *Spectroscopie par absorption saturée avec interféromètre de Sagnac et modulation de fréquence. Application à la stabilisation de lasers*, Master's thesis, Observatoire de la Côte d'Azur and Université de Nice Sophia-Antipolis, 2006.

[136] C. Kilian, *Modern Control Technology: Components and Systems* (Delmar Thomson Learning, 2005).

[137] M. Zawadzki, *Bose-Einstein condensate manipulation and interferometry*, PhD thesis, University of Strathclyde, 2010.

[138] D. A. Smith and I. G. Hughes, *The role of hyperfine pumping in multilevel systems exhibiting saturated absorption*, Am. J. Phys. **72**, 631 (2004).

[139] K. Lindquist, M. Stephens, and C. Wieman, *Experimental and theoretical study of the vapor-cell Zeeman optical trap*, Phys. Rev. A **46**, 4082 (1992).

[140] M. Greiner, I. Bloch, T. W. Hänsch, and T. Esslinger, *Magnetic transport of trapped cold atoms over a large distance*, Phys. Rev. A **63**, 031401 (2001).

[141] H. J. Lewandowski, D. M. Harber, D. L. Whitaker, and E. A. Cornell, *Simplified System for Creating a Bose-Einstein Condensate*, J. Low Temp. Phys. **132**, 309 (2003).

[142] D. A. Smith, A. S. Arnold, M. J. Pritchard, and I. G. Hughes, *Experimental single-impulse magnetic focusing of launched cold atoms*, J. Phys. B **41**, 125302 (2008).

[143] P. D. Lett *et al.*, *Optical molasses*, J. Opt. Soc. Am. B , 2084 (1989).

[144] M. Drewsen *et al.*, *Investigation of sub-Doppler cooling effects in a cesium magneto-optical trap*, Appl. Phys. B **59**, 283 (1994).

[145] N. P. Bigelow and M. G. Prentiss, *Observation of channeling of atoms in the three-dimensional interference pattern of optical standing waves*, Phys. Rev. Lett. **65**, 29 (1990).

[146] A. M. Steane and C. J. Foot, *Laser Cooling below the Doppler Limit in a Magneto-Optical Trap*, Europhys. Lett. , 231 (1991).

[147] Y. Shevy, D. S. Weiss, P. J. Ungar, and S. Chu, *Bimodal speed distributions in laser-cooled atoms*, Phys. Rev. Lett. **62**, 1118 (1989).

[148] M. Vangeleyn, P. F. Griffin, E. Riis, and A. S. Arnold, *Laser cooling with a single laser beam and a planar diffractor*, Opt. Lett. , 3453 (2010).

[149] G. Sagnac, *L'éther lumineux démontré par l'effet du vent relatif d'éther dans un interféromètre en rotation uniforme*, C.R. Acad. Sci. Paris **157**, 708 (1913).

[150] G. E. Stedman, *Ring-laser tests of fundamental physics and geophysics*, Rep. Prog. Phys. **60**, 615 (1997).

[151] L. J. Garay, J. R. Anglin, J. I. Cirac, and P. Zoller, *Sonic Analog of Gravitational Black Holes in Bose-Einstein Condensates*, Phys. Rev. Lett. **85**, 4643 (2000).

[152] K. Kärkkäinen, A. D. Jackson, and G. M. Kavoulakis, *Bright solitary waves in a Bose-Einstein condensate and their interactions*, Phys. Rev. A **78**, 033610 (2008).

[153] N. G. Parker, A. M. Martin, S. L. Cornish, and C. S. Adams, *Collisions of bright solitary matter waves*, J. Phys. B **41**, 045303 (2008).

[154] E. M. Wright, J. Arlt, and K. Dholakia, *Toroidal optical dipole traps for atomic Bose-Einstein condensates using Laguerre-Gaussian beams*, Phys. Rev. A **63**, 013608 (2000).

[155] E. Courtade, O. Houde, J.-F. m. c. Clément, P. Verkerk, and D. Hennequin, *Dark optical lattice of ring traps for cold atoms*, Phys. Rev. A **74**, 031403 (2006).

[156] S. K. Schnelle, E. D. van Ooijen, M. J. Davis, N. R. Heckenberg, and H. Rubinsztein-Dunlop, *Versatile two-dimensional potentials for ultra-cold atoms*, Opt. Express **16**, 1405 (2008).

[157] K. Henderson, C. Ryu, C. MacCormick, and M. G. Boshier, *Experimental demonstration of painting arbitrary and dynamic potentials for Bose-Einstein condensates*, N. J. Phys. **11**, 043030 (2009).

[158] D. S. Naik and C. Raman, *Optically plugged quadrupole trap for Bose-Einstein condensates*, Phys. Rev. A **71**, 033617 (2005).

[159] F. M. H. Crompvoets, H. L. Bethlem, R. T. Jongma, and G. Meijer, *A prototype storage ring for neutral molecules*, Nature **411**, 174 (2001).

[160] M. J. Madsen and C. H. Gorman, *Compact toroidal ion-trap design and optimization*, Phys. Rev. A **82**, 043423 (2010).

[161] S. Kraft *et al.*, *Anomalous longitudinal magnetic field near the surface of copper conductors*, J. Phys. B **35**, L469 (2002).

[162] A. E. Leanhardt *et al.*, *Propagation of Bose-Einstein Condensates in a Magnetic Waveguide*, Phys. Rev. Lett. **89**, 040401 (2002).

[163] A. E. Leanhardt *et al.*, *Bose-Einstein Condensates near a Microfabricated Surface*, Phys. Rev. Lett. **90**, 100404 (2003).

[164] M. P. A. Jones, C. J. Vale, D. Sahagun, B. V. Hall, and E. A. Hinds, *Spin Coupling between Cold Atoms and the Thermal Fluctuations of a Metal Surface*, Phys. Rev. Lett. **91**, 080401 (2003).

[165] J.-B. Trebbia, C. L. Garrido Alzar, R. Cornelussen, C. I. Westbrook, and I. Bouchoule, *Roughness Suppression via Rapid Current Modulation on an Atom Chip*, Phys. Rev. Lett. **98**, 263201 (2007).

[166] D. J. Griffiths, *Introduction to Electrodynamics* (Prentice Hall, 1999).

[167] J. D. Jackson, *Classical Electrodynamics* (Wiley, 1999).

[168] R. H. Good, *Elliptic integrals, the forgotten functions*, Eur. J. Phys. **22**, 119 (2001).

[169] W. H. Wing, *On neutral particle trapping in quasistatic electromagnetic fields*, Prog. Quant. Electron. **8**, 181 (1984).

[170] E. A. Hinds and I. G. Hughes, *Magnetic atom optics: mirrors, guides, traps, and chips for atoms*, J. Phys. D **32**, R119 (1999).

[171] A. L. Migdall, J. V. Prodan, W. D. Phillips, T. H. Bergeman, and H. J. Metcalf, *First Observation of Magnetically Trapped Neutral Atoms*, Phys. Rev. Lett. **54**, 2596 (1985).

[172] D. E. Pritchard, *Cooling Neutral Atoms in a Magnetic Trap for Precision Spectroscopy*, Phys. Rev. Lett. **51**, 1336 (1983).

[173] I. I. Rabi, N. F. Ramsey, and J. Schwinger, *Use of Rotating Coordinates in Magnetic Resonance Problems*, Rev. Mod. Phys. **26**, 167 (1954).

[174] E. Majorana, *Atomi orientati in campo magnetico variabile*, Nuovo Cimento **9**, 43 (1932).

[175] T. Bergeman, G. Erez, and H. J. Metcalf, *Magnetostatic trapping fields for neutral atoms*, Phys. Rev. A **35**, 1535 (1987).

[176] O. Zobay and B. M. Garraway, *Atom trapping and two-dimensional Bose-Einstein condensates in field-induced adiabatic potentials*, Phys. Rev. A **69**, 023605 (2004).

[177] O. Morizot, *Pièges radiofréquence très anisotropes pour un condensat de Bose-Einstein*, PhD thesis, Université Paris 13, 2007.

[178] Y. Colombe *et al.*, *Ultracold atoms confined in rf-induced two-dimensional trapping potentials*, Europhys. Lett. **67**, 593 (2004).

[179] P. Böhi *et al.*, *Coherent manipulation of Bose-Einstein condensates with state-dependent microwave potentials on an atom chip*, Nat. Phys. **5**, 592 (2009).

[180] M. F. Riedel *et al.*, *Atom-chip-based generation of entanglement for quantum metrology*, Nature **464**, 1170 (2010).

[181] M. Gildemeister *et al.*, *Trapping ultracold atoms in a time-averaged adiabatic potential*, Phys. Rev. A **81**, 031402 (2010).

[182] E. Hecht, *Optics* (Addison-Wesley, 1987).

[183] B. Davies, *Integral transforms and their applications* (Springer, 2002).

[184] B. M. Garraway, private communication, 2010.

[185] I. Lesanovsky, S. Hofferberth, J. Schmiedmayer, and P. Schmelcher, *Manipulation of ultracold atoms in dressed adiabatic radio-frequency potentials*, Phys. Rev. A **74**, 033619 (2006).

[186] Q. Beaufils *et al.*, *Radio-frequency-induced ground-state degeneracy in a Bose-Einstein condensate of chromium atoms*, Phys. Rev. A **78**, 051603 (2008).

[187] A. Messiah, *Quantum mechanics* (North-Holland Publishing Company, 1961).

[188] S. Hofferberth, B. Fischer, T. Schumm, J. Schmiedmayer, and I. Lesanovsky, *Ultracold atoms in radio-frequency dressed potentials beyond the rotating-wave approximation*, Phys. Rev. A **76**, 013401 (2007).

[189] R. K. Easwaran *et al.*, *RF spectroscopy in a resonant RF-dressed trap*, J. Phys. B **43**, 065302 (2010).

[190] T. Slight *et al.*, *A Liénard Oscillator Resonant Tunnelling Diode-Laser Diode Hybrid Integrated Circuit: Model and Experiment*, J. Quant Electron. **44**, 1158 (2008).